High-resolution X-Ray spectral diagnostics of Active Galactic Nuclei
Steenbrugge, K.C.

High-resolution X-ray spectral diagnostics of Active Galactic Nuclei

PROEFSCHRIFT

ter verkrijging van
de graad van Doctor aan de Universiteit Leiden,
op gezag van de Rector Magnificus Dr. D. D. Breimer,
hoogleraar in de faculteit der Wiskunde en
Natuurwetenschappen en die der Geneeskunde,
volgens besluit van het College voor Promoties
te verdedigen op woensdag 2 februari 2005
klokke 15.15 uur

door

Katrien Christine Steenbrugge
geboren te Gent, België
in 1976

Promotiecomissie

Promotor: Prof. dr. R. Schilizzi
Co-promotor: Dr. J. S. Kaastra (SRON)

Referent: Prof. F. Verbunt (Universiteit Utrecht)

Overige leden: Prof. dr. G. K. Miley
                 Prof. dr. K. Kuijken
                 Dr. H. Röttgering
                 Prof. Dr. P. T. de Zeeuw

Contents

iv

Chapter 1

Introduction

1.1 Motivation

In the center of most galaxies, even non active galaxies such as our own Milky Way, there is a super massive black hole (SMBH). The masses of these SMBH's range from 10^6 to 10^9 $M_\odot$. The luminosity radiated by the infalling gas depends on its mass and its trajectory in the gravitational potential. In the Milky Way the amount of gas captured by the SMBH is rather limited. The captured gas either belongs to a giant molecular cloud moving near the SMBH; or is accumulated from the outer layers of stars, which have been stripped due to a gravitational interaction with the SMBH. This gas falls into the SMBH without forming an accretion disk. As a result, the emission from our SMBH is barely detectable in most wavelength bands. However, the gravitational potential of our SMBH is traced by the stellar orbits in its vicinity. Using one such stellar orbit Schödel et al. (2002) determined the mass of our SMBH to be $3.7 \pm 1.5 \times 10^6$ $M_\odot$. In contrast, in an Active Galactic Nucleus (AGN) there is a large amount of gas, which presumably forms an accretion disk before spiraling into the SMBH. The observed luminosity of an AGN is in large part due to radiation from the accretion disk.

Using the standard thin disk theory (Shakura & Sunyaev 1973) one can calculate the temperature of the disk as a function of its radius. It is found that most of the energy is radiated at about 3 gravitational radii. The disk spectrum can be approximated by a multi-temperature black body. However, as most of the radiation is emitted from about 3 gravitational radii, the spectrum can also be approximated by a standard black body. This black body spectrum has a peak in the extreme UV/the soft X-ray range of the spectrum. Our Milky Way absorbs the extreme UV radiation, thus the accretion disks

1

of AGNs are best studied in the soft X-ray regime. Observing AGN in the X-rays we thus study the environment surrounding the SMBH.

1.2 Taxonomy

Active Galactic Nuclei are known under several different names, from classifying timing or spectral characteristics. Although originally all these classes were thought to be objects with different physical properties, more recently they have mostly been unified as due to an active SMBH fed through an accretion disk and producing a pair of jets. In this theory the inclination angle under which we view the AGN explains a number of the different characteristics observed (Antonucci & Miller 1985; Barthel 1989; Urry & Padovani 1995). For instance, blazars which are very variable in the optical have been identified as AGNs in which we look directly into the jet.

A large number of AGN can be classified into two broad classes, the unobscured (Type 1) and obscured (Type 2). The continuum emission of Type 2 AGNs is absorbed by gas and dust in the optical, UV and soft X-ray band and re-radiated in the infrared. Due to inverse-Compton scattering these AGNs are detected in the hard X-ray and soft gamma-ray band. Type 1 AGNs are not, or much less obscured by dust, and are bright in the extreme UV and soft X-rays. A subset of these Type 1 and Type 2 AGNs are the Seyfert galaxies, which are believed to be gas-rich spirals. Spectra of Seyfert 1 galaxies show broad and narrow emission lines; spectra of Seyfert 2 galaxies only show narrow emission lines, when viewed in unpolarized optical light.

Antonucci & Miller (1985) discovered that spectra of Seyfert 2 galaxies show broad emission lines in polarized light. Most of the photons emitted in the broad line region are scattered out of our line of sight by intervening cold gas. However, by suppressing the unscattered continuum with a polarization filter, Antonucci & Miller (1985) detected these broad emission lines. The detection of these broad emission lines in spectra of Seyfert 2 galaxies hinted that Seyfert 1 and Seyfert 2 galaxies have the same physical properties, but that the Seyfert 2 galaxies are obscured (Antonucci & Miller 1985). The source of obscuration is generally thought to be a torus in the equatorial plane.

1.3 Observational facts from X-ray observations

The black body spectrum emitted from the accretion disk, as predicted by the thin disk theory (Shakura & Sunyaev 1973) was already detected in early observations of Seyfert 1 galaxies. These observations also showed that AGNs emit a hard X-ray continuum,

which is modeled as a power-law with a cut-off energy above 100 keV, and is explained by inverse-Compton scattering of UV/soft X-ray photons on hot electrons. These hot electrons are located near the accretion disk and are collectively referred to as the hot corona. A possible location for this hot corona is the inner edge of the accretion disk (e.g. Chakrabarti & Titarchuk 1995).

The power law becomes harder around 10 keV, due to reflection on a dense and lowly ionized gas. Passing through this gas the photons lose energy through Compton scattering and absorption. As a result, the original power-law slope is changed, and appears to become harder at 10 keV. The narrow Fe Kα emission line observed in most Seyfert galaxies is also due to reflection on cold material. In the case of NGC 1068 this cold gas is located less than 2 pc from the nucleus and is unresolved with current infrared interferometry instruments such as MIDI. This observation severely limits possible models for this gas component, as the gas pressure can not support the gas in the strong gravitational field and it should collapse (Röttgering et al. 2004). This dense gas may be located in a torus at the outer edge of the accretion disk. Alternatively, the dense gas is the optically thick accretion disk (Lightman & White 1988; Guilbert & Rees 1988). However, the data are also consistent with a wind that is radiatively driven by dust grain opacity (Königl & Kartje 1994). Another possibility is that the dense gas is in the form of $5 - 10$ large clouds, which are preferentially located in the equatorial plane (Nenkova, Ivezić & Elitzur 2002). Common names for this neutral gas are the inner torus, molecular torus or obscuring torus. I will use the term torus, whether or not it occurs in a torus shape.

Some X-ray observations indicate that there is in addition to the narrow Fe Kα emission line a relativistically broadened Fe Kα emission line (Tanaka et al. 1995; Wilms et al. 2001) formed at the inner edge of the accretion disk. If this line is indeed relativistically broadened then from the line profile we can derive the distance between the inner edge of the accretion disk and the event horizon of the SMBH. From this distance one can determine the radius of the last stable circular orbit and thus the rotational velocity of the black hole. In the well studied case of MGC -6-30-15 the line profile is consistent with a maximally rotating (Kerr) black hole (Iwasawa et al. 1996; Wilms et al. 2001). Also the inclination angle of the accretion disk can be determined from the line profile. This measurement is important as it can discriminate between the different models for the cores of AGN's. Possibly, in the soft X-ray band, relativistically broadened emission lines from O VIII Lyα, N VII Lyα and C VI Lyα are also detected (Branduardi-Raymont et al. 2001; Sako et al. 2003). These relativistically broadened emission lines are presumably emitted from the accretion disk, similar to the relativistically broadened Fe Kα emission line.

For Seyfert 1 galaxies there is in addition to the continuum described above a wealth of absorption lines from very lowly ionized ions (Si IV) to nearly completely ionized

ions (Fe XXIV). The absorption lines are all blueshifted, indicating that the absorption occurs in an outflow. In the UV band, where higher spectral resolution is obtained, these absorption lines often have several different velocity components, indicating that there are several kinematic components. The location of the narrow absorption line region is still uncertain, with estimates ranging between < 0.1 pc (Reeves et al. 2004) and 300 pc (Behar et al. 2003) for NGC 3783.

In the optical, UV and X-ray band of the spectrum we detect narrow emission lines emitted at the narrow line region (NLR) and broad emission lines emitted at the broad line region (BLR). The narrow emission lines are ten times broader than the narrow absorption lines, the broad lines are ten times broader than the narrow emission lines. The ionization range of the broad and narrow emission lines is significantly smaller, at least in the well studied case of NGC 5548, than the range observed for the narrow absorption lines. The narrow emission lines are probably formed at a different location than the narrow absorption lines or the broad emission lines. The NLR is generally extended (several lightmonths) and is fragmentary in shape (Ulvestad, Wilson & Sramek 1981). The size of the BLR can be determined using reverberation mapping, and has a size of a few light days to a lightmonth (Peterson & Wandel 2000).

1.4 Cartoon models for the core of an AGN

The X-ray observations as well as those in the optical, radio and infrared can be explained by two different models describing the inner parsecs of an AGN. Both models unify the unobscured and obscured AGNs by invoking different viewing angles. The first model is based on optical and infrared observations (Antonucci & Miller 1985; Urry & Padovani 1995); the second model, by Elvis (2000), is based on X-ray and UV observations.

1.4.1 Standard model

The standard model is depicted in Fig. 1.1. In the center is the SMBH with its accretion disk and surrounded by a donut shape torus in the equatorial plane. However, other geometries for this torus are also possible, see Chapter 1.3. Thus if we look directly at the accretion disk, i.e. an inclination angle smaller than about $60°$, then the object is classified as a Seyfert 1 galaxy. For Seyfert 2 galaxies we look directly at the torus, which absorbs the continuum emission from the accretion disk. The inclination angle is thus between $60°$ and $90°$, however, the exact range depend on the opening angle of the torus. In a cone along the polar directions there is a hot outflowing wind accelerated by radiation pressure. Embedded in this wind are two types of clouds. Those
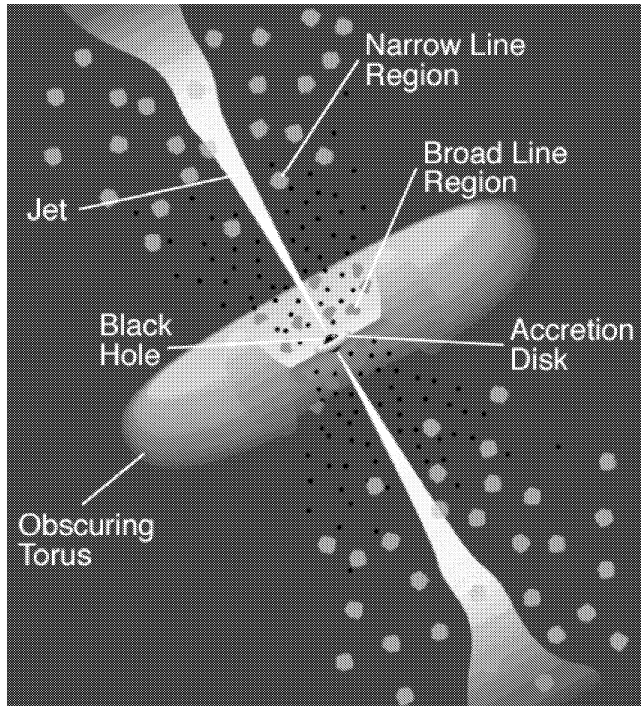
Figure 1.1: The standard model for the unification of AGN. For a Seyfert 1 galaxy one looks directly at the accretion disk, while for a Seyfert 2 galaxy one looks through the torus, here labeled obscuring torus. From Urry & Padovani (1995).

clouds close to the black hole emit broadened emission lines, those farther away emit the narrow emission lines. The broadening of these emission lines is due to Keplerian motion around the SMBH. These clouds are generally assumed to be in pressure equilibrium with the hot outflowing wind, as otherwise they will disintegrate (Krolik & Kriss 2001). However, other confinement mechanisms, such as magnetic confinement are also possible. These clouds could form from the irradiated inner edge of the torus, or from the accretion disk. The location of the narrow absorption lines is not specified, but probably the narrow absorption lines are formed in clouds embedded in the outflow.

1.4.2 Model by Elvis

The model by Elvis (2000) is depicted in Fig. 1.2. In the center is the SMBH and the accretion disk. Starting from an instability on the accretion disk there is an outflow in the form of a narrow stream. This outflow is bent and accelerated due to radiation pressure. As the outflow is bent, there is a large range of inclination angles for which absorption from this outflow can be seen. Depending on where the line of sight intersects this outflow, narrow absorption lines (close to the SMBH) or broad absorption lines as detected in broad absorption line quasars (far from the SMBH) are produced. The broadening of these absorption lines is due to the non-collimation of the outflow and not due to Keplerian rotation. The broad emission line clouds are carried along in the flow with which they are in pressure equilibrium. The broadening of these clouds is due to Keplerian rotation, similar to the standard model. In this model no torus is specified, as the outflow itself absorbs the continuum emission. However, an equatorial torus is not excluded.

One can generalize this this model to have several outflows to explain the different kinematic components observed in the UV band. In the Elvis model the clouds are in pressure equilibrium within an outflow. However, in a more general model this is not a prerequisite. An alternative is that the stream expands as it moves outward, and that there is a density gradient orthogonal to the outflow. This density gradient results in a gradient in the ionization of the gas.

1.4.3 Comparison between the models

The main difference between the models is the viewing angle one predicts is necessary to observe a Seyfert 1 or a Seyfert 2 galaxy. In the standard model if the disk is observed face on then the AGN is classified as a Seyfert 1 galaxy, if observed edge on, through the torus, it is classified as a Seyfert 2 galaxy. In the model by Elvis, Seyfert 1 galaxies which have warm absorbers are observed if the inclination angle of the disk is between $\sim 60°$ and $90°$.

Both models predict a warm absorber with a few ionization states, but a generalized Elvis model could explain a warm absorber with a continuous ionization range. There is observational evidence (Chapter 5) that at least some of the absorbing clouds cannot be in pressure equilibrium with the hot outflow. Thus some other form of confinement, such as magnetic, is necessary for a cloud model. Both models have a problem explaining the several, well separated outflow velocities observed for most UV absorption lines (Crenshaw et al. 1999). These velocity components are stable over timescales of decades, and only small velocity variations have been observed (Gabel et al. 2003). One of these kinematic components is present over an ionization range from C IV to

GEOMETRY

TAXONOMY

40–45%

No Absorbers

10–20%

Warm Highly Ionized Medium
'WHIM'

BAL

τ =1

τ =1

NAL

40–45%

Massive Black Hole

Accretion Disk

v=1000 km/s

NH~10(22)

τ =1

τ =1

r~10(16)cm

Compton scattered
radiation

v(vertical) = v(radial)

NH~10(24)

v=10,000–60,000 km/s
Δv=10,000–60,000 km/s

UV/X–ray luminosity source

PHYSICS

KINEMATICS
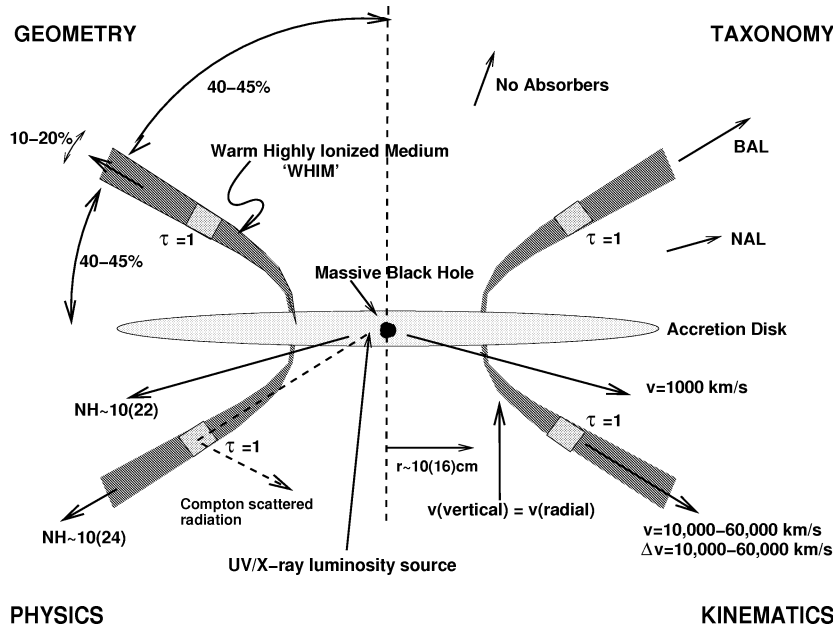
Figure 1.2: The model by Elvis (2000), where the outflow is in the form of narrow streams rather than a cone. The outflow is bent due to radiation pressure, and the narrow and broad absorption lines and broad emission lines are formed in this outflow.

Si XIII (Chapter 5). It seems improbable that clouds with different ionization parameters have the same outflow velocity, while clouds with the same ionization parameter have different outflow velocities. These different outflow velocities and their stability are more naturally explained in a generalized Elvis model.

In a generalized Elvis model one can explain the different outflow velocities by outflows formed at different distances. However, with time, radiation pressure will merge the different outflows (Proga, private communication). Assuming steady state accretion, then from the observed ionization parameters and the outflow velocity we conclude that the outflow has a small opening angle (Chapter 4). These narrow outflows are inconsistent with the ionization cone presented in the standard model.

Some observations cannot be explained by either model. From UV spectra cross-correlation results between different epoch spectra the minimum number of broad line clouds can be estimated. In the case of NGC 4151 the number of clouds estimated

7

is about an order of magnitude more than the number of clouds calculated the size of the BLR, R, the covering factor, C, and the size of the clouds, r: $N = 4CR^2/r^2 = 2\times10^5 LU^{-4}$ with L the luminosity in 10^{46} erg s $^{-1}$ and U the ionization parameter (Arav et al. 1998). This casts doubt on the cloud model for broad emission lines. In 3C273 a jet and broadened emission lines (Sellgren et al. 1983) are observed, which seems to indicate that the broad emission line clouds have a rotational plane perpendicular to the jet, or have chaotic instead of Keplerian motions.

1.5 Wind models

The measured blueshift of the UV absorption lines led to the conclusion that the absorbing gas is in the form of an outflow (Crenshaw et al. 1999). Several mechanisms for accelerating this outflow have been proposed, from gas pressure to magneto-centrifugal force and radiation pressure. The main problem for all these models is to explain why the gas is not fully ionized. The radiation field from the accretion disk and the comptonized photons is such that unless shielding occurs, the gas should be completely ionized. For this reason many models predict that the outflow has to be in the form of clouds, where there is a density gradient. Another possibility is that the outflow is somehow shielded, leading to an attenuated radiation field at the origin of the outflow.

If the wind is driven by line radiation pressure, then the wind is shielded by the X-ray opacity, and the wind itself has a density gradient resulting in a continuous ionization range (Proga, Stone & Kallman 2000). The radiation driven wind models indicates that a self-shielded wind can be launched from a radius $\leq 10^{14}$ m. The ratio of X-ray to UV opacity determines the outflow velocity. For a large ratio there will be a fast outflow, such as observed in broad absorption line quasars. For a small ratio a slow wind is created, as the radiation is nearly completely shielded by the X-ray gas resulting in a lessening of the line driving force. This slow wind is observed as the warm absorber in Seyfert 1 galaxies. These predictions are consistent with the observation that the soft X-ray luminosity is anti-correlated with the width of the C IV UV absorption line (Proga, Stone & Kallman 2000).

In all wind models most of the gas is completely ionized. In the radiation driven winds, the wind is bent due to radiation pressure, and is close to the accretion disk, while the regions near the poles are of low density and completely ionized. For the slow winds, as observed in Seyfert 1 galaxies, the radiation driven wind models predict a column density N_H of around 10^{28} m^{-2}. From the ionized X-rays spectra detailed in this thesis we find a N_H around 10^{27} m^{-2}, excluding completely ionized gas. From the line driven radiation pressure codes one predicts an asymmetric shape for the absorption lines, which has been confirmed by high resolution, high signal to noise UV

observations of Mrk 279 (Arav et al. 2004). These results make the radiation driven outflow models highly attractive to describe the real outflows occurring in the AGN's.

1.6 Spectral diagnostics

Using high resolution spectroscopy one can determine plasma properties such as ionization, temperature, velocities and abundances. The physical processes dominant in the ionization of the plasma, such as photoionization or collisional ionization can be determined from line ratios and radiative recombination lines. The advantage of high resolution X-ray spectroscopy is the availability of many atomic transitions that have detectable spectral lines. In particular, we observe many transitions from O and Fe, but also transitions from C, N, Ne, Na, Mg, Si, S, Ar and possibly Ca and Ni. These many transitions allow for elemental abundance determinations. In the studied wavelength range of 1.5 Å to 100 Å lines from neutral O I to highly ionized Fe XXVI have transitions. This allows for an accurate determination of the ionization parameter or temperature of the plasma. In AGN photoionization is dominant, and we will focus on this process in the rest of this section.

1.6.1 Determination of the ionization state

In photoionization equilibrium, the plasma conditions are determined by solving two equations: energy balance (heating versus cooling) and number density balance (recombination versus ionization). For a low density (n $< 10^{14}$ m^{-3}) thin slab, the equilibrium conditions are primarily determined by the shape of the spectral energy distribution (SED) and the so-called ionization parameter ξ, defined by $\xi = L/nr^2$, where L is the luminosity, n the density and r the distance from the ionizing source. Assuming a spectral energy distribution (SED) we know the range of ionization parameters for which a certain ion is created. Thus the column densities measured for the different ions determine the ionization parameter. However, differing elemental abundances can complicate this determination. Only for iron do we detect enough ions, from lowly ionized Fe VI to highly ionized Fe XXVI to determine the ionization parameters independently of elemental abundances. In Fig. 1.3 the ionization parameter for the different observable iron ions is shown. Obtaining the ionization parameters from iron allows for the determination of elemental abundances of the other elements relative to iron. However, in practice some iron ions are heavily blended, complicating this method. In general all transitions from the different ions are used to determine the ionization parameters. Because hydrogen doesn't have absorption lines in the X-ray band, the elemental abundances are in general given relative to oxygen or iron.

9
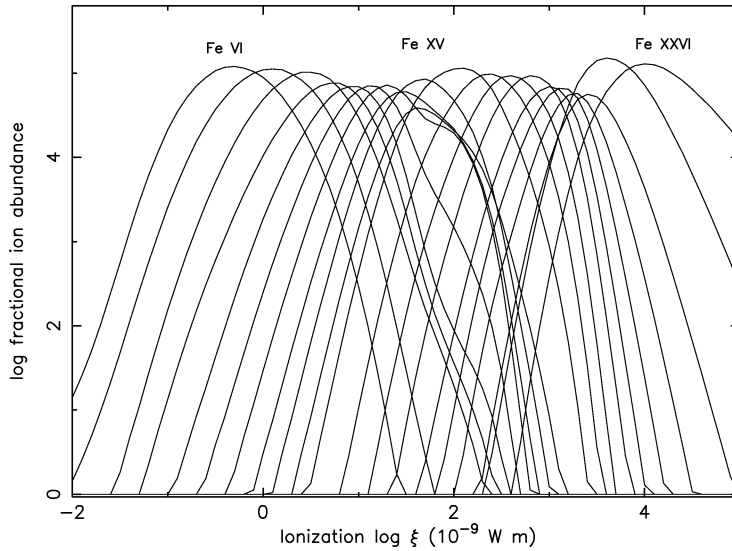
Figure 1.3: The fractional ion abundance versus ionization for Fe VI to Fe XXVI. The hydrogen abundance is 10 in this scale.

An important question is whether there are discrete ionization components, or whether the ionization has more continuous distribution. In this thesis we use both hypotheses. For the continuous ionization model the total hydrogen column density is derived from photoionization models for each individual ion. This hydrogen column density is then plotted against the ionization parameter for which the ion has its maximum column density. Consistency of the assumed continuous ionization distribution with the derived column densities shows then whether this model is appropriate or not. A more elegant method is to assume two extreme ionization parameters with a parametrized ionization distribution function and apply this model directly to fit the observed spectra. With this method we correctly take into account that an ion is formed over a range in ionization parameter.

An absorption model has been generated (Chapters 4 and 5) to test whether the distribution of column density versus ionization parameter is not continuous but discrete, with multiple different discrete ionization parameters. The model is the sum of individual components with only the ionization parameters and column density as free parameters. As many such components are added as necessary to obtain a good fit to the data. In general we need $2 - 5$ such components. All models depend on

the input SED and on the photoionization code used to obtain the ionization balance. However, differences in the SED or photoionization code have only a limited effect, mostly compressing or stretching the ionization scale.

1.6.2 Velocity broadening

In the X-ray band we observe several line series which allow for accurate velocity broadening and column density measurements. If the optical depth is small the equivalent width of the line gives the column density for the ion. However, if the line has a substantial optical depth, then the measured width of the line is a measure for both the column density and the velocity broadening. For the stronger lines, the optical depth is in general rather large, but the higher order lines in the line series or transitions with lower oscillator strengths do allow to separate the column density effect from the velocity broadening and measure both. The velocity broadening is a measure for the turbulent (and in some models the thermal) velocity fields. In the models where the ionization parameter or temperature is a free parameter, the thermal velocity is included in the modeling and the velocity width is an indication of turbulence.

1.6.3 Accuracy of atomic data

The above diagnostics are highly dependent on the availability of accurate atomic data such as wavelength and oscillator strength. For most of the stronger spectral lines and the Ly series these atomic data are well known. However, for some lines the calculated wavelength is not accurate, sometimes with errors similar to the full width half maximum (FWHM) resolution of the LETGS instrument. This is due to the difficulty of producing these ions in laboratory experiments. The O V absorption line at 22.374 Å, is a good example of a strong line where the calculated wavelength was inaccurate by 0.044 Å (see Chapters 4 and 5). The wavelength of this line was measured with the Electron Beam Ion Trap, which produces highly charged ions in a laboratory setting (Schmidt et al. 2004). Also for the O II line at 23.33 Å the calculated wavelength differs significantly from the one measured with the HETGS (Juett et al. 2004). For the stronger lines a mismatch is easily detected in high signal to noise ratio spectra, but for the many weaker lines the difference is harder to detect and correct. As we need to self-consistently model all the spectral lines present in the spectrum, these errors could potentially propagate into the determined ionization parameter or abundance. The oscillator strengths in general agree between the different calculations to about 10 %.

Another possible source of error is that certain recombination processes are not correctly included, which can lead to errors in the photoionization equilibrium calculations. For the lower ionized iron ions the dielectronic recombination rates used in

11

the atomic data calculations are inaccurate (Netzer et al. 2003; Kraemer, Ferland & Gabel 2004; Netzer 2004). As a result the calculated ionization for these ions is too low. As iron is very important in the ionization parameter determination this can cause systematic errors in the ionization parameter.

1.7 This thesis

The launch of the *Chandra* and XMM-*Newton* satellites allowed for the first time high resolution X-ray spectroscopy of the brighter extragalactic X-ray sources sources. In this thesis we take advantage of the high resolution to study Seyfert 1 galaxies and a quasar, and in particular their ionized winds.

In Chapter 2 we describe the instruments used to obtain the spectra and the statistical methods used in the analysis of these spectra. In Chapter 3 we describe the *Chandra* LETGS and XMM-Newton spectra obtained for NGC 4593. In the spectra we only detect weak lines from highly ionized gas and lowly ionized gas, and not a standard warm absorber. An important question discussed in this thesis is the geometry and the physical conditions of the outflows observed through absorption lines. Is this outflow in the form of clouds which are in pressure equilibrium within a hot medium, or are these outflows in the form of narrow streams? In the first model the outflowing gas can only have a few particular ionization values, depending on the SED assumed. In the second scenario there is a density gradient that results in a continuous ionization structure. Both scenarios are extensively discussed in Chapters 4 and 5. Another question discussed in Chapter 5 is whether these outflows escape the galaxy to enrich the inter galactic medium (IGM), or fall back onto the accretion disk of the host galaxy. In Chapter 6 we study in detail the broad emission lines observed in the X-ray and UV spectra of NGC 5548, and model these with the photo-ionization codes CLOUDY and XSTAR. In Chapter 7 we discuss the heavily absorbed spectrum of IC 4329A, for which we detect absorption from the host galaxy as well as from the warm absorber close to the core. The ionized absorption from the IGM itself was studied by using the quasar Ton 1388 (Chapter 8) to illuminate this gas.

References

Antonucci, R. R. J. & Miller, J. S., 1985, ApJ, 297, 621

Arav, N., Barlow, T. A., Laor, A., et al., 1998, MNRAS, 297, 990

Arav, N., Gabel, J., Scott, J., et al., in preparation

Barthel, P. D., 1989, ApJ, 336, 606

Behar, E., Rasmussen, A. P., Blustin, A. J., et al., 2003, ApJ, 598, 232

Branduardi-Raymont, G., Sako, M., Kahn, S. M., et al., 2001, A&A, 365, L140

Chakrabarti, S. K. & Titarchuk, L. G., 1995, ApJ, 455, 623

Crenshaw, D. M., Kraemer, S. B., Boggess, A., et al., 1999, ApJ, 516, 750

Elvis, M., 2000, ApJ, 545, 63

Gabel, J. R., Crenshaw, D. M., Kraemer, S. B., et al., 2003, ApJ, 595, 120

Guilbert, P. W. & Rees, M. J., 1988, MNRAS, 233, 475

Iwasawa, K., Fabian, A. C., Reynolds, C. S., et al., 1996, MNRAS, 282, 1038

Juett, A. M., Schulz, N. S. & Chakrabarty D., 2004, in press

Königl, A & Kartje, J. F., 1994, ApJ, 434, 446

Kraemer, S. B., Ferland, G. J., Gabel, J. R., 2004, ApJ, 604, 556

Krolik, J. H. & Kriss, G. A., 2001, ApJ, 561, 684

Lightman, A. P. & White, T. R., 1988, ApJ, 335, 57

Nenkova, M., Ivezić, Ž. & Elitzur, M., 2002, ApJ, 570, L12

Netzer, H., Kaspi, S., Behar, E., et al., 2003, ApJ, 599, 933

Netzer, H., 2004, ApJ, 604, 551

Peterson B. M. & Wandel, A., 2000, ApJ, 540, L13

Proga, D., Stone, J. M. & Kallman, T. R., 2000, ApJ, 543, 686

Proga, D., 2003, private communication

Reeves, J. N., Nandra, K., George, I. M., et al., 2004, ApJ, 602, 648

Röttgering, H., Jaffe, W., Meisenheimer, K., et al., 2004, Proc. SPIE, Ed. Traub, W. A., Vol. 5491, 9

Sako, M., Kahn, S. M., Branduardi-Raymont, G., et al., 2003, ApJ, 596, 114

Schmidt, M., Beiersdorfer, P., Chen, H., et al., 2004, ApJ, 604, 562

Schödel, R., Ott, T., Genzel, R., et al., Nature, 419, 694

Sellgren, K., Soifer, B. T., Neugebauer, G. & Matthews, K., 1983, PASP, 95, 289

Seyfert, C. K., 1943, ApJ, 97, 28

Shakura, N. I., & Sunyaev, R. A., 1973, A&A, 24, 337

Tanaka, Y, Nandra, K., Fabian, A. C., et al., 1995, Nat. 375, 659

Ulvestad, J. S., Wilson, A. S. & Sramek, R. A., 1981, ApJ, 247, 419

Urry, C. M. & Padovani, P., 1995, PASP, 107, 803

Wilms, J., Reynolds, C. S., Begelman, M. C., et al., 2001, MNRAS, 328, 27

13

Chapter 2

Instrumentation and statistical analysis

It has only been possible to obtain high resolution X-ray spectra of Active Galactic Nuclei since the launch of XMM-*Newton* and *Chandra*. The different instruments onboard each spacecraft provide complementary spectra. In this thesis we present spectra of NGC 5548, NGC 4593, IC 4329A and Ton 1388 taken with the grating spectrometers onboard XMM-*Newton* as well as the different grating spectrometers on *Chandra*. High resolution X-ray spectra of AGN are still photon limited, the statistical analysis methods used in this thesis will be briefly described at the end of this Chapter.

2.1 XMM-*Newton*

The XMM-*Newton* satellite has six instruments onboard and three X-ray telescopes. All instruments can observe simultaneously. An overview of the XMM-*Newton* satellite is shown in Fig. 2.1. Five of the instruments are X-ray instruments, the sixth is the optical monitor. The three European Photon Imaging Camera (EPIC) instruments contain CCDs with moderate spectral resolution, while the two Reflection Grating Spectrometers are dispersive instruments and have high spectral resolution.

The EPIC instruments are high-throughput, medium angular resolution ($\sim$ 15 arcsec half energy width) X-ray telescopes, which have a CCD camera at the focal plane. The CCDs have an energy resolution between 50 eV and 185 eV, allowing for non-dispersive spectroscopy. The peak effective area is 0.15 m^2 at 1 keV and 0.05 m^2 at 5 keV. The instruments are sensitive up to energies of about 15 keV. The EPIC in-
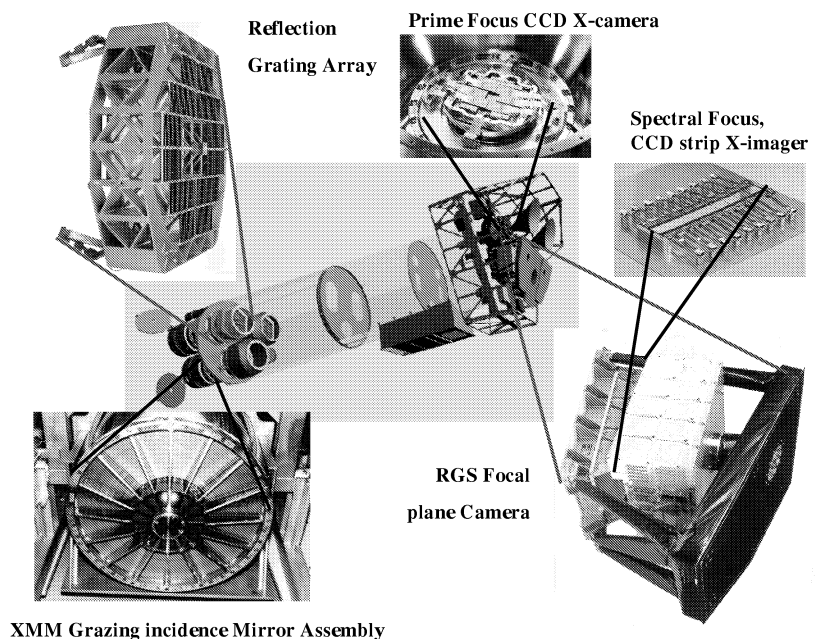
Figure 2.1: An overview of the different instruments onboard XMM-*Newton*. An advantage is that all instruments can observe simultaneously, covering a energy band between 0.2 and 15 keV (Courtesy of J. A. M. Bleeker).

struments consist of the pn-junction device (Strüder et al. 2001) which has an energy resolution ranging between 90 eV at 1 keV and 185 eV at 10 keV (XMM-*Newton* Users' Handbook) and the metal oxide semiconductors MOS 1 and MOS 2 (Turner et al. 2001). Each MOS camera shares a telescope with an RGS grating device. About half of the incoming X-rays are deflected toward the Reflection Grating Spectrometers, while 44 % of the incoming X-rays pass undeflected and are detected by the MOS cameras. As a result the throughput for each MOS instrument is about half that for the pn. The energy resolution of the MOS cameras ranges between 50 eV at 0.4 keV to 180 eV at 10 keV (XMM-*Newton* Users' Handbook). In this thesis the EPIC spectra were mainly used for determining the continuum, the broadened soft X-ray emission lines and fitting the Fe Kα emission line at 6.4 keV.

There are two high spectral resolution instruments, the Reflection Grating Spec-

16

trometers RGS 1 and RGS 2 (den Herder et al. 2001). These have a relatively large effective area of 0.09 m^2 at 24 Å (see Fig 2.4). The wavelength resolution is better or equal to 0.07 Å for first order spectra, and is 0.04 Å for second order spectra (XMM-*Newton* Users' Handbook). The uncertainty in absolute wavelength scale is 8 mÅ (den Herder et al. 2001). The instruments are sensitive between 5 and 38 Å, however, the calibration below 7 Å is still uncertain. Due to a failure of two CCD chains shortly after launch, there is a data gap between $10 - 14$ Å for RGS 1 and between $20 - 24$ Å for RGS 2. Fig. 2.2 shows the pn and RGS spectra of IC 4329A, illustrating the differences between both instruments. In this wavelength band oxygen, nitrogen, carbon and iron have strong absorption lines. Iron transitions from the lowly ionized Fe VI to highly ionized Fe XXIV are detectable in this wavelength band. In principle one can determine the ionization stage of the observed gas using only iron ions, and thus avoid having uncertainties due to unknown abundances of the other ions. The high resolution spectra from the RGS instruments are extensively used in this thesis. The only XMM-*Newton* instrument that was not extensively used in this thesis is the Optical Monitor
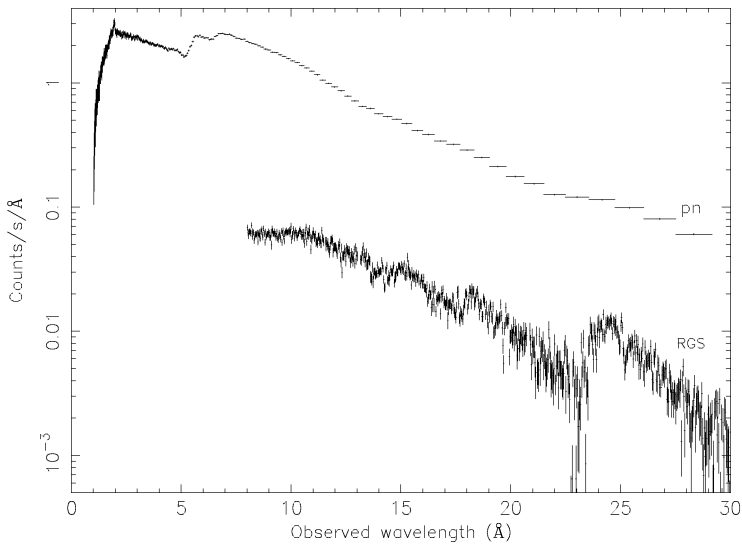
Figure 2.2: The pn and RGS spectrum of the heavily absorbed Seyfert 1 galaxy IC 4329A. RGS 1 and RGS 2 were averaged for clarity. The RGS data between 5 and 7 Å are not included due to calibration uncertainties. Note the difference in count rate as well as the difference in spectral resolution.

17

(OM). With this instrument optical and UV spectra and images can be obtained.

2.2   *Chandra*

For the current dispersive X-ray instruments the effective spectral resolution is a function of the size of the observed object. The AGN studied in this thesis are point sources in the X-ray band, as a result all high spectral resolution instruments onboard of both observatories can be used without loss of spectral resolution. The *Chandra* observatory has several instruments, which however cannot observe simultaneously as there is only one X-ray telescope. There are four cameras onboard: the Advanced CCD Imaging Spectrometer-S (ACIS-S) which is sensitive between 1 and 60 Å, the High Resolution Camera-S (HRC-S) which is sensitive between 1 and 180 Å, the Advanced CCD Imaging Spectrometer-I (ACIS-I) detector which is optimized for imaging, and the High Resolution Camera-I (HRC-I), which has the highest spatial resolution. The ACIS-I has a spatial resolution of 0.1 arcsec, but the High Resolution Mirror Assembly (HRMA) has a spatial point spread function of 0.5 arcsec, but the spectral resolution is similar to the EPIC instruments on XMM-*Newton* (Chandra at a Glance, http://cxc.harvard.edu/cdo/about_chandra/). This instrument and the HRC-I are not used in this thesis. In Fig. 2.3 the X-ray focusing mirror onboard *Chandra* is shown.

There are three grating arrays onboard: the Low Energy Transmission Grating (LETG), the High Energy Grating (HEG) and the Medium Energy Grating (MEG). The latter two gratings are operated simultaneously and are collectively called the High Energy Transmission Grating (HETG). Details of the characteristics of these three different gratings are listed in Table 2.1. The effective area of these instruments is significantly below that of the RGS instruments, except for wavelengths below 11 Å (see Fig 2.4).

The HEG is the grating with the highest resolution and was mainly used to study the Fe Kα emission line and the highly ionized absorber. The MEG has a lower resolution, but can be used to study also the less ionized gas. These grating instruments are usually used in combination with the ACIS-S detector. The LETG has the longest wavelength coverage of all high spectral resolution X-ray instruments, allowing study of the soft excess in AGN and the complete ionization range of the warm absorber. The LETG is in general used in combination with the HRC-S detector; this instrumental set-up is called LETGS. For all the spectrometers the spectral resolution is a constant as function of wavelength. Thus the velocity resolution of the LETG for wavelengths longer than 33.74 Å (C VI Lyα) is better than the velocity resolution of the MEG below 15.2 Å. For the LETGS, spectral order separation is not possible, and thus the higher order spectra need to be modeled during the analysis.

18
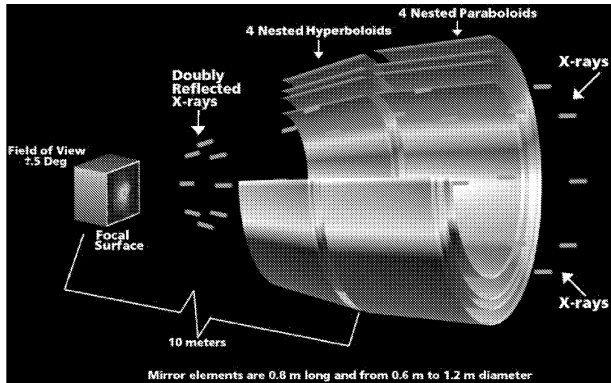
Figure 2.3: The X-ray focusing mirror of the *Chandra* telescope. This telescope is very similar to the one used on XMM-*Newton* (from http:chandra.harvard.edu/resources/illustrations/teleSchemGraz3D.html).

2.3 Comparison between observatories

The main advantage of the XMM-*Newton* observatory is the fact that all instruments observe simultaneously. This allows for an accurate continuum modeling as well as

Table 2.1: Comparison between the different spectrometers on *Chandra*. Data were taken from the Chandra calibration website. For comparison the values for the RGS are also given (from the XMM-Newton Users' Handbook).

Instr.	wavelength band	resolution (FWHM)	absolute wavelength scale
HEG	$1.5 - 15$ Å	0.012 Å	6 mÅ
MEG	$1.5 - 31$ Å	0.023 Å	11 mÅ
LETG	$1.5 - 170$ Å	0.05 Å	13 mÅ
RGS	$5 - 38$ Å	0.07 Å	8 mÅ

studying the spectral diagnostics of the source. This is especially important in the debate about relativistically broadened soft X-ray emission lines and the study of other broadened emission lines. Another advantage is the large effective area of the RGS instruments, allowing to study possible spectral variability in more sources and on shorter timescales than possible with *Chandra* spectrometers. Fig. 2.4 shows a comparison in effective area for the different high spectral resolution instruments.

An advantage of the *Chandra* instruments is the higher spectral resolution, allowing in some cases to resolve some velocity components. The LETGS has a large wavelength band, as a result L-shell lines from silicon, sulfur, neon, and other, less abundant elements are observed. In general, the RGS instruments are well suited to study heavily absorbed (due to Galactic or intrinsic absorption) AGN. Longer wavelengths are more affected by absorption than shorter wavelengths, thus relatively bright AGN with low Galactic or intrinsic absorption are optimally studied with the LETGS. The HETG is useful if the highest spectral resolution is required, for instance to disentangle outflow velocity components. Another advantage is that the *Chandra* observatory dithers, smoothing out any hot pixels and CCD-gaps. This is not (yet) the case for the XMM-*Newton* observatory.

2.4   Statistical analysis

In general the high resolution spectra of AGN are photon limited. As a result, the spectra which have exposure times less than 100 ks for RGS and HETG and less than 200 ks for the LETGS can be rather noisy. It is thus important that in the spectral analysis noise and real spectral features are separated. In fitting absorption lines we reduce the effects of noise by using self consistent models for all absorption features of each ion. As Seyfert 1 galaxies have an absorption dominated spectrum, the need for self-consistent emission line fitting is relatively small. The number of narrow emission lines in most AGN is in general very small (the O VII forbidden line and a few others). The absorber is photoionized, and all photoionization models used in this thesis assume that the absorber is a geometrically thin slab, with negligible (re)-emission from the slab itself. In the simplest case we fit the absorption lines and continuum absorption edges from a certain ion simultaneously. As the oscillator strengths and continuum opacities for the different lines and edges of the same ion are known and held fixed, this improves the stability of the fit. However, for those ions where continuum or edge absorption dominates over the wavelength range that is covered, this is not a stringent method. Weak continuum absorption features can be easily confused with any mismatch in the continuum emission model or remaining calibration uncertainties.

A more stringent method is to use a photoionization code to couple the different
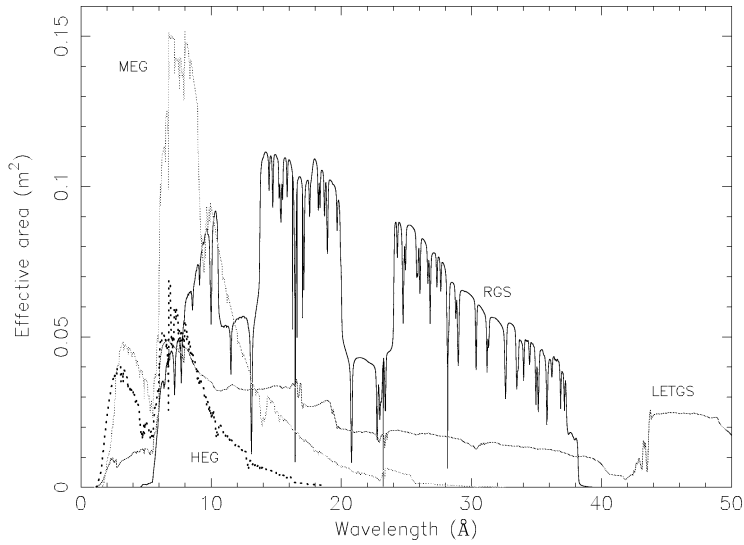
Figure 2.4: Comparison of the effective areas for the different high resolution spectrometers as a function of wavelength. For RGS 1 and RGS 2 we took the effective are from the IC 4329A data set and added RGS 1 and RGS 2 for clarity. For the LETGS, MEG and HEG (in combination with the ACIS-S) we took the effective area from the *Chandra* 2002 data on NGC 5548. For LETGS we added the effective area of the first 10 spectral orders.

ions. In this method only the ionization parameter, the total column density, the elemental abundances, the outflow velocity and velocity broadening are free parameters. With this method there are tens, and often hundreds of absorption lines fitted. This in general leads to high statistical significance of an absorption component, even if most individual lines are only detected with 1 or 2 σ significance. In this case the continuum and edge absorption is also self-consistently taken into account, even for ions with weak continuum absorption. However, there is a caveat: there are uncertainties in the photoionization codes, which result in systematic uncertainties in the analysis. These uncertainties are hard to quantify. Further, in most cases at least three such absorption components are necessary to fit the spectra, increasing the uncertainties, as the total column densities and the different ionization parameters are correlated parameters.

In a final method we force the distribution of the column density versus ionization parameter to be a power-law, leaving only the slope, the normalization, the elemen-

tal abundances, the outflow velocity and velocity broadening free parameters. If the assumption of a power-law distribution is correct, then this model should fit all the absorption lines and edges in the spectrum. Thus we need only one component, reducing the numbers of free parameters in the fit. However, here again any possible uncertainties in the photoionization code results in systematic uncertainties. Also, we do make an a priori assumption about the ionization structure which need not be correct.

We can derive accurate spectral diagnostics for the warm absorber with the above methods, even if the spectrum is rather noisy.

For the quasar Ton 1388, we do not detect a warm absorber, but only a few weak absorption lines. Toward this source there are 16 known Lyα absorbers detected in the optical and UV bands. We thus assumed that these absorption lines were associated with one or more known Lyα absorber. It is presumed that a large fraction of the local baryons are hot and form the Warm-Hot Intergalactic Medium (WHIM; Cen & Ostriker 1999). As these absorption lines are probably unrelated to the quasar, we can only fit ion per ion, either assuming photoionization or collisional ionization. As the absorption lines in the spectrum are weak, we allowed only identifications with X-ray absorption lines with high oscillator strengths and froze the redshift to one where in the UV band a Lyα absorber has been detected. With this method we tried to reduce the chances of fitting noise. Again, we tried to fit the absorption lines self consistently, namely if an ion of a certain ionization parameter is observed, then we try to ascertain whether or not we also see other ions with similar ionization parameter or temperature.

A similar situation occurs for the absorption lines at zero redshift detected in nearly all the spectra presented in this thesis. In general we only mention them briefly and quote an equivalent width as there are only one or two lines detected. However, from the fact that they occur in the different spectra we can conclude that they are real.

References

Cen, R. & Ostriker, J. P., 1999, ApJ, 514, 1

Chandra at a Glance, http://cxc.harvard.edu/cdo/about_chandra/

den Herder, J. W., Brinkman, A. C., Kahn, S. M. et al., 2001, A&A, 365, L7

Ehle, M., Breitfellner, M., González Riestra, R., et al., 2004, XMM-Newton Users' Handbook, version 2.2

Kaastra, J. S., Steenbrugge, K. C., Raassen, A. J. J., et al., 2002, A&A, 386, 427

Strüder, L., Briel, U. G., Dennerl, K., et al., 2001, A&A, 365, L18

Turner, M. J. L., Abbey, A., Arnaud, M., et al., 2001, A&A, 365, L27

Chapter 3

Chandra LETGS and XMM-Newton observations of NGC 4593

K.C. Steenbrugge, J.S. Kaastra, A. J. Blustin, G. Branduardi-Raymont, M. Sako, E. Behar, S. M. Kahn, F. B. S. Paerels, R. Walter

Abstract

In this paper, we analyze spectra of the Seyfert 1 galaxy NGC 4593 obtained with the *Chandra* Low Energy Transmission Grating Spectrometer (LETGS), the Reflection Grating Spectrometer (RGS) and the European Photon Imaging Camera's (EPIC) on-board of XMM-*Newton*. The two observations were separated by $\sim$7 months. In the LETGS spectrum we detect a highly ionized warm absorber corresponding to an ionization state of 400×10^{-9} W m, visible as a depression at $10 - 18$ Å. This depression is formed by multiple weak Fe and Ne lines. A much smaller column density was found for the lowly ionized warm absorber, corresponding to $\xi = 3 \times 10^{-9}$ W m. However, an intermediate ionization warm absorber is not detected. For the RGS data the ionization state is hard to constrain. The EPIC results show a narrow Fe Kα line.

23

3.1 Introduction

NGC 4593 is classified as a Seyfert 1 galaxy (Simkin et al. 1980). In the optical it has two prominent spiral arms and a clear central bar (Santos-Lleó et al. 1994). Because of its low redshift of 0.0084 (Paturel et al. 2002), it is one of the X-ray brightest Seyfert galaxies in the sky. A further advantage is the low galactic column density of 1.97×10^{24} m^{-2} (Elvis et al. 1989). As a result it has been intensively studied in the X-ray and UV bands.

A strong absorption-like feature in the spectrum between $10 - 18$ Å ($0.7 - 1.2$ keV) was detected in the ASCA and *Beppo*SAX observations (George et al. 1998, Guainazzi et al. 1999). Therefore, it was inferred that there were strong K-shell absorption edges for O VII and O VIII at 0.74 and 0.87 keV, respectively. From the depth of the edges the optical depth was derived as 0.3 and 0.1 for the O VII and O VIII edge, respectively (Reynolds 1997). It was thus deduced that NGC 4593 has a strong warm absorber, which would result in a complex absorption line spectrum, if observed with the current high resolution observatories. Both the ASCA and the *Beppo*SAX spectra required a moderately broadened Fe Kα line (Reynolds 1997; Guainazzi et al. 1999).

In Sect. 3.2 we discuss the observation and data reduction for both *Chandra* LETGS and XMM-*Newton*. The data analysis is described in Sect. 3.3. In Sect. 3.4 the luminosity variations for the LETGS data are analyzed, and in Sect. 3.5 we compare the LETGS spectrum with the RGS spectra.

3.2 Observations and data reduction

The *Chandra* data were obtained on the 16th of February 2001. NGC 4593 was observed in the standard configuration for the Low Energy Transmission Grating (LETG) in combination with the HRC-S camera. The total exposure time of the observation was 108000 s. The spectral data extraction procedure is identical to that described in Kaastra et al. (2002a) for NGC 5548.

The XMM-*Newton* data were obtained on the 2nd of July 2000. All instruments onboard XMM-*Newton* looked at the source with different exposure times, Table 3.1 lists the exposure times used in the analysis. The EPIC cameras were shut down early due to a high radiation background. The main results from XMM-*Newton* in this paper are based on the Reflection Grating Spectrometer (RGS). Due to the high radiation background the spectrum from RGS has a strong background component, about 50 times higher than during a normal observation. As a result, the background count rates are between half and a third of the total count rate. As the high radiation background lasted for more than 70 % of the observation, the entire observation of RGS was used

Table 3.1: The modes and exposure times used in the analysis for the different XMM-*Newton* instruments.

Instrument	exposure (s)	observational mode
RGS 1 and 2	27000	spectroscopy
EPIC MOS 2	8000	small window with medium filter
EPIC pn	6000	small window with thin filter
OM	6000	visible grism
OM	4500	UVW1 $(245 - 320$ nm$)$
OM	10000	UVW2 $(180 - 225$ nm$)$

in the analysis below. For RGS 1 all CCDs still functioned, while for RGS 2 CCD 4 did not function. The XMM-*Newton* EPIC, RGS and OM data were reduced with the standard SAS software, version 5.3.3. This version includes the calibration of the instrumental oxygen edge and up-to-date effective areas for RGS. All plots are shown in the observed frame.

The OM was operated in imaging mode with three consecutive filters: visible grism, UVW1 (245-320 nm) and UVW2 (180-225 nm). The source was not bright enough - and the straylight background was too high - for a satisfactory grism spectrum to be obtained. The UV source fluxes were obtained using the omsource task. A source extraction region 6" in diameter was used, and the background was estimated from an annular region surrounding the source. The resulting fluxes (Blustin et al. 2003), corrected for coincidence loss, deadtime, background and Galactic reddening, were F_ν of 2.46×10^{-14} and 1.58×10^{-14} W m^{-2} for UVW1 and UVW2 respectively. The errors on these fluxes are around 10 %.

Fig. 3.1 gives the Optical Monitor image of NGC 4593 taken with the UVW1 filter. Other than the central core, some spiral arm structure can be seen from the image. The image taken with the UVW2 filter shows only a point source and has a rather low count rate in general. These images indicate that in the X-ray spectra there should be little contamination of the spiral arms, consistent with the point source detected in the EPIC instruments.
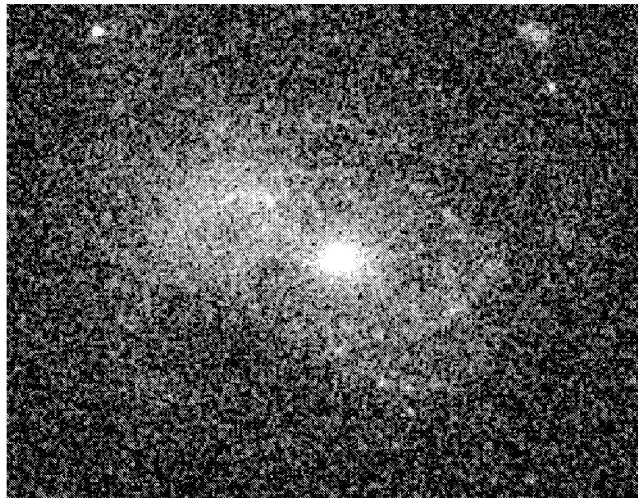
Figure 3.1: Image of NGC 4593 taken with the UVW1 filter of the Optical Monitor onboard of XMM-*Newton*. Besides the bright core the spiral arm structure is visible.

3.3   Data analysis

3.3.1   The warm absorber model

In this paper we use the *slab* and *xabs* model in SPEX (Kaastra et al. 1996; Kaastra et al. 2002b) for the modeling of the warm absorber. The *slab* model calculates the transmission of each ion individually, using all absorption lines and edges. The transmission of all ions is then combined to calculate the total transmission of the warm absorber. All ions have the same outflow velocity and velocity broadening (Kaastra et al. 2002b). The *xabs* model is the same as the slab model, except that the ion column densities are coupled by a grid of XSTAR photoionization models (Kallman & Krolik 1999), characterized by the ionization parameter, ξ. For more details see Kaastra et al. (2002b). All quoted errors are 1σ errors.

The *xabs* model has the advantage that ions, which are too weak to be detected individually, are automatically included to give a consistent ionization parameter and column density. The drawback is that the *xabs* model is more dependent on the details of the photoionization model, than a simple ion by ion fit.

For both models one can fit an overall blue- or redshift to the observed lines. Other parameters, which were not left free, as the detected absorption lines are too weak, are

26
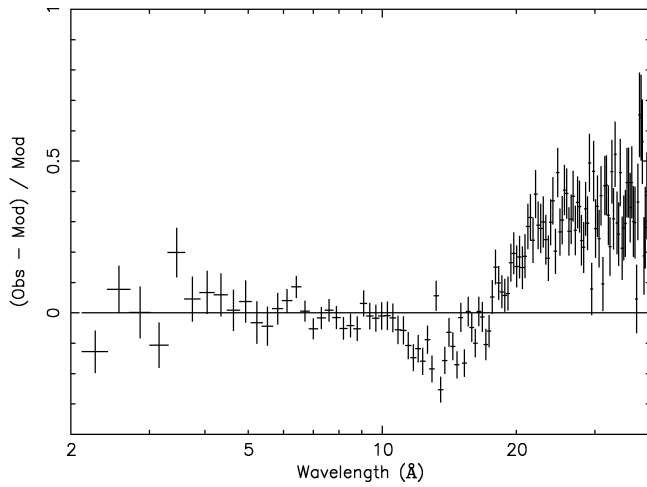
Figure 3.2: Fit residuals of a power-law fit to the LETGS data for NGC 4593, clearly showing a dip in the spectrum between 10 and 18 Å and the strong soft excess above 18 Å. The power-law was fit between 2 and 10 Å and the data are binned by a factor of 10.

the covering factor, the broadening due to a range in velocities, the width and separation of the velocity components (as obtained or estimated from, for example, UV data). The standard values for these parameters are as follows: covering factor is 1, velocity broadening is 250 $km\,s^{-1}$ and the width of the individual velocity components and their separation are both 100 $km\,s^{-1}$.

3.3.2 Spectral analysis: *Chandra*

The fluxed LETGS spectrum shows a dip between $10 - 18$ Å (see Fig. 3.2). However, few absorption lines can be detected by eye from the spectrum. The absorption edges of O VII or O VIII are not detected, although a narrow O VII forbidden and resonance line are observed at 22.3 and 21.8 Å (see Fig. 3.5). It is clear that no conventional warm absorber is detected.

Fitting the LETGS data with a power-law (PL) with galactic absorption gave a rather good fit to the data, except for the $10 - 18$ Å region, and at longer wavelengths where there is a soft excess (see Fig. 3.2). Adding a modified black body (MBB) component (Kaastra & Barr 1989), does improve the fit at longer wavelengths, but

Table 3.2: Fit parameters for the LETGS spectrum, assuming a distance of 50.0 Mpc for NGC 4593.

PL:	norm[a]	$(2.18 \pm 0.02) \times 10^{51}$ ph s^{-1} keV^{-1}
	Γ	1.69 ± 0.02
MBB:	norm[b]	$(1.0 \pm 0.1) \times 10^{32}$ m$^{1/2}$
	T	(0.13 ± 0.01) keV
O VIIf:	EW	(-152 ± 45) mÅ
	flux	(0.45 ± 0.13) ph s^{-1} m^{-2}
	λ^c	(22.069 ± 0.016) Å
	v^d	(-430 ± 218) km s^{-1}
xabs :	$N_{\rm H}$	$(1.6 \pm 0.4) \times 10^{25}$ m^{-2}
	$\log \xi^e$	2.61 ± 0.09
	v^d	(-400 ± 121) km s^{-1}
abun^f:	O	$0.2\,(-0.1, +0.2)$
xabs :	$N_{\rm H}$	$(6 \pm 3) \times 10^{23}$ m^{-2}
	$\log \xi^e$	0.5 ± 0.3
	v^d	(-380 ± 137) km s^{-1}

[a] at 1 keV.
[b] norm=emitting area times square root of electron density.
[c] wavelengths are given in the rest frame of NGC 4593.
[d] velocity shift from comparing rest and observed wavelengths.
[e] in 10^{-9} W m or in erg cm s^{-1}.
[f] only non-solar ratio abundances are noted; abundances relative to Fe, which is tied to solar abundance.

does not explain the dip between $10 - 18$ Å (see Fig. 3.3). The dip in the spectrum cannot be attributed to calibration uncertainties or well fitted with another model for the soft excess, therefore we fitted the data including also a *xabs* component for the warm absorber (Kaastra et al. 2002b).

The results of the fits with the *xabs* component are summarized in Table 3.2. In Fig. 3.3 and 3.4 the model with and without the *xabs* component are plotted, while Table 3.3 gives the χ^2 and degrees of freedom for the different models.

Using the *xabs* component and allowing only the ionization parameter ξ, the X-ray column density, $N_{\rm H}$ and the outflow velocity to be free parameters, we found a high

Table 3.3: The χ^2 and degrees of freedom, as well as the significance of the added component according to an F-test for the different model fits to the LETGS data, as described in the text. Best fit parameters of model 6 are listed in Table 3.2. Z stands for abundances.

	model	χ^2	dof	χ_ν^2	sign.
1	PL	2073	1312	1.58	
2	PL+MBB	1795	1310	1.37	0.99
3	PL+MBB+O VIIf	1775	1308	1.36	0.58
4	3+*xabs*	1603	1305	1.23	0.97
5	4+Z free	1575	1298	1.21	0.62
6	5+1 *xabs*	1556	1295	1.20	0.59
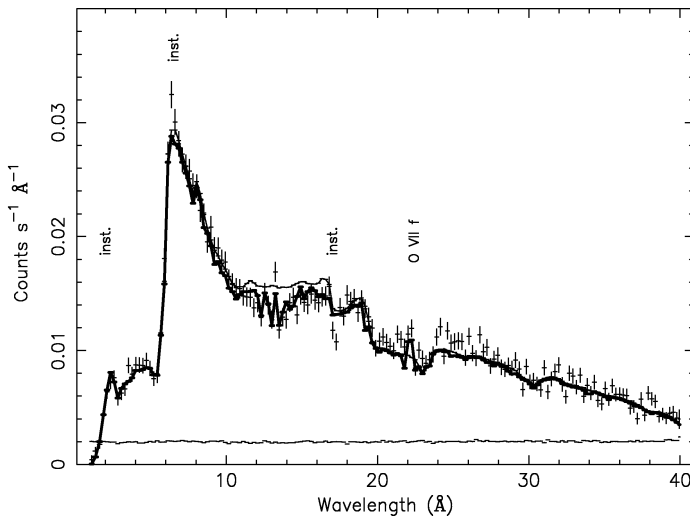
Figure 3.3: Power-law plus modified black body fit (thin solid line) and the model including the *xabs* components as described in Table 3.2 (thick solid line) to the LETGS data. The thin line at about 0.002 counts s^{-1} Å^{-1} is the subtracted background contribution. For clarity the data are binned by a factor of 5. Instrumental edges are labeled, as well as the O VII forbidden line.

ionization parameter of $\log \xi = 2.6$ in units of 10^{-9} W m. This component describes the $10 - 18$ Å dip even if solar abundances (Anders & Grevesse 1989) are assumed. There
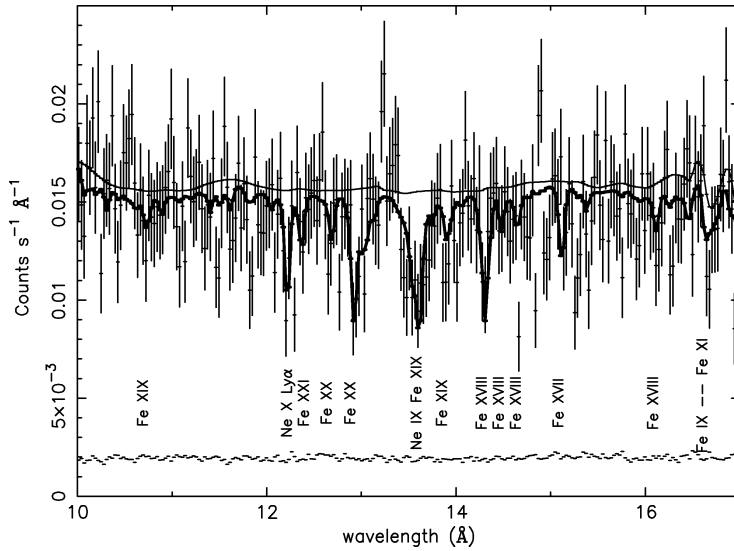
Figure 3.4: Detailing the $10 - 17$ Å region of Fig. 3.3. Power-law and modified black body fit (thin solid line) and the fit including the *xabs* components (thick solid line) to the unbinned LETGS data.

is an improvement in the fit if the abundances are left free. For this high ionization parameter Ar, Ne and Fe are the main elements absorbing the power-law component, as most other abundant elements such as C and N are already fully ionized. O VIII is the only oxygen ion expected in the spectrum.

Most of the Fe-absorption lines have small optical depths causing rather shallow lines. These are, therefore, not detectable per individual line, with the current sensitivity. The combination of these lines causes a significant depression in the continuum spectrum and blending results in some observable broadband absorption structures (see Fig. 3.4). The abundance quoted in Table 3.2 is effectively measured relative to Fe, which was fixed to solar abundance, because of its many absorption lines. Compared to iron, oxygen is underabundant, while all other elements have abundance ratios to iron consistent with the solar ratio.

A weak, redshifted emission component for the O VIII Lyα line is observed (see Fig. 3.5), which is partially blended with the absorption component. However, the non-detection of an O VIII Lyγ absorption line, and the weak O VIII Lyβ constrain the column density of O VIII and thus also the abundance ratio for oxygen. The oxygen

abundance in Anders & Grevesse (1989) might be too high (see Allende Prieto et al. 2001) resulting in the derived underabundance.

From a more detailed inspection of the LETGS spectrum we also observe weak absorption lines from O V as well as O VI in the spectrum (see Fig. 3.5). These lines represent a low ionization component and to account for them we added a second *xabs* component to our model. The ionization parameter for this second component is log ξ = 0.5 in units of 10^{-9} W m. However, the total column density for this component is about 25 times smaller than for the high ionization component (see Table 3.2).
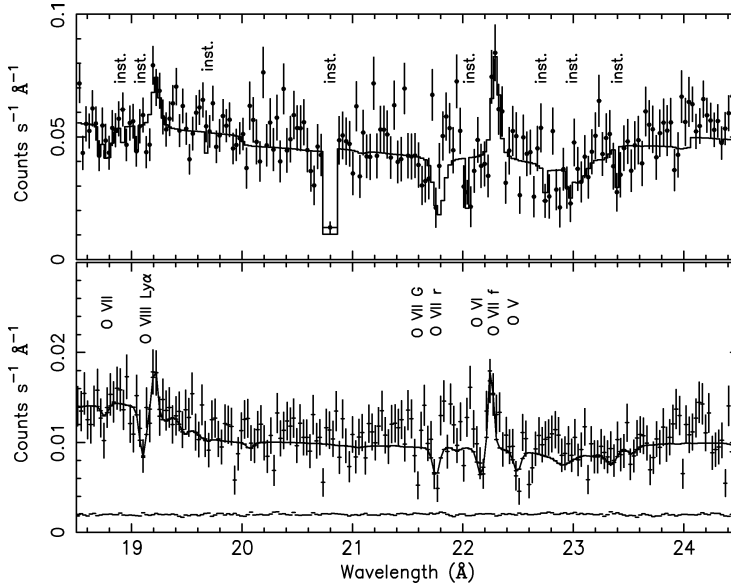
Figure 3.5: Detail of the RGS data (upper panel) and the LETGS data (lower panel). In the LETGS panel the absorption lines are indicated, G stands for Galactic absorption. In the upper panel the instrumental features for the RGS are labeled. The subtracted background is indicated for the LETGS data.

3.3.3 Spectral analysis: RGS

The RGS data, taken with the XMM-*Newton* satellite are noisy due to the short exposure time and the high background radiation level. As a result, it is hard to constrain any model for the warm absorber. We fitted RGS 1 and 2 simultaneously, but for clarity

Table 3.4: The different χ^2 and degrees of freedom, as well as the significance of the added component according to an F-test for the different models fit to the RGS data, as described in the text.

	model	χ^2	dof	χ_ν^2	sign.
1	PL+MBB	1317	1045	1.26	
2	1+O VIIf	1298	1043	1.24	0.59
3	2+Ne IXr	1275	1041	1.22	0.61
4	1+xabs	1260	1040	1.21	0.76
5	1+slab	1186	1020	1.16	0.95
6	5+rel.N VII Lyα	1166	1009	1.16	0.61
7	2+3rel.lines	1162	1035	1.12	0.96

added RGS 1 and 2 in the figures. The only significant narrow features in the spectrum are the O VII forbidden line in emission (see Fig. 3.5), and the Ne IX resonance line in absorption. We applied the model used for the analysis of the *Chandra* data: a power-law, modified black body, galactic absorption, the forbidden O VII emission line and a *xabs* component. Due to the noise in the data, however, the *xabs* component is hard to constrain. Therefore we fitted the warm absorber with the *slab* component (see Table 3.6). From the *slab* model we find a rather large spread in ionization parameters.

The *xabs* model could not constrain the absorption, because not all ions at a certain ionization state are observed. For instance, O VIII and Ne X are too weak to be detected, while highly ionized iron is observed. A possible explanation is that the O VIII Lyα absorption line is partly blended by its emission component. A narrow O VIII Lyα line in emission is observed with 1.6 σ significance. This absorption model is consistent with the higher S/N LETGS data.

Interestingly, in the RGS data set we see evidence for galactic absorption from O VII and O VIII, with logarithms of the column densities, in m^{-2}, of 20.2 ± 0.5 and 20.1 ± 0.9 respectively. For the LETGS data the galactic O VII resonance line, which is the most prominent galactic line, has an equivalent width (EW) of 45 ± 31 mÅ.

An excess above the continuum is noted at 24.9 Å (see Fig. 3.7). This excess is consistent with an extremely broadened relativistic emission line from N VII Lyα, and the normalization has a 2 σ significance (see Table 3.5). The disk inner radius implied by this emission line corresponds to ∼0.6 c. We found no significant O VIII and C VI Lyα lines. The model including the N VII relativistic line and the warm absorber (i.e. model 6 in Table 3.4) is plotted in Fig. 3.6.

Table 3.5: Continuum and emission parameters, describing the preferred model (i.e model 6 in Table 3.4), for RGS1 and RGS2, assuming a distance of 50.0 Mpc for NGC 4593.

PL:	norm^a	$(3.86 \pm 0.2) \times 10^{51}$ ph s^{-1} keV^{-1}
	Γ	1.8 ± 0.2
MBB:	norm^b	$(1.4 \pm 0.4) \times 10^{32}$ m$^{1/2}$
	T	(0.16 ± 0.01) keV
O VIIf:	EW	(-110 ± 34) mÅ
	flux	(0.84 ± 0.28) ph s^{-1} m^{-2}
	λ^c	(22.12 ± 0.02) Å

	Relativistic emission line:	
	i (degrees)	30 ± 11
	q ^{d}	3 ± 6
	$R_{\rm in}$ (GM/c^2)	< 89
	$R_{\rm out}$ (GM/c^2)	400
N VII:	norm	(2.1 ± 0.9) ph s^{-1} m^{-2}
	EW	(0.3 ± 0.2) Å
	λ^c	(24.9 ± 0.8) Å

^{a} at 1 keV.

^{b} norm = emitting area times square root of electron density.

^{c} wavelengths are given in the rest frame of NGC 4593.

^{d} the emissivity slope.

As a second model, we fitted the RGS data with only a power-law, modified black body and three relativistic emission lines, namely, for O VIII, N VII and C VI Lyα. This model (i.e. model 7 in Table 3.4) has a χ^2 of 1162 for 1035 degrees of freedom, a rather flat photon index of 1.4, and a 30 % lower normalization. The modified black body parameters are not as sensitive, and consistent within 3 σ of those quoted in Table 3.5. In this model we find a 3 σ detection for the N VII Lyα and a 2 σ measurement for the O VIII Lyα line. The C VI Lyα line is not detected in both models. In this model only absorption by Ne IX is detected with a 3 σ significance. However, this model over predicts the flux at higher energies, compared to those measured by pn and MOS 2. This is due to the flat photon index. As a result we exclude this model, and prefer

Table 3.6: The logarithms of the column density in m^{-2} for absorption in the NGC 4593 RGS data.

C VI	20.3 ± 0.4	Fe VIII	20.0 ± 0.7
N VI	20.0 ± 0.4	Fe IX	20.1 ± 0.4
O VII	21.1 ± 0.5	Fe XIII	19.8 ± 0.4
Ne IX	20.6 ± 0.5	Fe XVI	19.9 ± 0.8
Na XI	21.1 ± 0.7	Fe XVII	19.9 ± 0.5
Si IX	21.0 ± 0.5	Fe XVIII	20.1 ± 0.4
Si XII	20.7 ± 0.6	Fe XIX	20.5 ± 0.6
S XII	19.7 ± 0.7	Fe XX	20.5 ± 0.3
Ar X	19.6 ± 0.6	Fe XXI	20.5 ± 0.3
Ar XII	19.5 ± 0.7		
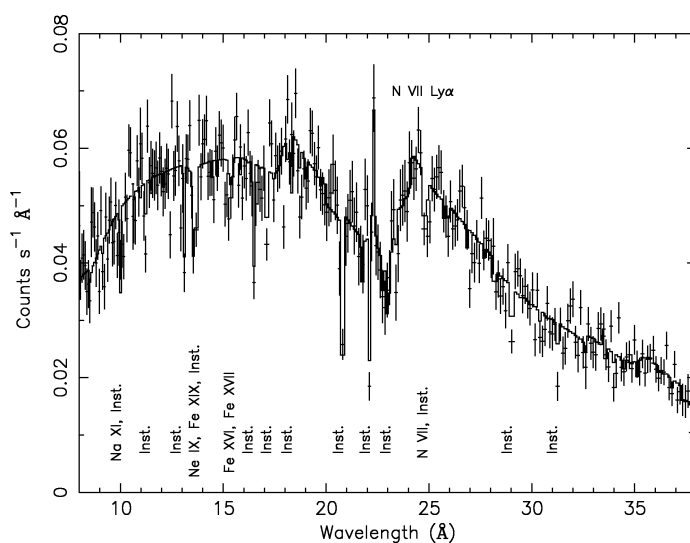
Figure 3.6: Fit to the RGS data with model 6 of Table 3.4. For clarity RGS 1 and RGS 2 were binned by a factor of 10 and added. The relativistic N VII Lyα line is indicated by N VII Lyα written horizontally. The features labeled Inst. are periodic dips due to CCD-gaps, or due to instrumental calibration.
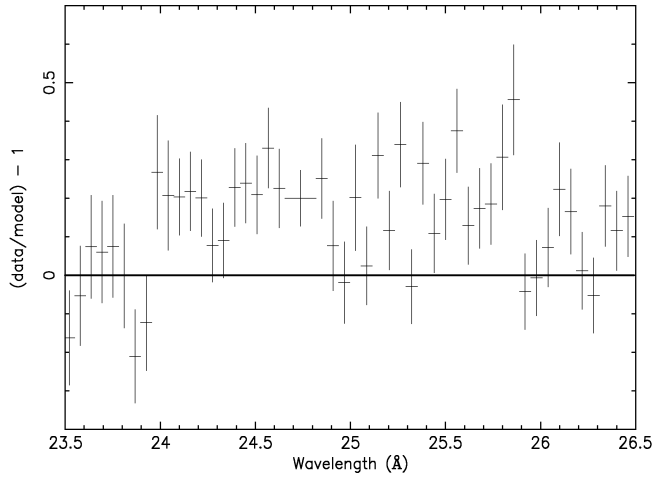
Figure 3.7: Fit residuals between 23.5 and 26.5 Å, showing the observed excess at the N VII Lyα wavelength, which is fitted in model 6 (Table 3.4) with a relativistic emission line.

the absorption model (model 6 in Table 3.4) as the continuum is consistent with the one observed with the EPIC instruments. This model does include a relativistic N VII Lyα line which was not detected in the LETGS data. In the *Chandra* LETGS spectrum of NGC 5548 (Kaastra et al. 2002a) the observed equivalent width for the relativistic N VII Lyα is nearly twice that of O VIII Lyα. Our findings are thus consistent with some earlier results on relativistic emission lines. The absence of the relativistic N VII Lyα line in the LETGS spectrum could indicate that the strength of this emission line is variable. Previous studies of relativistic lines in the soft X-ray band have shown some evidence for time variability (Steenbrugge et al. 2002). Due to the weakness of these relativistic lines, the EPIC data cannot be used to constrain either model further.

3.3.4 EPIC continuum and Fe Kα

The EPIC continuum was fitted with a power-law (PL), reflection (Refl) component and a modified black body (MBB). The power-law and reflection component were fitted in the $2 - 10$ keV range. Afterward we fitted a modified black body assuming the warm absorber parameters as determined from the RGS data (see Table 3.6), including the $0.3 - 2$ keV range. Note that for MOS the photon index for the reflection component is

35

not given, as we could not constrain it. The differences between the best fit model with a warm absorber (continuum parameters given in Table 3.7) and without are negligible, certainly for the MOS data. In both datasets the models overpredict the count rate between 0.8 and 1 keV, even if the warm absorber is included.

The MOS and pn spectra show clear evidence for a narrow Fe Kα line (see Fig. 3.8), but no broad component can be detected. The line was modeled with a Gaussian profile and is detected with a 3 σ significance in both datasets. The fit results for pn and MOS 2 are given in Table 3.7. No relativistically broadened Fe Kα component has been found before in NGC 4593.

3.4   Timing analysis

In the long *Chandra* LETGS observation, we observe a flare near the end of the observation. At the peak of the flare the luminosity increases by a factor of ~1.5 in about 27 ks (see Fig. 3.9). The flare peak lasted about 7 ks, afterward there is a 15 ks period were the flux level decreased and possibly leveled off. Due to the low count rates
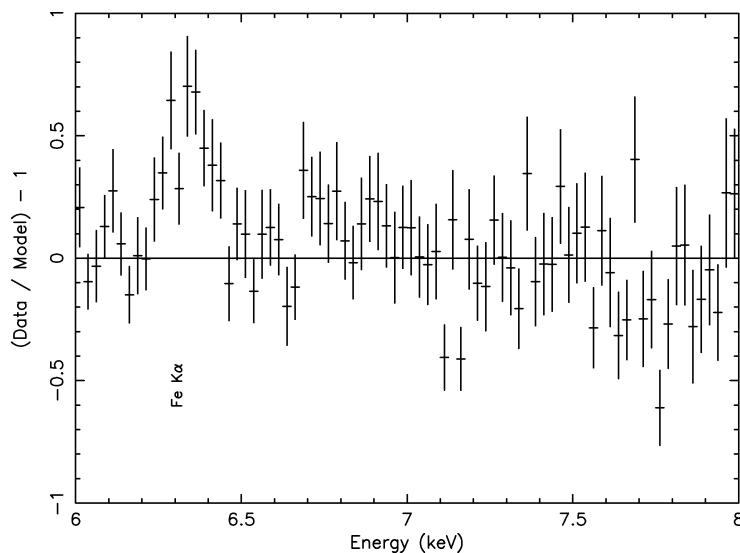
Figure 3.8: The relative fit residuals with respect to a simple power-law fit for the pn and MOS 2 data added together. The power-law was fit between 2 and 10 keV.

Table 3.7: pn and MOS 2 results for the continuum and the Fe Kα line.

	pn	MOS 2
PL norm[a]	3.3 ± 0.1	2.9 ± 0.2
Γ	1.83 ± 0.02	1.96 ± 0.05
Refl norm[a]	< 0.7	< 0.5
Refl Γ	1.97 ± 0.14	
MBB norm[b]	1.5 ± 1	8.8 ± 6
T (keV)	0.16 ± 0.005	0.09 ± 0.008
flux Fe Kα[c]	0.42 ± 0.09	0.37 ± 0.12
FWHM (keV)	< 0.13	< 0.55
rest E (keV)	6.40 ± 0.05	6.40 ± 0.05

[a] in 10^{51} ph s^{-1} kev^{-1}
[b] in 10^{32} m$^{1/2}$
[c] ph s^{-1} m^{-2}

measured and the relatively short duration of the peak, only a broadband comparison between the peak and the quiescence state is possible.

We took the spectrum of quiescence and the peak separately and binned them to 1 Å bins in order to have reasonable errors for the data points. The flux increase during the peak was mainly wavelength independent above 15 Å, while the flux increase at lower wavelengths was significantly smaller (Kaastra & Steenbrugge 2001). We separate the light curve into three components: one representing the power-law component (1 − 10 Å), one representing the soft excess component (20 − 40 Å) and finally an intermediate component between 10 − 20 Å. A detail of the lightcurves, indicating the softening of the spectrum during the rise and peak phase is shown in Fig. 3.10. Also during the smaller flare in the beginning of the observation the spectrum is softer than during quiescence (between 20 ks and 70 ks).

The major contribution to the flare was an increase in the soft excess, i.e. from the accretion disk spectrum. The 10 − 20 Å component is near constant during the rise phase with respect to the 1 − 10 Å component, but does rise during the peak. The rise of the power-law component is smaller and more complex: it has two maxima (83 and 102 ks) while the soft excess rises smoothly to the flare peak (87 and 102 ks). This is not consistent with the picture that the power-law is produced solely by Inverse Compton scattering of UV and soft X-ray photons. Several authors have noted that the

37

power-law component is variable on time scales smaller than the variability detected in the soft excess (see e.g. Dewangan et al. 2002; Turner et al. 2001). A possible explanation is that magnetic flares take place in a corona (Merloni & Fabian 2001) on these shorter time scales.

The power-law component decays, after the first peak, in 9 ks between 87.5 ks and 96.5 ks. We derive a half-life of 18 ks. This decay seems independent of the soft excess component, and might thus be representative of a magnetic reconnection decay time. After the second peak also the soft excess component decays, therefore the decay of the power-law component can be caused by both magnetic reconnection decay and a decrease of seed photons for the Inverse Compton scattering.

For the XMM-*Newton* data the study of luminosity variations is complicated due to the short observation time and the high radiation background. Over the good time interval, of only 8000 s, the luminosity was constant.
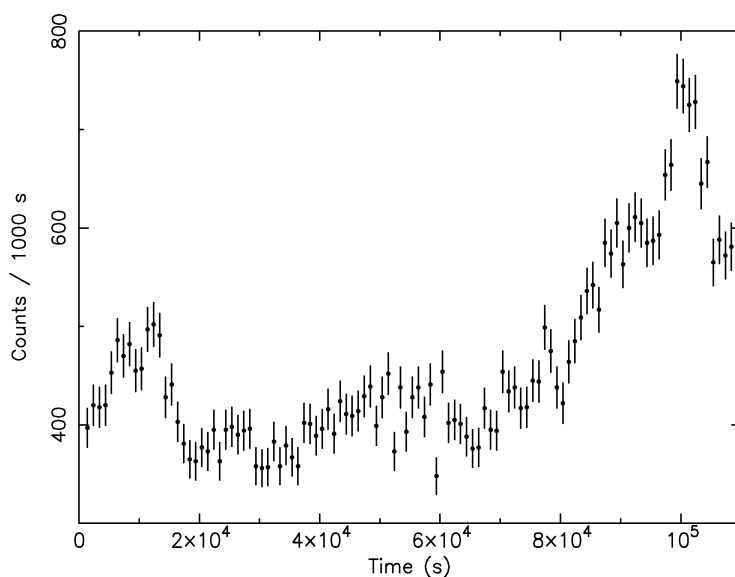
Figure 3.9: The light curve for the LETGS data, in the zeroth spectral order. Note the rise phase between 70 and 97 ks, and the peak phase between 97 and 105 ks.

38
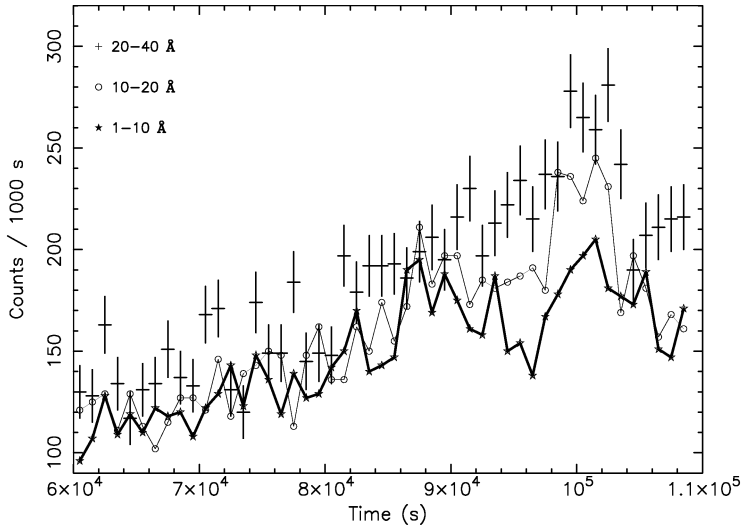
Figure 3.10: The light curve during the rise and peak phase for the LETGS data, but now split up into three wavelength bands. The stars joined by the thick line represent the power-law component, or the 1-10 Å photons. The crosses represent the soft excess component, i.e. the 20-40 Å photons and the open circles joined by a thin line are the intermediate wavelength range of 10-20 Å. The errors for the power-law and intermediate component are similar to those plotted for the soft excess component.

3.5   Discussion

The $2 - 10$ keV luminosity of NGC 4593 during the XMM-*Newton* observation was $1.2{\times}10^{36}$ W, estimated from model 6 in Table 3.4. For pn and MOS 2 we find $1.1{\times}10^{36}$ W and $8.5{\times}10^{35}$ W respectively. The LETGS luminosity was $9.0{\times}10^{35}$ W and during the ASCA observation it was $1.15{\times}10^{36}$ W (Reynolds 1997). The temperatures found for the MBB are consistent at the 3 σ level between the *Chandra* LETGS and XMM-*Newton* results, while the photon index is consistent between the LETGS and RGS data, but inconsistent at the 3 σ level between the LETGS and EPIC results.

Guainazzi et al. (1999) found a moderately broad neutral Fe Kα line, with $\sigma >$ 60 eV or a FWHM greater than 141 eV. Reynolds (1997) quotes a σ of 66 ± 22 eV or equivalently a FWHM of 155 ± 52 eV. The upper limit to the FWHM for the Fe Kα line from the pn instrument is 130 eV. This is consistent with the result from Reynolds (1997), but is marginally inconsistent with the best fit results obtained by Guainazzi et

39

al. (1999) from the *Beppo*SAX data. The results from MOS 2 are less constraining and consistent with both previous observations.

Comparing our spectra with the earlier *Beppo*SAX observation, we find a similar power-law slope for our XMM-*Newton* data set. Guainazzi et al. (1999) note an excess between 0.3 and 0.6 keV in the *Beppo*SAX spectrum, but conclude it is most likely a calibration feature and not a soft excess. However, we find a significant soft excess in both the *Chandra* LETGS and XMM-*Newton* observations. Guainazzi et al. (1999) explained the dip around 0.7 keV as due to absorption edges of O VII, O VIII, Ne IX and Ne X. For the LETGS spectrum we explain this dip by absorption of highly ionized iron and neon ions. Also in the RGS there is evidence for absorption from highly ionized ions. We cannot compare the reflection component detected in the *Beppo*SAX data, as our dataset cuts off at around 10 keV, and the reflection component is minimal there. The width of the FeKα line derived from the EPIC data is consistent with those derived from the *Beppo*SAX and ASCA observations (Guainazzi et al. 1999; Reynolds 1997). However, in a more recent observation Yaqoob & Padmanabhan (2003) conclude from the line intensity difference between simultaneous *Chandra* HEG and RXTE PCA observations that there is a broad component to the Fe Kα line.

Both the LETGS and the RGS data show a prominent O VII forbidden emission line. The fluxes measured for this line in the two observations are consistent and the line is unresolved in both cases. We expect that this narrow emission line is formed further out from the ionization source than the absorption lines.

For the *Chandra* LETGS observation we observe two distinct warm absorbers which have an ionization state different by two orders of magnitude. The high ionization component is only detected through shallow, highly ionized iron and neon lines. The low ionization component has a 25 times smaller column density, but is represented by a few well detected absorption lines. From simple outflowing wind models a more continuous ionization range would be expected. A possible explanation is that the highly ionized warm absorber is only formed during the peak. However, the statistics are too poor to verify this. Due to the large errors the RGS data set is consistent with the absorber model derived from the LETGS spectrum.

tribution to early analysis of the XMM-*Newton* data.

References

Allende Prieto, C., Lambert, D. L. & Asplund, M., ApJ, 556, L63, 2001

Anders, E. & Grevesse, N., 1989, Geochim. Cosmochim. Acta 53, 197

Blustin, A.J., Branduardi-Raymont, G., Crawford, et al., 2003, to be published in Advances in Space Research, COSPAR 2002 Special Issue

Branduardi-Raymont, G., Sako, M., Kahn, S. M., et al., 2001, A&A, 365, L140

Dewangan, G. C., Boller, Th., Singh, K. P. & Leighly, K. M., 2002, A&A, 390, 65

Elvis, M., Wilkes, B. J., & Lockman, F. J., 1989, AJ, 97, 777

Gebhardt, K., Kormendy, J., Ho, L. C., et al., 2000, ApJ, 543, 5

George, I. M., Turner, T. J., Netzer, H., et al. 1998, ApJS, 114, 73

Guainazzi M., Perola G.C., Nicastro F., et al., 1999, A&A, 346, 407

Kaastra, J. S., Mewe, R., Nieuwenhuijzen, H., 1996, in: UV and X-ray Spectroscopy of Astrophysical and Laboratory Plasmas: Proceedings of the Eleventh Colloquium on UV and X-ray Spectroscopy, eds. K. Yamashita and T. Watanabe

Kaastra, J. S. & Barr, P., 1989, A&A, 226, 59

Kaastra, J. S. & Steenbrugge, K. C., 2001, X-ray Emission from Accretion onto Black Holes, eds. Yacoob, T. & Krolik, J. H., published electronically (http://www.pha.jhu.edu/groups/astro/workshop2001/papers/index.html)

Kaastra, J. S., Steenbrugge, K. C., Raassen A. J. J., et al., 2002, A&A, 386, 427

Kaastra, J. S., Mewe, R., Raassen, A. J. J., 2002b, Proceedings Symposium 'New Visions of the X-ray Universe in the XMM-*Newton* and *Chandra* Era'

Kallman, T. R. & Krolik, J. H., 1999, XSTAR photoionization code, ftp://legacy.gsfc.nasa.gov/software/plasma_codes/xstar/

Merloni, A., & Fabian, A. C., 2001, MNRAS, 321, 549

Paturel, G., Dubois, P., Petit, C, et al., 2002, LEDA

Reynolds C. S., 1997, MNRAS, 286, 513

Santos-Lleó M., Clavel J., Barr P., et al., 1994, MNRAS, 270, 580

Simkin, S. M., Su, H. J., Schwarz, M. P., 1980, ApJ, 237, 404

Steenbrugge, K. C., Kaastra, J. S., de Vries, C. P. et al., 2002, A&A, 402, 477

Turner, T. J., Romano, P., George, I. M., et al., 2001, ApJ, 561, 131

Yaqoob, T. & Padmanabhan, U., 2003, Active Galactic Nuclei: From Central Engine to Host Galaxy, eds. Collin, S., Combes, F. & Shlosmann, I., ASP Conferences

Chapter 4

XMM-Newton High Resolution Spectroscopy of NGC 5548

K.C. Steenbrugge, J.S. Kaastra, C. P. de Vries, R. Edelson

Abstract

We analyze a 137 ks exposure X-ray spectrum of the Seyfert 1 galaxy NGC 5548 obtained with the XMM-*Newton* Reflection Grating Spectrometer. Due to the long exposure time, the spectrum is of higher statistical quality than the previous observations of this AGN. Therefore, we detect for the first time in NGC 5548 inner-shell transitions from O III to O VI ions, and the Unresolved Transition Array of M-shell iron. The warm absorber found from this X-ray observation spans three orders of magnitude in ionization parameter. We detect O III, which is as lowly ionized as the warm absorber detected in the UV band, to Fe XXIV. For O VI the column density determined from our X-ray data is an order of magnitude larger than the column density measured in previous UV observations. We conclude that there is substantially more low ionized material than previously deduced from UV observations. However, only a few percent of the warm absorber detected in the X-rays is lowly ionized. A 99.9% significant increase in the derived absorbing column density with higher ionization states is observed. The outflow velocities determined from the X-ray absorption lines are consistent with those deduced from the UV lines, evidence, together with the detection of

O VI, that the X-ray and UV warm absorber are different manifestations of the same phenomenon. From a simple mass conservation argument, we indicate that our data set is consistent with an outflow with small opening angle formed due to instabilities in the accretion disk. Possibly due to uncertainties in the radiative transport mechanism, an apparent deviant iron to oxygen abundance is detected. No strong relativistically broadened emission lines of O VIII, N VII and C VI were detected.

4.1 Introduction

The immediate environment of active galactic nuclei (AGN) is poorly understood. The black hole is fed from an accretion disk, which becomes visible through high energy radiation. Possibly powered by radiation pressure, an outflowing wind is formed from the accretion disk. In some AGN, the wind is visible through its continuum and line absorption of the radiation from the nucleus. These absorption lines were already detected in the UV part of the spectrum (Mathur, Elvis & Wilkes 1995), and have now been confirmed in the X-ray spectra (Kaastra et al. 2000).

NGC 5548, a Seyfert 1 galaxy, has been well studied in the X-rays due to its relative X-ray brightness, and the fact that it is a nearby active galactic nucleus with a redshift of z=0.01676 (Crenshaw & Kraemer 1999). This Seyfert galaxy was studied in detail with ROSAT (Done et al. 1995). They detected an O VII and O VIII K-shell absorption edge, and concluded that there was a warm absorber present. Therefore, NGC 5548 is an ideal Seyfert 1 galaxy to study with the high resolution spectroscopy instruments on-board of XMM-*Newton* and *Chandra*. Table 4.1 list the observations made with these instruments. In this paper we discuss a 137 ks exposure time Reflection Grating Spectrometer (RGS) spectrum from the guest observation program of XMM-*Newton*.

4.2 Observations and data reduction

Here we present data taken with the RGS instrument (den Herder et al. 2001). The EPIC data (the continuum spectrum, and the Fe Kα line) are presented separately (Pounds et al. 2002). The time variability of the combined XMM-*Newton* and RXTE data sets will be presented by Markowitz et al. (2002).

Shortly after launch two of the eighteen CCD chains failed. For RGS 1 this causes a data gap in the $10 - 14$ Å range (where most Fe-L and Ne absorption lines are), for RGS 2 the gap is between $20 - 24$ Å (where the O VII triplet is).

The data were reduced using the developer's version of the XMM-*Newton* data analysis package SAS version 5.3, which comprises a correct calibration of the effec-

Table 4.1: High resolution X-ray observations of NGC 5548. LETGS: Low Energy Transmission Grating in combination with the High Resolution Camera; HETGS: High Energy Transmission Grating in combination with the ACIS camera both on-board *Chandra*; RGS: Reflection Grating Spectrometer onboard XMM-*Newton*. The exposure time is given in in ks.

Date	Instr.	Expos.	References-comments
1999 Dec. 11	LETGS	86.4	Kaastra et al. 2000, 2002
2000 Feb. 5	HETGS	83	Yaqoob et al. 2001,
			Kaastra et al. 2002
2000 Dec. 24	RGS	28	noisy spectrum
			low flux state
2001 Jul. 09–12	RGS	137	present work

tive area and the instrumental O-edge. The latter is important as the 1s-2p absorption lines of O II and O III are cosmologically redshifted toward the instrumental O I edge.

In this paper we analyze the first and second order spectra obtained from both RGS 1 and 2. Although the second order spectrum has a lower count rate and only a wavelength coverage from 5 to 19 Å, it does have a higher wavelength resolution than the first order. Throughout the paper we have fitted RGS 1 and 2 simultaneously, but for clarity of representation we have added the RGS 1 and RGS 2 spectra in the figures.

All the spectral analysis was done with the SPEX package (Kaastra et al. 2002b). Fig. 4.1 shows the fluxed spectrum of NGC 5548, indicating the Unresolved Transition Array (UTA) of inner-shell iron absorption lines and some other prominent features.

4.2.1 Wavelength scale accuracy

In general the RGS wavelength scale can be reconstructed to an accuracy of 8 mÅ (den Herder et al. 2001). However, in our case larger uncertainties exist, due to errors in the recorded satellite attitude and right ascension in the data files available. From the analysis of the first order data we find that the O VII forbidden line is blueshifted by 285 km s^{-1} (-0.021 Å). The O VII forbidden line is not blueshifted in the earlier LETGS data of NGC 5548 (Kaastra et al. 2002a). No blueshift for the forbidden line can be determined in second order. However, comparing first and second order results for the warm absorber, we find a smaller outflow velocity in the second order data set. The difference in wavelength between first and second order, for the strongest line in the
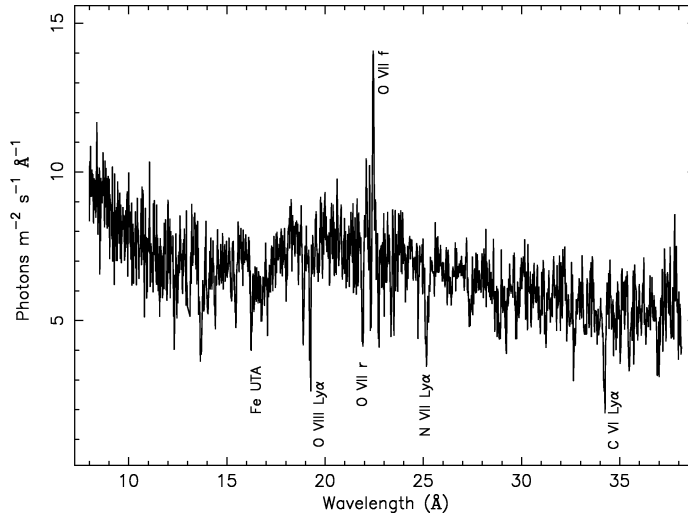
Figure 4.1: The fluxed spectrum of NGC 5548, RGS 1 and 2 are added together and no error bars are plotted for clarity. The typical 1 σ error on the data is 1 photon m^{-2} s^{-1} Å^{-1}. Some of the strongest features are identified.

second order, O VIII Lyβ (both orders were fitted with the *xabs* model, see Sect. 3) is -0.019 ± 0.005 Å. Finally, in the first order data set there is a weak Galactic O VII recombination line, which has a rest wavelength of 21.6 Å. This absorption line also shows an apparent velocity shift of -230 km s^{-1} (-0.017 Å), although no blueshift should be expected. To correct for this wavelength calibration problem we applied a constant wavelength shift of -0.017 Å to the model for the first order spectra. If not corrected, this wavelength shift would result in a velocity error between 130 km s^{-1} for the longest wavelengths to 620 km s^{-1} for the shortest wavelengths. The residual error in the wavelength scale should be within the 8 mÅ uncertainty of the calibration. All velocities quoted in this paper are corrected for this wavelength shift.

4.3 Modeling the warm absorber

In NGC 5548 there is an intricate pattern of densely spaced absorption lines as well as the possible presence of weak relativistic emission lines (Kaastra et al. 2002a). Blending, mostly of iron lines, is important in many wavelength ranges, making equivalent

width (EW) estimations rather complicated. On the other hand, in the X-ray band many of the observed ions have more than one detected absorption line, significantly improving the column density and velocity outflow measurements. This is also important in order to disentangle possible partial covering factors and column densities of the ions. The possibility of relativistic emission lines complicates the analysis of the continuum spectral shape, which is already complicated to derive due to the presence of many edges and absorption lines. We consider here two approaches for fitting the warm absorber. In the first approach all absorption lines and edges of each individual ion are calculated, using a separate value for the column density for each ion. The transmission of all ions is then combined to calculate the total transmission of the warm absorber. Outflow velocity and velocity broadening are coupled for the different ions. This is the *slab* model in SPEX (Kaastra et al. 2002b).

In the second approach the column densities of the ions are coupled through a photoionization model. In this case only the total column density, ionization parameter, elemental abundances and the outflow and broadening are free parameters. This is the *xabs* model. For a full description of both methods see Kaastra et al. (2002b).

The results obtained with the *xabs* model are more dependent on theory, because the ionization parameter determines the column density ratios of the ions. An advantage of the *xabs* model is that different ionization components, each with their own velocity structure can be combined. This is harder to accomplish with *slab* components, in particular if the velocity components are barely separable with the current spectral resolution. This is the case in NGC 5548, and would lead to strongly correlated parameters in the spectral fitting procedure. One further difference between the models is that ions which have a rather small cross-section are automatically included in *xabs*, but since these are more difficult to discern individually, they are not usually included in the *slab* modeling.

4.4 Data analysis

4.4.1 The continuum

The continuum model consists of a power-law spectrum with Galactic absorption, and a modified black body (see Kaastra & Barr 1989 for more details). A second modified black body with a high temperature is required to describe the EPIC data, but is not detected in the limited RGS band (Pounds et al. 2002). This indicates that RGS data alone cannot constrain the continuum accurately. Table 4.2 gives the continuum parameters used for the analysis of the RGS data.

The temperature (T) of the modified black body was allowed to vary as well as the

Table 4.2: The parameter values quoted are those obtained in the *xabs* model fitting and differ from the best fit continuum without absorption. The continuum model was used as a basis for adding the warm absorber, either with a *slab* component (see Table 4.3) or with *xabs* components (see Table 4.4). The quoted $\chi_\nu{}^2$ is for the best fit continuum parameters without absorption, and thus not the parameters quoted in the table, which we derived including absorption.

$$\chi_\nu{}^2 \text{ equals } 1.96 \text{ for } 2441 \text{ degrees of freedom}$$

pl:	norm[a]	$(1.57 \pm 0.03) \times 10^{52}$ ph s^{-1} keV^{-1}
	Γ	1.77 ± 0.02
mbb:	norm[b]	$(6.5 \pm 0.7) \times 10^{32}$ m$^{1/2}$
	T	(97 ± 6) eV

[a] at 1 keV.
[b] norm=emitting area times square root of electron density.

normalizations of the power-law and the modified black body. However, the photon index (Γ), which is very sensitive to small changes in the model, as well as the Galactic H I column density (1.65×10^{24} m^{-2}, Nandra et al. 1993) were kept fixed throughout the fitting process. The obtained parameters are within calibration uncertainties consistent with those obtained from simultaneous EPIC and BeppoSAX observations.

4.4.2 Spectral fit using the *slab* model

As a first approach to the analysis of the warm absorber, we modeled it by adding a *slab* component to the continuum model. We refitted the data, leaving the same parameters free as above for the continuum, as well as the overall outflow velocity, and all the relevant ion column densities. Finally, after obtaining this overall fit we also let the photon index vary, and now obtain a reasonable result. The results of this fit were then used to fine-tune the column density and outflow velocity of each ion which has a detectable absorption line or edge in the RGS wavelength range. To do so we decoupled subsequently for each ion its outflow velocity from the outflow velocity of all the other ions in the model. This method was followed to minimize the effects from blending. The significance of the different ionic columns can be derived from the best fit column densities and their error bars. The result of this fitting is summarized in Table 4.3. This Table also lists the ionization state for the maximum column density of the particular

Table 4.3: Best fit values for the logarithms of the column densities in m^{-2} and the outflow velocity, using the *slab* component. The ionization parameter for which the ion has the largest column density as determined from XSTAR is given in column 4. a indicates that the ion is discussed in the text, b indicates a possible error in wavelength.

ion	log N_H (m^{-2})	v (km s^{-1})	log ξ (10^{-9} W m)	ion	log N_H (m^{-2})	v (km s^{-1})	log ξ (10^{-9} W m)
C IV[a]	21.4 ± 0.1	—	− 0.6	S XIV	20.1 ± 0.3	+90 ± 280	2.4
C V	20.4 ± 0.2	−490 ± 200	0.2	Ar XIII	19.4 ± 0.4	−630 ± 210	1.8
C VI	21.1 ± 0.1	−510 ± 70	1.2	Ar XIV	< 19.4	—	2.1
N V[a]	20.6 ± 0.3	—	0.0	Ar XV	20.1 ± 0.3	−470 ± 400	2.3
N VI	20.1 ± 0.1	−470 ± 130	0.7	Fe I	< 19.8	—	< − 4.0
N VII	20.5 ± 0.1	−390 ± 150	1.5	Fe II	19.9 ± 0.3	—	− 3.0
O III	20.0 ± 0.6	—	− 1.8	Fe V	< 19.7	—	− 1.3
O IV	< 20.2	—	− 0.7	Fe VI	19.8 ± 0.4	—	− 0.9
O V[b]	20.7 ± 0.3	+430	0.0	Fe VII	< 19.7	—	− 0.3
O VI	20.5 ± 0.1	−250 ± 160	0.5	Fe VIII	20.1 ± 0.1	−340 ± 450	0.1
O VII	21.57 ± 0.05	−450 ± 90	1.2	Fe IX	20.1 ± 0.1	+130 ± 220	0.4
O VIII	22.24 ± 0.03	−310 ± 70	1.8	Fe X	19.9 ± 0.1	−670 ± 430	0.6
Ne IX	21.82 ± 0.06	−30 ± 200	1.7	Fe XI	20.1 ± 0.1	−430 ± 400	0.8
Ne X	21.5 ± 0.2	+10 ± 230	2.3	Fe XII	< 19.7	—	1.0
Na X	20.5 ± 0.4	—	1.9	Fe XIII	19.4 ± 0.6	—	1.2
Na XI	20.6 ± 0.6	—	2.4	Fe XIV	< 19.5	—	1.4
Mg X	21.4 ± 0.1	−560 ± 250	1.5	Fe XV	< 19.7	—	1.6
Mg XI	20.5 ± 0.5	—	2.1	Fe XVI	19.7 ± 0.3	−500 ± 450	1.6
Mg XII	20.8 ± 0.5	−970 ± 990	2.6	Fe XVII	20.1 ± 0.1	−480 ± 170	2.1
Si IX	21.3 ± 0.1	—	0.9	Fe XVIII	20.1 ± 0.1	−420 ± 240	2.3
Si X	< 20.4	—	1.3	Fe XIX	20.49 ± 0.09	−350 ± 230	2.5
Si XI	< 20.1	—	1.7	Fe XX	20.4 ± 0.2	−960 ± 710	2.8
Si XII	< 20.5	—	2.1	Fe XXI	20.5 ± 0.2	−65 ± 550	3.0
S X	20.3 ± 0.2	−400 ± 380	1.1	Fe XXII	20.6 ± 0.2	—	3.2
S XI	20.3 ± 0.1	−820 ± 420	1.7	Fe XXIII	20.4 ± 0.4	—	3.3
S XII	20.3 ± 0.1	−410 ± 80	1.7	Fe XXIV	20.7 ± 0.5	—	3.5
S XIII	20.1 ± 0.2	−640 ± 200	2.1				

49

ion. Note however, that each ion exists for a range of ionization states, and thus the quoted ionization is only an indication. Adding the *slab* component significantly improves the χ_ν^2 from 1.96 to 1.26 (with 2404 degrees of freedom).

For the ions with only an upper limit for their column densities, absorption is only detected through continuum absorption (Ar XIV, Fe V and Fe VII) or a single/few weak lines (O IV, Si X, Si XI, Fe I, Fe XII and Fe XIV). As a result the column density as well as the velocity of these ions are poorly determined. The other ions with poorly determined velocity shifts, but with solid column densities, are those for which the column density is determined from an edge (C IV, N V and Si IX), for which the absorption lines are strongly blended (Fe XII), or because only a few weak absorption lines are detected.

We find a very well constrained column density for C IV and N V, although both these ions have in the RGS band only an absorption edge, at 36 Å and 25 Å (rest wavelength) respectively. As the depth of the edge correlates with the assumed underlying continuum, these column densities are rather more uncertain than the fit results indicate. To ascertain how these column densities change the overall continuum shape we refitted the data, but now forcing a column density for C IV and N V of zero. For the new fit, which gives a similarly good χ_ν^2, the normalization of the modified black body increased by an order of magnitude, while the temperature of the same component decreased by an order of magnitude. As a result of this change in the continuum model, the column densities found for O III and Ne IX also changed significantly. In this respect the *xabs* modeling is more reliable, as the column densities determined for ions that are only detected through an edge, are based upon the determined ionization state.

The same method for modeling the warm absorber was used for fitting the second order data. The second order data for RGS 1 and 2 were not fitted together with the first order data, as the systematic shift in the first order spectra is corrected for in the applied model and not in the data itself. However, both orders are in excellent agreement, see Fig. 4.2.

The average outflow velocity found, including only those ions with well determined velocities in both orders, is -350 ± 250 km s^{-1} for the first order data set, in comparison with -420 ± 340 km s^{-1} for the second order data set. For further analysis we focus on the first order data, because the better statistics outweigh the better spectral resolution of the second order data.

4.4.3 Spectral fit using the *xabs* model

Using the same continuum model as in the previous section, we replaced the *slab* model by the *xabs* model for the warm absorber. First we fitted only the ionization parame-

ter (ξ), the hydrogen column density (N_H) and the outflow velocity (v), in addition to the continuum parameters that we leave free throughout the fitting procedure. The abundances were kept to the solar values (Anders & Grevesse 1989). Later, the abundances were left as free parameters. However, as hydrogen produces no X-ray lines, we normalized the abundance relative to oxygen, which was frozen to solar abundance. Finally we added two more *xabs* components to the model, both with lower ionization parameters, significantly improving the spectral fit.

Adding the first *xabs* component improved χ_ν^2 from 1.97 to 1.66. The addition of the second *xabs* component, which was the one with the lowest ionization parameter, further improved χ_ν^2 to a value of 1.46. However, for this *xabs* component we found two abundances which have unphysical values. Namely, Ne and S are overabundant by a factor of 43 and 106, respectively. From detailed fitting, it is clear that both these abundances are mainly determined from the absorption edges in the spectrum, and are
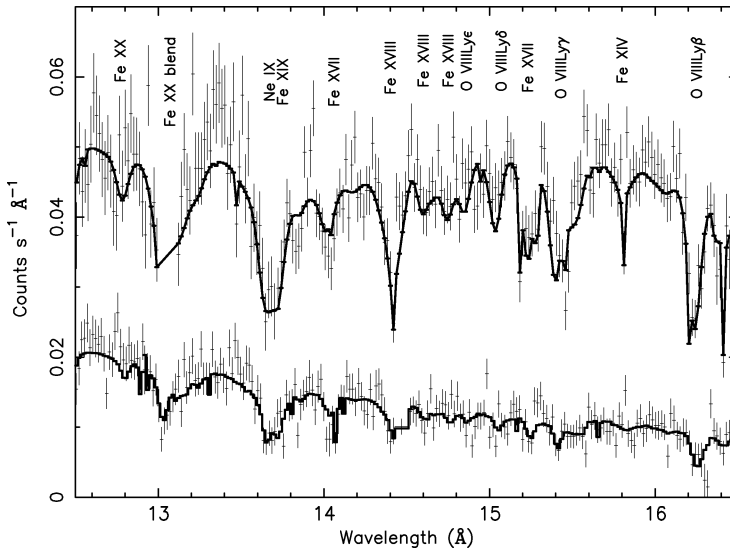
Figure 4.2: Best *xabs* fit to the first (top) and second order (bottom) data. First order data are rebinned by a factor of 2, second order by a factor of 3. For the first order data a CCD gap related feature can be seen at 13 Å and a dead pixel is seen short-ward of 16.5 Å. Between 12.5 and 14 Å only RGS 2 gives results, hence the larger error bars. For second order data a dead pixel is seen at 14.05 Å and a CCD gap related feature can be seen at 14.45 Å.

Table 4.4: The best fit results for the first order data *xabs* fit. Further details are given in the text.

Component	A	B	C
$\log \xi$ (10^{-9} W m)	2.69±0.04	1.98±0.06	0.40±0.03
$\log N_H$ (m^{-2})	25.68±0.05	25.52±0.06	24.15±0.01
outflow v (km s^{-1})	−311±60	−440±100	−290±70
abundances[a]:			
C	<4.9	0.6±0.2	1.8±0.6
N	2.2±1.0	<0.3	1.7±0.5
Ne	2.5±1.4	0.1±0.7	b
Na	<8.3	3.9±3.9	<350
Mg	1.0±0.8	<0.6	<5.8
Si	2.2±2.2	<0.2	<3.9
S	0.6±0.7	0.5±0.2	b
Ar	2.2±2.2	0.4±0.5	<5.4
Fe	0.70±0.06	0.11±0.03	7.4±0.6

[a] The abundances are relative to O, which is kept at solar value.
[b] Frozen to solar value, see text for explanation.

thus rather uncertain. Fitting the model again, but fixing the abundance of Ne and S in the lowest ionization component to solar, we find a similar good fit, namely with χ_ν^2 of 1.48. The addition of the last *xabs* component gives a final $\chi_\nu^2 = 1.22$. Table 4.4 lists the best fit parameters, with the *xabs* components labeled to be consistent with the components found by Kaastra et al. (2002a). The significance, according to F-tests, is at least 100, 99.8 and 99.9 percent for components A, B and C, respectively. Only in the last step we left the photon index free, but this did not improve the χ_ν^2. The continuum parameters for this model correspond within 1 σ with the continuum parameters as found from the *slab* fit.

4.4.4 Emission and absorption by oxygen

Fig. 4.3 shows the spectrum around the O VII triplet. In Table 4.5 we list the parameters of the O VII forbidden line in emission. For the O VII forbidden line Table 4.6 gives the fluxes, outflow velocity as well as an upper limit to the width of the line, as measured from the HETGS and LETGS spectra (data taken from Kaastra et al. 2002a)

Table 4.5: Values determined for the forbidden line of O VII.

O VIIf:	EW	(-170 ± 22) mÅ
	flux	(0.9 ± 0.1) ph m^{-2} s^{-1}
	FWHM	< 36 mÅ
		< 490 km s^{-1}
	λ^a	(22.096 ± 0.005) Å
	v^b	(-110 ± 80) km s^{-1}

[a] Wavelengths are given in the rest frame of NGC 5548.
[b] Velocity shift from comparing rest and observed wavelengths.

Table 4.6: Comparison of the O VII forbidden line from three different observations.

Instrument	v (km s^{-1})	σ_v (km s^{-1})	flux (ph m^{-2} s^{-1})
HETGS	-70 ± 100	<310	0.8 ± 0.2
LETGS	0 ± 50	<330	0.8 ± 0.3
RGS	-110 ± 80	<490	0.9 ± 0.1

and our data set. Note that this line has the same measured flux over a period of 1.5 years, despite large variations in the continuum. In all three observations the line is unresolved. The above indicate that the O VII forbidden line is formed at least 0.46 pc from the ionizing source.

Interestingly, the inter-combination line is not present in the data. An excess is observed at 21.74 Å rest wavelength, shifted by 0.06 Å from the rest wavelength of the inter-combination line. The relative wavelength accuracy of RGS is 2 mÅ. Assuming that the inter-combination and forbidden lines are formed at the same distance from the ionizing source and under the same conditions, a blueshift of 620 km s^{-1} is inconsistent with the lack of blueshift for the forbidden line. Because the forbidden line is strong, models predict that even tenuous gasses should produce a weak but detectable inter-combination line. One possible explanation is that the inter-combination line blends with an O VI absorption line at 21.79 Å.

Another emission feature for oxygen is the radiative recombination continuum (RRC) of O VII between 16.9 and 17 Å (see Fig. 4.4). As there is severe blending

with iron absorption lines, we approximated the RRC simply with a delta function. We find a $2\,\sigma$ detection for this RRC and the narrowness of the feature (unresolved by the instrument) indicates a low temperature. The flux is 0.06 ± 0.03 ph m^{-2} s^{-1} which is consistent with the 0.06 ± 0.10 ph m^{-2} s^{-1} value as determined from the LETGS spectrum (Kaastra et al. 2002a).
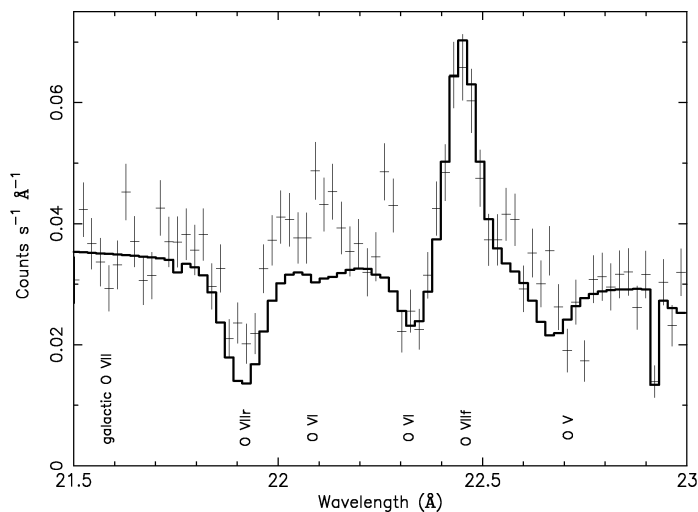
Figure 4.3: Detail of RGS 1 showing the O VII triplet as well as absorption lines for O VI and O V. The *xabs* model was used for fitting the warm absorber. The Galactic O VII absorption line is indicated.

The presence of inner-shell absorption lines of oxygen together with the higher ionized O VII and O VIII absorption lines allow for an accurate ionization determination, independent of elemental abundances. The ionization parameter determined for oxygen spans three orders of magnitude from $\log \xi = -1.8$ for O III to $\log \xi = +1.8$ for O VIII.

The deepest absorption line in the spectrum is the O VIII Lyα line. For O VIII we also detect the Lyβ, Lyγ and Lyδ lines and some hints for the Lyϵ line in absorption (see Fig. 4.2). The multitude and depth of these absorption lines allow thus for an accurate column density and outflow velocity determination (see Table 4.3). These higher order lines are important for the detection of variability in the warm absorber, as they have an optical depth close to unity. However, we did not detect significant variability in the measured column densities as compared to the previous LETGS observation, which

has rather large error bars. Also within this observation no variability in the warm absorber was detected.

Fig. 4.3 shows that our model overestimates the O VII resonance line. A probable explanation is that the emission component of this line partly refills the absorption line due to the imperfect spectral resolution. In the LETGS data (Kaastra et al. 2002a) this line has a clear P Cygni profile, and also in the RGS there is excess emission at wavelengths just longer than the resonance line. Both models for the warm absorber don't include possible P Cygni profiles. The excess emission just longward of 22.25 Å is noise, as the width of the feature is narrower than the point spread function of the instrument. The Galactic absorption by O VII, detected with 1.5 σ significance is also indicated in Fig. 4.3.

Shortward of the forbidden line of O VII there is a deep O VI absorption line, and 0.25 Å longward of the forbidden line there is a deep O V absorption line. Both are inner-shell absorption lines, indicating the importance of these transitions in AGN. For O V two absorption lines are detected. However, the line at 22.33 Å is redshifted by about 700 km s^{-1} relative to the weaker line at 19.92 Å, and the other oxygen absorption lines. To check the possible uncertainty on the wavelength for the strongest O V line, the O V wavelength and oscillator strength were also calculated using the Cowan code (1981) (Raassen, private communication). This gives a rest wavelength of 22.38 Å, closer to the observed rest wavelength of 22.39 Å, and indicates that uncertainties in the rest wavelength can be of order 0.05 Å; i.e. equivalent to the instrumental FWHM.

4.4.5   Absorption by iron

Iron is the best indicator for the ionization structure of the warm absorber, as it has absorption lines in the RGS band from neutral Fe I to the highly ionized Fe XXIV. For NGC 5548 we detect absorption from Fe VI to Fe XXIV (see Table 4.3). The lowest ionization component is represented by the UTA (Sako et al. 2001) formed from inner-shell transitions of Fe VI through Fe XI. These ions represent the lower ionized iron ions. Fig. 4.4 gives a detailed view of the spectrum between 16 and 17.5 Å, where the UTA is located. Note that although there are some individual absorption features visible, the dominant effect of the UTA is the depression of the continuum due to an unresolved blend of transitions with small cross-sections. The UTA clearly shows the importance of these inner-shell transitions in determining the continuum correctly.

The moderately ionized component is represented by Fe XIII through Fe XIX, where we only find an upper limit for Fe XII and Fe XIV. The highest ionized component is represented by absorption by Fe XIX through Fe XXIV. For Fe XIX through Fe XXII we detect a multitude of absorption lines between 8 (lowest wavelength that we included
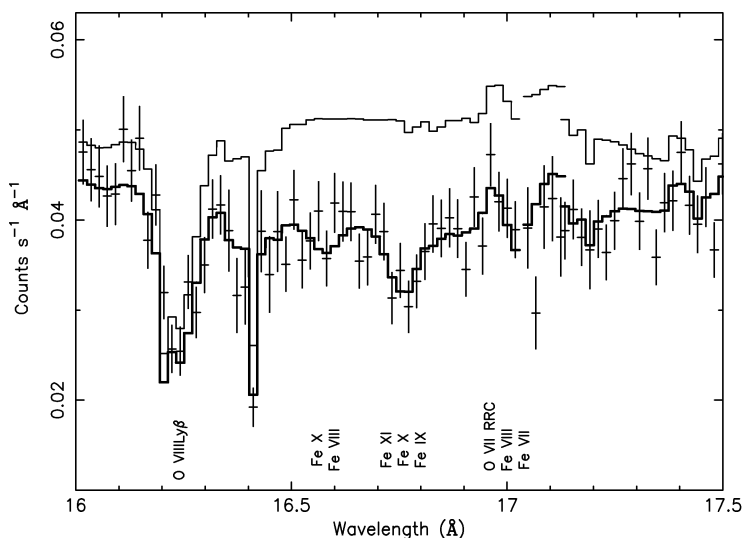
Figure 4.4: Detail of the first order data showing the UTA between 16 and 17.5 Å. The thick line is the best fit through the data, the thin line indicates the same model if we set the iron abundance for the lowest ionization component to 0. A dead pixel occurs at 16.4 Å. The gaps in the model at 17.05 and 17.15 Å are due to missing data. Only the deepest features are labeled.

in the fit) and 15 Å. For Fe XXIII and Fe XXIV only two absorption lines are detected, resulting in uncertain velocity determinations.

It is thus clear that all three ionization components as fitted with *xabs* are amply confirmed by iron absorption. The question arises whether a continuous ionization structure would be a better fit to the data. From Fe VI through Fe XXIV we detect all iron ions with the exception of Fe VII, Fe XII and Fe XIV. Between Fe XII and Fe XV all column densities are low. Forcing Fe XII to Fe XVI to have a similar column densities as Fe XI or Fe XVII worsens the fit, increasing χ_ν^2 by 0.24. This indicates that for $\log \xi$ between 1 and 1.4 (ξ between 10 and 25) (in 10^{-9} W m) the column densities are lower than for the other ionization states. However, no clear depression in column densities is seen for the transition between the middle and highly ionized component. A more continuous ionization structure than presented by the *xabs* model for the warm absorber is not excluded by the data.

4.4.6 Absorption by carbon and nitrogen
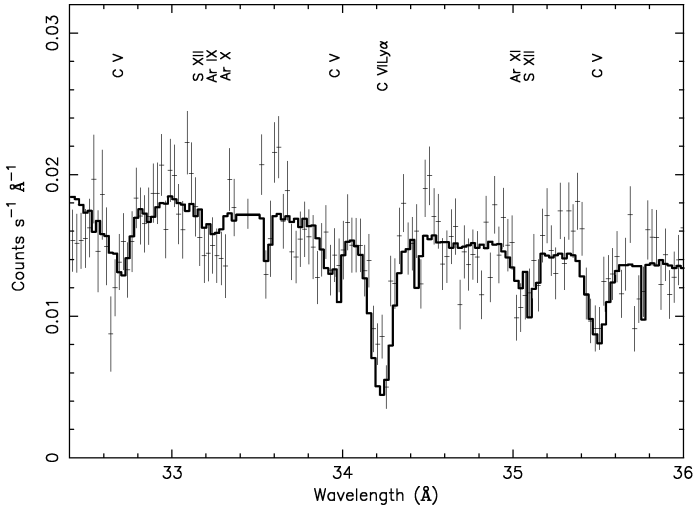
Figure 4.5: Detail of first order RGS 1 and 2 data, indicating the C VI Lyα absorption line as well as some C V, S XII, Ar IX, Ar X and Ar XI absorption lines. A dead pixel is seen at 34 and 35.8 Å.

For carbon we detect a strong C VI Lyα line (see Fig. 4.5), the Lyβ line (see Fig. 4.7), Lyγ and hints of Lyδ lines (see Fig. 4.6). These higher order lines are important in the correct determination of the column density as well as any possible time variability, as their optical depth is around unity. C VI and N VII are produced mainly in the middle ionization component, while C V and N VI are produced in the middle and lowest ionization component. Finally, C IV and N V are produced only in the lowest ionization component (see Table 4.3 for an indication of the ionization state). The C VI Lyα line is rather deep and at a relatively long rest wavelength of 33.736 Å, resulting in a very good velocity shift determination. The velocity component found from the X-rays is consistent with component 3 from the UV, which has an outflow velocity of -540 km s^{-1} instead of -510 km s^{-1}. There is a hint in our data that the line has substructure, consistent with the earlier LETGS results.

57
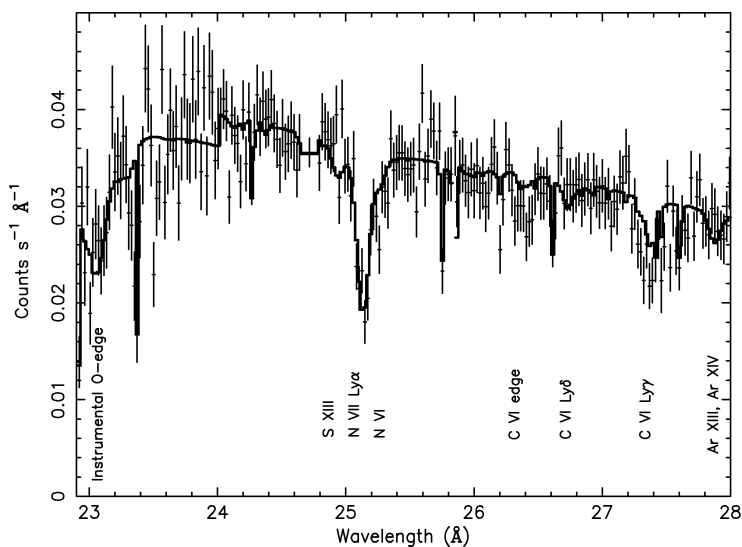
Figure 4.6: Detail of first order RGS 1 and 2 data, indicating the N VII Lyα absorption line as well as the C VI Lyγ and Lyδ lines. Absorption of S XIII, Ar XIII, and Ar XIV are labeled. Dead pixels are seen at 23.4 Å, 24.3 Å, 25.7 Å, 26.2 Å, 26.6 Å, and 27.6 Å.

4.4.7 Relativistically broadened emission lines

After finding a model for the warm absorber that is as complete as possible, we added relativistically broadened emission lines of O VIII, N VII, and C VI Lyα to the model. Such lines were observed in MCG−6-30-15 and Mrk 766 (Branduardi-Raymont et al. 2001, Sako et al. 2002).

In NGC 5548 Kaastra et al. (2002a) found evidence for weak broadened emission lines of O VIII Lyα and N VII Lyα. However, no indication for a relativistically broadened C VI Lyα line was detected. We applied the best fit parameters found from the LETGS model to the RGS data but found no significant improvement for any of the relativistically broadened emission lines. Leaving the parameters for the Laor line profile (Laor 1991) free, we find that a broad Gaussian would better describe the line/excess. However, the improvement in fit is still small for all three emission lines. The results are given in Table 4.7, together with the best fit values for the LETGS data of NGC 5548 (Kaastra et al. 2002a), and the RGS data of MCG−6-30-15 and Mrk 766 (Branduardi-Raymont et al. 2001, Sako et al. 2002). Note, that the values found for the
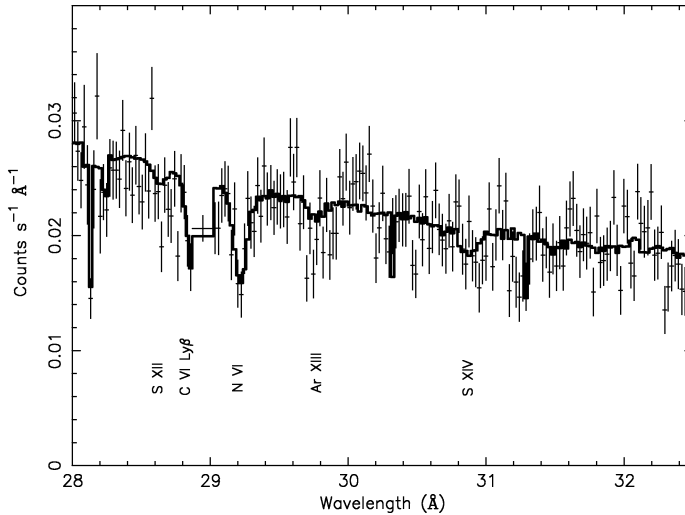
Figure 4.7: Detail of first order RGS 1 and 2 data, indicating an N VI absorption line as well as the C VI Lyβ line. Further absorption by S XII, S XIV and Ar XIII are labeled. Dead pixels are seen at 28.1 Å and 30.3 Å. A CCD gap related feature is seen at 28.9 Å.

EW between our RGS results and the LETGS results are consistent within 3 σ, except for the inner radius. These relativistic lines should be time variable, considering that they are formed in the accretion disk close to the black hole. Possibly, time variability explains the differences between the previous LETGS results and ours. Given their weakness, in the further analysis and in all the plots we did not include these broadened emission lines. Fig. 4.8 gives the wavelength band where the relativistic O VIII Lyα line should be situated, and a small excess is seen between 18 and 18.4 Å.

4.5 Discussion

4.5.1 Outflow velocity versus ionization

No evidence is found for a correlation between the outflow velocity and the ionization parameter (see Fig. 4.9). Rather the outflow velocity, for first order, is consistent with $-380 \, \mathrm{km \, s^{-1}}$ and $-350 \, \mathrm{km \, s^{-1}}$ for the *slab* and *xabs* model respectively over the three orders of magnitude sampled in ionization scale. This is consistent with the UV data (Crenshaw & Kraemer 1999), and the results for the C VI Lyα line in the LETGS data

Table 4.7: Values for the relativistically broadened emission lines in NGC 5548, MCG−6-30-15 and Mrk 766 (Sako et al. 2001). LETGS measures are taken from Kaastra et al. (2002a).

	RGS	LETGS	MCG−6-30-15	Mrk 766
i^a	46±35	46(−3,+8)	38.5±0.4	34.3±0.74
q^b	3.9±5	3.9±0.6	4.49±0.15	3.66±0.22
r$_{in}$^{c}	100±30	<2.6	3.21±1.2	<2.3
r$_{out}$^{c}	400±90	>10	100(−48,+95)	81(−20,+73)
C VI^d	<0.8	<0.7	2.0±0.2	2.3±0.2
N VII^d	<0.03	1.1±0.4	4.4±0.2	5.8±0.3
O VIII^d	0.2±0.1	0.6±0.2	13.1±0.6	11.4±0.7

^{a} The inclination derived for the AGN from the relativistic lines, in degrees.
^{b} The emissivity slope.
^{c} In GM/c^2.
^{d} EW measured in Å.

(Kaastra et al. 2002a). Kaastra et al. (2002a) found a trend of decreasing outflow velocity for higher ionized iron and oxygen ions, although all outflow velocities were consistent with an outflow velocity of −340 km s^{-1}. This result is not reproduced here. The outflow velocities observed in both data sets are consistent with the five UV velocity components, suggesting a similar origin of both absorbers.

4.5.2 Hydrogen column density versus ionization

The derived absorbing column density per ion, as determined from the *slab* modeling, versus the ionization parameter is plotted in Fig. 4.10. In the Figure we use the ionization parameter corresponding to the state with maximum column density. In reality, however, the ion is produced over a range of ionization states. Fig. 4.10 thus assumes a continuous ionization distribution, and is dependent on the spectral energy distribution (SED) in our models with XSTAR. We tested a model with and without a UV bump, and found a maximum displacement in log ξ of 0.3 for very highly ionized iron, and a maximum change in the derived absorbing column density of 0.1 on the log scale used. However, as most ions at a particular ionization state have a similar shift, the derived abundances and the derived absorbing column density are rather insensitive to the input SED.
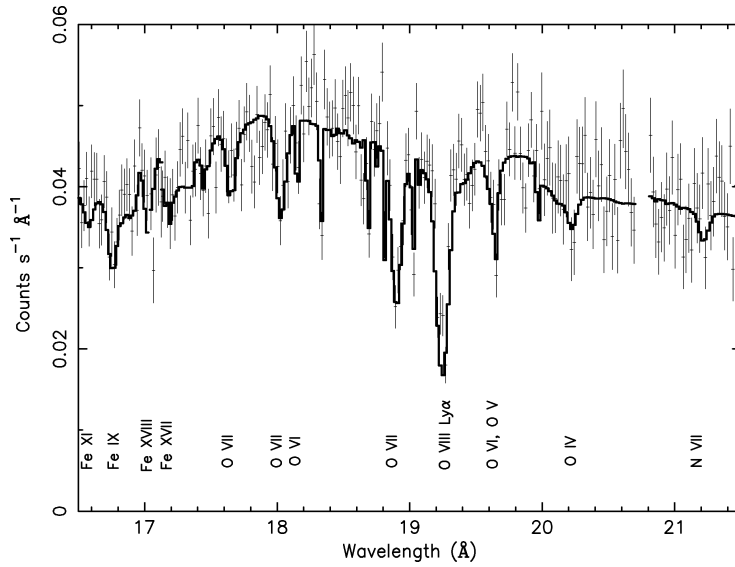
Figure 4.8: Best *xabs* fit to the first order data, detailing the wavelength band around the position of the relativistic O VIII Lyα emission line. Note that in this plot no relativistic line is fitted. Dead pixels are seen at 17.4 Å, 18.3 Å, 18.7 Å, 18.8 Å, 19 Å, and 19.95 Å. A CCD gap related feature can be seen between 20.7 and 20.8 Å.

In general, the derived absorbing column density increases for higher ionization parameters. The correlation coefficient, for all data points, excluding upper limits, is 0.71, and the related significance is 0.999997; for iron these values are 0.82 and 0.9982, respectively. The derived absorbing column density from the three component *xabs* model is very similar to the absorbing column density as derived from the *slab* model, and a similar increase for higher ionization is observed.

In general the abundances found are consistent with solar. An exception is iron, for which both models have lowly ionized iron overabundant compared to lowly ionized oxygen, while a reverse trend occurs for highly ionized iron and oxygen. As carbon and nitrogen are consistent with oxygen, the effect is probably due to uncertainties for the lowly ionized iron ions. A similar overabundance for iron in the lowest ionization state was noted by Blustin et al. (2002) for NGC 3783. In the LETGS observation of NGC 5548 (Kaastra et al. 2002a) found a similar abundance pattern for iron, throughout the ionization range. The explanations listed by Kaastra et al. (2002a) for this

61
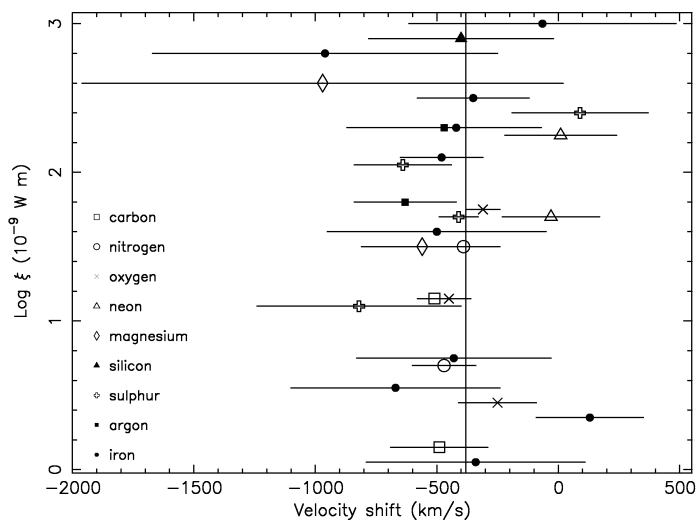
Figure 4.9: The velocity shift as given in Table 4.3 versus the the ionization parameter. The vertical line represents the average outflow velocity.

discrepancy have been tested using this data set. First, a calibration effect is unlikely as RGS and LETGS give consistent results. Secondly, we determined the column density for lowly ionized oxygen ions from our own X-ray spectrum; and thus we do not need to rely on non-simultaneous UV measurements. Spectral variability is thus not a possible explanation for the apparent overabundance of lowly ionized iron. Thirdly, we tested the sensitivity of the model to different values for the line broadening, ensuring that saturation due to narrow line widths cannot be responsible for the overabundance of lowly ionized iron. Reducing the width of the lowly ionized absorption lines, has the effect that iron saturates first, worsening the overabundance already found. The maximum width of the lowly ionized lines is set by the width of the inner-shell oxygen lines, which are unresolved.

Possible explanations for the iron overabundance are an uncertainty in the wavelength of the M-shell iron absorption lines; or if the optical depth, $\tau \gg 1$, an uncertainty in the radiative transfer models used. Another possibility is the omission of certain processes like re-emission and Bowen fluorescence in the radiative transfer models used. Finally, the iron abundance could be non-solar, although the physical process causing such an overabundance of iron in Seyfert galaxies is unknown. Non-solar abundances have been detected in IRAS 13349+2438 (Sako et al. 2001) and NGC 1068 (Kinkhab-
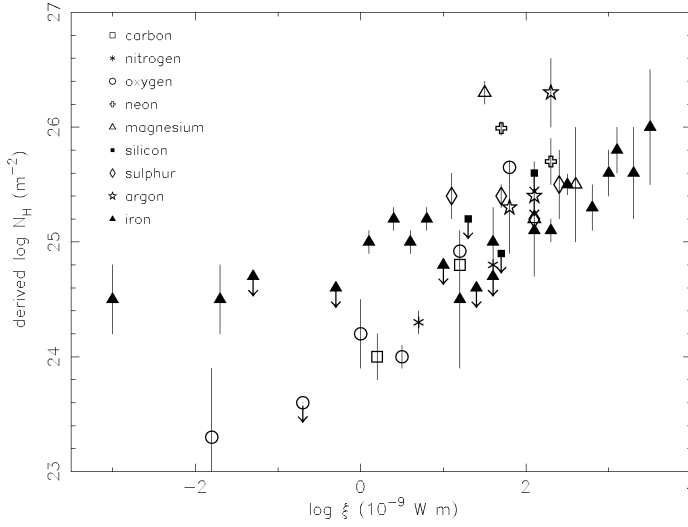
Figure 4.10: The derived absorbing column density per ion as derived from the column densities given in Table 4.3. There is an increase of the derived column density with higher ionization.

wala et al. 2002).

4.5.3 Outflow geometry

The geometry and physics of the warm absorber as observed in some AGN is poorly understood. One of the outstanding questions is whether this outflow is spherical, in which case the ionization of the gas is mainly dependent on the distance. Alternatively, the outflow could be in localized streams formed due to instabilities in the accretion disk. The ionization parameter is then mainly dependent on the density. As distance and density cause a degeneracy in the determination of the ionization parameter, the location of the outflowing X-ray and UV warm absorber is uncertain. Constraining the geometry of this outflow will help solve these outstanding problems.

From mass conservation ($\dot{M}_{\mathrm{loss}} = 4\,\pi r^2 n m_{\mathrm{p}} v \Omega$), the ionization parameter ($\xi = L/nr^2$), the outflow velocity (v), and the bolometric luminosity (L), one can determine the mass loss rate, $\dot{M}_{\mathrm{loss}}$, as a function of the opening angle (Ω) of the outflowing wind. This is summarized in eq. (4.1), where m_{p} is the proton mass. Assuming that the mass loss rate of the wind cannot be higher than the mass accretion

rate onto a black hole and that the system is stationary, one can equate both and obtain an upper limit for the opening angle. Eq. (4.2) gives the mass accretion rate, $\dot{M}_{\mathrm{acc}}$, with a mass conversion efficiency of η.

$$\dot{M}_{\mathrm{loss}} = \frac{4\pi L m_{\mathrm{p}} v \Omega}{\xi} \tag{4.1}$$

$$\dot{M}_{\mathrm{acc}} = \frac{L}{c^2 \eta} \tag{4.2}$$

In the case of a Schwarzschild black hole, as considered here, $\eta = 0.057$. For our average outflow velocity of 380 km s^{-1} the upper limits of the opening angle vary between 3.8×10^{-7} sr for log $\xi = -1.8$ and 0.024 sr for log $\xi = 3$, with log ξ in 10^{-9} W m. For an average ionization state of log $\xi = 1.7$ in 10^{-9} W m, we find an upper limit to the opening angle of 0.0019 sr. The upper limits to the opening angle indicate that the outflow is mostly in a narrow stream, where the densest part of the stream is the narrowest and lowest ionized. For higher outflow velocities or a higher mass conversion efficiency, i.e. in the case of a Kerr black hole, the stream is even narrower.

From Fig. 4.10 we determine that the derived absorbing column density scales with the ionization parameter, $N_{\mathrm{H}} \sim \xi^{\alpha}$. α ranges from 0.25 to 0.5 depending on whether one uses the N_{H} obtained for the iron or oxygen ions at the lower ionization states. We define $N_{\mathrm{H}} \equiv nd$, where n is the density and d is the thickness of the outflow in the line of sight. Equating N_{H} to ξ^{α}, where $\xi = L/nr^2$, one can determine a relation between the density, thickness and distance. If one further assumes that for a fixed distance (r) from the ionizing source, there is a range in densities, resulting in a range in ionization states, one finds that the density is related to the thickness $n \sim d^{-5/4}$ or $n \sim d^{-3/2}$ for $\alpha = 0.25$ and $\alpha = 0.5$, respectively. From both simple models we conclude that the outflow occurs in streams with a very small opening angle for the dense and lowly ionized gas, and with a larger opening angle for the less dense and higher ionized gas.

4.5.4 Comparison of UV and X-ray detection of O VI

O VI has absorption lines in both the UV ($\lambda\lambda$1032, 1038 Å) and X-ray band (22.01 Å, 19.34 Å and 21.79 Å). Our X-ray column density of O VI of $10^{20.5}$ m^{-2} is nearly an order of magnitude larger than the UV column density ($10^{19.62}$ m^{-2}) of Brotherton et al. (2002). However, the outflow velocities in the UV and the X-rays are comparable. The difference in derived absorbing column density indicates that the UV data are severely saturated, leading to an underestimate in the column density. Arav et al.

(2002) compare the column density of O VI as observed in this data set and an earlier FUSE UV measurement, and conclude that the column densities could be equal if velocity dependent covering is considered. However, simultaneous observations are necessary to exclude the possibility of column density variability (see Arav et al. 2002 for more details). Generally, in the X-rays, we find significantly more low ionization gas than previously deduced from UV data. The discovery of O III to O V absorption lines, in addition to O VI, gives us for the first time an estimate for the column densities of these ions, which are inaccessible in the UV.

4.6   Summary

We have presented here the highest signal to noise high resolution X-ray spectrum of NGC 5548 obtained yet. The spectrum shows a rich structure in narrow and broad spectral features. We detected a very weak O VII RRC, consistent with a low temperature. Inner-shell oxygen lines, together with the higher order absorption lines from O VIII Lyα and C VI Lyα have an optical depth near unity, important in the detection of spectral variability of the warm absorber, although no spectral variability was detected in this data set or from comparison with the earlier LETGS spectrum. Uncertainties in rest wavelengths for the inner-shell ions complicate the study of these absorption lines, certainly for the lowly ionized ions. Possibly this or uncertainties and the omission of certain processes in the radiation transfer models lead to an deviant iron to oxygen abundance ratio.

The detected warm absorber spans three orders of magnitude in ionization, from ions as lowly ionized as those measured in the UV band, to nearly fully ionized iron. Only a few percent of the X-ray warm absorber column density is lowly ionized, represented by oxygen and iron inner-shell transition lines. The outflow velocities determined from the X-rays are all consistent with those measured in higher resolution UV spectra, and no correlation between the ionization state and velocity was detected. The similarity in outflow velocity and the detection of O VI give strong evidence that the UV and X-ray warm absorber are different manifestations of the same outflowing wind phenomenon. However, we detect an order of magnitude more O VI in the X-rays than previous UV measurements. In general, we detect substantially more low ionized gas, than is deduced to be present from UV observations. Probably the UV band underestimates the true column densities due to saturation and velocity dependent covering factor. From simple arguments, we found that the outflow detected is consistent with a narrow stream, with smallest opening angles for the densest and lowest ionized gas.

References

Anders, E. & Grevesse, N., 1989, Geochim. Cosmochim. Acta 53, 197

Arav, N., Kaastra, J. S., Steenbrugge, K. C. et al., 2002, submitted to ApJ

Blustin, A. J., Branduardi-Raymont, G., Behar, E., et al., 2002, A&A, 392, 453

Branduardi-Raymont, G., Sako, M., Kahn, S. M., et al., 2001, A&A, 365, L140

Brotherton, M. S., Green, R. F., Kriss, G. A. et al., 2002, ApJ, 565, 800

Cowan, R. D., 1981, The theory of atomic structure and spectra, Univ. of California Press, Berkeley

Crenshaw, D. M. & Kraemer, S. B., 1999, ApJ, 521, 572

Done, C., Pounds, K. A., Nandra, K. & Fabian, A. C., 1995, MNRAS, 275, 417

den Herder, J. W., Brinkman, A. C., Kahn, S. M., et al., 2001, A&A, 365, L7

Kaastra, J. S. & Barr, P., 1989, A&A, 226, 59

Kaastra, J. S., Mewe, R., Liedahl, D. A., Komossa, S., Brinkman, A. C., 2000, A&A, 354, L83

Kaastra, J. S., Steenbrugge, K. C., Raassen, A. J. J., et al., 2002a, A&A, 386, 427

Kaastra, J. S., Mewe, R. & Raassen, A. J. J., 2002b, Proceedings Symposium 'New Visions of the X-ray Universe in the XMM-*Newton* and *Chandra* Era'

Kaspi, S., Brandt, W. N., Geoerg, I., et al., 2002, ApJ, 574, 643

Kinkhabwala, A., Sako, M., Behar, E., et al., 2002, ApJ, 575, 732

Laor, A., 1991, ApJ, 376, 90

Markowitz, A., Edelson, R., Vaughan, S., et al., 2002, submitted to ApJ

Mathur, S., Elvis, M. & Wilkes, B., 1995, ApJ 452, 230

Nandra, K., Fabian, A. C., George, I. M., et al., 1993, MNRAS 260, 504

Pounds, K., Reeves, J. N., Page, K. L., et al., 2002, accepted by MNRAS

Sako, M., Kahn, S. M., Behar, E., et al., 2001, A&A, 365, 168

Sako, M., Kahn, S. M., Branduardi-Raymont, G., et al., submitted to A&A

Yaqoob, T., George, I. M., Nandra, K. et al., 2001, ApJ, 546, 759

Chapter 5

Simultaneous X-ray and UV spectroscopy of the Seyfert galaxy NGC 5548. II. Physical conditions in the X-ray absorber

K.C. Steenbrugge, J.S. Kaastra, D. M. Crenshaw, S. B. Kraemer, N. Arav,
I. M. George, D. A. Liedahl, R. L. J. van der Meer, F. B. S. Paerels, T. J. Turner and
T. Yaqoob

Abstract

We present the results from a 500 ks Chandra observation of the Seyfert 1 galaxy NGC 5548. We detect broadened emission lines of O VII and C VI in the spectra, similar to those observed in the optical and UV bands. A 30 % increase in luminosity between the HETGS and LETGS observations was observed, but no variability in the warm absorber was detected between the individual spectra. The longer wavelength range of the LETGS resulted in the detection of absorption lines from a broad range of ions, in particular of C, N, O, Ne, Mg, Si, S and Fe. The velocity structure of the X-ray absorber is consistent with the velocity structure measured simultaneously

in the ultraviolet spectra. We find that the highest velocity outflow component, at $-1040 \, \text{km s}^{-1}$, becomes increasingly important for higher ionization parameters. This velocity component spans at least three orders of magnitude in ionization parameter, producing both highly ionized X-ray absorption lines (Mg XII, Si XIV) as well as UV absorption lines. A similar conclusion is very probable for the other four velocity components.

Based upon our observations, we argue that the warm absorber probably does not manifest itself in the form of photoionized clumps in pressure equilibrium with a surrounding wind. Instead, a model with a continuous distribution of column density versus ionization parameter gives an excellent fit to our data. From the shape of this distribution and the assumption that the mass loss through the wind should be smaller than the accretion rate onto the black hole, we derive upper limits to the solid angle as small as 10^{-4} sr. From this we argue that the outflow occurs in density-stratified streamers. The density stratification across the stream then produces the wide range of ionization parameter observed in this source. We determine an upper limit of $0.3 \, \text{M}_\odot \, \text{yr}^{-1}$ for the mass loss from the galaxy due to the observed outflows.

5.1   Introduction

Over half of all Seyfert 1 galaxies exhibit signatures of photoionized outflowing gas in their X-ray and UV spectra. Studying these outflows is important for a better understanding of the enrichment of the Inter Galactic Medium (IGM) as well as the physics of accretion of gas onto a super-massive black hole.

One of the best candidates to study these processes is NGC 5548. A recent XMM-*Newton* Reflection Grating Spectrometer (RGS) observation of NGC 5548 showed evidence for an X-ray warm absorber that has a nearly continuous distribution of ionization states (Steenbrugge et al. 2003). There is a pronounced increase in column density as a function of ionization parameter. The average outflow velocity measured in the X-ray band is consistent with the range of outflow velocities measured in the UV band, however, the spectral resolution in the X-ray band is not sufficient to resolve the individual velocity components observed in the UV band. The detection of the 1s-2p line of O VI in X-rays allows for a direct comparison with the column density as determined from measurements of the 2s-2p lines by FUSE in the UV band (Brotherton et al. 2002). From this direct comparison, as well as the total column density derived from other lowly ionized ions, Arav et al. (2003) and Steenbrugge et al. (2003) concluded that there is substantially more lowly ionized gas than has been claimed from previous UV observations. It was concluded that the X-ray and UV warm absorbers are different manifestations of the same phenomenon. Mathur, Elvis & Wilkes (1995)

already noted this possibility before the advent of high resolution X-ray spectroscopy. However, their model included only one ionization component and this is unrealistic for the observed NGC 5548 high resolution spectra.

The difference in derived column densities in the UV band versus X-rays can be understood if the UV absorption lines do not cover the narrow emission line (NEL) region. The column densities derived from the UV lines are then only lower limits due to saturation effects, because these lines then locally absorb almost all the radiation from the continuum and the broad emission line (BEL) region (Arav et al. 2002; Arav et al. 2003).

The discrepancy in the O VI column density mentioned above is based on non-simultaneous X-ray and UV observations and therefore it remains possible that the difference is due to variability in the absorber. The present *Chandra* observation was proposed to remedy this, by having simultaneous HST STIS, FUSE and *Chandra* observations. Unfortunately, due to technical problems FUSE was unable to observe at the scheduled time, so that no simultaneous O VI observations were obtained. However, the spectral resolution of *Chandra* allows us to resolve the $-1040 \, \text{km s}^{-1}$ component from the four other velocity components detected in the UV, for the strongest lines. This is a rather stringent test of the kinematic relation between both absorbers.

The long wavelength range of the LETGS allows us to map out the column density as a function of ionization parameter for iron from Fe VI to Fe XXIV, or over about two orders of magnitude. Due to the high signal-to-noise ratio, we are sensitive to changes in ionization parameter as small as 0.15 in log ξ. This is the first Seyfert 1 spectrum where the signal to noise is such that we are able to study in detail the absorption lines between $60 - 100 \, \text{Å}$.

The details of the observations and the data reduction are given in Sect. 5.2. In Sect. 5.3 we present the spectral data analysis and study the time variability of the warm absorber. The long term spectral variability of the warm absorber is discussed in Sect. 5.3.7 In Sect. 5.4 we discuss our results. In Sect. 5.5 we discuss the ionization structure; the geometry and the mass loss through the outflow discussed in Sect. 5.6. The continuum time variability is discussed in a separate paper (Kaastra et al. 2004a). Limits on the spatial distribution of the X-ray emission are given by Kaastra et al. (2003). The data were taken nearly simultaneously with HST STIS observations detailed by Crenshaw et al. (2003).

5.2   Observation and data reduction

NGC 5548 was observed for a full week with the *Chandra* High Energy Transmission Grating Spectrometer (HETGS) and the Low Energy Transmission Grating Spectrom-

Table 5.1: The exposure time and the observation details for the *Chandra* and HST observations of NGC 5548. ACIS stands for the Advanced CCD Imaging Spectrometer and HRC for High Resolution Camera. The E140M grating covers the wavelength range between $1150 - 1730$ Å, the E230M grating between $1607 - 3119$ Å.

Instrument	detector	start date	exposure (ks)
HETGS	ACIS-S	2002 Jan. 16	154
LETGS	HRC-S	2002 Jan. 18	170
LETGS	HRC-S	2002 Jan. 21	170
HST STIS	E140M	2002 Jan. 22	7.6
HST STIS	E230M	2002 Jan. 22	2.7
HST STIS	E140M	2002 Jan. 23	7.6
HST STIS	E230M	2002 Jan. 23	2.7

eter (LETGS) in January 2002. In Table 5.1 the instrumental setup and the exposure times are listed.

The LETGS data were reduced as described by Kaastra et al. (2002a). The LETGS spans a wavelength range from $1 - 180$ Å with a resolution of 0.05 Å (full width half maximum, FWHM). The data were binned to 0.5 FWHM. However, due to Galactic absorption toward NGC 5548, the spectrum is heavily absorbed above 60 Å, and insignificant above 100 Å. In the present analysis we rebinned the data between $60 - 100$ Å by a factor of 2 to the FWHM of the instrument and ignore the longer wavelengths.

The HETGS data were reduced using the standard CIAO software version 2.2. The HETGS spectra consist of a High Energy Grating (HEG) spectrum which covers the wavelength range of $1.5 - 13$ Å with a FWHM of 0.012 Å, and a Medium Energy Grating (MEG) spectrum which covers the wavelength range of $1.5 - 24$ Å with a FWHM of 0.023 Å. The MEG and HEG data are binned to 0.5 FWHM. In the reduction of both HETGS datasets the standard ACIS contamination model was applied (see http://cxc.harvard.edu/caldb/about_CALDB/index.html).

The data shortward of 1.5 Å were ignored for all the instruments, as were the data above 11.5 Å for the HEG spectrum and above 24 Å for the MEG spectrum. The higher orders are not subtracted from the LETGS spectrum, but are included in the spectral fitting, i.e. the response matrix used includes the higher orders up to order $\pm$ 10, with the relative strengths of the different orders taken from ground calibration and in-flight calibrations of Capella. We did not analyze the higher order HETGS spectra, due to their low count rate. All the spectra were analyzed with the SPEX software (Kaastra et

al. 2002b), and the quoted errors are the 1 σ rms uncertainties, thus $\Delta\chi^2 = 2$.

Kaastra et al. (2002a) found a difference in the wavelength scale between the MEG and LETGS instrument of about 170 km s^{-1}. This wavelength difference is within the absolute calibration uncertainty of the MEG instrument. We detected no such wavelength difference between our data sets, comparing the centroids of the strongest lines in both spectra. The best line in NGC 5548 to test the wavelength calibration is the O VII forbidden emission line, as it is found to be narrow. However, due to the noise in the MEG spectrum in the vicinity of this line, the wavelength in the MEG spectrum is not well determined, but it is consistent with the wavelength measured from the LETGS spectrum. We also looked for differences in the line centroid of the O VIII Lyα and O VIII Lyβ absorption line. However, as these lines are broadened, centroids are less accurate. These lines have consistent centroids for both instruments, and no systematic blue- or redshift is detected.

5.3   Spectral data analysis

In the appendix the spectrum between 1.5 Å $-$ 100 Å is shown. The overall X-ray spectrum is qualitatively similar to the spectra observed before by *Chandra* (Kaastra et al. 2000; Kaastra et al. 2002a; Yaqoob et al. 2001) and XMM-*Newton* (Steenbrugge et al. 2003). A large number of strong and weak absorption lines cover a smooth continuum. In addition, a few narrow and broadened emission lines are visible. Most absorption lines can be identified with lines already observed in these previous spectra or with predicted lines that, due to the increased sensitivity of the present spectra, become visible for the first time.

The spectral model applied here is based on results obtained from earlier *Chandra* and XMM-*Newton* spectra of NGC 5548 (Kaastra et al. 2002a; Steenbrugge et al. 2003). The current spectrum is described by the same spectral components as in the earlier observations, albeit with different parameters. In the next subsections we discuss the results for the different components as obtained from our global fit to the spectra. These previous observations as well as the present observation have a continuum that is well fitted by a power-law and modified black body component (Sect. 5.3.1). The high resolution spectra reveal a warm absorber (WA) modeled by combinations of *slab*, *xabs* or *warm* components (Sect. 5.3.2), narrow emission lines (Sect. 5.3.4 and 5.3.5) and broadened O VIII, O VII and C VI emission lines (Sect. 5.3.6).

5.3.1 Continuum

Throughout the analysis we fitted the continuum with a power-law (pl) and a modified black body (mbb) component (Kaastra & Barr 1989) modified by Galactic extinction and cosmological redshift. The Galactic H I column density was frozen to 1.65×10^{24} m^{-2} (Nandra et al. 1993), as was the redshift of 0.01676 from the optical emission lines (Crenshaw & Kraemer 1999). The continuum parameters for our best fit model, namely the one with three *slab* components (Sect. 5.3.2), are listed in Table 5.2. For comparison, the continuum parameters for the earlier RGS observation are included (Steenbrugge et al. 2003).

5.3.2 Warm absorber

Warm absorber models

In our modeling of the warm absorber we use combinations of three different spectral models for the absorber. The most simple is the *slab* model (Kaastra et al. 2002a), which calculates the transmission of a slab of a given column density and a set of ion concentrations. Both the continuum and the line absorption are taken into account. As in the other absorption models, the lines are modeled using Voigt profiles. Apart from the ionic column densities, the average outflow velocity v and Gaussian r.m.s. velocity broadening σ are free parameters of the model. The last two parameters have the same

Table 5.2: The best fit parameters for the continuum for the earlier RGS observation (Steenbrugge et al. 2003) and the present HETGS and LETGS observations of NGC 5548. The parameters for the HETGS and LETGS are for the best fit model including the three *slab* components with the outflow velocities frozen to the UV values.

Parameter	RGS	HETGS	LETGS
pl:norm[a]	1.57 ± 0.03	0.90 ± 0.01	1.30 ± 0.01
pl:lum[b]	5.7 ± 0.1	3.62 ± 0.04	4.02 ± 0.03
pl:Γ	1.77 ± 0.02	1.71 ± 0.01	1.88 ± 0.01
mbb:norm[c]	6.5 ± 0.7	< 400	3.5 ± 0.9
mbb:T (in eV)	97 ± 6	$-$	100 ± 10

[a] At 1 keV in 10^{52} ph s^{-1} keV^{-1}.
[b] The luminosity as measured in the $2 - 10$ keV band in 10^{36} W.
[c] norm = emitting area times square root of electron density in 10^{32} m$^{1/2}$.
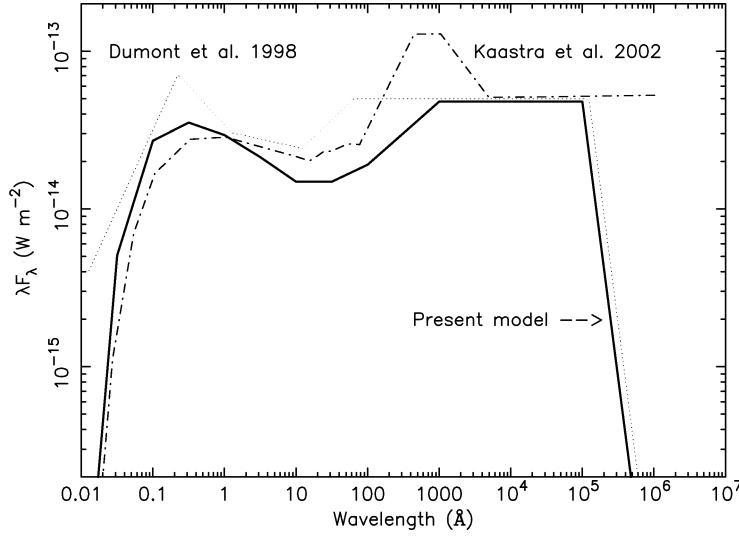
Figure 5.1: The SED used (solid line) in the present analysis and the analysis of the HST STIS data by Crenshaw et al. (2003). For comparison, the SED used by Kaastra et al. (2002a) and Steenbrugge et al. (2003) in earlier papers on NGC 5548 is plotted as the dot-dash line. The SED adopted by Dumont et al. (1998) is plotted as the dotted line.

value for each ion. The slab is assumed to be thin in the sense that $e^{-\tau}$ gives a fair description of its transmission.

The second model (*xabs*) is similar to the *slab* model, however now the ionic column densities are coupled through a set of photoionization calculations (Kaastra et al. 2002a). As a result, instead of the individual ionic concentrations we now have the ionization parameter $\xi = L/nr^2$ and the elemental abundances as free parameters. The set of photoionization calculations was done using the XSTAR code (Kallman & Krolik 1999), with the SED as shown in Fig. 5.1. The same SED was used by Crenshaw et al. (2003) in the analysis of the simultaneous HST STIS data. As there is no evidence of a blue bump this was not included in the currently used SED. This is the main difference with the SED used by Kaastra et al. (2002a) and Steenbrugge et al. (2003), which is plotted as the dot-dash line. For the X-ray part of the spectrum we used the continuum model as measured from the present LETGS spectrum, instead of the continuum obtained from the 1999 LETGS spectrum. For the high energy part of the SED we used

73

a power law component as measured in our *Chandra* spectrum but with an exponential cut-off at 130 keV, consistent with the Beppo*SAX* data (Nicastro et al. 2000). As reflection components are time variable and the LETGS has insufficient high energy sensitivity to model it properly, we did not include any reflection component in our SED. Between 50 and 1000 Å we used a power-law and at even longer wavelength used the energy index obtained by Dumont et al. (1998) of 2.5.

The third method used is the *warm* model, which is a model for a continuous distribution of the $dN_H/d\xi$ as a function of ξ. At each value of ξ, the transmission is calculated using the *xabs* model described above. In our implementation of this model $\xi dN_H/d\xi$ is defined at a few (in our case two) values of ξ. At the intermediate points the logarithm of this function is determined by cubic spline interpolation on the $\log \xi$ grid. This determines N_H as a function of ξ. Integration between the lowest and the highest values of ξ (ξ_1 respectively ξ_2) yields the total ionic column densities. In our model, as we have taken only two points, the ionization extrema ξ_1 and ξ_2, the total hydrogen column density is therefore a power-law function of ionization. The *warm* model correctly incorporates the fact that ions are formed at a range of ionization parameters. Free parameters of this model are ξ_1, ξ_2, $\xi_1 \, dN_H \, (\xi_1)/d\xi$, $\xi_2 \, dN_H \, (\xi_2)/d\xi$, and similar to the *xabs* model the outflow velocity v, velocity broadening σ and the elemental abundances. The wavelength for the O V $1s^22s^2$ - $1s2s^22p$ $^1P_1$ X-ray line was changed from 22.33 Å (the HULLAC value) to 22.374 Å (Schmidt et al. 2004).

Short term variability

During our study of the individual LETGS and HETGS spectra it appeared that apart from the different continuum, the best fit parameters of the warm absorber appeared to be very similar and in general consistent within the error bars. Here we study the time variability in more detail in order to demonstrate this consistency.

In our first approach, we have taken the fluxed MEG spectrum and folded this through the LETGS response matrix. This is possible because of the two times higher spectral resolution of the MEG as compared to the LETGS. We adjusted the MEG continuum to match the higher LETGS continuum. Restricting our analysis to the 1.5– 24 Å band, where both instruments have sufficient sensitivity, we find good agreement between both spectra.

We find no significant difference in the equivalent width of the strongest absorption lines such as the Lyα and Lyβ lines of Ne X and O VIII and the resonance lines of Ne IX and O VII. There may be a small enhancement of the most highly ionized lines in our spectrum (Si XIV and Mg XII Lyα and the Si XIII resonance line), corresponding to a $\sim$50 % increase in ionic column density in the LETGS observation. For the Si XIII line this is uncertain because the line coincides with an instrumental edge in the MEG

Table 5.3: Comparison of the best fit parameters for the LETGS and HETGS spectra. The labeling of the different components follows Kaastra et al. (2002a).

Comp.	LETGS $\log \xi^{a}$	HETGS $\log \xi^{a}$	LETGS $\log N_{H}{}^{b}$	HETGS $\log N_{H}{}^{b}$
1	2.26 ± 0.09	2.3 ± 0.3	25.47 ± 0.06	25.36 ± 0.08
2	1.77 ± 0.04	1.9 ± 0.1	24.85 ± 0.14	25.02 ± 0.12
3	-0.2 ± 0.2	-0.1 ± 2.5	24.33 ± 0.16	24.8 ± 0.4

[a] Ionization parameter in 10^{-9} W m.
[b] Hydrogen column density in m^{-2}.

spectrum (see Fig. 5.12). Moreover, at the high ionization parameter where these ions are formed ($\log \xi \sim 2.5$) the opacity of the O VIII Lyα line is even higher than for the Mg and Si lines. Since we do not observe an enhanced column density for O VIII, we conclude that the evidence for enhanced opacity at high ionization parameter during the LETGS observation is uncertain. A formal fit to the difference spectrum shows that any additional high ionization component emerging during the LETGS observation has a hydrogen column density less than 10^{24} m^{-2}, or an order of magnitude less than the persistent outflow.

In a different approach, we have fitted the warm absorber in the LETGS spectrum using a combination of three *xabs* components, the results are listed in Table 5.3. Fitting the HETG spectra with the same ionization parameters and column densities, but fixing the continuum parameters to the best fit parameters (see Table 5.2) we find an excellent fit. Allowing the ionization and column densities to be free parameters, we obtain the results listed in Table 5.3. The improvement for allowing the ionization and column densities to be free is $\Delta\chi^{2} = 10$ for 4242 degrees of freedom. The maximum difference between the two data sets occurs for the lowest ionization component 3. For the HETG spectra this component has $\log \xi = -0.1 \pm 2.5$, this clearly indicates the lack of sensitivity at the longer wavelengths in the HETG spectra. The flux in the soft band increased by $\sim$50 % between the HETGS and LETGS observation. Therefore, an increase of ξ by 50 % is excluded for component 2. However, our data cannot rule out that the ionization parameter responds linearly to continuum flux enhancements for components 1 and 3.

A similar situation holds for the time variability during the LETGS observations. Despite the significant flux increase during the observation (see Kaastra et al. 2004a),

the signal to noise ratio of our data is insufficient to rule out or confirm a significant response of the warm absorber to the change in ionizing flux.

We conclude that the difference in ionization parameter of the warm absorber between the HETG and the LETGS observation is small and below the sensitivity in $\log \xi$ of ~ 0.15. Therefore we simultaneously fit the LETGS and HETGS data in our spectral modeling, profiting from both the high spectral resolution of the HETGS and the long wavelength sensitivity of the LETGS spectrum.

Warm absorber model A: column densities with UV velocity structure

Our first method (dubbed model A here) allows us to further ascertain that the X-ray warm absorber and the UV absorber are the same phenomenon, a major goal for proposing this observation. We fitted the warm absorber in the X-ray spectra with the outflow velocities frozen to those measured in the UV spectra. Due to the lower resolution of the X-ray spectra as compared to the UV spectra and our limited signal to noise ratio, this was only possible for the deepest lines in the spectrum (C VI, O V, O VII, O VIII, Ne IX and Si XIII).

We implemented this by modeling the WA using three *slab* components, with the outflow velocities frozen. These outflow velocities were frozen to -1040 km s^{-1}, -530 km s^{-1} and -160 km s^{-1}, corresponding to UV velocity components 1, the average of $2 - 4$, and 5, respectively. Note that the velocities of components $2 - 4$ (-667, -530 and -336 km s^{-1}, respectively) are too close to be separated in our X-ray spectra. In the fit we left the velocity broadening of each of the three components a free parameter. Allowing for three velocity components instead of one, substantially improved the fit from $\chi^2 = 2916$ to 2441 for 2160 degrees of freedom (only LETGS is quoted here). However, the absorption lines are still only partially resolved, leading to strongly correlated errors for the derived column densities of the velocity components. Only for the six ions with the deepest lines (C VI, O V, O VII, O VIII, Ne IX and Si XIII) we measure column densities with meaningful error ranges (Table 5.4). For these six ions the velocity structure of the X-ray warm absorber closely resembles the UV velocity structure. Fig. 5.2 shows the line profiles as a function of outflow velocity for four lines of the ions listed in Table 5.4. The HEG spectrum shows most clearly substructure in the Mg XII Lyα absorption lines (Fig. 5.12 in the Appendix).

Warm absorber model B: column densities with simple velocity structure

Using model A we can only derive accurate column densities for six ions. In order to obtain column densities for other ions we need to reduce the number of free parameters. We use the same model as in model A, but now we fit the spectra with only one

76

Table 5.4: Parameters for six ions measured using model A. The first row gives the component number as listed in the UV. The second row lists the outflow velocity v, which was frozen to the UV values, the third row lists the velocity broadening σ_{X-ray} as derived from the X-ray spectra. In the fourth row the velocity broadening σ_{UV} = FWHM/2.35, where FWHM is the measured and resolved Full Width Half Maximum of the UV absorption lines (Crenshaw et al. 2003). All are in km s^{-1}. For the -530 km s^{-1} component we added the velocity broadening on component 3 and 4. We list the logarithms of the column densities in m^{-2}. For comparison we also list the C IV and N V column densities as measured by Crenshaw et al. (2003).

comp.	1	2 − 4	5	
v	-1040	-530	-160	
σ_{X-ray}	40 ± 5	100 ± 15	90 ± 13	
σ_{UV}	94 ± 8	140 ± 15	26 ± 6	
ion				total
C IV	18.05 ± 0.05	18.66 ± 0.02	17.76 ± 0.03	18.8
C VI	20.2 ± 0.6	21.4 ± 0.2	20.8 ± 0.4	21.5
N V	18.44 ± 0.02	19.24 ± 0.02	18.16 ± 0.03	19.3
O V	20.0 ± 0.5	20.5 ± 0.3	20.2 ± 0.6	20.8
O VII	21.3 ± 0.5	21.4 ± 0.3	20.3 ± 0.7	21.7
O VIII	22.2 ± 0.1	21.5 ± 0.3	21.9 ± 0.3	22.4
Ne IX	20.5 ± 0.9	20.4 ± 0.6	20.7 ± 0.8	21.0
Si XIII	20.8 ± 0.6	20.6 ± 0.6	20.5 ± 1.1	21.1

outflow velocity component, but leaving the velocity broadening as well as the outflow velocity free. This allows us to obtain total column densities, outflow velocities and velocity broadening for the ions with stronger lines. We first made a fit with a single *slab* component. This *slab* component has a single outflow velocity and velocity broadening for all the ions. After this fit is obtained, we freeze all the parameters in this *slab* component. The second *slab* component is then added containing only a single ion, leaving the column density, outflow velocity and velocity broadening as free parameters. The column density for this particular ion is frozen to zero in the first *slab* component, and the spectra are fit again in order to fine tune the column density, outflow velocity and velocity broadening for each ion. Each ion was cycled through the second *slab* component in this manner, and the results for those ions which have well determined outflow velocity and velocity broadening are listed in Table 5.5. In this Table we also list the

77
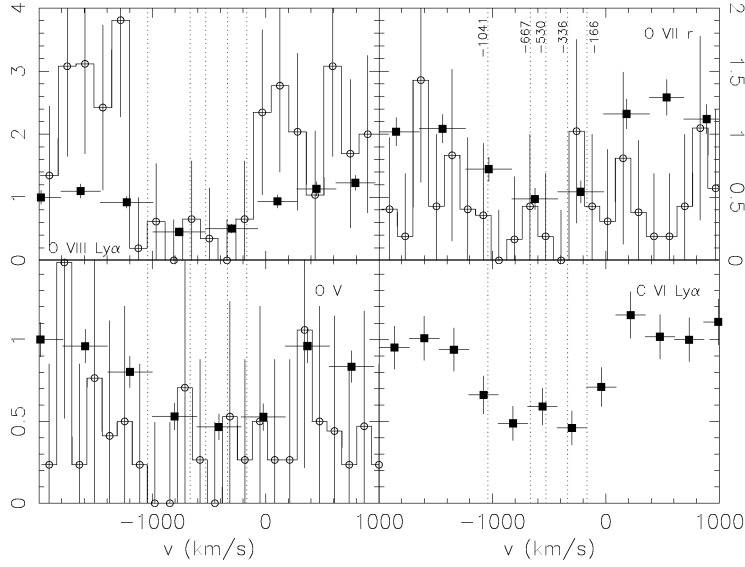
Figure 5.2: The MEG (open circles) and LETGS (filled squares) line profiles for the deepest line of O VIII, O VII, O V and C VI. The five outflow velocities measured in the UV are indicated by the dotted line. No correction was made for possible blending.

ionization parameter for which the column density of the particular ion peaks. We list both $\xi = L/nr^2$ expressed in 10^{-9} W m and $U = Q_{\text{tot}}/(4\pi r^2 cn)$. $Q_{\text{tot}}/(4\pi r^2)$ is the total photon flux for photons with an energy greater than 13.6 eV, L the luminosity, n is the density, r the distance. This Table indicates a weak correlation between outflow velocity and the ionization of the ion, which is shown in Fig. 5.3. As a side effect, leaving the outflow velocity free potentially allows to correct for any remaining wavelength inaccuracies.

As it is not possible to determine the outflow velocity and broadening accurately for all ions, we fitted the spectra using a fixed velocity broadening of 140 km s^{-1} (average σ for O VII and O VIII) and 70 km s^{-1} (average σ for Si XIII and Si XIV). Those two values were chosen to study the influence of saturation and velocity broadening on the determined column density. In this fit the outflow velocity was fixed to either the derived value (see Table 5.5) or a value between -400 and -800 km s^{-1}, depending on the ionization parameter of the ion. This method allows us to obtain an accurate column density for the less abundant ions. The results of this fit are listed in Table 5.6.

For several ions we find a higher column density and larger velocity broadening in Table 5.5, which can be explained by the fact that a velocity broadening of 140 km s^{-1} does not include the full blend due to the five different velocity components. As in Table 5.5 we list the ionization parameter for which the column density of the particular ion peaks.

Table 5.5: The best fit column densities using model B for the ions for which the outflow velocity and velocity broadening are well constrained. The outflow velocity v and the r.m.s. velocity broadening σ are listed as well as the ionization parameters ξ and U for which the ion has its maximum column density. The column densities are from the fit including the broad emission lines (Sect. 5.3.6).

ion	log N_{ion} (m^{-2})	$-v$ (km s^{-1})	σ (km s^{-1})	log ξ (10^{-9} W m)	log U
C V	21.2 ± 0.5	530 ± 90	185 ± 70	0.10	-1.50
C VI	21.6 ± 0.1	480 ± 60	180 ± 35	1.00	-0.60
N VI	21.2 ± 0.2	550 ± 130	200 ± 120	0.50	-1.10
N VII	21.5 ± 0.2	320 ± 110	390 ± 120	1.35	-0.20
O V	20.8 ± 0.2	530 ± 120	280 ± 100	-0.20	-1.80
O VI	20.6 ± 0.2	380 ± 150	160 ± 110	0.30	-1.30
O VII	22.18 ± 0.03	590 ± 60	150 ± 20	0.95	-0.65
O VIII	22.53 ± 0.04	540 ± 60	130 ± 20	1.65	0.05
Ne IX	21.2 ± 0.3	660 ± 170	210 ± 110	1.50	-0.10
Ne X	21.9 ± 0.2	830 ± 140	290 ± 60	2.05	0.45
Mg IX	21.0 ± 0.3	560 ± 70	55 ± 30	1.00	-0.60
Mg XII	21.3 ± 0.1	680 ± 120	430 ± 120	2.35	0.75
Si VIII	20.2 ± 0.2	620 ± 210	330 ± 190	0.40	-1.20
Si X	20.2 ± 0.2	790 ± 150	340 ± 150	1.05	-0.55
Si XI	20.0 ± 0.2	810 ± 180	350 ± 150	1.50	-0.10
Si XIII	21.0 ± 0.1	660 ± 280	80 ± 40	2.20	0.60
Si XIV	21.0 ± 0.3	880 ± 120	60 ± 30	2.60	1.00
S XI	20.0 ± 0.3	560 ± 200	310 ± 170	1.20	-0.30
S XII	20.2 ± 0.2	620 ± 300	450 ± 200	1.45	-0.15
Fe XVII	20.3 ± 0.4	740 ± 110	50 ± 30	1.80	$+0.20$
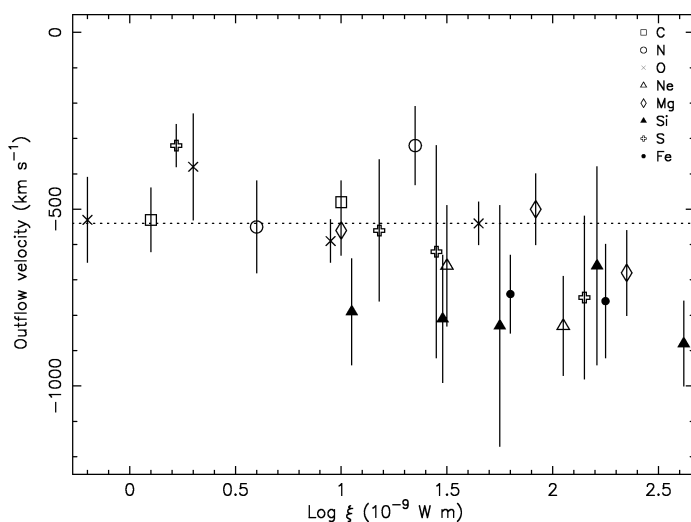
Figure 5.3: The measured outflow velocity versus the logarithm of the ionization parameter, which was corrected for the fact that each ion is formed over a range of ionization according to Eq. 5.3. The dotted line indicates the $-530\ \mathrm{km\ s^{-1}}$ outflow velocity, the dominant component in the UV absorber. A trend toward higher outflow velocities for higher ionized ionization parameters is observed.

Warm absorber model C: multiple separate ionization components

In our previous models A and B we determined ionic column densities independently from any photoionization model. A disadvantage of this method is that the column densities of the many ions with small abundances are poorly constrained, while the combined effect of these ions may still be noticeable in the spectrum. Therefore we have tried spectral fits with three *xabs* components (see Sect. 5.3.2 for a description of the *xabs* model).

The fit with three *xabs* components is not statistically acceptable. As in previous papers the iron abundance is measured to be overabundant for lower ionization ions (Kaastra et al. 2002a; Blustin et al. 2002; Steenbrugge et al. 2003; Netzer et al. 2003). A possible explanation was given by Netzer et al. (2003). Namely, the ionization balance for M-shell iron in low temperature, photoionized plasmas depends strongly on the dielectronic recombination rates. These rates are sometimes poorly known due to resonance effects at low energies, and are thus not correctly incorporated in the pho-

toionization codes that are used to predict the ionic column densities. In recent articles Kraemer, Ferland & Gabel (2003) and Netzer (2003) estimate that the ionization parameter for the iron ions that produce the UTA can change by as much as a factor of two or more. An increase of the effective ionization parameter ξ by a factor ~ 2 for Fe VII - Fe XIII indeed would bring these ions more in line with the trend observed for the other elements.

Table 5.6: The best fit column densities (in m^{-2}) as measured using model B. The outflow velocity (in km s^{-1}) was taken from Table 5.5 or a function of ionization and frozen. The velocity broadening (in km s^{-1}) was also frozen during the fit. In the last two columns we list the ionization parameter for which the ion has its maximum column density. The units of the ionization parameter ξ are 10^{-9} W m. The column densities quoted are for those measured in the fit including the broad emission lines (Sect. 5.3.6). All ions for which we determine one column density and an upper limit should be considered uncertain. Other uncertain column densities are indicated by * (see Sect. 5.3.3).

ion	$\log N_{\mathrm{ion}}$	$\log N_{\mathrm{ion}}$	v	$\log \xi$	$\log U$
	$\sigma = 140$	$\sigma = 70$			
C IV*	21.3 ± 0.1	20.6 ± 0.4	500	-0.65	-2.25
C V	20.6 ± 0.2	21.2 ± 0.1	530	0.1	-1.50
C VI	21.2 ± 0.1	21.5 ± 0.1	480	1.0	-0.60
N V	< 19.8	< 19.8	$-$	-0.15	-1.75
N VI	20.3 ± 0.2	21.2 ± 0.2	550	0.5	-1.10
N VII	21.2 ± 0.2	21.7 ± 0.1	320	1.35	-0.25
O III	< 20.5	20.2 ± 0.4	400	-1.7	-3.30
O IV*	20.3 ± 0.3	20.2 ± 0.3	400	-0.85	-2.45
O V	20.6 ± 0.2	20.9 ± 0.2	530	-0.2	-1.80
O VI	20.4 ± 0.2	21.0 ± 0.1	380	0.3	-1.30
O VII	21.83 ± 0.05	21.94 ± 0.03	590	0.95	-0.65
O VIII	22.31 ± 0.04	22.37 ± 0.03	540	1.65	0.05
Ne VII	21.6 ± 0.1	< 20.7	500	0.35	-1.25
Ne VIII*	21.4 ± 0.1	20.3 ± 0.8	500	0.9	-0.70
Ne IX	21.3 ± 0.1	20.9 ± 0.2	660	1.5	-0.10
Ne X	21.5 ± 0.2	21.3 ± 0.1	830	2.05	0.45
Na VII*	21.4 ± 0.1	< 20.3	500	0.25	-1.35
Na VIII	< 20.4	< 19.3	500	0.7	-0.90

Table 5.6 – continued from previous page

ion	log N_{ion}	log N_{ion}	v	log ξ	log U
	$\sigma = 140$	$\sigma = 70$			
Na IX	< 20.1	< 23	600	1.25	-0.35
Na X	< 20.2	20.1 ± 0.3	700	1.7	0.10
Na XI	< 20.3	< 23	700	2.3	0.70
Mg VI	< 20.1	< 19	500	-0.3	-1.90
Mg VII	20.6 ± 0.9	< 19.7	500	0.1	-1.50
Mg VIII	< 20.2	< 19.8	500	0.5	-1.10
Mg IX	20.3 ± 0.2	20.3 ± 0.3	560	1.0	-0.60
Mg X	< 20.2	< 19.4	700	1.4	-0.20
Mg XI	20.9 ± 0.2	20.4 ± 0.2	500	1.9	0.30
Mg XII	21.0 ± 0.1	20.8 ± 0.1	680	2.35	0.75
Al VII	< 20.8	< 19.9	400	0.05	-1.55
Al VIII*	21.1 ± 0.2	20.7 ± 0.4	400	0.45	-1.15
Al IX	< 19.6	< 19.3	600	0.9	-0.70
Al XI	< 19.3	< 19.5	700	1.7	0.10
Al XII	< 20.0	< 19.9	700	2.05	0.45
Al XIII	< 20.3	< 20.7	800	2.45	0.85
Si VII	19.7 ± 1.0	< 19.8	400	0.05	-1.55
Si VIII*	19.7 ± 0.3	20.9 ± 0.1	620	0.4	-1.20
Si IX*	20.0 ± 0.4	21.1 ± 0.1	400	0.75	-0.85
Si X	19.9 ± 0.2	20.0 ± 0.2	790	1.05	-0.55
Si XI	19.7 ± 0.2	19.8 ± 0.4	810	1.5	-0.10
Si XII	20.6 ± 0.5	20.3 ± 0.5	800	1.75	0.15
Si XIII	20.7 ± 0.1	20.5 ± 0.2	660	2.2	0.60
Si XIV	20.9 ± 0.1	20.7 ± 0.2	880	2.6	1.00
S VII	< 19.4	< 19.3	400	-0.2	-1.80
S VIII	19.8 ± 0.3	19.7 ± 0.2	400	0.2	-1.40
S IX*	19.9 ± 0.1	19.6 ± 0.1	600	0.6	-1.00
S X*	20.3 ± 0.3	20.1 ± 0.2	600	1.0	-0.60
S XI	19.7 ± 0.3	19.7 ± 0.4	560	1.2	-0.30
S XII	19.7 ± 0.3	19.8 ± 0.4	620	1.45	-0.15
S XIII	19.9 ± 0.9	19.7 ± 0.6	700	1.8	0.20
S XIV	20.3 ± 0.3	< 20.0	700	2.15	0.55
S XV	< 20.7	< 20.1	800	2.4	0.80
S XVI	< 20.8	21.0 ± 0.4	800	2.85	1.25
Ar IX*	19.5 ± 0.5	19.6 ± 0.3	500	0.4	-1.20
Ar X*	19.9 ± 0.3	19.4 ± 0.3	500	0.8	-0.75

Table 5.6 – continued from previous page

ion	$\log N_{\mathrm{ion}}$	$\log N_{\mathrm{ion}}$	v	$\log \xi$	$\log U$
	$\sigma = 140$	$\sigma = 70$			
Ar XI*	19.9 ± 0.2	19.7 ± 0.2	600	1.1	-0.40
Ar XII*	19.3 ± 0.8	19.2 ± 0.4	600	1.3	-0.20
Ar XIII*	19.6 ± 0.6	19.5 ± 0.5	700	1.5	-0.10
Ar XIV	< 20.0	< 19.5	700	1.75	0.15
Ar XV	< 20.0	< 20.1	700	1.95	0.35
Ar XVI	< 21.7	22.1 ± 0.1	800	2.30	0.70
Ar XVII	< 20.0	< 20.2	800	2.60	1.00
Ar XVIII	< 21.2	< 20.7	800	3.05	1.45
Ca XI	< 18.8	19.2 ± 0.4	600	0.70	-0.90
Ca XII	< 19.4	< 19.5	600	1.00	-0.60
Ca XIII	< 19.6	19.3 ± 0.8	700	1.40	-0.20
Ca XIV*	19.7 ± 0.3	19.6 ± 0.3	700	1.60	0.00
Ca XV	< 18.6	< 19.2	700	2.00	0.40
Ca XVI	< 20.2	< 19.8	800	2.25	0.65
Ca XVII	20.0 ± 0.5	< 19.8	800	2.40	0.80
Ca XVIII	20.2 ± 0.4	< 20.2	800	2.60	1.00
Ca XIX	< 20.9	< 20.5	800	2.80	1.20
Ca XX	< 20.9	< 20.4	800	3.25	1.65
Fe III	< 19.9	< 23	400	-1.95	-3.55
Fe IV	< 19.5	< 19.1	400	-1.60	-3.20
Fe V	< 20.4	< 19.9	400	-1.30	-2.90
Fe VI	< 23	< 19.4	400	-1.00	-2.60
Fe VII	19.9 ± 0.6	< 19.8	500	-0.50	-2.10
Fe VIII	20.0 ± 0.3	< 19.8	500	-0.10	-1.70
Fe IX	20.2 ± 0.4	20.97 ± 0.08	500	0.20	-1.40
Fe X	20.4 ± 0.1	20.2 ± 0.1	500	0.40	-1.20
Fe XI	20.1 ± 0.2	19.8 ± 0.2	500	0.60	-1.00
Fe XII	19.7 ± 0.5	< 19.7	600	0.80	-0.80
Fe XIII	19.5 ± 0.6	19.4 ± 0.4	600	0.95	-0.65
Fe XIV	< 19.7	19.3 ± 0.9	700	1.15	-0.45
Fe XV	< 19.6	< 19.0	700	1.40	-0.20
Fe XVI	< 18.9	< 18.6	700	1.40	-0.20
Fe XVII	20.7 ± 0.2	20.5 ± 0.2	740	1.80	0.20
Fe XVIII	20.3 ± 0.2	20.1 ± 0.2	700	2.05	0.45
Fe XIX	20.7 ± 0.1	20.5 ± 0.1	800	2.25	0.65
Fe XX	20.4 ± 0.2	20.4 ± 0.1	800	2.40	0.80

Table 5.6 – continued from previous page

ion	$\log N_{\mathrm{ion}}$	$\log N_{\mathrm{ion}}$	v	$\log \xi$	$\log U$
	$\sigma = 140$	$\sigma = 70$			
Fe XXI	20.7 ± 0.2	20.5 ± 0.2	800	2.60	1.00
Fe XXII	20.2 ± 0.2	20.3 ± 0.3	800	2.75	1.15
Fe XXIII	20.5 ± 0.2	20.4 ± 0.2	800	2.90	1.30
Fe XXIV	20.7 ± 0.2	20.8 ± 0.2	800	3.10	1.50
Ni I*	20.3 ± 0.2	20.4 ± 0.2	400	< -4	< -5.6
Ni II*	20.0 ± 0.3	20.0 ± 0.3	400	< -4	< -5.6
Ni III*	20.0 ± 0.7	< 20.2	400	-1.70	-3.30
Ni IV*	< 20.2	< 20.1	400	-1.50	-3.10
Ni V*	< 19.9	< 19.9	400	-1.40	-3.00
Ni VI*	< 20.0	20.1 ± 0.2	400	-1.20	-2.80
Ni VII*	20.3 ± 0.1	20.3 ± 0.1	400	-0.95	-2.55
Ni VIII*	19.9 ± 0.3	20.1 ± 0.2	500	-0.50	-2.10
Ni IX*	20.2 ± 0.1	20.4 ± 0.1	500	-0.05	-1.65
Ni X*	< 19.8	20.0 ± 0.3	500	0.40	-1.20
Ni XI*	20.1 ± 0.4	20.8 ± 0.1	600	0.70	-0.90
Ni XII*	20.3 ± 0.1	20.4 ± 0.1	600	0.90	-0.70
Ni XIII*	20.0 ± 0.2	20.0 ± 0.2	600	1.10	-0.50
Ni XIV*	< 19.7	19.5 ± 0.5	700	1.25	-0.25
Ni XV*	< 18.9	< 19.3	700	1.50	-0.10
Ni XVI*	< 19.4	19.7 ± 0.2	700	1.40	-0.20
Ni XVII*	19.6 ± 0.4	20.8 ± 0.3	700	1.60	0.00
Ni XVIII*	19.7 ± 0.3	19.7 ± 0.3	700	1.70	0.10

There are several reasons why dielectronic recombination effects iron more than other ions. Dielectronic recombination rates depend roughly on the residual nuclear charge, which is higher for iron than for other elements. If any of these lines are saturated (which is unlikely for the numerous Fe UTA lines), they do not vary much with relatively small changes in ionization parameter. Finally, models tend to get "tuned" to the strongest features and therefore are susceptible to bias (e.g. the iron UTA).

A solution is to decouple iron from the other elements, using the current set of photoionization models that form the basis of the *xabs* model. Since however we need at least three *xabs* components, this would imply doubling of the number of free parameters to six *xabs* models. Another option is to fit iron separately with a *slab* model. However, as iron has the largest ionization range and is the only element that samples

Table 5.7: The best fit results for a model with three *xabs* components fitting all ions but iron. To fit the full blend we froze the velocity broadening to 200 km s^{-1} and the outflow velocity to -530 km s^{-1}.

Comp.	A	B	C
LETGS:			
log N_H (m^{-2})	< 25.9	< 25.8	24.56±0.09
log ξ (10^{-9} W m)	< 5	2.1±0.6	0.8±0.1
LETGS, HEG and MEG:			
log N_H (m^{-2})	< 28	25.43±0.06	24.55±0.08
log ξ (10^{-9} W m)	< 5	2.17±0.05	0.80±0.09

both the highest ionized and lowest ionized absorber, this severely limits the ionization range we are able to detect. In such a fit the error bars derived are much larger and the ionization parameters measured should not be compared with earlier ionization measurements in which iron was fit. Forcing a large velocity broadening to fit all the outflow velocity components, and fitting the iron ions separately with a *slab* model, we find a decent fit for three ionization components ($\chi^2 = 3435$ for 2758 degrees of freedom). Adding more *xabs* components leads to highly correlated errors and fitting results. We list the results of this fit in Table 5.7.

Warm absorber model D: continuous ionization structure

We have seen in the previous section that a model using multiple *xabs* components has its complications due to the discordance between iron and other elements in the photoionization calculations. As a result of our modeling with the *slab* model, we have found apparently a power law like distribution of deduced hydrogen column density versus ionization parameter (Fig. 5.4). In order to test whether this apparent power law distribution can be produced indeed by an underlying power law, we have fitted the spectrum directly to such a distribution using the *warm* model (Sect. 5.3.2). Similar to model C, we get a poor fit if iron is included. Modeling all iron ions using a *slab* model and all remaining elements with the *warm* model, then we obtain a good fit to the data, namely $\chi^2 = 3305$ for 2754 degrees of freedom, assuming solar abundances. Table 5.8 lists the best fit parameters using the *warm* model. In this fit the best fit outflow velocity is -530 km s^{-1} and the measured velocity broadening is 140 km s^{-1}. The derived column density distribution is in excellent agreement with the results obtained from model B (see Fig. 5.5).
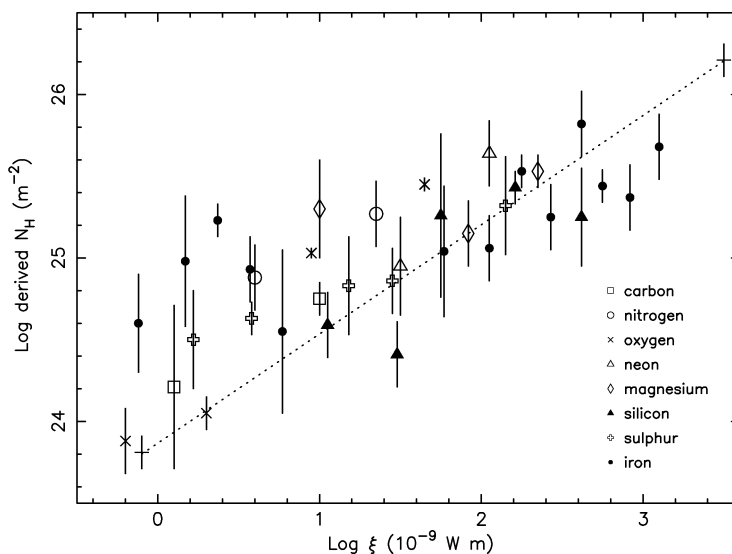
Figure 5.4: The total hydrogen column density $N_{\rm H}$, assuming solar abundances (Anders & Grevesse 1989) derived using Eq. 5.2, plotted versus ionization parameter. The ionic column densities were taken from Table 5.5 and Table 5.6 assuming a velocity broadening of 140 km s^{-1}. For clarity, no upper limits have been plotted. The best fit results for model D are plotted as the two crosses connected by a dotted line.

5.3.3   Reliability of column density estimates

In Table 5.6 we list all the ions that we fitted with the *slab* model. As the *slab* model fits both for the absorption lines and the corresponding edges, some column density determinations could be dominated by an edge measurement, rather than by absorption lines. Measurements dominated by an edge, although resulting in quite accurate column densities are highly dependent on the correct calibration of the instrument and the continuum fit, and thus potentially have a large systematic error. A further uncertainty is introduced by unknown blending at the longer wavelengths, as the atomic data for lines produced at this wavelength region are sometimes poorly known. Below, we discuss those ions for which the column density maybe affected by the above effects.

   Carbon, Oxygen and Neon: For C IV the strongest line at 41.42 Å coincides with the instrumental C I edge, which is deep and susceptible to calibration uncertainties. For O IV the wavelength of the dominant line in the X-ray range is not well known and
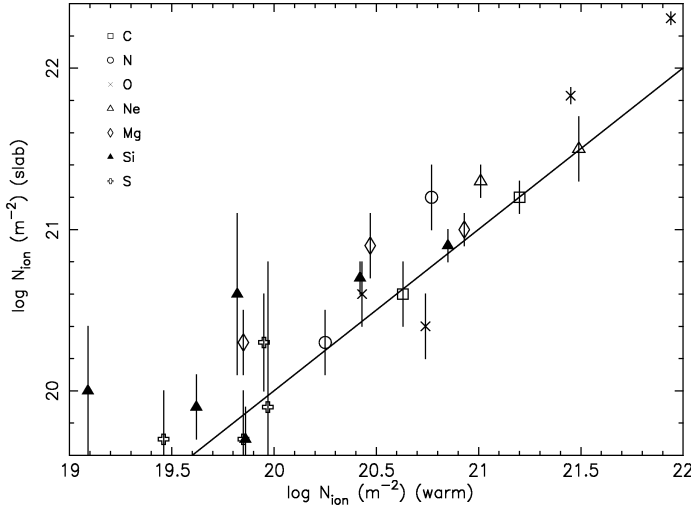
Figure 5.5: Comparison between the ionic column densities calculated with the *warm* model (x-axis is model D) and the ionic column densities obtained with the *slab* model (y-axis is model B). The solid line represents the solution where the predicted *warm* and measured *slab* column densities are equal.

the absorption line is weak. For Ne VIII the deepest line at 88.10 Å is at a rather noisy part of the spectrum, the other line at 67.38 Å is blended with an Al VIII line.

   Sodium and Aluminum: Both Na VII and Na VIII are only detected through lines above 60 Å. The column density for Al VII is mainly determined from the $2p_{1/2}$ edge at 43.56 Å and several lines above 60 Å. A similar situation occurs for Al VIII, where the $2p_{1/2}$ and $2p_{3/2}$ edges at 51.36 Å dominate in the column density determination.

   Silicon and Sulfur: The deepest lines for Si VIII and Si IX at 61.04 Å and 55.30 Å, respectively are saturated. For Si VIII this line is also blended. The saturation of these well detected lines explains the difference in column density obtained for the different velocity broadening assumed. For S X the strongest lines form a blend in the instrumental C I edge.

   Argon: The column density of Ar IX is determined from an absorption line which coincides with the instrumental C I edge and the C V forbidden line. Ar X has only one detectable line at 37.45 Å, which is at a rather noisy part of the spectrum. For Ar XI the deepest line is blended with the -1040 km s^{-1} component of S X at 34.29 Å. Ar XII has only one weak line in the spectrum at 31.37 Å, and for Ar XIII we detect only two

87

Table 5.8: The best fit values for model D, using one *warm* component and fitting iron separately as a *slab* component.

$\log \xi$ (10^{-9} W m)	N_H
−0.1	$(6.3 \pm 1) \times 10^{23}$ m^{-2}
3.5	$(1.6 \pm 0.3) \times 10^{26}$ m^{-2}

weak lines at 29.27 Å and 27.44 Å. The deepest Ar XV absorption line is blended with the N VII Lyα line. The blending is further complicated by the possible substructure in the N VII Lyα line due to the different outflow velocities. Ar XVI is detected from only two edges in the spectrum at 15 and 25 Å.

Calcium: Ca XIV has only one unblended line at 21.13 Å. However, the fit is driven by only one data point of the LETGS spectrum, making the column density uncertain. For all the other calcium ions the detection is very sensitive to the velocity broadening. If we leave σ free, we mostly find upper limits to the velocity broadening of 30 km s^{-1}, implying highly saturated lines and therefore unrealistically high column densities. The lower ionized states of calcium (Ca I to Ca VIII) have edges in the spectra, which dominate the fit.

Nickel: The detection of all nickel ions is uncertain. Nickel only produces weak absorption lines, most of them are blended with stronger iron absorption lines. Small errors in wavelength for these iron lines could be compensated in our model by absorption from nickel. For Ni I the column density is determined from the observed short wavelength tail of the edge at 105.97 Å and a smaller edge at 14.42 Å. For Ni II the 3s edge at 87.93 Å dominates the column density determination. The strongest Ni VI and Ni VII lines are blended by Fe XVI at 14.30 Å and Fe XVIII at 14.26 Å, respectively. The strongest Ni IX line is blended by an Fe XX line at 13.73 Å. The column density for Ni XI was determined mainly from the 3p-edge at 38.62 Å, close to the instrumental C I edge, and in a noisy part of the spectrum. The two strongest lines of Ni XII are blended with the Ne IX resonance line at 13.45 Å. Ni XIII causes a slight depression in the spectrum due to many weak absorption lines. However, the detection is uncertain as the continuum spectrum of the MEG around the relevant wavelength of 13.27 Å differs by about 5 % from the LETGS spectrum, a similar level as the expected depression. The deepest line for Ni XVII is blended with an Fe XX at 12.90 Å; Ni XVIII has several weaker lines that are blended with Fe XX at 12.60 Å.

Due to the uncertainties in the determined column densities for the above listed ions, we decided not to use them in the further analysis.

Table 5.9: Narrow emission lines. The Equivalent Width (EW) as measured with the LETGS, except for the Mg XI, Al XIII and Si XIII forbidden lines (MEG), and flux are listed. In the last column the ionization parameter, ξ, where the ion has the highest column density is given. Forbidden lines are indicated by f, intercombination lines by i. Below the line the C V and O VII RRC are listed. The wavelengths are taken from Drake (1988).

line	wavelength (Å)	EW (mÅ)	flux (ph m^{-2} s^{-1})	log ξ^a
C Vf	41.435	283 ± 170	1.0 ± 0.6	0.1
N VIf	29.518	37 ± 19	0.26 ± 0.13	0.6
N VIi	29.082	< 17	< 0.1	0.6
O VIIf	22.093	103 ± 14	0.88 ± 0.12	0.95
O VIIi	21.804	< 5	< 0.04	0.95
Ne IXf	13.690	28 ± 10	0.14 ± 0.05	1.5
Ne IXi	13.566	12 ± 9	0.05 ± 0.03	1.5
Mg XIf	9.314	< 4	< 0.02	1.9
Al XIIf	7.864	4 ± 2	0.04 ± 0.02	2.05
Si XIIIf	6.739	5 ± 2.7	0.03 ± 0.02	2.2
C V	31.63	23 ± 16	0.08 ± 0.06	0.1
O VII	16.77	51 ± 32	0.08 ± 0.05	0.95

^{a} Given in 10^{-9} W m.

5.3.4 Narrow emission lines

Our spectrum shows the presence of a few narrow emission lines. Table 5.9 lists the measured strength or upper limits of forbidden and intercombination lines of several ions as well as the Radiative Recombination Continua (RRC) observed in the spectra. For all narrow emission lines, with the exception of the O VII and Ne IX forbidden lines, the wavelength was frozen to the value in the restframe of NGC 5548. For the O VII and Ne IX forbidden lines we determined blueshifts of −0.009 ± 0.004 Å and −0.005 ± 0.007 Å, corresponding to an outflow velocity of −150 km s^{-1} and −175 km s^{-1}, respectively. These blueshifts, however, become negligible if instead the redshift of 0.01717 based upon the 21 cm line (Crenshaw & Kraemer 1999) is assumed.

The intercombination lines as well as the RRC's are undetectable or very weak. In particular the O VII intercombination line is not detected, likely due to blending by the absorption line of O VI at 21.79 Å rest wavelength. The forbidden O VII line seems

89

Table 5.10: Parameters of the Fe Kα line from the present HEG spectrum (2002), previous HEG spectrum (2000, Yaqoob et al. 2001), and EPIC spectrum (2001, Pounds et al. 2003). The FWHM is given in km s^{-1}, the flux in ph m^{-2} s^{-1}.

	HEG (2000)	EPIC (2001)	HEG (2002)
E (keV)	6.402 ± 0.026	6.39 ± 0.02	6.391 ± 0.014
EW (eV)	133 ± 50	60 ± 15	47 ± 15
FWHM	4515 ± 2650	6500 ± 2200	1700 ± 1500
flux	0.36 ± 0.16	0.38 ± 0.10	0.24 ± 0.08

double-peaked in the MEG spectrum (see appendix Fig. 5.15), and is poorly fit by a single Gaussian line. However, the LETGS spectrum and the earlier MEG spectrum of 2000 do not show this line profile. None of the other forbidden lines show any broadening or a double-peak profile. We thus conclude that the MEG O VII forbidden line shape is due to noise.

5.3.5   Fe Kα

The narrow Fe Kα emission line is clearly seen in the HEG spectrum (see appendix Fig. 5.11). The flux of the line is (0.24 ± 0.08) ph m^{-2} s^{-1}. Our results are in good agreement with the EPIC results presented by Pounds et al. (2003) and the earlier HEG data presented by Yaqoob et al. (2001) (Table 5.10). The Fe Kα emission line is also discussed by Yaqoob & Padmanabhan (2004). There is no evidence for a broadened Fe Kα emission line, consistent with the results obtained by Yaqoob et al. (2001) and Pounds et al. (2003).

5.3.6   Broad emission lines

Kaastra et al. (2002a) detected a 3σ significant relativistically broadened emission line for N VII Lyα and O VIII Lyα, and a non-relativistically broadened emission line for C VI Lyα. Ogle et al. (2004) detect a broadened C VI Lyα line with a FWHM of 1100 km s^{-1} in NGC 4051. No relativistically or non-relativistically broadened emission lines were detected in the high flux state RGS spectrum (Steenbrugge et al. 2003). The LETGS and MEG spectra show clear, broad excess emission centered on some of the deeper absorption lines, although none show the asymmetric line profile of a relativistically broadened line (Fig. 5.6). We fit these broad excesses with Gaussians. Due to the noise in the data, the broadness of these features, and the rather low contrast
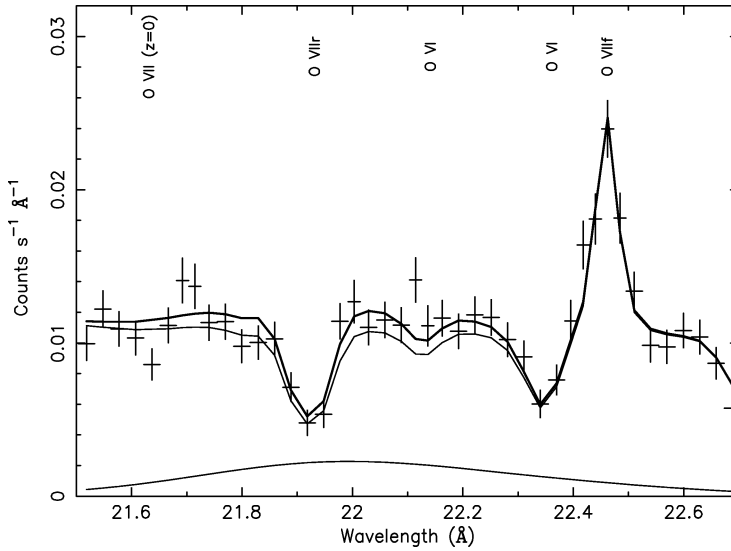
Figure 5.6: Detail of the LETGS spectrum showing the fit with (thick line) and without (thin line) a broad emission line for the O VII resonance line. The profile of the broadened emission line is also plotted.

with the continuum, we fixed the width of these Gaussians to 8000 km s^{-1} (Arav et al. 2002) as observed for the broadest component of the C IV and Lyα broad emission lines in the UV. The wavelength was fixed to the rest wavelength, i.e. assuming no outflow velocity. Table 5.11 lists the broad emission line fluxes for the LETGS and MEG spectra. A detail of the LETGS spectrum of the O VII triplet broadened line is shown in Fig. 5.6.

To ascertain the significance of these broad emission lines, we checked the lines at shorter wavelengths separately in the LETGS and MEG spectra, and for the Mg XII line also in the HEG data. The line fluxes are consistent within the error bars, between the MEG and LETGS observations. Inclusion of these broad emission lines in the model alters the derived column densities for the different ions in the warm absorber. Therefore the differences between the model with and without a broad emission line is not equal to the flux of this line (see Fig. 5.6). As a result the column densities quoted in this paper, which are based on the fit with the broad emission lines included, should not be compared directly with column densities derived from earlier observations (e.g. Kaastra et al. 2002a; Steenbrugge et al. 2003) in a search for variability of the warm

Table 5.11: Flux of the broad emission lines, from the simultaneous LETGS, MEG and HEG fit. The wavelength was frozen to the rest wavelength of the line, while the FWHM was frozen to 8000 km s^{-1}. The lines for which upper limits are detected were not used in the further analysis of the data.

ion	λ (Å)	flux (ph m^{-2} s^{-1})	EW (mÅ)
C v f^a	41.421	1.0 ± 0.6	300 ± 180
C v 1s^2-1s2p ^{1}P$_1$	40.268	< 0.6	< 230
C vi 1s-2p (Lyα)	33.736	0.5 ± 0.2	150 ± 80
N vii 1s-2p (Lyα)	24.781	< 0.05	< 70
O vii triplet^b	21.602	0.56 ± 0.13	130 ± 40
O viii 1s-2p (Lyα)	18.969	0.4 ± 0.2	60 ± 30
O vii 1s^2-1s3p ^{1}P$_1$	18.627	0.19 ± 0.07	70 ± 30

^{a} This coincides with the instrumental C-edge, therefore its detection is less certain due to possible calibration uncertainties.
^{b} The resonance intercombination and forbidden lines significantly overlap, so separate measurements are difficult.

absorber. As an example, the logarithm of the derived column density for O vii (using one *slab* component) in a model without a broad emission line is 21.72 m^{-2}, compared to 22.18 m^{-2} if the broad emission lines are included. The broad emission lines are more easily detected than in previous observations, this partly results from the low continuum flux level, and thus the larger contrast during the present observation. Further discussion on these broad emission lines will be given in a forthcoming paper (Steenbrugge et al. 2004).

5.3.7 Long term spectral variations

We have tested for the presence of long term variations in the warm absorber of NGC 5548 by comparing our best fit model for the present data with the LETGS spectrum of December 1999 (Kaastra et al. 2000, 2002a). To do this, we have fit the 1999 spectrum keeping all parameters of the warm absorber and all fluxes of narrow or broadened emission lines fixed to the values of our 2002 spectrum. Only the parameters of the power law and modified blackbody component were allowed to vary. Then we subtracted the relative fit residuals for our 2002 spectrum from the fit residuals of the
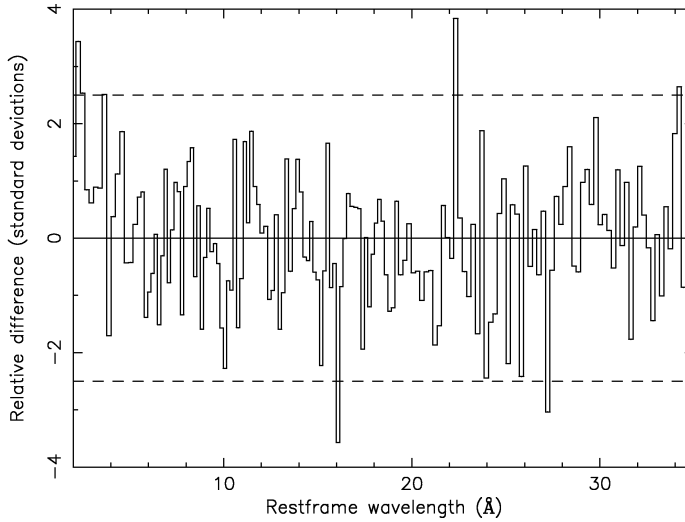
Figure 5.7: Fit residuals of the 1999 LETGS spectrum minus the fit residuals of the 2002 spectrum, normalized as described in the text. For clarity, the residuals have been rebinned by a factor of 8. The dashed lines indicate the 2.5 σ significance level used in the analysis.

1999 spectrum (Fig. 5.7). The relative fit residuals r are defined by $r = (o - m)/m$ where o is the observed spectrum, m the best fit model spectrum. Subtracting the fit residuals instead of dividing the spectra allows us to take out continuum variations. Further, as the higher orders are not subtracted any changes in the continuum will produce broad band features in the ratio of two spectra. In Fig. 5.7 we normalized the difference of the fit residuals by the standard deviation of this quantity. This erases all remaining errors due to either shortcomings in the effective area calibration or in the spectral modeling.

The figure shows clear evidence for five features with more than 2.5σ significance. There is evidence for an increasing flux toward smaller wavelengths starting around 5 Å and resulting in about a 20 % excess at 2 Å in the 1999 spectrum. This corresponds to a difference in the continuum and not in the warm absorber. The remaining features are not due to continuum variations (Table 5.12). As the optical and UV broad emission lines are known to be variable on timescales as short as a day, we identify the broader features with changes in the broad emission lines. We identify the 34.13 Å feature as the red wing of a broad C VI Lyα line (restframe wavelength 33.74 Å, hence velocity of

Table 5.12: Features in the difference spectrum of the 1999 and 2002 LETGS data. We list Gaussian centroids λ (in the restframe of NGC 5548), σ and peak value p; peaks are expressed as a fraction of the 2002 spectrum at the same energy.

λ (Å)	σ (Å)	p
16.10 ± 0.06	$0.10^{+0.09}_{-0.04}$	-0.25 ± 0.09
22.36 ± 0.02	0.03 ± 0.02	$+0.85 \pm 0.29$
27.18 ± 0.07	$0.08^{+0.07}_{-0.05}$	-0.27 ± 0.12
34.13 ± 0.08	0.12 ± 0.07	$+0.34 \pm 0.14$

$+3500 \pm 700$ km s^{-1}). Similarly, the 27.18 Å feature can be identified as the red wing of C VI Lyγ (restframe wavelength 26.99 Å, hence velocity of $+2100 \pm 800$ km s^{-1}). Apparently, the red wing of the C VI Lyα line has decreased while the red wing of Lyγ increased and no change in the Lyβ line. However, the process that would cause the Lyα line to decrease while the Lyγ line increases is unknown. The intrinsic width, σ, of the variable parts of both lines corresponds to about 900–1000 km s^{-1}, this is much smaller than the assumed FWHM of 8000 km s^{-1}. The 16.10 Å feature can be identified by a red wing of O VIII Lyβ (restframe wavelength 16.01 Å, hence velocity of $+1700 \pm 1100$ km s^{-1}). A change in the strength of the broad emission line due to the O VII triplet can also explain the dip at $21 - 22$ Å.

Finally, the 22.36 Å feature most likely has a different origin. First, it is intrinsically narrow and poorly resolved (the upper limit to its Gaussian width corresponds to 700 km s^{-1}). Its wavelength coincides within the error bars with the wavelength of the strongest O V absorption line (22.374 ± 0.003 Å) measured at the University of California EBIT-I electron beam ion trap, which has been optimized for laboratory X-ray astrophysics measurements (M. Schmidt et al. 2004). The 2002 spectrum shows a deep O V absorption line, which is much weaker in the 1999 spectrum. This demonstrates that the O V column is variable on the time scale of a few years. Note that the O V line is by far the strongest absorption line in the LETGS spectrum for the ionization parameter $\log \xi = -0.2$, the ionization parameter where O V reaches its maximum concentration. The Fe M-shell lines are formed at the same ionization parameter, but are much weaker.

5.4   Discussion

5.4.1   Comparison between the warm absorber models

In our model B we determined the column density, the average outflow velocity, and the velocity broadening for all observed ions separately (Table 5.5). The total column densities determined using this method, for the six ions C VI, O V, O VII, O VIII, Ne IX, and Si XIII are consistent with the results obtained using method A, with fixed velocity structure. This gives confidence that the column densities as listed in Tables 5.5 and 5.6 are reliable, even if there is substructure to the lines. The average outflow velocity determined for these six ions is consistent with the outflow velocity of the deepest UV components. Comparing our measured column densities with those obtained in the UV for the five outflow velocity components, we conclude that the column density measured for the -160 km s^{-1} component is in fact the blend of UV components 4 and 5. Our -530 km s^{-1} component is a blend of UV components 2 and 3. Components 2 through 5 form one unresolvable blend in X-rays, and only component 1 is clearly separated.

In Fig. 5.5 we compare the ionic column densities predicted by model D with the column densities measured by model B. The correlation between the measured and predicted column density is rather tight, with a measured slope of 1.10 ± 0.07. However, one also notes that the measured column densities using model B are higher than for model D. This is due to the fact that with method B we optimized the outflow velocity. This is not possible with model D, where the outflow velocity and velocity broadening are tied for all ions.

5.4.2   Outflow velocity

Our method B does not resolve the full velocity structure of the outflow. Therefore one should take care in interpreting the relation between the ionization parameter and the average outflow velocity (Fig. 5.3). Namely, all line profiles probably are a blend of five outflow velocities, but due to limited signal to noise ratio and spectral resolution, components 3 and 4 of the UV dominate the blend.

In general, there is a trend that more highly ionized ions have a larger average outflow velocity. This could indicate that the -1040 km s^{-1} outflow velocity component becomes more prominent for the more highly ionized ions. The -530 km s^{-1} outflow velocity component dominates for lower ionized ions observed in X-rays and the UV band. To further study this effect we plot the total column density as a function of outflow velocity (Fig. 5.8) for the six ions of Table 5.4. We also added C IV and N V taken from Crenshaw et al. (2003) and O VI taken from the non-simultaneous FUSE data

95

by Brotherton et al. (2002). For the UV data we added the two components with the lowest outflow velocity to compare it with the -160 km s^{-1} X-ray component. The two middle outflow velocity components were added to represent the -530 km s^{-1} component. Finally, for O VI we indicate the total column density as measured in the X-rays. From Fig. 5.8 we note that the ionic column density of the -1040 km s^{-1} velocity component is the smallest of the five velocity components for low ξ, while it becomes the largest for highly ionized gas. There is thus a clear difference in ionization structure between the -1040 km s^{-1} outflow component and the lower outflow velocity components. A possible explanation for this difference in ionization structure is that the outflowing wind at -1040 km s^{-1} is less dense, leading to a higher overall ionization of the gas, while overall the column density is smallest.

5.4.3 Velocity broadening

In Table 5.4 we list the measured Gaussian velocity broadening σ of the three velocity components as well as the velocity broadening of the UV components 1, $2-4$, and 5. For components $2-4$ we find a slightly smaller X-ray width, while for component 5 we find a larger width as compared to the UV lines. We attribute this to the blending of (a part of) component 4 into component 5. We note that UV component 4 has $\sigma = 62$ km s^{-1} compared to 68 km s^{-1} in component 3 and only 18 km s^{-1} in component 2, hence we need approximately half of component 4 to blend into component 5 in order to explain the difference.

Interestingly, we find a much smaller velocity broadening for UV component 1, the only one we can resolve. Modeling the O VIII Lyα line with a column density of $10^{22.2}$ m^{-2} and a velocity dispersion σ of 40 km s^{-1}, we find that the line is heavily saturated, and effectively produces a FWHM of 240 km s^{-1}. This is similar to the 222 ± 18 km s^{-1} value measured from the UV spectrum. We are, however, able to obtain the velocity broadening σ from the line ratios of the non-saturated Lyman series of O VIII and the other five ions.

In Table 5.5 the velocity broadening σ is listed based upon model B. It is small compared to the velocity range of the components measured from the UV spectra. This indicates that we do not fully resolve the blend of the five outflow velocity components. The velocity broadening in our case is mainly determined from equivalent width ratios of absorption lines from the same ion. The velocity broadening for the majority of absorption lines is less than 220 km s^{-1}. This is consistent with detecting mainly the -667 km s^{-1}, -530 km s^{-1} and -336 km s^{-1} outflow components, which are the dominant velocity components in the UV. These three velocity components form an unresolved blend in the X-rays. Plotting the velocity broadening versus the ionization parameter produces a scatter plot.
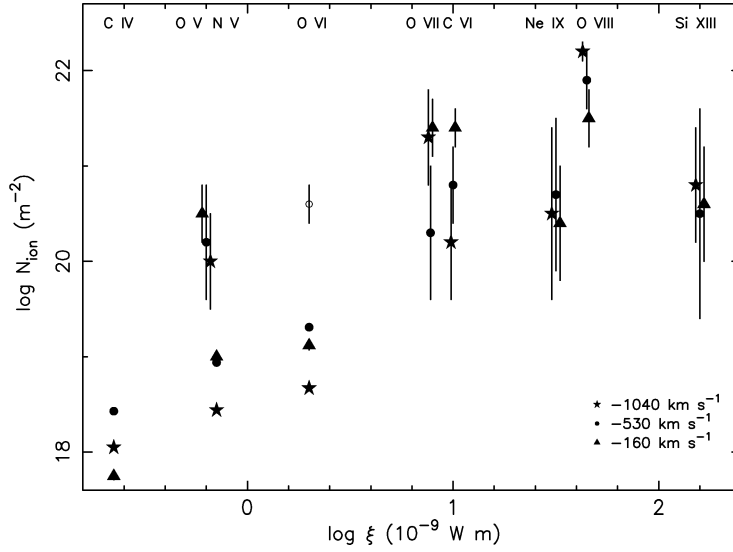
Figure 5.8: The ionic column density versus the logarithm of the ionization parameter for the three outflow velocity components as measured for six ions in X-rays, 2 ions (C IV and N V) measured simultaneously with HST STIS (Crenshaw et al. 2003) and the lower limits for O VI from non-simultaneous FUSE data (Brotherton et al. 2002, taking their preferred uncovered model; Arav et al. 2003). In calculating the column densities for the UV data we kept the highest outflow value separate, added the two middle ones and the two lower ones (see Sect. 5.4.1). For O VII the ionization parameter was decreased by 0.05 for easier identification. The open circle indicates the total column density for O VI obtained from the LETGS and MEG spectra.

5.5   Ionization structure

An important question about the physical nature of these outflows is whether they occur as clumps in an outflow or in a more homogeneous wind. In the first case these clumps should be in pressure equilibrium with the outflowing less dense wind, with a finite number of solutions for temperature and ionization ξ for the same constant pressure ionization Ξ value. In the second case one expects a continuous ionization distribution, which depends on the density of the particular part of the wind. Thus less dense material will be higher ionized, while more dense regions will be lower ionized. In this section we elaborate on both scenario's, confronting them with our observations.

97

5.5.1 Clumps in a wind

In several AGN outflow scenario's, instabilities in the wind may cause the formation of clumps. Such clumps can survive for longer times if they are in pressure equilibrium with the surrounding wind and are on the stable branch of the $T(\Xi)$ curve. Where the ionization parameter for constant pressure, Ξ, is given by $\Xi = L/(4\pi c r^2 P) = 0.961 \times 10^4 \, \xi/T$, with L the luminosity, P the pressure, r the distance from the ionizing source, c the speed of light and T the temperature. Ionization codes, like XSTAR (Kallman & Krolik 1999) predict a specific ionization range for which pressure equilibrium can occur (Krolik & Kriss 2001). Krongold et al. (2003) claim that there are only two ionization components in such an equilibrium in the Seyfert 1 galaxy NGC 3783. Netzer et al. (2003) needed three ionization components in pressure equilibrium to fit the same NGC 3783 spectrum. Ogle et al. (2004) find that in the case of NGC 4051 the different ionization components are not in pressure equilibrium. Another possibility is that the clumps are magnetically confined.

In order to test the presence of a finite number of ionization components, each with its own value for ξ and $N_{\rm H}$, we fitted the ionic column densities obtained with model B (Table 5.6) to a model with a finite number of ionization components. Since there are potential problems with the iron ionization balance (see Sect. 5.3.2), we did our analysis separately for iron and the other elements. The results of these fits are listed in Table 5.13 and Table 5.14.

Using the measured column densities for all ions, except iron, we notice that the fit does not improve if more than three ionization components are fitted. The program even prefers to split up one component rather than add another in the case we fitted for five ionization components. The fit is never statistically acceptable, which is unlikely due to abundance effects as most elements have abundances consistent with solar. As an extra test we decided to fit oxygen, silicon and sulfur separately. However, due to the smaller span in ionization range and the fewer points (maximum of five), all were well fit with three ionization components.

For iron we decided to use the column densities measured by the RGS (Steenbrugge et al. 2003), as here several more ions have a measured column density and the errors are somewhat smaller. For Fe XII and Fe XXIV, which have the same measured column density in the RGS and *Chandra* spectra, we used the smaller *Chandra* error bars. To fit these column densities adequately, one needs at least five ionization components ($\log \xi = 3.10, 2.48, 1.56, 0.65, -0.03$). In Fig. 5.9 we show the fit to the measured column densities with four and five ionization components. The main problem with the fit for four ionization components is Fe XXIV, which is severely under-predicted. As the RGS and *Chandra* spectra measure the same column density for this ion, this is a rather certain measurement.

Table 5.13: Fits with a finite number of ionization components to the column densities of all elements but iron derived with model B, assuming solar abundances. The number of ionization components is indicated by N. In the last column we give the significance according to an F-test of the added component.

N	χ^2/d.o.f.	$\log \xi$ 10^{-9} W m	$\log N_{\mathrm{H}}$ m^{-2}	sign.
1	147/22	1.2	25.5	
2	86/20	2.45, 1.15	26.1, 25.4	89
3	83/18	2.47, 1.17, -0.70	26.1, 25.4, 23.6	53

Table 5.14: Fits with a finite number of ionization components to the iron column densities for the RGS data (Steenbrugge et al. (2003). The number of ionization components is indicated by N. In the last column we give the significance according to an F-test of the added component.

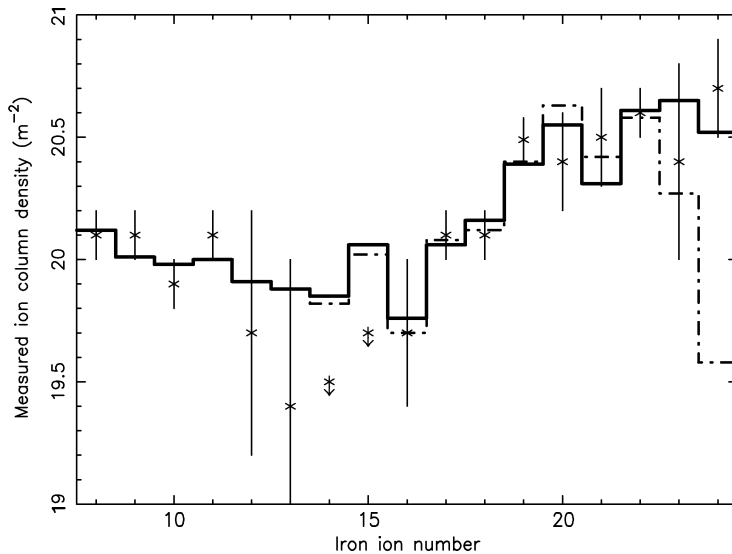| N	χ^2/d.o.f.	$\log \xi$ 10^{-9} W m	$\log N_{\mathrm{H}}$ m^{-2}	sign.
1	79/15	0.22	25.2	
2	22.9/13	2.50, 0.20	25.7, 25.2	98.8
3	10.5/11	2.57, 1.61, 0.20	25.7, 25.1, 25.2	90.9
4	7.2/9	2.57, 1.62, 0.65 -0.03	25.7, 25.1, 25.0 25.0	72.7
5	4.9/7	3.10, 2.48, 1.56 0.65, -0.03	25.8, 25.6, 25.1 25.0, 25.0	71.1

Figure 5.9: The column densities for iron as measured by the RGS instrument, with the fit for a model with four (dash-dot line) and five (thick solid line) ionization components. The fit with four ionization components clearly underpredict the Fe XXIV column density.

We conclude that we need at least five different ionization components to explain the measured ionic column densities in NGC 5548. These components span a wide range in ionization parameter (log ξ between -0.03 and 3.10). Are these ionization components in pressure equilibrium? In Fig. 5.10 the ionization parameter if pressure is held constant (Ξ) versus temperature is shown for the SED used in the current analysis and the earlier RGS and LETGS analysis. The marginally stable part, where different temperature and therefore different ξ are in pressure equilibrium ranges only from log $\xi = 1.3$ to 2.7. The curve has nowhere a negative slope, the smallest positive slope is between log $\xi = 1.4 - 1.5$. Increasing the hard X-ray component (for example by including a reflection component) shifts the turn-over point at log $\Xi = 0.85$ and $T = 6 \times 10^5$ K to lower Ξ values, but the ξ value at this turn-over point remains the same. It should be noted that the difference between the results produced by different codes are larger than the change in turn-over for a larger reflection component.

For the three different ionization components as observed in the earlier LETGS and RGS spectra of NGC 5548 (Kaastra et al. 2002a; Steenbrugge et al. 2003), the lowest

ionization component has log ξ = 0.4, which from Fig. 5.10 cannot be in equilibrium with the other two components at log ξ = 1.98 and 2.67. If we take the five ionization components from the iron analysis, then the highest and the lowest ionization component cannot be in pressure equilibrium. This clearly suggests that the current photo-ionization models are either too simple, or that at least the lowest ionization component is confined by another process, possibly magnetic. As the lowest ionization component does have the same kinematics as the higher ionized absorbers, all absorbers must co-exist in a single confined outflow. This result that not all ionization components are in pressure equilibrium is rather robust, even accounting for inaccuracies in the photoionization codes, in particular for lowly ionized iron, or the inclusion of the blue bump.
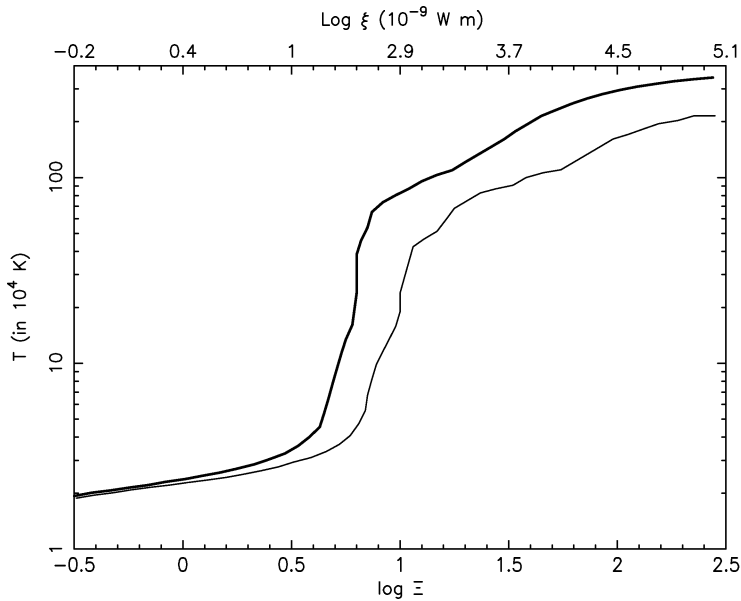

Figure 5.10: The temperature versus ionization parameter for constant pressure Ξ diagram for the SED used in the present analysis (thick line) and for the SED used in earlier LETGS (Kaastra et al. 2002a) and RGS (Steenbrugge et al. 2003) analysis (thin line). The ξ values corresponding to the currently used SED are indicated on the x-axis on top.

Another possible method to distinguish between a continuous and discrete ioniza-

tion is to look for spectral variability. No spectral variability of the warm absorber, with the exception of O V, was detected although the source was observed at a $2 - 10$ keV luminosity of 4.9×10^{36} W (1999 LETGS, Kaastra et al. 2002a), 5.7×10^{36} W (2001 RGS, Steenbrugge et al. 2003) and 4.0×10^{36} W (present LETGS spectrum). If the ionization parameter varies linearly with the luminosity, then we should not detect a variation in ionization, as the smallest change in ionization detectable is 0.15 in log ξ. Further complicating the possible detection of changes in the ionization parameters is the fact that in the UV the different velocity components show opposite column density variations for the same ion. The net effect will be hard to discern in the X-rays for velocity components $2 - 5$. Component 1, which can be resolved with *Chandra* is the most variable component, and should be studied in the future for signs of variability. A further lack of variation in the ionization structure of component 1 possibly indicates that the ionization distribution is continuous. In the case of two or three ionization components, a luminosity change should result in a shift in the ionization parameters. A change larger than 0.2 in log ξ is detectable in the present spectra for the lower ionized component. The iron UTA blend shifts in wavelength with ionization parameter, and for the highest ionized component there are many ions with well determined column densities. In a continuous model one would expect a decrease in column density for the lowest ionization states and an increase in highly ionized material for an increase in luminosity. However, as the warm absorber is detected up to Fe XXIV, and our sensitivity for Fe XXV and Fe XXVI is insufficient, this is hard to measure with this data set. However, for the long NGC 3783 XMM-*Newton* observation this behavior was indeed detected. Behar et al. (2003) studying the RGS spectra detected no spectral variability in the lowly ionized absorber, and in particular no change in the iron UTA. Reeves et al. (2004) however did detect spectral variability of the highly ionized absorber with the EPIC pn instrument.

5.5.2 Continuous ionization distribution

We decided to derive the total hydrogen column density as a function of ξ, similar to Steenbrugge et al. (2003). Contrary to the previous analysis we did not assume that the ion column densities are predominantly determined by the ionization parameter at which the relative concentration is at its maximum. In the present analysis we took into account that each ion is formed over a range of ionization. We implemented this by assuming a power-law distribution:

$$\xi \mathrm{d}N_\mathrm{H}(\xi)/\mathrm{d}\xi = A\xi^\alpha \qquad (5.1)$$

with a given normalization A and index α, and calculating the predicted ionic column densities $N_\mathrm{i,p}$ for this distribution similar to the *warm* model. As the ionization

parameter in reality will be finite, this power law needs to have a cut-off value. We will use the results from model B to determine A and α. If $f_i(\xi)$ is the ionic concentration relative to hydrogen at a given ionization parameter ξ, then $N_{i,p}$ is given by $N_{i,p} = \int_0^\infty f_i(\xi)A\xi^{\alpha-1}\,d\xi$. Comparing this with the observed ionic column density $N_{i,obs}$ gives the equivalent hydrogen density for each ion as

$$N_{H,i} \equiv \xi_i \frac{dN_H(\xi_i)}{d\xi} = \frac{N_{i,obs}}{N_{i,p}} A\xi_i^\alpha \qquad (5.2)$$

where the effective ionization parameter ξ_i is given by

$$\xi_i \equiv \frac{\int_0^\infty f_i(\xi)\xi^\alpha d\xi}{\int_0^\infty f_i(\xi)\xi^{\alpha-1}d\xi} \qquad (5.3)$$

This value of ξ_i is typically 25 % larger than the value of $\xi_{i,m}$ for which $f_i(\xi)$ reaches its maximum. The difference in calculated total hydrogen column density is larger and can be as large as a factor of 3. Ion concentrations were determined using a set of runs with XSTAR (Kallman & Krolik 1999) for a thin photoionized layer with solar abundances (Anders & Grevesse 1989).

The derived hydrogen column densities $N_{H,i}$ versus the ionization parameter ξ_i are presented in Fig. 5.4. For lower ionized ions (log $\xi < -0.7$) we can only determine upper limits to the column density, in contrast to the earlier RGS results (Steenbrugge et al. 2003). This results from the lower effective area of the LETGS compared to the RGS in the iron UTA region. However, due to the longer wavelength band, we do detect many previously unobservable medium ionized ions. This strengthens the relationship between log $\xi = 0$ and 1. The column density increases by nearly 2 decades for a 3 decades increase in ξ, consistent with Steenbrugge et al. (2003).

A formal fit of the column densities of all ions except iron yields A = $10^{24.4\pm0.1}$ (at log $\xi = 0$) and $\alpha = 0.40 \pm 0.05$ with $\chi^2 = 107$ for 30 d.o.f. A similar fit to the iron ions only yields A = $10^{25.0\pm0.2}$ (at log $\xi = 0$) and $\alpha = 0.2 \pm 0.1$, with a $\chi^2 = 16$ for 13 d.o.f.

The relationship obtained is rather tight, and the assumption of solar abundances seems justified, if we do not include those ions which may suffer from systematic bias in their column density determinations (Sect 5.3.3). If the same analysis is repeated for sodium, aluminum, argon and nickel, we find that these elements are overabundant compared to solar, except for sodium. This strengthens our conclusion that these ions may suffer from strong systematic errors in their column density estimates. These ions are therefore not plotted in Fig. 5.4.

5.6 The outflow

5.6.1 Outflow geometry

In trying to get a physical picture of the outflows in AGN it is important that we know the geometry, as well as the ionization structure. By estimating the opening angle of the outflow, we can distinguish between a spherical outflow model or a model with localized streams. The model by Elvis (2000) prefers a localized stream, however there are some problems with modeling 5 different localized outflows as radiation pressure would merge them with time (Proga, private communication). The model by Urry & Padovani (1995), on the other hand predicts a less collimated outflow.

Similar to Steenbrugge et al. (2003) we can obtain an upper limit to the opening angle for the outflow (eq. 5.4). We use the mass conservation formula ($\dot{M}_{\mathrm{loss}}=r^2 n m_{\mathrm{p}} v \Omega$), with r the distance from the ionizing source, n the density, m_{p} the proton mass, v the outflow velocity and Ω the opening angle. Further we assume that the system is stationary and that the mass loss rate is equal or less than the mass accretion rate $\dot{M}_{\mathrm{acc}} = L/\eta c^2$, with L the bolometric luminosity and η the accretion efficiency. The outflow velocities of the wind are taken from the UV measurement. This leads to the following constraint on the solid angle Ω:

$$\Omega \leq \frac{\xi}{\eta c^2 m_{\mathrm{p}} v} \tag{5.4}$$

where we used:

$$\xi = \frac{L}{nr^2} \tag{5.5}$$

We assume a Schwarzschild black hole, thus the accretion efficiency $\eta = 0.057$. For a Kerr black hole, with an efficiency of 0.31, the opening angle is reduced by a factor of 5.4. Even higher efficiencies will further reduce the opening angle. Assuming that only 50 % of the mass that is accreted is lost through an outflow halves the upper limit to the opening angle.

As the ionization parameter, as well as the outflow velocities measured in this analysis closely resemble those found with the RGS, also the resulting upper limits for Ω have a similar range (but now corrected for the extra 4π). Table 5.15 lists the upper limits to the opening angle for the five different outflow velocity components observed in the UV and the ionization range observed in the X-rays.

We thus find that the opening angle of the outflow is very small, down to 10^{-4} sr for the lowest ionization component. This implies that the wind occurs in the form of narrow streamers. The range in ionization parameters at a given outflow velocity component then implies density stratification perpendicular to the outflow.

Table 5.15: The upper limit to the opening angle as calculated from eq. 5.4 for the five outflow velocities measured in the UV, over the ionization range observed in the *Chandra* spectra. The angles are given in sr.

	5	4	3	2	1
$\log \xi^a$	-166	-336	-530	-667	-1041
	km s^{-1}	km s^{-1}	km s^{-1}	km s^{-1}	km s^{-1}
0	7×10^{-4}	3.5×10^{-4}	2×10^{-4}	2×10^{-4}	1×10^{-4}
1	7×10^{-3}	3.5×10^{-3}	2×10^{-3}	2×10^{-3}	1×10^{-3}
2	7×10^{-2}	3.5×10^{-2}	2×10^{-2}	2×10^{-2}	1×10^{-2}
3	7×10^{-1}	3.5×10^{-1}	2×10^{-1}	2×10^{-1}	1×10^{-1}

^{a} in 10^{-9} W m.

A further quantitative diagnostic of the thickness of the outflow can be derived from Fig. 5.4. There is a clear power-law relation between the total hydrogen column density and the ionization parameter. This power-law relation is also established by the fact that one can fit the spectra with the *warm* model, using only two points, the lowest and highest ionization state observed. From Fig. 5.4 we find a power-law slope $\alpha = 0.40 \pm 0.05$, and a normalization $\log A = 24.4 \pm 0.1$ at $\log \xi = 0$. Similar to Steenbrugge et al. (2003) we combine Eq. 5.1 with Eq. 5.5 and use $dN_{\mathrm{H}} = n \, dr$ with r the distance from the axis of the streamer, resulting in a simple differential equation for $d\xi/dr$ with formal solution $n/n_o = (1 + r/r_o)^{-\beta}$ where n_o is the density at the axis and $r_o = A\xi_o^{\alpha+1}/n_o(\alpha + 1)$ and $\beta = 1/(\alpha + 1)$. As we do not know the distance r of the absorber to the nucleus of the AGN, we do not know n_o; however we know $r_o n_o = 1.0 \times 10^{24}$ m^{-2} at $\xi = 0$ and $\beta = 0.71 \pm 0.01$. Accordingly, at large distance from the axis of the streamer (low density, high ionization parameter), the density scales as $n \sim r^{-0.71}$. Steenbrugge et al. (2003) found a similar result, but due to the detection and overabundance of the iron UTA with the RGS, the power-law slope was less well determined.

5.6.2   Mass loss through outflow

Outflows from AGN are potentially important contributors to the enrichment of the IGM. A critical factor is the amount of mass that escapes from the host galaxy through the observed outflows. Here we estimate an upper limit to the mass loss and discuss briefly the difficulties associated with this estimate.

First the outflowing gas has to escape the potential of the massive black hole. Matter

can escape if its radial velocity v_r is larger than the escape velocity $v_e = \sqrt{2GM/r}$. Inserting a black hole mass of 6.8×10^7 M$_\odot$ (Wandel 2002) we find that matter escapes only if $r > (0.58/v_r^2)$ pc with v_r expressed in units of 1000 km/s. The measured outflow velocities are only lower limits, namely the velocity component along our line of sight, and range between -1041 km s^{-1} and -166 km s^{-1}. Taking the measured outflow velocities, then r needed for the outflow to escape corresponds to 0.5–20 pc. The location of the wind is thus important in determining whether the gas will escape or not. Crenshaw et al. (2003) argue that the wind should cover at least a part of the inner, high ionization narrow line region (NLR), while Arav et al. (2002) argue that the narrow line region is not covered. The NLR spans at least the distance range of 1 pc (highly ionized) to 70 pc (lowly ionized) (Kraemer et al. 1998). If the argument of Crenshaw et al. (2003) holds, then in particular the highest velocity gas may be able to escape. If the v_r is significantly higher than the measured v, the lower velocity components will also escape.

After escaping the immediate environment of the central black hole, the gas must escape from the bulge and halo of the galaxy. The stellar velocity dispersion of the bulge is 180 km s^{-1} (Ferrarese et al. 2001), and hence it is likely that most of the gas can escape the bulge provided it has not been decelerated. The effects of the disk and halo of NGC 5548 are expected to be of equal or less importance.

We neglect the possibility that ram pressure in the host galaxy terminates the outflow. Wilson & Ulvestad (1982) note the possibility that the linear radio structure observed in the host galaxy of NGC 5548 is due to material ejected from the nucleus and stopped due to ram pressure. This seems to indicate that the outflows as observed in the UV and the X-rays can escape the nucleus, whether or not the host galaxy.

If all gas escapes, then our earlier argument that the total mass loss through the wind must be smaller than the accretion rate through the disk leads to an upper limit of the mass loss of about 0.3 M$_\odot$ yr^{-1}. NGC 5548 had a major interaction with another galaxy some 0.6–1.0 Gyr ago (Tyson et al. 1998); assuming that the AGN phase lasts for at least 0.6 Gyr with a steady mass loss rate, the upper limit to the mass enrichment of the IGM is 2×10^8 M$_\odot$.

5.7   Summary and conclusions

Our long Chandra observation of NGC 5548 allowed us to obtain a unique, high signal to noise, high spectral resolution, broadband spectrum of this Seyfert 1 galaxy.

The fluxes measured for the Fe-K line and the narrow emission lines are within 1 σ consistent with earlier Chandra and XMM-Newton spectra. There is thus no evidence for long-term variability. The only narrow feature that shows column density variations

is O v.

We found clear evidence for broad emission lines, similar to the optical and UV Broad Line Region lines. In particular C VI, O VII and O VIII showed significant broad lines. From a comparison of our spectrum taken in 2002 with the earlier LETGS observation of 1999, we find significant changes in the red wing (at 1700-3500 km s^{-1}) of C VI lines and the O VIII Lyβ line. A more extensive discussion of these broad lines will be given in a forthcoming paper (Steenbrugge et al. 2004). The presence of these broad lines affects our estimates of column densities in the warm wind, by factors up to 3, a similar situation as has been found in the UV band (Arav et al. 2002).

We find evidence for the presence of an inner-shell X-ray absorption line of N v at 29.42 Å. The long exposure time and the combination of LETGS and HETGS spectra allows us to fit the warm absorber using three different spectral models. Based upon these models, we conclude that there is a good agreement between the properties of the outflow as measured through UV absorption lines and X-ray absorption lines, although in the X-ray band we do not fully resolve the spectral lines. But line centroids and derived line width are in good agreement. We find that the highest velocity component 1 at -1040 km s^{-1} has a different ionization structure than the other components 2–5.

We have compared our results with models for the ionization structure of a wind. We conclude that our data are not in agreement with a model with discrete clumps that are in gas pressure equilibrium with the surrounding medium. This conclusion is based upon the following arguments:

1. the need for at least five discrete components to span the broad range (at least 3 orders of magnitude) of ionization parameter ξ;

2. the limited range in ξ for which multiple solutions of constant Ξ can co-exist, assuming our SED;

3. the lowest ionization gas that we found is incompatible with this range;

4. the fact that there are five discrete velocity components, instead of a continuous range, with at least the -1040 km s^{-1} component spanning the observed range in ionization.

Our data are in agreement with a model with a continuous distribution of N_{H} as a function of ξ. Comparing the mass outflow through the wind with the accretion rate onto the black hole, we derived upper limits to the solid angle sustained by the outflowing wind. These upper limits are of the order of 10^{-4} sr for the lowest ionized gas in velocity component 1. We conclude that the wind occurs in the form of narrow streams with density variations perpendicular to the flow velocity. Most likely these streamers are caused by accretion disk instabilities and cross our line of sight when

107

being radiatively accelerated. Assuming density stratification, the dependency of N_H upon ξ gives the density profile across these streamers. At large distances the density is proportional to $r^{-0.71}$, with r the distance from the densest part of the streamer.

Unfortunately the LETGS is not sensitive enough to detect significant variations of the warm absorber as a response to the continuum flare occurring during the LETGS observation. Reverberation studies with more sensitive X-ray instruments will allow us to determine the densities and hence the location of the wind. However regular monitoring of NGC 5548 in both X-rays and UV will allow us to derive important constraints on the long term variability of the wind. A clear example is the variability of O v between 1999 and 2002 that we found with our observations.

References

Anders, E. & Grevesse, N., 1989, Geochim. Cosmochim. Acta, 53, 197

Arav, N., Korista, K. T. & de Kool, M., 2002, ApJ, 566, 699

Arav, N., Kaastra, J. S., Steenbrugge, K. C. et al., 2003, ApJ, 590, 174

Behar, E., Rasmussen, A. P., Blustin, A. J., et al., 2003, ApJ, 599, 933

Blustin, A. J., Branduardi-Raymont, G., Behar, E., et al., 2002, A&A, 392, 453

Brotherton, M. S., Green, R. F., Kriss, G. A. et al., 2002, ApJ, 565, 800

Crenshaw, D. M. & Kraemer, S. B., 1999, ApJ, 521, 572

Crenshaw, M., Kraemer, S., Gabel, J. R, et al., 2003, ApJ, 594, 116

Drake, G. W., 1988, Can. J. Phys., 66, 586

Dumont, A-M., Collin-Souffrin, S. & Nazarova, L., 1998, A&A, 331, 11

Elvis, M., 2000, ApJ, 545, 63

Ferrarese, L., Pogge, R. W., Peterson, B. M., et al., 2001, ApJ, 555, L79

Gabel, J. R., Crenshaw, D. M., Kraemer, S. B., et al., 2003, ApJ, 595, 120

Kaastra, J. S. & Barr, P., 1989, A&A, 226, 59

Kaastra, J. S., Mewe, R., Liedahl, D. A., Komossa, S., Brinkman, A. C., 2000, A&A, 354, L83

Kaastra, J. S., Steenbrugge, K. C., Raassen, A. J. J., et al., 2002a, A&A, 386, 427

Kaastra, J. S., Mewe, R. & Raassen, A. J. J., 2002b, Proceedings Symposium 'New Visions of the X-ray Universe in the XMM-*Newton* and *Chandra* Era'

Kaastra, J. S., Steenbrugge, K. C., Brinkman, A. C., et al., 2003, Proceedings of the meeting 'Active Galactic Nuclei: from Central Engine to Host Galaxy'

Kaastra, J. S, Steenbrugge, K. C., Crenshaw, D. M., et al., 2004a, A&A, in press

Kallman, T. R. & Krolik, J. H., 1999, XSTAR photoionization code, ftp://legacy.gsfc.nasa.gov/software/plasma_codes/xstar/

Kraemer, S. B., Crenshaw, D. M., Filippenko, A. V. & Peterson, B. M., ApJ, 499, 719

Kraemer, S. B., Ferland, G. J., Gabel, J. R., 2003, astroph/0311568

Krolik, J. H. & Kriss, G. A., 2001, ApJ, 561, 684

Krongold, Y., Nicastro, F., Brickhouse, N. S., 2003, ApJ, 597, 832

Mathur, S., Elvis, M. & Wilkes, B., 1995, ApJ 452, 230

Nandra, K., Fabian, A. C., George, I. M., et al., 1993, MNRAS, 260, 504

Netzer, H., Kaspi, S., Behar, E., et al., 2003, ApJ, 599, 933

Netzer, H., 2003, ApJ, in press

Nicastro, F., Piro, L., De Rosa, A., et al., 2000, ApJ, 536, 718

Ogle, P. M., Mason, K. O., Page, M. J., et al., 2004, ApJ, 606, 151

Pounds, K. A., Reeves, J. N., Page, K. L., et al., 2003, MNRAS 341, 953

Proga, D., 2003, private communications

Reeves, J. N., Nandra, K., George, I. M., et al., 2004, ApJ, 602, 648

Schmidt, M., Beiersdorfer, P., Chen, H., et al., 2004, ApJ, 604, 562

Steenbrugge, K. C., Kaastra, J. S., de Vries, C. P. & Edelson, R., 2003, A&A, 402, 477

Steenbrugge, K. C., Kaastra, J. S., 2004, in preparation

Tyson, J. A., Fisher, P., Guhathakurta, P., et al., 1998, AJ, 116, 102

Urry, C. M. & Padovani, P., 1995, PASP, 107, 803

Wandel, A., 2002, ApJ, 565, 762

Wilson, A. S. & Ulvestad, J. S., 1982, ApJ, 260, 56

Yaqoob, T., George, I. M., Nandra, K., et al., 2001, ApJ, 546, 759

Yaqoob, T. & Padmanabhan, U., 2004, ApJ, 604, 63
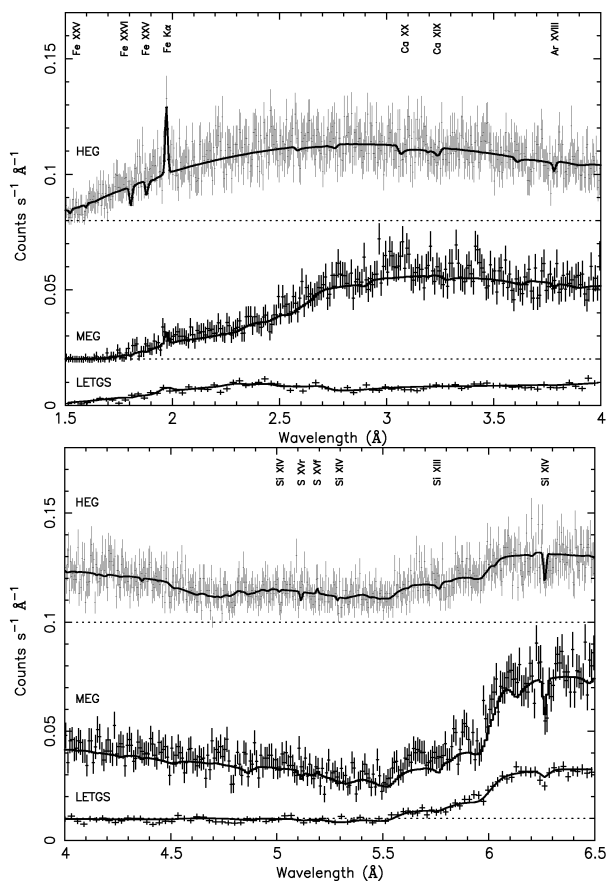
Appendix

Figure 5.11: Detail of the HEG, MEG and LETGS spectra. The dotted lines indicate the zero flux level for the HEG and MEG spectra. The Fe $K\alpha$ line appears slightly shifted in wavelength between the HEG and the MEG spectra, due to calibration uncertainties or noise in the MEG spectrum. Between 4 Å and 6.2 Å there is a calibration mismatch between the HEG and the MEG spectra. The thick line is for the model with broadened emission lines, the thin line is the same model but without broadened emission lines.
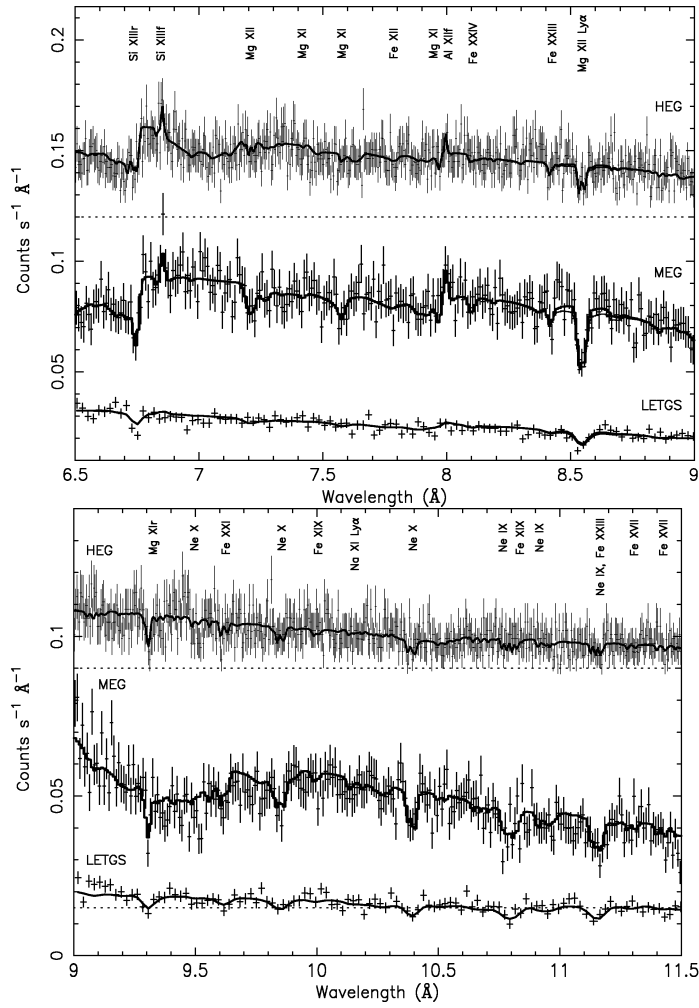
Figure 5.12: Continued.
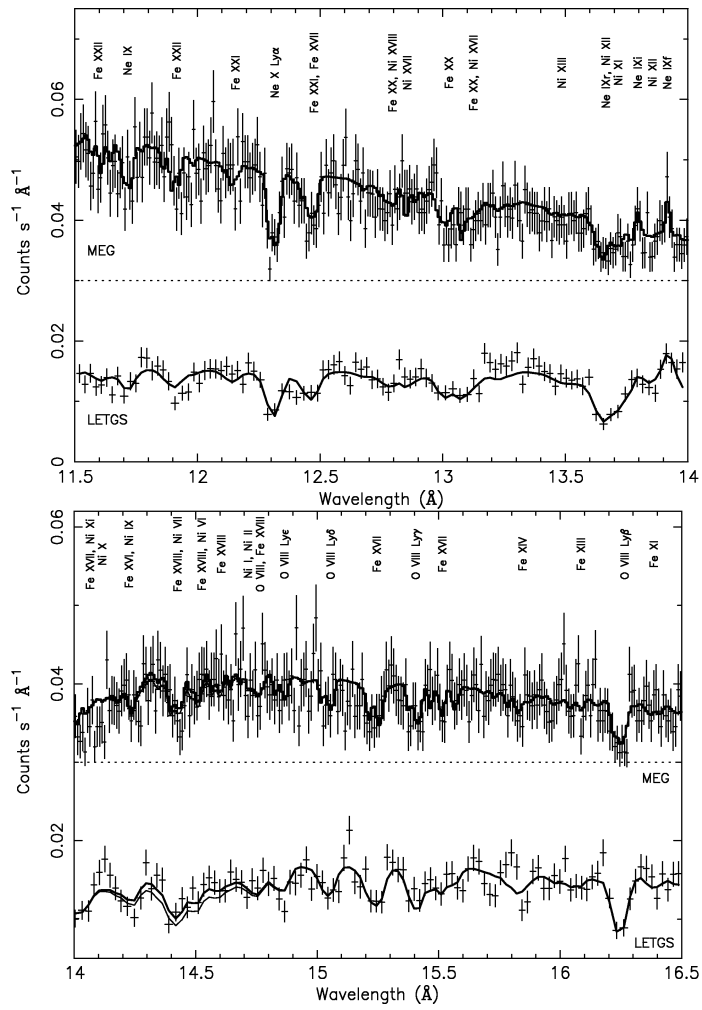
Figure 5.13: Continued.
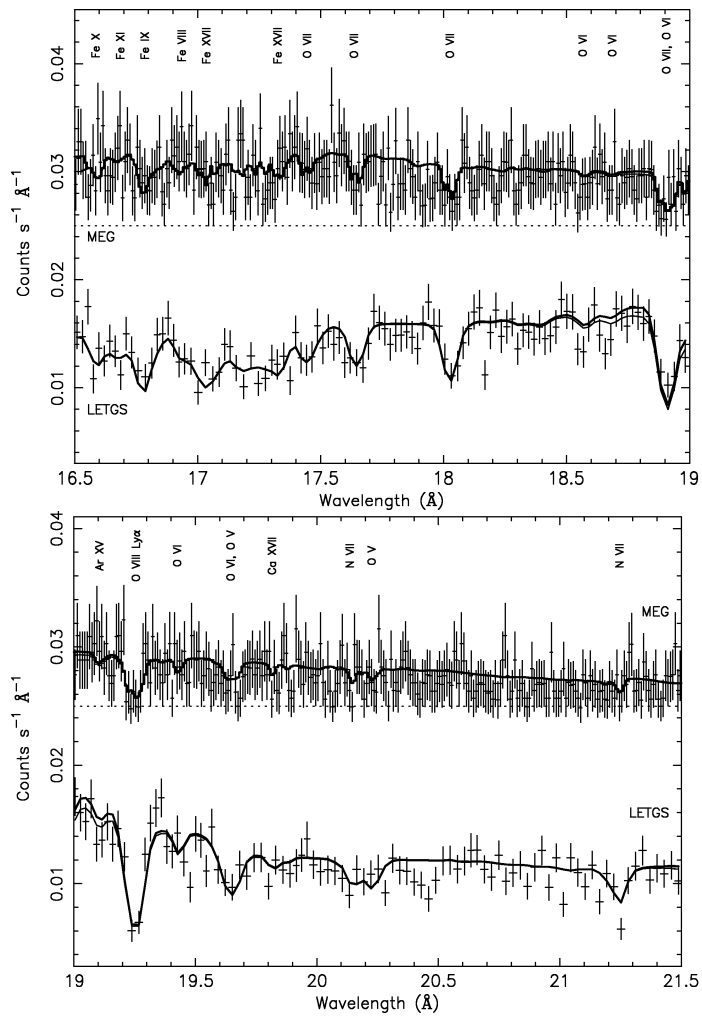
Figure 5.14: Continued.
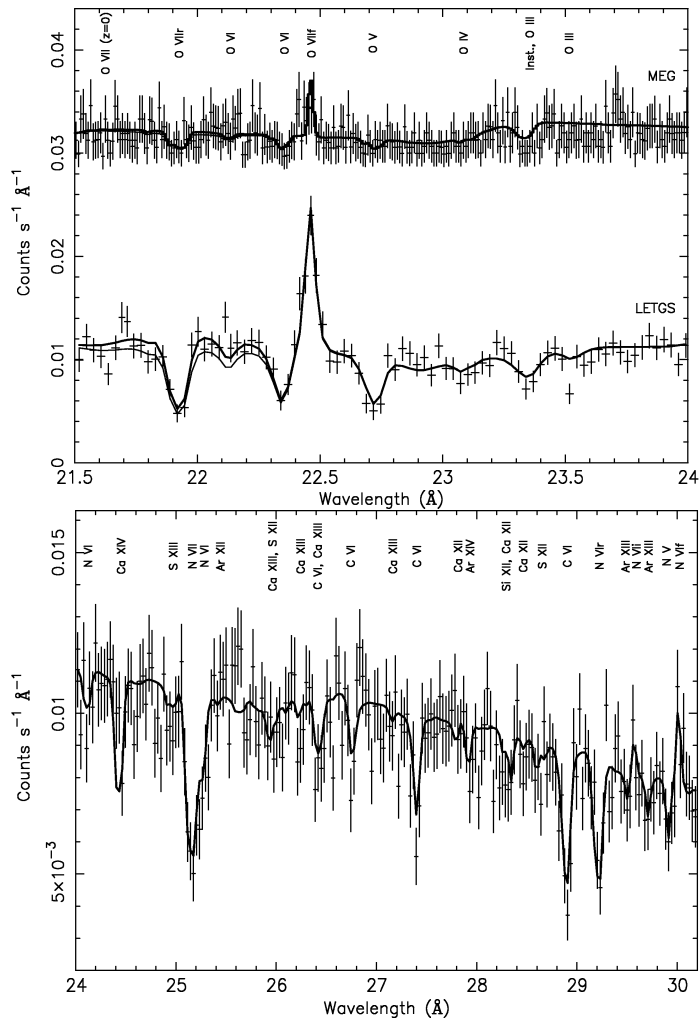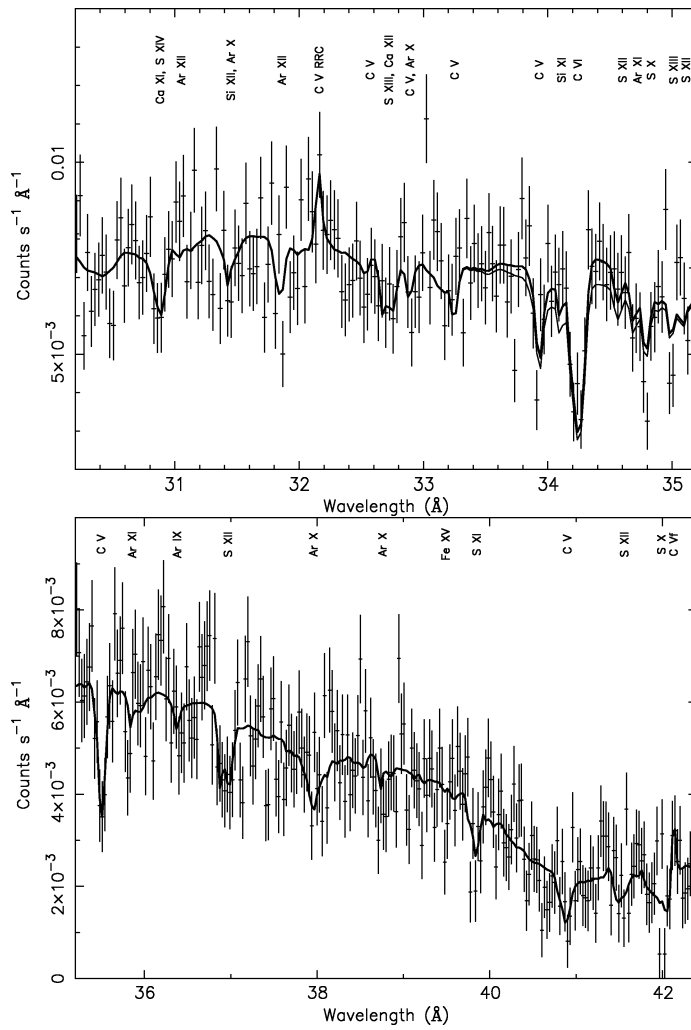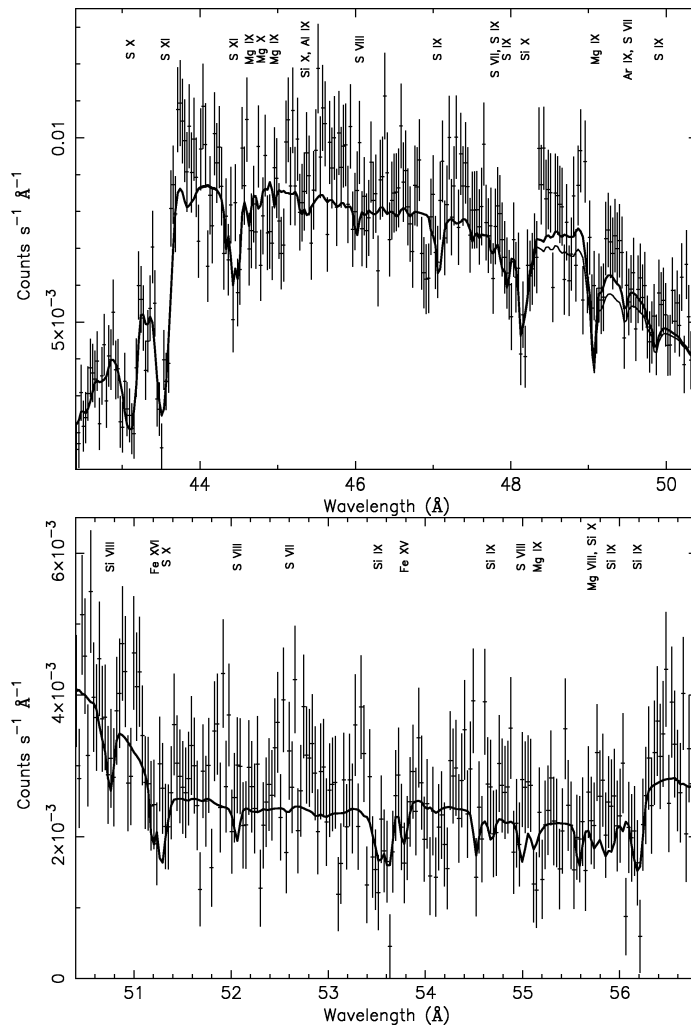
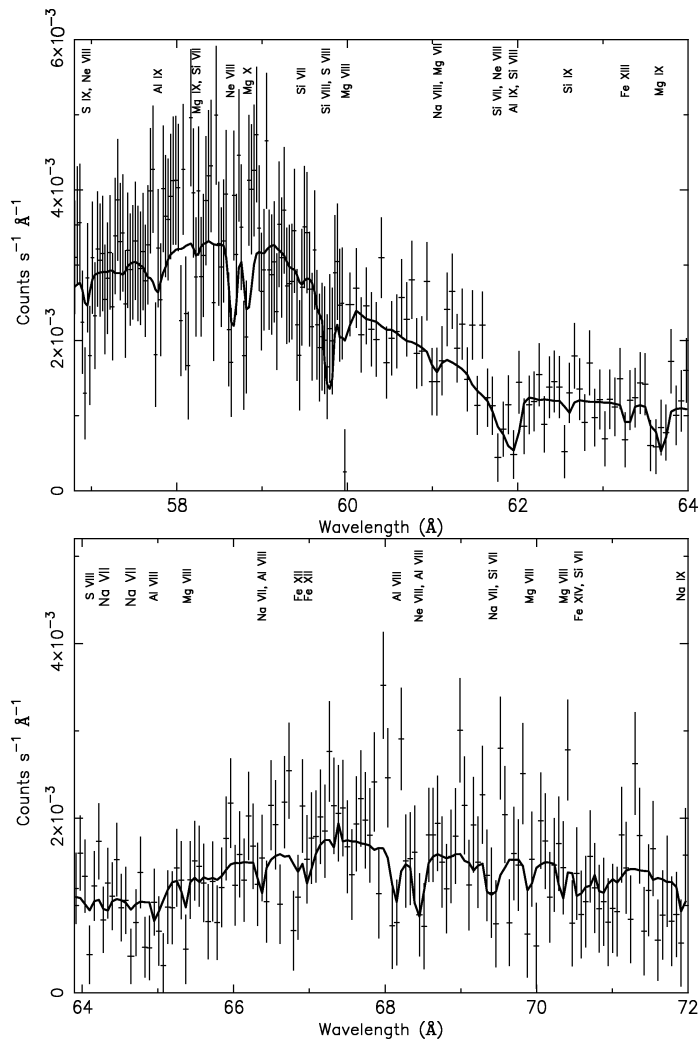Figure 5.15: Continued.

Figure 5.16: Continued.

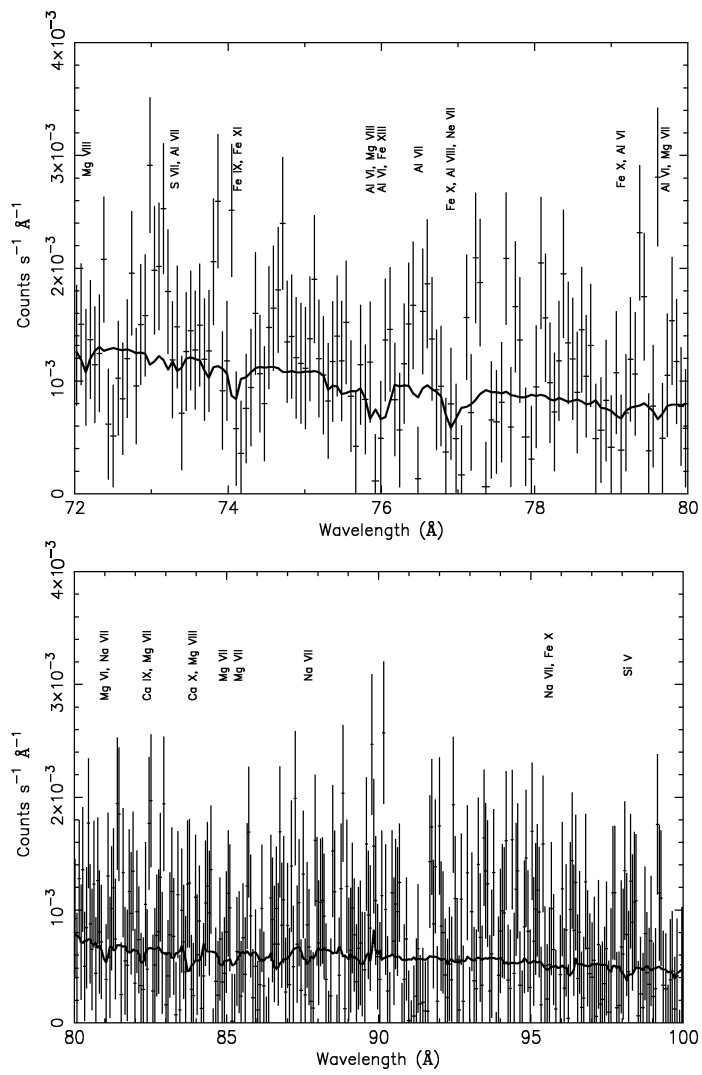Figure 5.17: Continued.

116

Figure 5.18: Continued.

Figure 5.19: Continued.

118

Chapter 6

Modeling broad X-ray emission lines observed in NGC 5548

K.C. Steenbrugge, J.S. Kaastra, D. M. Crenshaw, S. B. Kraemer, N. Arav,
E. Costantini, I. M. George

Abstract

We discuss the detection in the X-ray band of broad emission lines, similar to the broad emission lines detected in the optical and the UV bands, in the Seyfert 1 galaxy NGC 5548. Simultaneous HST STIS observations allow us to model the line strengths measured in the X-ray and the UV band. We determined how the line luminosity is dependent on the input parameters and assumed spectral energy distribution. Unless the density is very high or the covering factor rather low, differences in density, covering fraction and elemental abundances and column density were negligible in both codes. Also the spectral energy distribution used has a negligible effect on the line luminosity predictions. To restrict the possible parameter space, we assumed that the broad line clouds were at a distance of either 2 light days (shortest reverberation distance) or 20 light days (reverberation distance of the Hβ line). We can model the lines with a cloud with one ionization parameter, which is the same for both distances. However, the total column density and the covering factor are larger for the 2 light-day models. This suggests that the region has a density stratification by a factor of 100, rather than an

ionization stratification. The ten times larger total column density and 2.5 times larger covering factor are consistent with a our line of sight crossing the edge of a cloud.

6.1 Introduction

In 1943 Seyfert detected broadened emission lines in the optical spectra in the centers of nearby galaxies. These AGN are now called Seyfert galaxies, and have line widths of several thousands to tens of thousands of km s^{-1}. These emission lines are now used to classify active galaxies as Seyfert galaxies; and they have been well studied in the optical and UV range of the spectrum. Variability studies of these broad emission lines (BEL's) spanning several years found that the lines are variable. The Broad Line Region (BLR) is spatially unresolved using ground based telescopes. However, reverberation mapping (Blandford & McKee 1982) allows for a determination of the size of the BLR, which span a range from a few light-days to light-months.

The broadening of these emission lines is generally thought to be due to the Doppler effect as originally suggested by Seyfert (1943). In the scenario of McKee & Tarter (1975) the broad emission lines are the result of a large number ($\gg 10^6$) of clouds in Keplerian rotation around the central super-massive black hole. The main problem with this scenario is that in high signal-to-noise cross-correlation studies of the broad lines in the UV band, no correlation signal in emission line profile was detected. Further, any line profile variations are not correlated to continuum variability and the velocity fields are not dominated by radial motion, as there is no correlation between the time lag observed and the radial velocity (Peterson 1994). In the case of NGC 4151, the lack of correlation signal in the line profiles in the cross-correlation of high signal to noise spectra, puts a lower limit on the number of clouds of 3×10^7 (Arav et al. 1998). This number exceeds, by an order of magnitude, the number of clouds expected from photoionization models (Arav et al. 1998). If the clouds are small, as required from the large number of clouds and the small measured covering fraction, the radiation pressure should dominate over the gravitational force, as radiation pressure is inversely related to the radius of the cloud. This means that the clouds should form an outflow, which is not observed (Peterson 1994). However, there is not yet a good alternative to the clouds model.

Until the advent of XMM-*Newton* and *Chandra* such broad emission lines were not detected in the X-rays. XMM-*Newton* detected relativistically broadened emission lines in several AGN (Lyα lines from hydrogenic CNO, Branduardi-Raymont et al. 2001; Fe Kα, Wilms et al. 2001) similar to the first Fe K lines discovered by ASCA (Tanaka et al 1995). However, these lines are formed very close to the black hole, in a different region from the BLR, and will not be discussed in this paper. The first de-

tection of a broad emission line in the X-ray band was the C VI Lyα line found in a 90 ks exposure of NGC 5548 with the Low Energy Transmission Grating spectrometer (LETGS) onboard of *Chandra* (Kaastra et al. 2002a). A later XMM-*Newton* observation of the same source in a brighter state did not show such a broad emission line, probably because the higher flux level further decreased the contrast level. A C VI Lyα broad emission line was detected in the spectrum of NGC 4051, which is dominated by relativistically broadened emission lines from O VIII (Ogle et al. 2004). Also in Mrk 279 several broad X-ray emission lines have been detected (Costantini et al. 2005).

For NGC 5548 photoionization and variability studies of the optical broad emission lines have shown that a single zone emitter is insufficient for proper modeling the BLR (Peterson 1994). A stratified zone with either a constant ionization parameter U or constant density n is adequate to fit the lowly ionized versus highly ionized UV broad emission line ratios. From an analysis of the time variability, a constant ionization model better describes the broad line emitting clouds (Goad & Koratkar 1998). In this scenario the density is proportional to r^{-2}, with r the distance from the ionizing source. From reverberation mapping the BLR size of NGC 5548 is found to range between 2 ld, the timescale on which variability is detected in He II (Peterson & Wandel 1999) and 20 ld, the timescale of variability in Hβ (Peterson et al. 1994). The covering fraction is about 30 %, higher than the standard 10 % (Goad & Koratkar 1998). In this paper we investigate whether the higher ionized X-ray lines can be modeled with one ionization parameter and are formed at the same distance, or whether multiple ionization parameters are necessary.

In this paper we analyze the broad emission lines which are observed in a 540 ks *Chandra* observation of NGC 5548 and a simultaneous HST STIS observation. As a result we can model both the X-ray and UV broad emission lines together. In Sect. 6.2 an overview of the analysis of the continuum spectrum and the warm absorber observed in the X-rays and the UV band is given. In Sect. 6.3 we discuss the detection and fitting of the broad emission lines in both spectral bands. The model predictions obtained from XSTAR 2.1h (Kallman & Krolik 1999) and CLOUDY 95.06 (Ferland 2002) are detailed and compared to the measured line luminosities in Sect. 6.4. In Sect. 6.5 we discuss the results obtained from both codes and list the conclusions.

6.2 The X-ray and UV spectrum of NGC 5548

NGC 5548 was observed for a full week with the *Chandra* High Energy Transmission Grating Spectrometer (HETGS) and the Low Energy Transmission Energy Grating (LETGS) in January 2002. Simultaneous HST STIS observations were obtained,
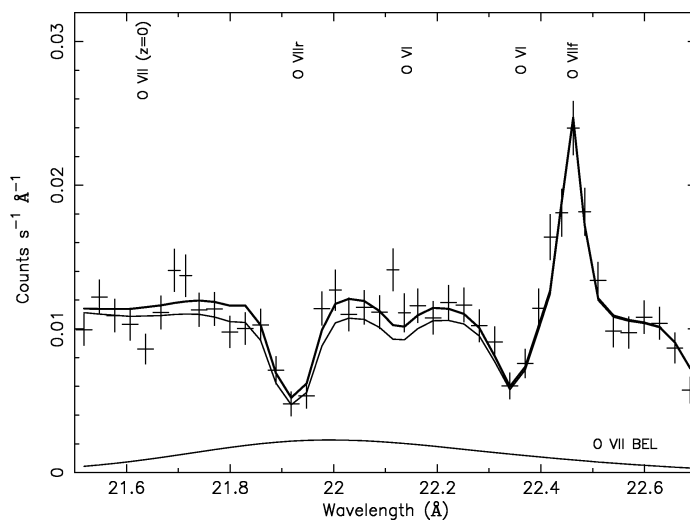
Figure 6.1: Detail of the LETGS spectrum showing the fit with (thick line) and without (thin line) a broad emission line for the O VII resonance line. The profile of the O VII broad emission line is also plotted.

and the analysis of the UV absorber is discussed by Crenshaw et al. (2003). A full analysis of the X-ray spectrum is given by Steenbrugge et al. (2004). We refer to that paper for full details about the analysis, a description of the warm absorber fitting and modeling of the continuum. No spectral variability in the warm absorber was detected and therefore the full dataset was used in order to maximize the signal to noise ratio.

The continuum of NGC 5548 was fit by a power-law and a modified black body component (Kaastra & Barr 1989) corrected for Galactic extinction ($N_H = 1.65 \times 10^{24}$ m^{-2}, Nandra et al.1993) and a cosmological redshift of 0.01676 (Crenshaw & Kraemer 1999). An excellent fit to the spectra was obtained using either an absorption model with three outflow velocities (model A of Steenbrugge et al. 2004) or an absorption model with a power-law distribution of the hydrogen column density N_H versus the ionization parameter ξ (model D). As found earlier (Steenbrugge et al. 2003) the higher ionization gas in NGC 5548 has a higher total hydrogen column density than the lower ionized gas. The final model includes some narrow emission lines, most notable the O VII forbidden line and the Fe Kα line.

122

6.3 Broad emission lines

6.3.1 X-ray broad emission lines

The data show a clear broad excess over the spectral fit (thin line Fig. 6.1) at the O VII triplet wavelength (see Fig. 6.1). Broad excesses at other wavelengths are also observed, but they are weaker.

From UV spectra it is clear that these broad lines have complex shapes, and each line can have a different width and line profile (Arav et al. 2002). Due to the lower spectral resolution and signal to noise ratio of the *Chandra* spectra as compared with the optical and UV band spectra, we need to constrain the fit for the broad lines. The broad excesses were fit with Gaussians, leaving the normalization as a free parameter, but freezing the energy to the rest energy of the line and the full width half maximum (FWHM) to 8000 km s^{-1}. This FWHM was taken from Arav et al. (2002) for the broadest component of C IV and Lyα emission line. Kaastra et al. (2002a) measure a FWHM of 10600 km s^{-1} $\pm$ 3300 km s^{-1} for the C VI Lyα line in an earlier LETGS observation of NGC 5548, consistent with the value adopted here. In Table 6.1 we summarize the measured flux, luminosity (L), and Equivalent Width (EW) for the observed lines in the *Chandra* spectra.

The most pronounced of these broad emission lines in the X-rays is the one centered on the O VII triplet. This is in agreement with expectations as oxygen is the most abundant metal and the resonance, intercombination and the forbidden line produce one broad blend. The spectral separation between the triplet components of 0.2−0.3 Å is small compared to the intrinsic FWHM of the lines (0.6 Å). Therefore it is not possible to derive the intensity of the three broad lines individually. In the further analysis we will use the value centered on the recombination line, with the caution that this could under-predict the flux from the triplet as we held the FWHM frozen in the fit. Using the observed broad emission lines we can study the ionization distribution of the BLR. We do not detect highly ionized broad emission lines, evident from the lack of excess at the wavelengths around the Ne IX and Si XIII triplet, and Ne X and Si XIV Lyα lines.

6.3.2 UV broad emission lines

HST performed near simultaneous observations during this observing campaign, allowing to fit the UV and X-ray broad lines simultaneously. The UV broad emission lines in NGC 5548 are known to vary on timescales as short as a few days. As the *Chandra* campaign lasted for a week and we added all the X-ray data to detect the broad emission lines, this might cause complications in the analysis. In contrast the HST observations were shorter, and they are spread over 2 days, at the end of the X-ray

Table 6.1: Flux and the luminosity of the broad emission lines, from the simultaneous LETGS, Medium Energy Grating (MEG) and High Energy Grating (HEG) fit. The wavelength was frozen to the rest wavelength of the line, while the FWHM was frozen to 8000 km s^{-1}.

ion	λ (Å)	flux (ph m^{-2} s^{-1})	EW (mÅ)	log L W
C v f	41.421	1.0 ± 0.6	300 ± 180	34.2 ± 0.4
C v[a]	40.268	< 0.6	< 230	< 33.8
C vi	33.736	0.5 ± 0.2	150 ± 80	33.8 ± 0.2
N vii	24.781	< 0.05	< 70	< 32.9
O vii[b]	21.602	0.56 ± 0.13	130 ± 40	34.1 ± 0.1
O viii	18.969	0.4 ± 0.2	60 ± 30	33.4 ± 0.3
O vii	18.627	0.19 ± 0.07	70 ± 30	33.5 ± 0.2

[a] This coincides with the instrumental C-edge, and could be due to possible calibration uncertainties.
[b] The resonance, intercombination and forbidden line significantly overlap and are fit as one blend.

observations.

We fit the UV broad lines using multiple Gaussians, leaving the normalization, the wavelength as well as the FWHM free parameters. We did not attempt a detailed profile fitting, rather we focused on obtaining reliable flux measurement for these lines so as to be able to model them with the photoionization codes. Table 6.2 lists the rest wavelength, the measured wavelength, flux and luminosity for the UV broad emission lines.

In the UV the O iv and Si iii lines substantially overlap and thus we only list one flux value for this blend, although separate fluxes are given by Goad & Koratkar (1998). Also the 1218 Å O v, the 1215 Å He ii, the 1221 Å Fe ii and 1216 Å Fe xiii lines, and the 1216 Å Lyα line form a blend, and are reported as a blend. For the 1640 Å He ii and 1892 Å Si iii] lines we list an upper limit, as it is hard to deblend the narrow from the broad line component. For both lines the width of this line is smaller than the width of the other detected broad emission lines.

Table 6.2: The rest wavelength from Kelly (1987a, 1987b), with the exception of Mg II which was taken from CLOUDY, the measured wavelength, λ_{rest}, the fluxes and luminosities for the broad UV lines are listed. The errors in the listed luminosities are estimated to be 0.2 in log of the line luminosity, as systematic errors in continuum fit will dominate the errors in fluxes or luminosities.

ion	λ_{Kelly} Å	λ_{rest} Å	flux 10^{-15} W m^{-2}	log L W
Lyα, O V	1216, 1218	1222	2.8	35.6
He II, Fe II	1215, 1221	1222	2.8	35.6
Fe XIII	1216	1222	2.8	35.6
N V	1240	1239	0.5	34.8
Si IV, O IV]	1398, 1403	1398	0.3	34.5
N IV	1487	1485	0.1	33.9
C IV	1549	1547	3.8	35.7 5
He II[a]	1640	1639	0.09	33.8 5
O III	1666	1661	0.2	34.3
Si III][a]	1892	1891	0.02	33.3
C III]	1909	1903	0.6	34.9
Mg II	2798	2800	1.0	35.1

[a] This line is rather narrow and difficult to deblend from the narrow component. The measured line flux and luminosity is an upper limit.

6.4   Modeling the broad emission lines

We modeled the broad emission lines with two photoionization codes: XSTAR version 2.1h (Kallman & Krolik 1999) and CLOUDY version 95.06 (Ferland 2002).

In modeling the broad lines we used the same Spectral Energy Distribution (SED) (labeled Steenbrugge et al. in Fig. 6.2) as was used to study the warm absorber using the simultaneous HST-STIS spectra (Crenshaw et al. 2003) and *Chandra* spectra (Steenbrugge et al. 2004). As there is no evidence for a blue bump in the UV spectra, this bump was not included in our SED. For the X-ray part of the SED we used the continuum of the present LETGS spectrum. For the high energy part of the SED we used a power law component as measured in our *Chandra* spectrum but with an exponential cut-off at 130 keV, consistent with the previous Beppo*SAX* data (Nicastro et al. 2000). We did not include a reflection component in our SED, because the *Chandra* spectrum could not constrain it. Between 50 and 1000 Å we used a power-law and at even longer

wavelength we used the energy index of 2.5 adopted by Dumont et al. (1998).

For comparison we also plot in Fig. 6.2 the SED used by Goad & Koratkar (1998). The SED Goad & Koratkar (1998) has a lower high-energy cut-off of 65 keV (0.19 Å); and a higher low-energy cut-off of 1.2 eV(10^4 Å), thus producing less infrared radiation. The different results obtained for these different SEDs gives a good indication of how the ionization balance depends on the assumed SED, and will be discussed later.
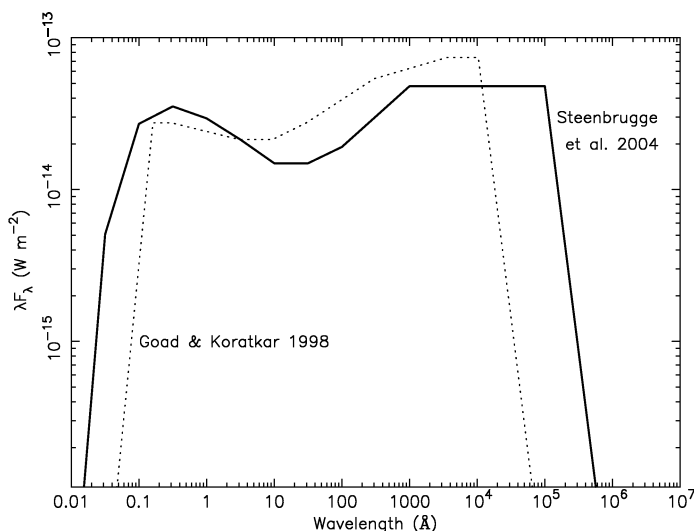

Figure 6.2: The SED used in the present analysis (solid line) and that used by Goad & Koratkar (1998) (dotted line).

As a starting point we took the ionization parameter, total hydrogen column density, density and temperature as deduced from the UV measurements of Goad & Koratkar (1998). We assumed their low state ionization parameter of $\log U = -0.6$ or $\log \xi = 1$ in units of 10^{-9} W m which will be used throughout the paper. In both codes we used the standard solar abundances as given in the CLOUDY code. In XSTAR only the following elements are included: H, He, C, N, O, Ne, Mg, Si, S, Ar, Ca, Fe and Ni, while CLOUDY lists all elements up to zinc. This difference is not expected to change the temperature structure of the gas and thus the ionization balance significantly. CLOUDY uses the values given in Grevesse & Sauval (2001) solar abundances, with the exception of C and O, for which it uses Allende Prieto et al. (2001, 2002), and N, Ne, Mg, Si and Fe, for which it uses Holweger (2001). In all models we assumed a

source luminosity of 1.91×10^{37} W (Goad & Koratkar 1998).

Goad & Koratkar (1998) list a broad Fe II feature at 2798 Å, but neither XSTAR nor CLOUDY list an Fe II line at 2798 Å. The measured luminosity should be used as an upper limit to the predicted value, if indeed there is an Fe II line at this wavelength. The Fe II and Fe XIII lines at 1216 Å are not included in XSTAR.

6.4.1 CLOUDY

As an initial trial we again used the parameters derived by Goad & Koratkar (1998) for the low luminosity state to model the broad lines. We will call this model the standard model, although this model shows large discrepancies with the data (see Fig. 6.3 and Table 6.3). Certainly for the X-ray lines, which are the lines with lower predicted luminosities, the match is poor. Most of the UV line luminosities are over-predicted; this is especially the case for N IV (1487 Å), Si III (1892 Å), He II (1640 Å) and O III (1666 Å). To investigate the sensitivity of these differences to the SED, we used the SED used by Goad & Koratkar (1998) instead of our own SED. The luminosities (triangles in Fig. 6.4 and model 3 in Table 6.3) are consistent with the results from the standard model within the measurement errors. Therefore the difference in SED can not explain the poor match.

Another difference may be the version of CLOUDY that is used. In model 2 (Table 6.3), we replace version 95.06 by the older 94 version (open diamonds in Fig. 6.4). The predictions of both versions of CLOUDY are shown in Fig. 6.3. This indeed gives some rather large differences, especially for the O VII triplet, the C V forbidden line and the Lyα blend. However, these differences can not explain the discrepancies obtained for some of the UV lines. Even if we use the UV fluxes as quoted by Goad & Koratkar (1998) we obtain poor agreement, although the agreement is better than with our present measurements.

A very important difference between the two versions of CLOUDY, is that the 94 version does not contain the O V line at 1218 Å. In the 95.06 version this line has a substantial flux, for the input parameters considered. The presence of this line, as well as possible S X, Fe XIII and Fe II can change the ionization parameter estimate for the broad line gas. Another difference occurs for the O VII triplet, where the 94 version had only two lines, with the total triplet luminosity three orders of magnitude weaker. This clearly indicates that the parameters as listed by Goad & Koratkar (1998) are probably not the best set to be used to model the X-ray and UV broad emission lines using the 95.06 version.

In order to be able to explain the measured line luminosities we need to understand how the predicted line luminosities change with varying parameters. Fig. 6.4 shows a comparison between our standard model (see Table 6.3 for a list of the input param-

Table 6.3: The measured luminosity (first column) versus the predicted luminosity for some of the different models described in the text. The standard model is indicated by the model name stan. CL stands for CLOUDY, XS for XSTAR. Our SED is shown as Steenbrugge et al. 2004, GK as Goad & Koratkar 1998 in Fig. 6.2. r is the distance of the cloud from the ionizing source, n the density of the gas, N_H the total column density, C_f is the covering factor.

	meas.	stan.	2	3	4	5	stan.	7	8	9
code		CL	CL	CL	CL	CL	XS	XS	XS	XS
vers.		95.06	94	95.06	95.06	95.06	2.1h	2.1h	2.1h	2.1h
SED		our	our	GK	our	our	our	GK	our	our
r (ld)		17	17	17	20	2	17	17	20	2
n^a		1	1	1	0.48	48	1	1	2.4	240
$N_H{}^b$		1	1	1	1	10	1	1	0.05	1
C_f		0.38	0.38	0.38	0.20	0.50	0.38	0.38	0.20	1.0
ξ		10	10	10	15	15	10	10	3	3
ion	log L (W)	log L (W)	log L (W)	log L (W)	log L (W)	log L (W)	log L (W)	log L (W)	log L (W)	log L (W)
C v f	34.2	33.9	31.5	33.6	33.8	32.4	34.9	34.9	34.5	34.6
C v	< 33.8	33.1	31.5	33.2	32.9	33.2	33.7	33.7	33.9	34.5
C vi	33.8	33.2	33.3	33.4	33.1	33.5	34.3	34.2	33.8	34.2
N vii	< 32.9	32.4	32.4	32.5	32.3	32.8	33.4	33.3	32.8	33.2
O vii t	34.1	34.8	31.9	34.9	34.7	35.1	35.0	35.0	34.3	34.6
O viii	33.4	32.7	32.7	32.8	32.7	33.2	33.8	33.6	32.8	33.2
O vii	33.5	32.0	31.7	32.0	31.8	32.4	33.5	33.5	31.0	32.6
Lyα	35.6	35.0	34.4	35.1	35.7	35.5	36.2	36.2	35.6	35.6
N v	34.8	35.0	34.9	35.0	34.6	35.2	34.7	34.4	34.9	35.1
Si iv	34.5	35.1	35.1	35.0	34.6	35.1	35.6	35.5	34.7	35.3
N iv	33.9	34.7	34.6	34.6	34.4	34.2	34.5	34.5	33.8	33.4
C iv	35.7	35.9	35.9	35.9	35.6	35.5	35.8	35.8	35.7	35.4
He ii	33.8	34.8	34.6	34.9	34.2	34.7	35.7	35.6	34.7	35.5
O iii	34.4	35.2	35.2	35.1	34.8	34.5	34.4	34.3	33.4	33.8
Si iii]	33.3	34.5	34.7	34.2	33.3	33.3	33.3	33.0	31 3	33.5
C iii]	34.9	35.2	35.2	35.1	34.9	33.5	34.1	33.9	33.0	33.2
Mg ii	35.1	34.2	34.2	34.2	33.4	33.5	34.4	34.3	31.0	34.5

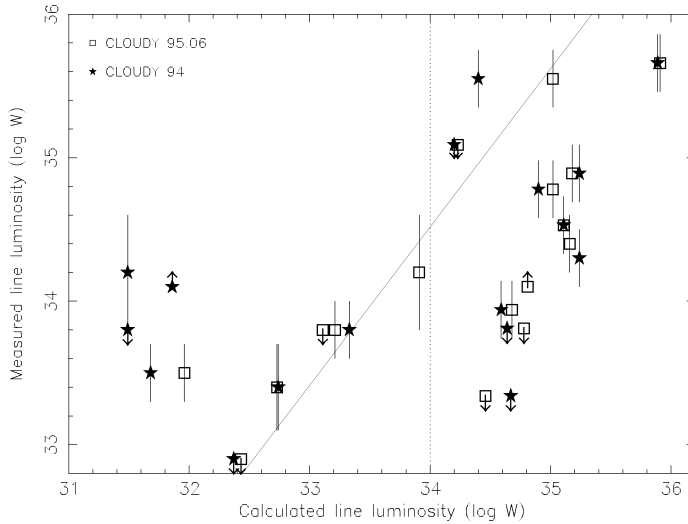^{a} in 10^{16} m^{-3}.
^{b} 10^{27} m^{-2}.

Figure 6.3: Comparison of the line luminosities calculated by CLOUDY versions 95.06 (open squares) and 94 (filled stars) and the measured line luminosity. All the lines for which CLOUDY 95.06 predicts less than 10^{34} W are X-ray lines. The lines to the right of the dotted line are UV lines with the exception of the O VII triplet. The solid line indicates a perfect match. Note that the match is rather poor for both versions of CLOUDY, even if the X-ray lines are ignored.

eters and predicted line luminosities) and other models tested. Note that the effect of covering factor (open squares), which we changed from 0.38 to 1, and the assumed SED (open triangles) are very minor on the calculated line luminosities. However, the covering factor does become important for lower covering factor values or higher ionization parameters. Also a model with lower density, but larger radius, such that the ionization parameter is the same (open circles), gives similar results as the standard model. This indicates that most line strengths are only weakly or not at all dependent on density. This is expected, as otherwise the density would be a known parameter. The spread in line luminosities for variations in ionization parameter are up to several orders of magnitude larger, the model with a lower ionization parameter (slanted crosses) or significantly higher ionization parameter (stars) give deviating line luminosities. A moderate increase in ionization parameter (crosses) is detectable in a few lines.

From Fig. 6.3 and Fig. 6.4 it is clear that a higher ionization parameter is needed to fit the measured luminosities. Namely, the luminosities measured in the X-rays are
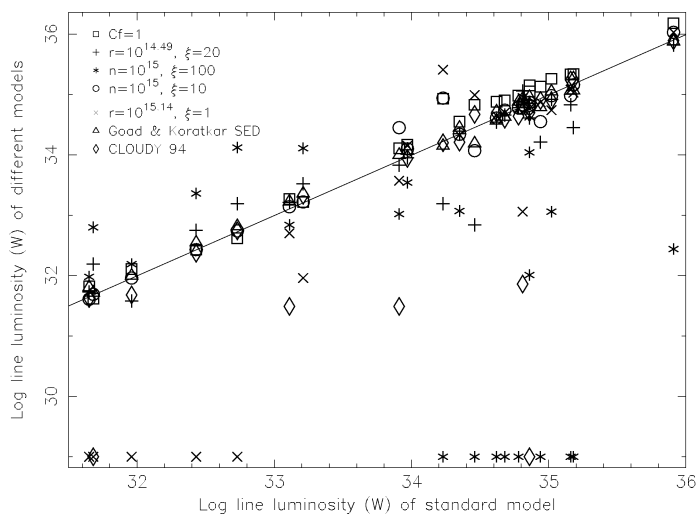
129

Figure 6.4: A comparison of the line luminosities as calculated by the standard model (see Table 6.3) and other models. Open squares denote a covering factor of 1, crosses for a radius of 12 ld, resulting in a higher ionization parameter of $\xi = 20$. Asterisks denote a lower density, namely 10^{15} m^{-3}, resulting in an ionization parameter of $\xi = 100$. Open circles denote a 10^{15} m^{-3} density, but with a radius of 53 ld and thus $\xi = 10$. The slanted crosses are for a radius of 53 ld, with a density of 10^{16} m^{-3} and thus $\xi = 1$. Finally the triangles depict the SED assumed by Goad & Koratkar (1998) and the diamonds are for the standard input parameters, but for CLOUDY version 94. A value of log $L = 10^{29}$ W indicates that this value was not calculated by CLOUDY in this particular run. The solid line indicates where the line luminosity are equal for both models.

underpredicted, while those in the UV are overpredicted. To have a physical basis, we made models for a distance of 2 light days (ld), the shortest distance listed from reverberation mapping of He II (Peterson & Wandel 1999); and 20 light days, the distance obtained from reverberation mapping of Hβ (Peterson et al. 1994). For both assumptions we can model the measured broad emission lines with one ionization parameter, $\xi = 15$. The resulting match for both distances is plotted in Fig. 6.5.

In the case of a distance of 20 ld, we can model the observed line luminosities rather well with one ionization parameters (open squares in Fig. 6.5). There is actually a range in density (and thus ionization parameter) for which we obtain a reasonable

match. In the case of a distance of 2 ld (open stars in Fig. 6.5), the match is worse. If only one ionization parameter is assumed, there are always several ions poorly fit. This worsening in fit is solely dependent on the large density necessary for such a short distance. For the 2 ld match we need to increase the total hydrogen column density by a factor of 10 and the covering factor by a factor of 2.5, as otherwise the line luminosities are systematically underpredicted. This underprediction holds for all the lines, and cannot be improved by a change in ionization parameter. A line luminosity that is overpredicted in all models is the He II line at 1640 Å, which is the only line that is variable on timescales as short as 2 ld (Peterson & Wandel 1999). The O VII triplet is also consistently overpredicted, but this seems the result of not implementing all triplet processes in the CLOUDY code. As we will see later, XSTAR finds a better match. If we assume the SED used by Goad & Koratkar (1998), we find a very similar match, thus confirming that a different SED only changes the predicted line luminosities slightly.

It thus would seem that one needs at least 2 different ionization parameters to model the line luminosities, if one assumes the lines are formed at a distance of only 2 ld. However, from reverberation mapping we know that most lines are formed further out. Thus the density is substantially smaller, and the line luminosities are less dependent on density effects. Assuming a two ionization model, we have the problem that one ionization parameter already produces too much He II. He II is one of the ions that is formed over a large range in ionization parameter. To reduce the He II line luminosity, we would need to have a substantially higher ionization parameter. However, the limit to the ionization parameter is set by the lack of highly ionized X-ray lines. Both conditions make a two ionization parameter model less likely. A possible explanation for the overprediction in He II line luminosity is that the line is more readily destroyed than currently assumed. An interesting difference between the models for 20 ld and 2 ld is that, due to the larger covering factor and higher density in the 2 ld model, a part of the 1216 Å broad emission line should be due to Fe II. This line is not included in the 20 ld model.

6.4.2 XSTAR

We followed a similar approach in modeling the broad emission lines using XSTAR as for CLOUDY. First we used the input parameters listed by Goad & Koratkar (1998) but with our SED, called the standard model (Table 6.3). In Fig. 6.6 we plot the calculated and measured line luminosity. The match is similarly poor to that obtained with CLOUDY. The match to the UV data is not as good as with CLOUDY; however, the match to the X-ray data is significantly better than with CLOUDY. In general XSTAR overpredicts the UV line luminosities, but from Fig. 6.6 a one ionization parameter
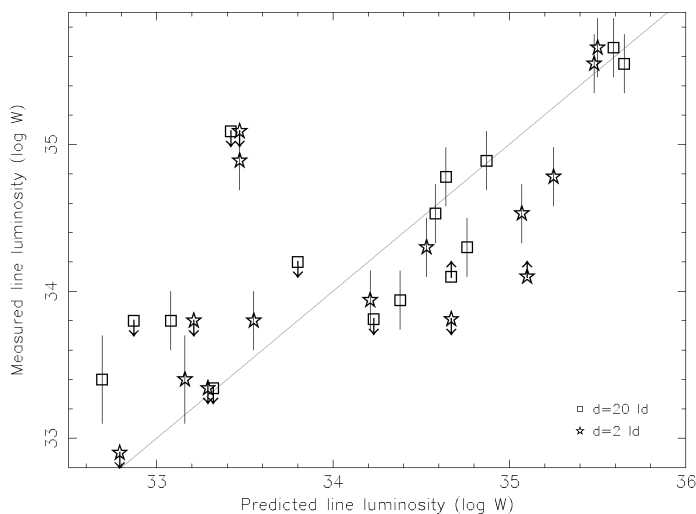
Figure 6.5: Results for our best match between line luminosities predicted by the CLOUDY code and the measured line luminosities. The open squares are for a cloud at a distance of 20 ld, the open stars are for a distance of 2 ld. The parameters are listed in Table 6.3, model 4 and 5. The O VII triplet is indicated as a lower limit (see text), the Mg II line, probably a blend is indicated as a upper limit. The other upper limits are measured upper limits.

model seems plausible.

For XSTAR we also compared our standard model with other models which have one parameter altered (see Fig. 6.7). The difference in abundances used (open stars), the SED used (open triangles) or a lower density (open circles) do not alter the predicted line luminosities. The difference in covering fraction (open squares) is larger than in the study with CLOUDY, albeit still rather small. Similar to the results obtained with CLOUDY the difference in ionization parameter (crosses, slanted crosses and asterisks) give the largest differences in line luminosities. In general the differences in predicted line luminosity with XSTAR are similarly dependent on the input parameters, as with CLOUDY.

We generated models for cloud distances of 20 ld and 2 ld with XSTAR. To start, we took the parameters for our best match obtained with CLOUDY for a distance of 20 ld. The XSTAR-predicted line luminosities in this case give a rather poor match to the measured line luminosities. Most noticeable are the discrepancies for the 1640 Å He II
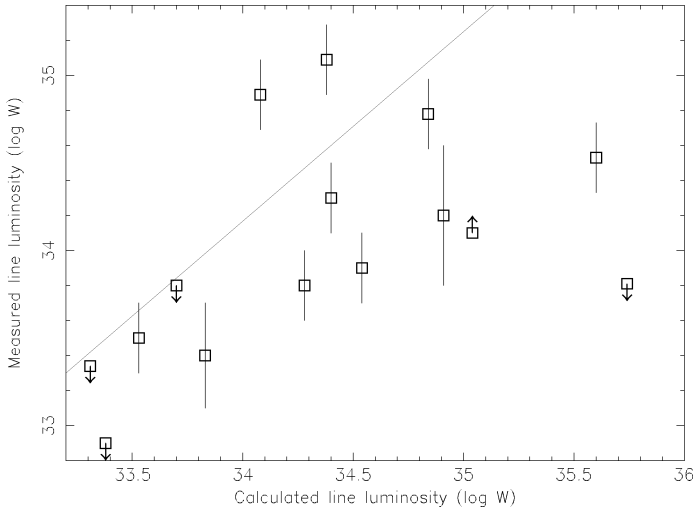
Figure 6.6: The XSTAR calculated line luminosities for the standard model versus the measured line luminosities. Note that the match for the predicted weaker lines, mostly X-ray lines, is decent, but that the match for the lines predicted to have larger luminosities is poor.

line, the 1487 N IV line, the O VII triplet, the 1216 Å blend and the blend due to Si IV and O IV at about 1400 Å. This is in line with the difference in predicted luminosities for the standard model (see Fig. 6.8). In general, from Fig. 6.6 we find that an ionization parameter similar to the value in the standard model or lower is required.

For a distance of 20 ld, our best model (Table 6.3 model 8 and Fig. 6.9) predicts indeed a rather low ionization parameter of $\xi = 3$ (log $\xi = 0.477$), with a lower total column density. A change in ionization parameter at such a low ionization parameter, is very noticeable. Even small changes in column density are noticeable, and as a result we do not have a range of possible values for a good match, unlike the results obtained with CLOUDY. Although the column density, the ionization parameter and thus the density are different from the values obtained with CLOUDY, the covering factor is similar. A large difference between XSTAR and CLOUDY is the predicted line luminosities for the C III line at 1909 Å and the O III line at 1666 Å, which are both severely underpredicted by XSTAR. Similar to the results obtained with CLOUDY, the He II line at 1640 Å is overpredicted. We need a higher ionization parameter and a lower total column density to obtain a good match for He II. However, in such models
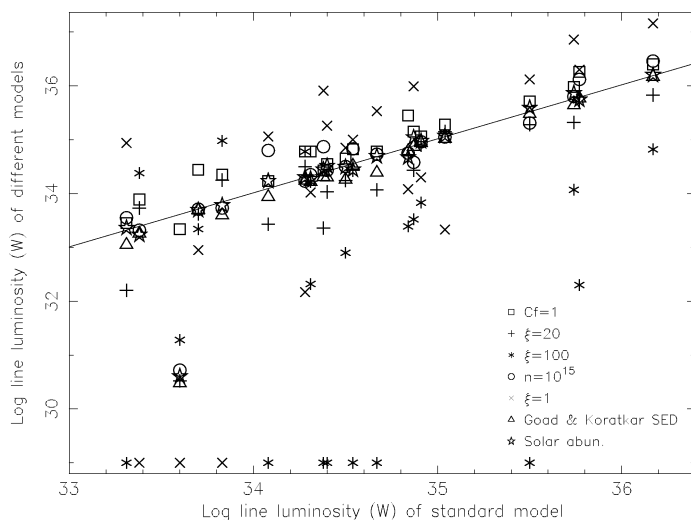
133

Figure 6.7: Comparison of the line luminosities predicted by the standard model and models with one parameter altered. In this plot O VIII is missing, due to the low predicted luminosity for the standard model. Symbols are the same as in Fig. 6.5. Open squares is for a covering faction of 1, crosses are for a ξ value of 20, asterisks for ξ = 100. Open circles are for a density of 10^{15} m^{-3}, slanted crosses for ξ = 1. Open triangles are for the SED assumed by Goad & Koratkar (1998) and open stars are for the standard solar abundances assumed by XSTAR.

the 1216 Å blend is severely underpredicted, and other broad emission lines, such as O VIII are overpredicted. Similar to our CLOUDY results, a two ionization model seems unlikely due to the limit of the highest ionization parameter possible, and the fact that He II is produced over a larger ionization range.

For the best model assuming a distance of 2 ld (Table 6.3 model 9 and Fig. 6.9), the covering factor needs to be increased. Consistent with our results from CLOUDY, a density increase of 100 does noticeably change the predicted line luminosities, and the best match covering factor and total column density are thus different for the two distances. If the column density and covering factor were not increased, the line strengths are systematically underpredicted. Also consistent with our CLOUDY result is the fact that the 2 ld model gives a poorer match to the measured line luminosities than the 20 ld model.
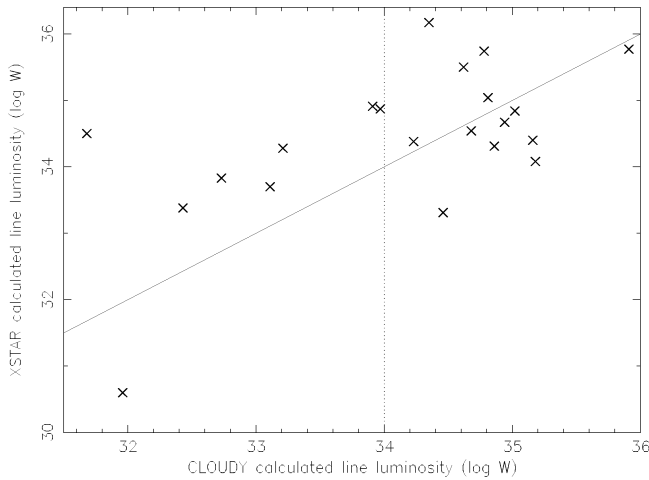
134

Figure 6.8: A comparison of the predicted line luminosities using our standard model (Table 6.3) for CLOUDY and XSTAR. The solid line indicates equal line strengths. The dotted line indicates the distinction between X-ray (with lower predicted CLOUDY luminosity) and the UV lines and the O VII triplet. Note the systematic difference between both codes for the X-ray lines, and a scatter for the UV lines.

6.5   Discussion

Comparison between CLOUDY and XSTAR

Comparing the predicted line luminosities obtained with CLOUDY and XSTAR for the standard model (see Fig. 6.8, Table 6.3), we find that XSTAR systematically predicts higher luminosities for the X-ray lines, with the exception of O VIII Lyα. The XSTAR values for the UV lines cluster around the CLOUDY values, which are larger than for the X-ra lines. However, the predicted line luminosities for individual UV lines can significantly differ between both codes. Clearly, the differences in the luminosities obtained with CLOUDY and XSTAR are larger than differences produced by possible changes in covering factor or assumed SED. This is also the conclusion we draw from comparing the difference in ionization parameter and column density obtained with both codes.

An important difference between both codes is the 1218 Å O V, the 1216 Å Fe XIII and 1221 Å Fe II lines. Not including these lines will affect the model ionization parameter obtained from the 1216 Å blend, which mostly consists of H I Lyα. This might
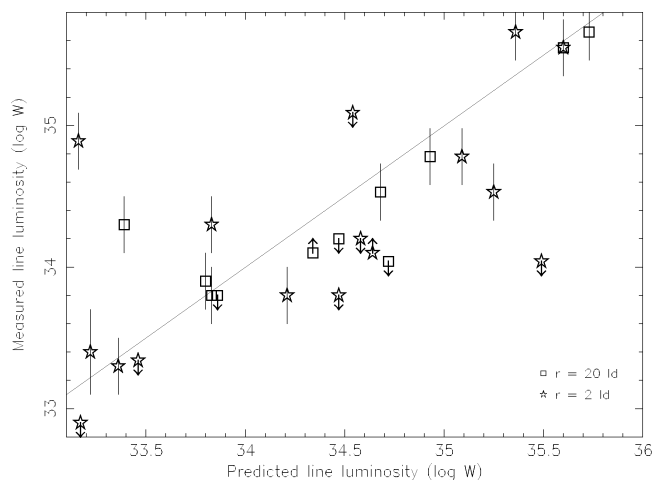
135

Figure 6.9: The best fit obtained with the XSTAR code for a distance of 20 ld (open squares) and 2 ld (open stars), for which the parameters are listed in Table 6.3 model 8 and 9. The line luminosity predictions for Si III, the O VII line at 18.63 Å and the Mg II 2798 Å line fall for the 20 ld model below $10^{32.5}$ W. Note that the differences between in line luminosities for the different distances are very similar to the differences obtained with CLOUDY (Fig. 6.5).

be the reason why XSTAR gives a lower ionization parameter. Interestingly, we find a good match to the 1216 Å blend with both codes for both distances. It is for the unblended C III and O III lines that we find a poor match with XSTAR.

To further investigate these differences, we compared how the predicted line luminosities change between the different distance models in both codes. For both codes we find an increase in covering factor, a higher column density and the same ionization parameter for the lower distance model. The differences in predicted line luminosities for the different distance models mimic each other as well (see Fig. 6.5 and Fig. 6.9). So does the predicted luminosity increase in the lower distance model for the O VII triplet, the O VII line at 18.63 Å, He II, N V, the Si IV and O IV blend, O VIII Lyα line, Si III, Mg II, C VI and N VII. There is a decrease in predicted luminosity for the C V forbidden line. The only difference between the codes is for C III, which increases in XSTAR, while decreasing in CLOUDY. However, note that this line is not well predicted with XSTAR. The correlation in line strengths with density gives confidence that, although we obtain different parameters from the different codes, the basic physics applied is
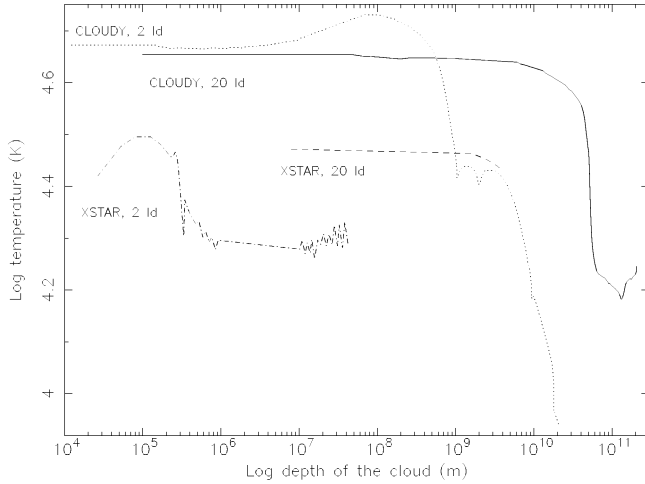
Figure 6.10: The temperature as a function of the depth of the cloud for a distance of 20 ld (solid line for CLOUDY prediction, dashed line for XSTAR prediction) and 2 ld (dotted line for CLOUDY prediction, dash-dotted line for XSTAR prediction). Note the broad dip between 5×10^{10} m and 2×10^{11} m in the 20 ld CLOUDY model that corresponds with the peak in fractional abundance for C IV (see Fig. 6.11). There is a smaller dip between 10^9 m and 2×10^9 m in the 2 ld CLOUDY model corresponding to the C IV peak in fractional abundances (see Fig. 6.12).

similar and the difference is a calibration problem between the codes.

Both codes have a problem with predicting the line luminosity for He II, and in both cases the match worsens for the 2 ld model. As we have already discussed, the UV and X-ray broad emission lines can be modeled with one ionization parameter and density, and thus one expects that all these lines are emitted from the same distance. However, the reverberation distances for the UV ions are not the same. From our modeling of the broad emission lines we find that He II is formed over a large range of ionization parameters, but is most efficiently formed at very low ionization parameter. It is thus counter-intuitive that He II does has the shortest reverberation mapping distance. This problem needs further investigation.

The fact that we need a higher total column density and covering factor for the 2 ld models, is consistent with a picture where our line of sight crosses the edge of a rotating cloud.

137

Temperature of the absorbing cloud

We can study the temperature (see Fig. 6.10) and the fractional ion abundance (see Fig. 6.11 to Fig. 6.14) as a function of depth of the cloud for both distance models. Comparing both codes we find that the cloud depth for our results is about two orders of magnitude smaller in XSTAR. Due to the higher density, the depth of the cloud for the 2 ld distance model is smaller in both codes. From the calculations by CLOUDY we see that the cloud for the 2 ld distance model is hotter near the illuminated side, but shows a rather steep drop at $\sim 7 \times 10^8$ m. The cloud at 20 ld has a less drastic drop in temperature further into the cloud, and seems to recover at the non-illuminated side of the cloud. With XSTAR we find a significantly lower temperature for both distance models. The temperature of the 2 ld model has a similar increase in temperature near the illuminated surface, and a decrease in temperature at a similar cloud depth as has the CLOUDY model for the same distance. However, in XSTAR the temperature levels off for this distance, while the temperature for the CLOUDY model still decreases.
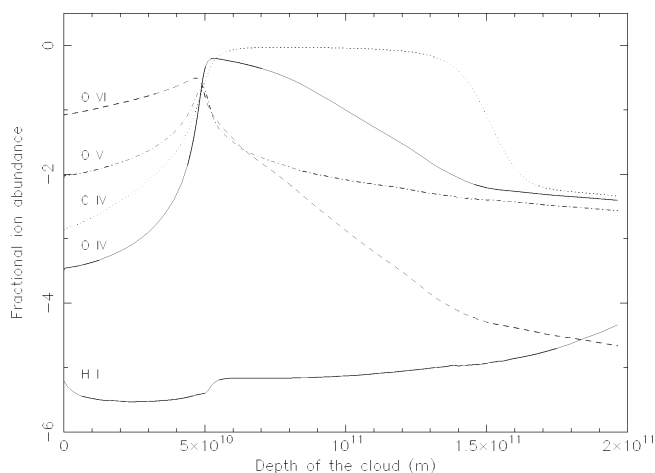
Fractional abundances

Figure 6.11: The fractional abundances (given as logs) versus the depth of the cloud for O IV, H I (solid lines), C IV (dotted line), O VI (dashed line), and O V (dash-dotted line) for the 20 ld model. Note the range in depth of the cloud for which C IV has a high fractional abundance. This broad peak corresponds to a broad dip in temperature (see Fig. 6.10).
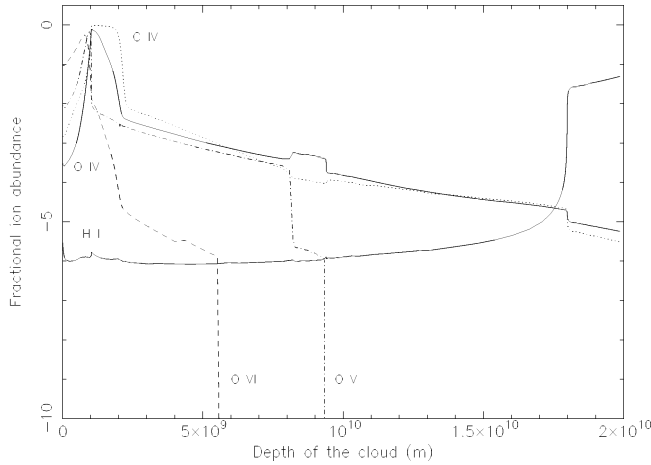
138

Figure 6.12: Same as Fig. 6.11, but for the 2 ld model. Note the smaller depth of the cloud and the strong increase of H I at the unilluminated edge of the cloud.

Both codes calculate fractional abundances as a function of depth in the cloud. The fractional abundances of H I, C IV, O IV, O V and O VI for both distance models and both codes are plotted in Fig. 6.11 to Fig. 6.14. For a distance of 20 ld CLOUDY finds a peak in fractional ion abundance at about 5×10^{10} m, with the exception of H I which peaks near the non illuminated edge of the cloud. C IV has a high fractional ion abundance over a large part of the cloud, which explains why this is the most luminous line detected in the UV and X-ray band. For the 2 ld distance model the fractional ion abundances peak much closer to the illuminated edge of the cloud. Again H I peaks at the non illuminated face of the cloud, but the cloud is much smaller. The profiles of the fractional ion abundance curves are similar, but in absolute scale much smaller than for the 20 ld distance model. H I has a much stronger peak at the non illuminated edge of the cloud, which compensates for the lack of Fe XIII and S X in the 1216 Å blend.

Using the best match parameters we find different fractional abundances as a function of depth in the cloud with XSTAR than with CLOUDY. The fractional ion abundances obtained with XSTAR are about an order of magnitude larger at the illuminated face of the cloud, with the exception of H I. In the 20 ld model, due to the low total column density, we find a slight increase in fractional abundances for all ions except H I. The results for the 2 ld model are more similar to the results obtained with CLOUDY. This similarity is due to the larger total column density used in this model. Thus the physical parameters in the cloud are different for XSTAR and CLOUDY.
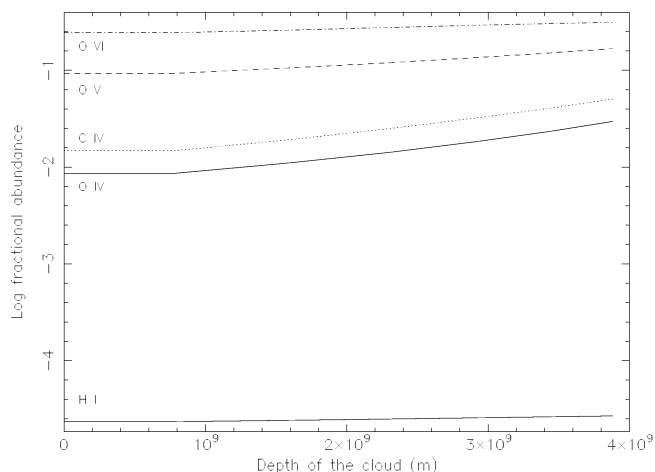
139

Figure 6.13: Same as Fig. 6.11, but now calculated by XSTAR. Note the very different result compared to the CLOUDY result for a 20 ld distance.

Comparison with other X-ray observations

Comparing our results with the earlier results on NGC 5548 (Kaastra et al. 2002a) we find a much weaker line in our data, with a similar FWHM. Kaastra et al. (2002a) detected a broad C VI Lyα emission line, with a derived flux of $5.6^{+3.5}_{-1.7}$ photons m^{-2} s^{-1}, an order of magnitude larger than the flux measured from the 2002 LETGS spectrum which is 0.5 ± 0.2. The FWHM of 10600 km s^{-1} $\pm$ 3300 km s^{-1} is consistent with the FWHM we assumed. In NGC 4051 Ogle et al (2004) find a broad O VII resonance line and a C VI Lyα emission line with a FWHM of 11000 km s^{-1} $\pm$ 3000 km s^{-1} and 1200 km s^{-1} $\pm$ 70 km s^{-1} respectively. The width of the C VI line is much narrower than the lines we detect, however, the width for the O VII resonance line is very similar to our assumed 8000 km s^{-1}.

6.6 Summary

We determined how the line luminosity calculated by the photoionization codes CLOUDY and XSTAR is dependent on the density, abundances, covering factor, ionization parameter, total column density and SED assumed. The line luminosity is nearly independent of abundances and the SED for the parameters tested. The line
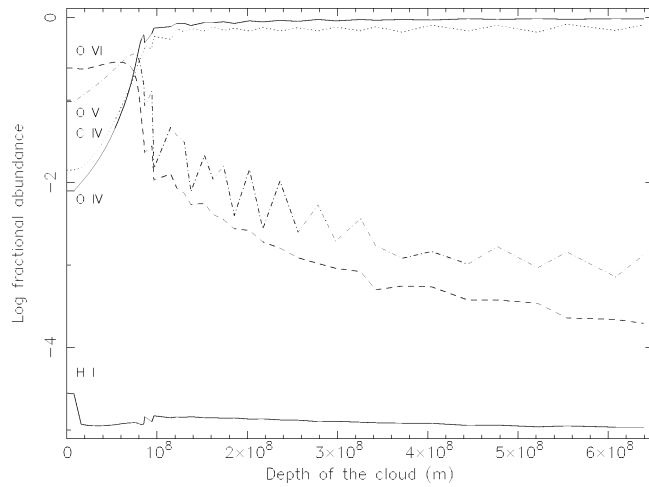
Figure 6.14: Same as Fig. 6.11, but for the 2 ld model and calculated by XSTAR.

luminosity is dependent on the covering factor if less than 5 %; and the density and column density, if the density is more than 10^{18} m^{-3}. We modeled the lines for a cloud distance of 20 ld and 2 ld. We can model the broad emission lines detected in the simultaneous *Chandra* and HST STIS observations with one ionization parameter. However, this ionization parameter differs from $\xi = 15$ for CLOUDY to $\xi = 3$ for XSTAR. The temperature, ion abundance profiles and the size of the cloud are different in both codes. In both codes the match in the 20 ld model is better, has a lower total column density and covering factor. This is consistent with a flattened rotating structure which we observe through the edge.

References

Allende Prieto, C., Lambert, D. L. & Asplund, M., 2001, ApJ, 556, L63

Allende Prietro, C., Lambert, D. L. & Asplund, M., 2001, ApJ, 573, L137

Anders, E. & Grevesse, N., 1989, Geochim. Cosmochim. Acta, 53, 197

Arav, N., Barlow, T. A., Laor, A., et al., 1998, MNRAS, 297, 990

Arav, N., Korista, K. T. & de Kool, M., 2002, ApJ, 566, 699

Arav, N., Gabel, J., Kaastra, J. S., et al., 2004, in preparation

Blandford, R. D. & McKee, C. F., 1982, ApJ, 255, 419

Branduardi-Raymont, G., Sako, M., Kahn, S. M., et al., 2001, A&A, 365, 140

Costantini, E., Kaastra, J. S., Steenbrugge, K. C., et al., in prep.

Crenshaw, D. M. & Kraemer, S. B., 1999, ApJ, 521, 572

Crenshaw, D. M., Kraemer, S. B., Gabel, J. R., et al., 2003, 594, 116

Dumont, A-M., Collin-Souffrin, S. & Nazarova, L., 1998, A&A, 331, 11

Elvis, M., 2000, ApJ, 545, 63

Ferland, G. J., 2002, *Hazy, A Brief Introduction to Cloudy 96*, http://www.pa.uky.edu/~gary/cloudy

Goad, M. & Koratkar, A., 1998, ApJ, 495, 718

Grevesse, N. & Sauval, A. J., 2001, Space Science Review, 85, 161

Hewitt, A., Burbidge, G., 1991, ApJS, 75, 297

Holweger, H., 2001, Joint SOHO/ACE workshop: "solar and Galactic Composition".

Kaastra, J. S. & Barr, P., 1989, A&A, 226, 59

Kaastra, J. S., Steenbrugge, K. C., Raassen, A. J. J., et al., 2002a, A&A, 386, 427

Kaastra, J. S., Mewe, R. & Raassen, A. J. J., 2002b, Proceedings Symposium 'New Visions of the X-ray Universe in the XMM-*Newton* and *Chandra* Era'

Kaastra, J. S., Arav, N., Steenbrugge, K. C., 2004, in preparation

Kallman, T. R. & Krolik, J. H., 1999, XSTAR photoionization code, ftp://legacy.gsfc.nasa.gov/software/plasma_codes/xstar/

Kelly, R. L., 1987, Journal of Physical and Chemical Reference Data, Vol. 16 Suppl. 1

Kelly, R. L., 1987, Journal of Physical and Chemical Reference Data, Vol. 16 Suppl. 2

McKee, C. F. & Tarter, C. B., 1975, 202, 306

Nandra, K., Fabian, A. C., George, I. M., et al., 1993, MNRAS, 260, 504

Nicastro, F., Piro, L., De Rosa, A., et al., 2000, ApJ, 536, 718

Ogle, P. M., Mason, K. O., Page, M. J., et al., 2004, ApJ, 606, 151

Peterson, B. M., 1994, ASP Conference Series, Vol. 69

Peterson, B. M. & Wandel, A., 1999, ApJ, 521, L95

Seyfert, C. K., 1943, ApJ, 97, 28

Steenbrugge, K. C., Kaastra, J. S., de Vries, C. P. & Edelson, R., 2003, A&A, 402, 477

Steenbrugge, K. C., Kaastra, J. S., Crenshaw, D. M., submitted to A&A

Tanaka, Y., Nandra, K., Fabian, A. C., et al., 1995, Nature, 375, 659

Wilms, J., Reynolds, C. S., Begelman, M. C., et al. 2001, MNRAS, 328, 27

Chapter 7

XMM-Newton observations of the heavily absorbed Seyfert 1 galaxy IC 4329A

K.C. Steenbrugge, J.S. Kaastra, M. Sako, G. Branduardi-Raymont, E. Behar,
F. B. S. Paerels, A. J. Blustin, S. M. Kahn

Abstract

We detect seven distinct absorbing systems in the high-resolution X-ray spectrum
of the Seyfert 1 galaxy IC 4329A, taken with XMM-*Newton*. Firstly we detect absorption
due to cold gas in our own Galaxy and warm gas in the Galactic halo or the Local
Group. This local warm gas is only detected through O VII absorption, from which
we deduce a temperature between 0.03 and 0.2 keV. In IC 4329A we detect absorption
from the host galaxy as well as from a warm absorber, close to the nucleus, which has 4
components. The absorption from the host galaxy is well modeled by neutral material.
The warm absorber detected in IC 4329A is photoionized and has an ionization range
between $\log \xi = -1.37$ and $\log \xi = 2.7$. A broad excess is measured at the O VIII Lyα
and N VII Lyα emission lines, which can be modeled by either disklines or multiple
Gaussians. From the lightcurve we find that the source changed luminosity by about

Table 7.1: Instrumental set-up and exposure time used for the spectral analysis.

Instrument	exposure (s)	observational mode
RGS 1 and 2	136017	spectroscopy
pn	44363	Small window with thin filter
MOS 1	97857	PrimePartialW3 with medium filter
MOS 2	94709	Small window with thin filter

20 % over the 140 ks observation, while the spectral shape, i.e. the softness ratio did not vary. In the EPIC spectra a narrow Fe Kα and Fe XXVI Lyα emission line are detected. The narrowness of the Fe Kα line and the fact that there is no evidence for flux variability between different observations leads us to conclude that the Fe Kα line is formed at a large distance from the central black hole.

7.1 Introduction

IC 4329A is one of the X-ray brightest Seyfert 1 galaxies in the sky. The spiral galaxy is seen almost edge on and is the closest companion to the elliptical galaxy IC 4329, the central galaxy in a cluster. IC 4329A has rather extreme properties, such as the full width at zero intensity (FW0I) of the Hα line which equals 13,000 km s^{-1} (Disney, 1973). On the basis of the reddening observed in the optical, $A_v = 2.5 - 4.8$ magnitudes, Wilson & Penston (1979) have classified IC 4329A as the nearest quasar, with an absolute magnitude between -23.0 and -25.3. In the optical spectra prominent Na I D, Ca II and weaker Mg I absorption lines are observed, indicating the presence of dust, consistent with the dust lane observed in the equatorial plane of the galaxy (Wilson & Penston 1979). The optical spectrum shows that the absorber is neutral or very lowly ionized. The observed line emission is due to lowly ionized material with strong [O III] (Wilson & Penston 1979). Crenshaw & Kraemer (2001) classified IC 4329A as a dusty luke-warm absorber on the basis of similarities with the known absorbers of this type in NGC 3227 and Ark 564. These similarities are the high inclination angle and the reddening determined between the far UV and optical band. Crenshaw & Kraemer (2001) predict that only lowly ionized absorption should be detected, namely the dust that causes the reddening observed in the optical and the UV band.

The redshift of IC 4329A is 0.01605 ± 0.00005 (Willmer et al. 1991). However, Wilson & Penston (1979) note that the optical lines are double peaked, with the second peak at a mean redshift of 0.0224 ± 0.0001. Throughout our analysis we fixed the

redshift to $z = 0.01605$, as we did not detect any evidence for a component at $z = 0.0224$. All spectra were corrected for a Galactic hydrogen absorption column density $N_H = 4.55 \times 10^{24}$ m^{-2} (Elvis, Lockman & Wilkes 1989).

Earlier X-ray spectra contained a reflection component (Miyoshi et al. 1988) and a moderately broadened Fe Kα emission line (Done et al. 2000). In an earlier 12 ks XMM-*Newton* observation Gondoin et al. (2001) detected only a narrow Fe Kα line, with a width $\sigma = 0.01 \pm 0.05$ keV. The earlier *Chandra* HEG spectrum shows a complex double line at the Fe Kα energy, which can be fit either by two Gaussians, two disklines, or a single diskline (McKernan & Yaqoob 2004). Gondoin et al. (2001) fitted the soft X-ray part of the spectrum with a set of absorption edges of O I, O VI, O VIII and N VII. They noted the lack of an O VII absorption edge and concluded that the warm absorber must have at least 2 phases.

In this paper we analyze a deep 140 ks XMM-*Newton* observation of IC 4329A. In Sect. 7.2 we describe the observation and data reduction. The variability is analyzed in Sect. 7.3. In Sect. 7.4 the spectral analysis is detailed, while Sect. 7.5 details the analysis of the absorbers present in the spectrum. In Sect. 7.6 we discuss our results and the conclusions are summarized in Sect. 7.7. Power density spectra analysis as
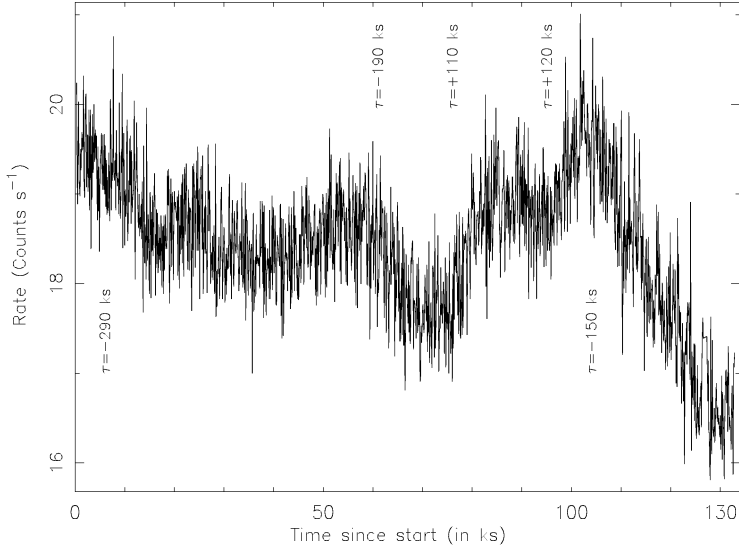

Figure 7.1: The background subtracted lightcurve for the pn instrument, using the complete 140 ks observation.

well as possible variability in the Fe Kα line will be described by Markowitz et al. (2006) once the complete RXTE long term monitoring campaign is completed.

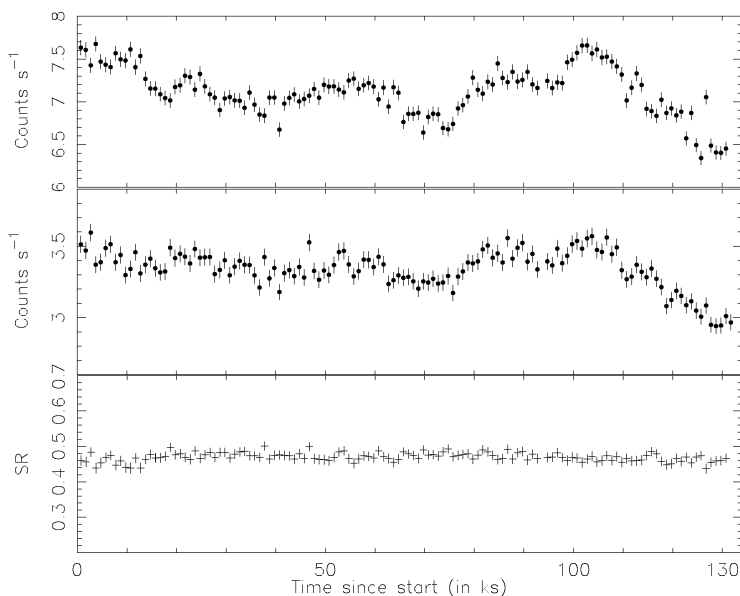## 7.2 Observation and data reduction

Figure 7.2: Lightcurves for the pn instrument. Top: the hard band between $2 - 10\,\mathrm{keV}$; middle: the soft band between $0.4 - 1\,\mathrm{keV}$. Bottom: the softness ratio: the $0.4 - 1$ keV count rate divided by the $2 - 10\,\mathrm{keV}$ count rate. All the data were binned in 1000 s bins.

IC 4329A was observed on August 6 and 7, 2003, for a total exposure time of 136 ks. Throughout the observation there were periods of high background, which were removed for the EPIC data using the Good Time Interval (GTI) produced with the online Processing Pipeline Subsystem PPS data files. For the RGS spectra we use the whole exposure time, to maximize the statistical quality of the data. For the data reduction we used the PPS data products, downloaded from the XMM-*Newton* website. The data were reduced with the SAS software version 5.4.1. Table 7.1 lists the instrumental set-up and the net exposure time used in the further spectral analysis.

For the time variability analysis we used the full 140 ks pn observation. The pn, MOS 1 and MOS 2 spectra were fitted between $0.4 - 12$ keV, the first order RGS spectra were originally fitted between $7 - 38$ Å, the second order spectra between $7 - 19$ Å. Due to the low count rate, we limited our analysis to the first order spectra of RGS, and the 7 to 26 Å wavelength range. RGS 1 and 2 were averaged in the presented plots for clarity, but fit as separate spectra. For both RGS instruments the count rate ranged between 30 and 250 counts per bin for the part of the spectrum up to 26 Å, allowing the use of χ^2 statistics. The RGS and MOS spectra were binned by a factor of 3, for the RGS this corresponds to about half the FWHM resolution of 0.07 Å or a bin size of 0.03 Å. The MOS cameras have a FWHM resolution of 50 eV at 0.4 keV and 180 eV at 10 keV. The pn data were binned by a factor of 5, and have a FWHM resolution ranging between 90 eV and 185 eV at 1 keV and 10 keV respectively. All the spectra were analyzed using the SPEX software (Kaastra et al. 2002b). All quoted errors are rms errors, i.e. $\Delta\chi^2 = 2$.

7.3   Time variability

We constructed the light curve using the pn in the $0.4 - 10$ keV band (see Fig. 7.1). Time is measured from the start of the observation, at the 6th of August 2003 at 6^h 13^m 47^s UT. Fig. 7.2 shows the lightcurves in the hard ($2 - 10$ keV) band, the soft ($0.4 - 1$ keV) band and the softness ratio determined from these two bands.

The count rate of the pn varied between 20 counts s^{-1} at the start of the observation and 16 counts s^{-1} at the end of the observation. The most noticeable part of the light

Table 7.2: The best fit continuum parameters, for the fit including the absorbers detailed in Sect. 7.5, fitting the pn and RGS 1 and RGS 2 simultaneously.

pl	norm.^{a}	2.90×10^{52} ph s^{-1} keV^{-1}
	lum.^{a,b}	1.17×10^{37} W
	Γ^a	1.709
mbb	norm.^{a}	7.2×10^{31} m$^{1/2}$
	kT^a	473 eV

^{a} The systematic errors dominate over the statistical errors, which are on the order of 1%.

^{b} in the $2 - 10$ keV band, calculated from the measured normalization, photon index.
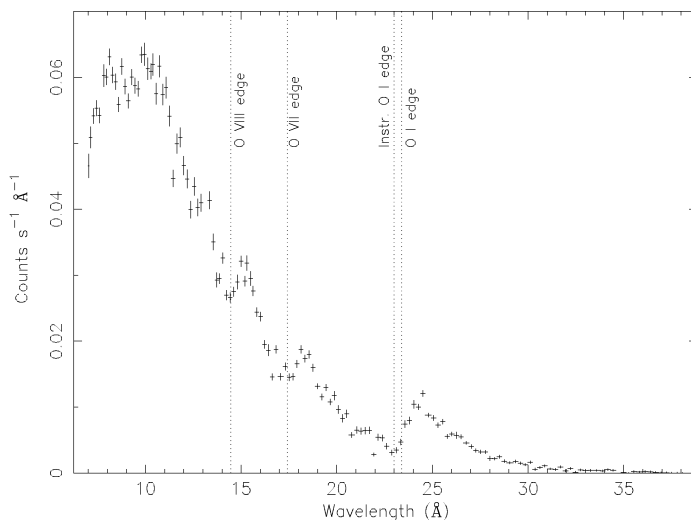
Figure 7.3: RGS spectrum of IC 4329A with the strongest absorption edges identified. RGS 1 and RGS 2 are averaged for clarity. Note that the edges are convolved with the resolution of the RGS and are heavily blended, thus they are not sharp.

curve is the steady decline lasting 25 ks near the end of the observation, after which it levels off for the last 3 ks. Throughout the observation several gradual luminosity changes are observed.

We identify in Fig. 7.1 several parts in the light curve where the total luminosity decreases or increases nearly monotonically. The smallest duration for a 5 % luminosity variation is ~ 10 ks. The characteristic timescale, $\tau = |dt/d\ln L|$, for these luminosity variations is between 100 and 300 ks. The r.m.s. variance measured as the intrinsic spread for this dataset is 5 %. From the softness ratio (see Fig. 7.2) no time lag can be discerned and there is no spectral change with increasing luminosity observed.

7.4 Spectral analysis

7.4.1 Continuum

The spectrum is heavily absorbed, with several deep edge-like structures (see Fig. 7.3 for RGS and 7.4 for EPIC-pn). Below energies of about 1.3 keV (i.e. above ~ 10 Å) we need a complex absorption model (see Sect. 7.5), a power law continuum and a

148

Table 7.3: The best fit parameters for the Fe Kα and Fe XXVI Lyα emission lines for the pn and MOS 1 and MOS 2 spectra, using Gaussian profiles. As the line at ~6.9 keV is rather weak, we fitted MOS 1 and MOS 2 simultaneously. The energies quoted are for the restframe of IC 4329A. The errors on the line energies are the statistical uncertainties since these are larger than the systematic uncertainties in the energy scale. All quoted results have been corrected for the redshift of IC 4329A.

	pn	MOS1	MOS2
norm[a]	9.5 ± 0.9	7.6 ± 0.9	6.4 ± 0.8
flux[b]	0.85 ± 0.08	0.66 ± 0.08	0.58 ± 0.07
E (keV)	6.45 ± 0.01	6.42 ± 0.01	6.40 ± 0.01
FWHM (eV)	240 ± 50	110 ± 50	< 100
EW (eV)	87 ± 8	68 ± 8	64 ± 8
norm[a]	3.0 ± 0.8	3.2 ± 0.9	
flux[b]	0.27 ± 0.07	0.28 ± 0.08	
E (keV)	6.92 ± 0.05	6.89 ± 0.05	
FWHM (eV)	300 ± 100	300 ± 100	
EW (eV)	30 ± 8	36 ± 10	

[a] in $\times 10^{49}$ ph s^{-1}.
[b] in ph m^{-2} s^{-1}

soft excess which we successfully model with a high temperature modified black body. This is a black body component modified by coherent Compton scattering, for more detail see Kaastra & Barr (1989). Above 1.3 keV the spectrum is well described by a power-law plus two Gaussians for Fe Kα and Fe XXVI Lyα emission line probably blended with the Fe Kβ line (see Sect. 7.4.2), corrected for Galactic absorption (see Fig. 7.4 and Fig 7.6). We modeled the Galactic absorption toward IC 4329A with an absorber in collisional ionization equilibrium, namely the *hot* model in SPEX. The *hot* model determines the transmission for a certain temperature and total hydrogen column density. This model includes more accurate atomic data for the oxygen edge and includes the neutral oxygen absorption lines. We froze the temperature to 0.5 eV (resulting in an almost neutral gas) and the column density to $N_{\rm H} = 4.55 \times 10^{24}$ m^{-2} (Elvis et al. 1989). We froze the abundances to solar and the velocity broadening, the Gaussian σ to the standard 100 km s^{-1}.

In our spectral analysis of the low energy part of the spectrum we focus on the pn and RGS spectra. The pn spectrum is used to determine the continuum and broad emis-

sion line parameters, while the RGS spectra are used for fitting the different absorbers in detail. We did not fit the MOS 1 and MOS 2 spectra simultaneously with the pn and RGS spectra as the $\sim 10\%$ systematic uncertainties in the effective areas between the different instruments influence the fit noticeably. The best fit absorption model obtained from the pn and RGS spectra alone matches the MOS spectra rather well, if we allow for different continuum parameters. Table 7.2 lists the best continuum parameters for the simultaneous pn, RGS 1 and RGS 2 fit. We did not include a continuum reflection component as detected by Gondoin et al. (2001) from the *Beppo*SAX data in our spectral analysis. The XMM-*Newton* spectra only extend to about 12 keV, where the continuum reflection component is still negligible (see Fig. 7.6).

7.4.2   Fe Kα and Fe XXVI Lyα line

A narrow Fe Kα line is clearly detected in all three EPIC spectra. There is a second, weaker line detected at about 6.9 keV, which we identify as a blend of the 6.95 keV and 6.97 keV Fe XXVI Lyα lines and probably blended with the Fe Kβ line at 7.06 keV (Palmeri et al. 2003). In Fig. 7.5 the pn, MOS 1 and MOS 2 spectra around the Fe Kα line are plotted, in Fig. 7.6 the residuals to a power-law fit of the pn spectrum is shown.

We tested the accuracy of the energy scale for all instruments by looking at instru-
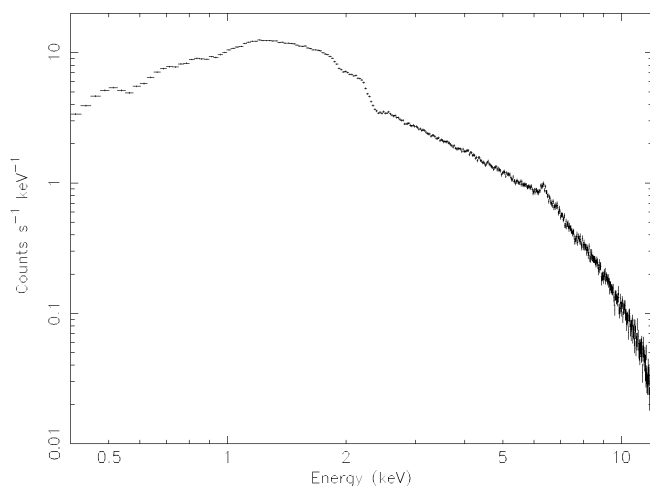

Figure 7.4: The pn spectrum of IC 4329A. Note the strong absorption at lower energies (see Fig. 7.6 for the residuals to a power-law fit) and the strong Fe Kα emission line.

mental background lines, to avoid any gain problem. For the MOS cameras the outer CCDs are exposed, and we used the whole exposed area to find the instrumental background lines. For MOS 1 the strongest instrumental line, Al at 1.4866 keV is detected at the expected energy. For MOS 2 all the background lines, with the exception of the weak Ni line at 7.4724 keV are detected at the expected energy. Therefore the energy scale of the MOS spectra should be correct. For pn we are limited to CCD 4; however, we do not detect any of the the instrumental background lines with sufficient significance to be able to verify the energy scale. There can thus still be a small gain problem for the pn.

Table 7.3 lists the best fit values fitting Gaussian profiles to both iron emission lines in the pn and the MOS spectra. The full width half maximum (FWHM) and energy of the Fe Kα line are consistent within the instrumental uncertainties. For the line at 6.9 keV data for the pn and the MOS instruments are consistent. Interestingly, we do not detect the Fe XXV triplet around 6.70 keV.

Gondoin et al. (2001) find an absorption edge at 7.1 keV with an depth of 0.03 $\pm$ 0.02. There is a 1 σ jump in our data at 7.1 keV, corresponding to an optical depth of < 0.04. However, we do not detect sufficient iron L line absorption between 15.5 Å and
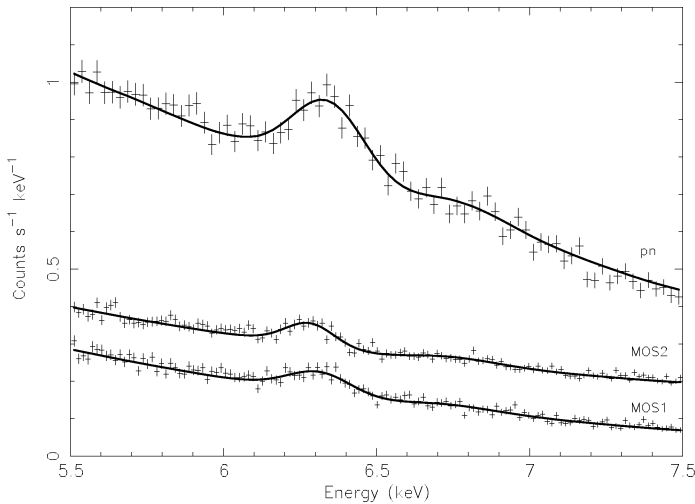

Figure 7.5: Detail of the pn, MOS 1 and MOS 2 spectra showing the Fe Kα and Fe XXVI Lyα emission lines. The model through the data is given in Table 7.3. The MOS 2 data were shifted by adding 0.006 counts s^{-1} for clarity.
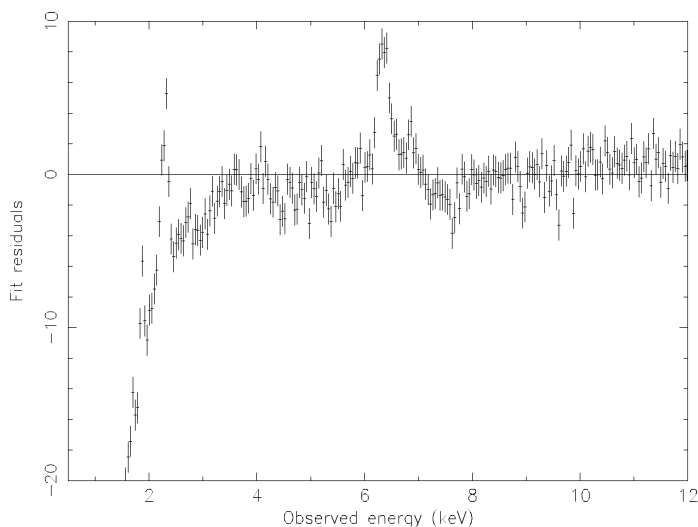
151

Figure 7.6: A power-law plus Galactic absorption fit to the pn spectrum, rebinned by a factor of 9. Note the Fe Kα and Fe XXVI Lyα emission lines, as well as the absorption at lower energies. The feature at 2 keV is an artifact of the absorption spectrum and the soft excess. Note that the reflection component has at most a 1 σ significance.

16.5 Å and edge absorption between 8 Å and 10 Å in the RGS spectra to explain such an edge. As a result we decided against the interpretation that this feature is an edge. McKernan & Yaqoob (2004) note two emission features in the *Chandra* HEG spectrum, which they model with either two Gaussians or two disklines. In the model with two Gaussians they obtain for the Fe Kα line an energy of 6.30 ± 0.08 keV, for the Fe XXVI Lyα line an energy of 6.91 ± 0.04 keV. Both are consistent with our results, as are the measured EWs and intensities. We also tested a double diskline model (Laor 1991), which gives a similarly good fit, for two more free parameters as compared to the fit with two Gaussians. For pn we find an inclination angle $i < 17°$ and an emissivity slope $q < 1.4$, where for large radii $I(r) \sim r^{-q}$. This is consistent with the parameters determined by McKernan & Yaqoob (2004) who find an inclination angle of $12° \pm 1°$ and a flat emissivity slope. For the MOS spectra we find similar, but less constrained upper limits. The diskline profile for $i = 12°$ and $q = 1$ is shown in Fig. 7.7 (dashed line). Note that this profile is very similar to a Gaussian line profile. As a result, the pn and MOS spectra do not allow us to distinguish between a model with two disklines or two Gaussian emission lines. As we cannot constrain the diskline parameters, we use
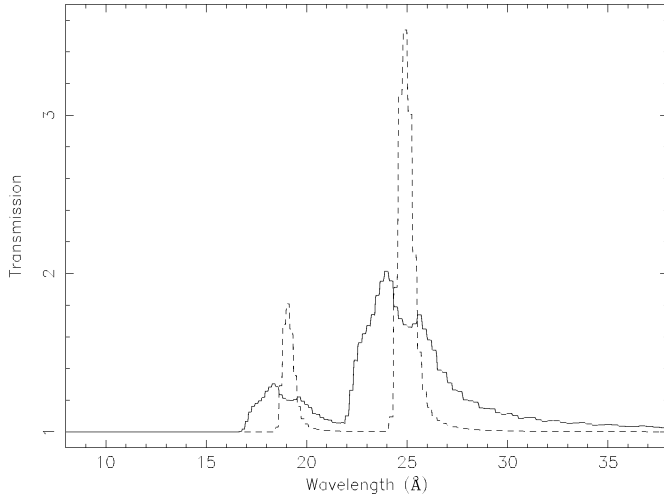
152

Figure 7.7: Models for the two broadened emission features detected in the RGS spectrum (see Sect 7.5.4) and the two emission features detected in the pn spectrum. The thin solid line represents the best fit for the relativistically broadened lines detected in the RGS spectra, with $q = 1.9$ and $i = 80.9$ (see Table 7.7). The dashed line represents the model for the emission features adopting the parameters found for the relativistically broadened Fe Kα and Fe XXVI emission lines: emissivity slope $q = 1$ and $i = 12°$, consistent with the values obtained by McKernan & Yaqoob (2004). Note that this profile is very similar to a Gaussian profile.

the model with two Gaussians in the following data analysis.

We re-analyzed the pn spectrum for the 2001 XMM-*Newton* observation of IC 4329A. We used SAS version 6.0 and the PPS data files for the data reduction. The data are noisy (total exposure time of 9.7 ks), leading to large error bars or upper limits for the Fe Kα parameters, even if we fit the emission line with a Gaussian. In Table 7.4 we compare the different literature values for the Fe Kα emission line. Note that the flux of the Fe Kα line is consistent with a constant value since August 1997, although there is a rather large spread in FWHM. However, the error bars on the flux values are large, and thus we can not exclude variability. The large spread in FWHM is partially a result from differing spectral resolution of the different instruments. An indication of the uncertainty in absolute calibration between the different instruments are the differing parameters for the simultaneous ASCA and RXTE observations (Done et al. 2000).

153

Table 7.4: Comparison of the Fe Kα emission line as observed in earlier observations.

	ASCA[a] 1997 Aug. 7-16	RXTE[a] 1997 Aug. 7-16	*Beppo*SAX[b] 1998 Jan. 02	XMM-*Newton*[c] 2001 Jan. 31	*Chandra*[d] 2001 Aug. 26
Energy[e]	6.37±0.06	6.3±0.1	6.5±0.2	6.5±0.2	6.30±0.08
FWHM[f]	920±240	1150±450	850±590	410±500	440±190
flux[g]	0.7±0.2[h]	1.2±0.2[h]	1.6±0.7	<0.9[i]	1.9±0.8
EW[f]	180±50	240±45	109±44	<72[i]	110±43

[a] Done et al. (2000), the ASCA and RXTE data were taken simultaneous.

[b] Perola et al. (1999).

[c] based on our own analysis of the pn data.

[d] McKernan & Yaqoob (2004) for the fit with two Gaussian lines.

[e] in keV.

[f] in eV.

[g] in ph m^{-2} s^{-1}.

[h] Calculated from the given EW and continuum level.

[i] The 3 σ upper limit.

7.5 Absorbers

The RGS spectra are dominated by absorption edges (see Fig. 7.3), as was also concluded by Gondoin et al. (2001). The earlier 12 ks RGS observation is too short to include useful high resolution spectral information. As the warm absorber could be variable on timescales much shorter than the time difference between both observations, we did not use the earlier RGS data in our analysis. There are only a few absorption lines that can be easily identified. We model the absorber using a combination of *hot* and *xabs* components. The *hot* model calculates the transmission (both lines and continuum) of a thin slab in collisional ionization equilibrium. The *xabs* model does the same for a photoionized model. In both models the total column density, outflow velocity v and velocity dispersion (Gaussian σ) σ_v are free parameters, as well as the temperature T for the *hot* model and the ionization parameter $\xi = L/nr^2$ for the *xabs* model. For more details see Kaastra et al. (2002a; 2002b). To fit the spectrum self-consistently we need at least seven absorbers (see Table 7.6). The best fit spectrum including these absorption components is shown in Fig 7.8 − 7.10. Component 1 is the absorption due to our own Galaxy discussed in Sect. 7.4.1. The absorber with the
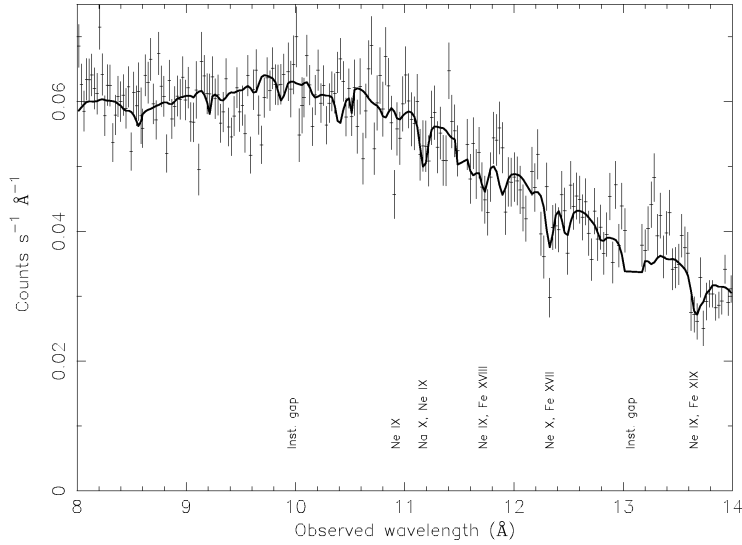
Figure 7.8: Detail of the RGS spectrum between 8 and 14 Å. The solid line through the data points is our best fit model as described in the text. RGS 1 and 2 are added for clarity in this and the next two spectra.

largest opacity is neutral and due to the host galaxy of IC 4329A, component 2, and is easily identified from its redshifted O I absorption line (see Fig. 7.10). Fitting this absorber improves the χ^2 from 100398 to 16872 for 1603 degrees of freedom (dof) for the continuum parameters quoted in Table 7.2. This absorber is discussed in Sect. 7.5.1.

The absorber with the highest column density, component 5, is highly ionized, and including this absorber further reduces χ^2 to 13559 for 1607 dof. This component is responsible for the O VII and Ne IX resonance lines, the N VII Lyα and O VIII Lyα lines; as well as absorption edges due to these ions. Further, a less ionized absorber, component 4 with also a lower column density is necessary to fit the O V − O VII lines and some iron M shell Unresolved Transition Array (UTA) (Behar, Sako & Kahn 2001). Adding component 4 reduces the χ^2 to 11947 for 1611 dof. A very highly ionized absorber could also be present (component 6), but is only weakly detected, and only improves the χ^2 by 507 for 4 extra degrees of freedom. This component produces (a part of) O VIII and Ne X Lyα lines. The fit improves significantly, reducing χ^2 to 2428 for 1615 dof, by adding a near neutral absorber (component 3). This fits a part of the UTA as well as absorption from O II. However, this component is not significant if
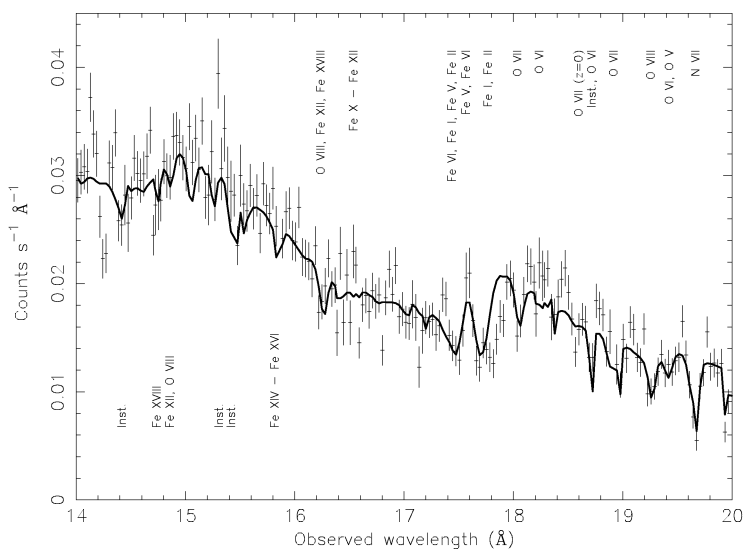
155

Figure 7.9: Detail of the RGS spectrum between 14 and 20 Å. The solid line through the data points is our best fit model as described in the text. The O VII absorption at z = 0 is indicated, but not fit in the plot.

we assume that the gas in the host galaxy is lowly ionized. To distinguish between a neutral or a cold absorber the detection of O II is crucial. All these absorbers are further discussed in Sect. 7.5.2.

Finally, we detect a weak O VII absorption component (7) from $z = 0$ plasma, which is discussed in Sect. 7.5.3.

7.5.1 Absorption from the host galaxy: component 2

This is the absorption component also detected in the optical and is responsible for the reddening observed in the optical and the UV. The X-ray O I absorption lines are well explained by a neutral absorber. This absorption system is the dominant component (2), in the sense of the opacity in the X-ray spectrum.

To ascertain that this absorber is neutral and not lowly ionized, we plot the transmission for a neutral and for a lowly ionized absorber in Fig. 7.11. The absorption lines from O II around 22 Å and the deep O II absorption line at about 23.3 Å are the only detectable differences between these transmission models. Juett, Schulz & Chakrabarty

156
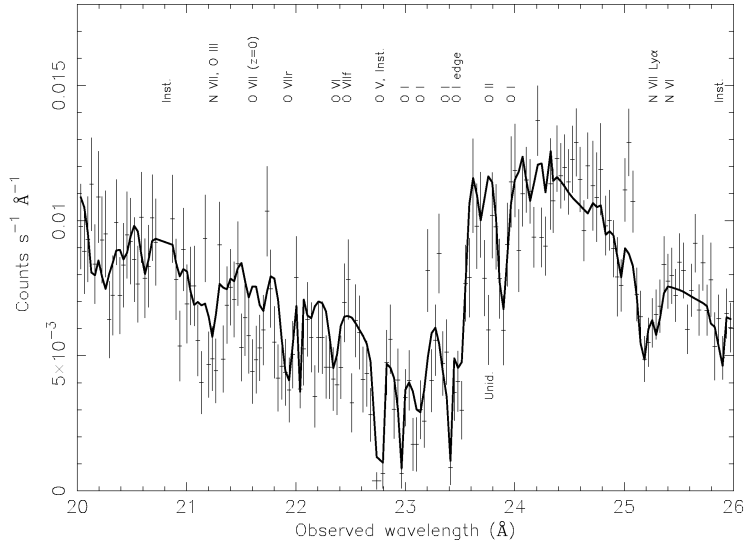
Figure 7.10: Detail of the RGS spectrum between 20 and 26 Å. The solid line through the data points is our best fit model as described in the text. The O VII absorption line at z = 0 and the O VII forbidden line are indicated, but not fit in the plot. The feature labeled as Unid. is further discussed in the text.

(2004) determined from a study of the interstellar medium with the *Chandra* HETG that the O II line wavelength is 23.33 Å. In the RGS spectrum of IC 4329A there is a deep line at 23.37 Å ± 0.01 Å rest wavelength (23.74 Å observed wavelength, identified as Unid. in Fig. 7.10) for which there is no straightforward identification. The 0.04 Å difference is larger than the 8 mÅ uncertainty in the absolute calibration of the RGS, and is inconsistent with the fact that we detect O I at the correct wavelength.

If this line at 23.37 Å is identified as an O II line, then the absorber of the host galaxy should be redshifted by 500 km s^{-1} and not neutral but very lowly ionized. Inflow is not expected if the gas is part of the host galaxy. Therefore we conclude that component 2 does not contain a significant amount of O II and in the further analysis we will assume that this absorber is neutral.

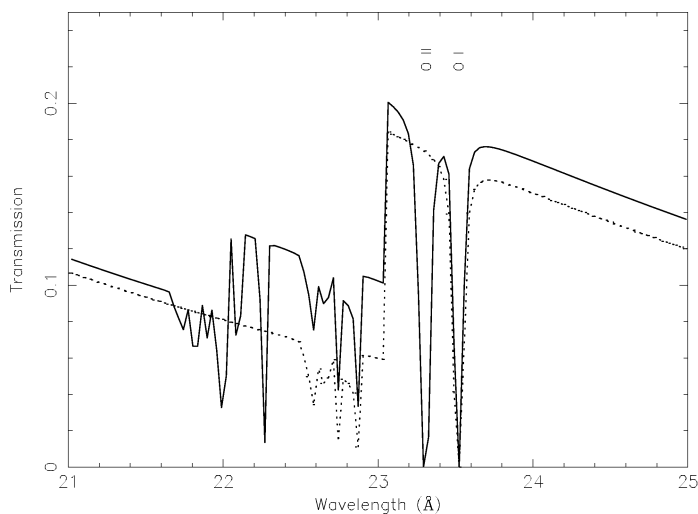Figure 7.11: The difference in transmission for the near neutral absorber ($T = 1.2$ eV, thin line) and a neutral absorber ($T = 0.5$ eV, dotted line) for the wavelength range between 21 and 25 Å. The absorption lines in both models are due to O I. The absorption lines only detected for the near neutral absorber are due to O II; note the deep O II line at 23.3 Å.

7.5.2 Warm absorbers

To explain most of the strongest lines we need an ionized absorber. The dominant component 5 is modeled by a *xabs* component and has an ionization parameter log $\xi = 1.92$, see Table 7.6. ξ is measured in units of 10^{-9} W m. Due to the low signal-to-noise ratio we froze the elemental abundances to solar while fitting the spectrum. This absorber fits the O VII and Ne IX resonance lines as well as the N VII Lyα and O VIII Lyα and (a part of) some weaker absorption lines such as Ne X and highly ionized iron. There is thus a warm absorber in IC 4329A similar to those detected in other narrow-line Seyfert 1 galaxies. The total hydrogen column density detected for this absorber ranges from 1.32×10^{25} m^{-2} for the lowest ionized absorber component 3 to 6.6×10^{25} m^{-2} for component 5. These total hydrogen column densities are similar to the hydrogen column density detected in other Seyfert 1 galaxies such as NGC 5548 (Kaastra et al. 2002a; Steenbrugge et al. 2003).

There are some remaining absorption features in the spectrum that can be fit by a relatively cool absorber (component 3, log $\xi = -1.37$), which in particular produces

158

lines and an edge of O III as well as some continuum depression due to the UTA of iron. We modeled this absorber with a *xabs* model. To test that this lowly ionized absorber is not part of the host galaxy we tried fitting this absorber with a *hot* component. This worsens χ^2 by 21 for 2377 dof, letting the other absorbers free in the fit. However, as the difference in the model is mainly the continuum depression due to the UTA, no strong conclusions can be drawn as to whether this absorber is photoionized and is part of the warm absorber or is collisionally ionized and belongs to the host galaxy. Fig. 7.13 details the models of these seven absorption components and the net absorption model.

In most warm absorbers known up to now, a range of ionization parameters is detected. Adding component 4 (log ξ = 0.56) improves χ^2 by 52 for 2373 dof. Finally, we detect a highly ionized absorber with log ξ = 2.70, but with a small total hydrogen column density.

No strong narrow emission lines are detected in the soft part of the spectrum. We found an upper limit of 1×10^{50} photons s^{-1} or an EW < 0.6 Å for the O VII forbidden
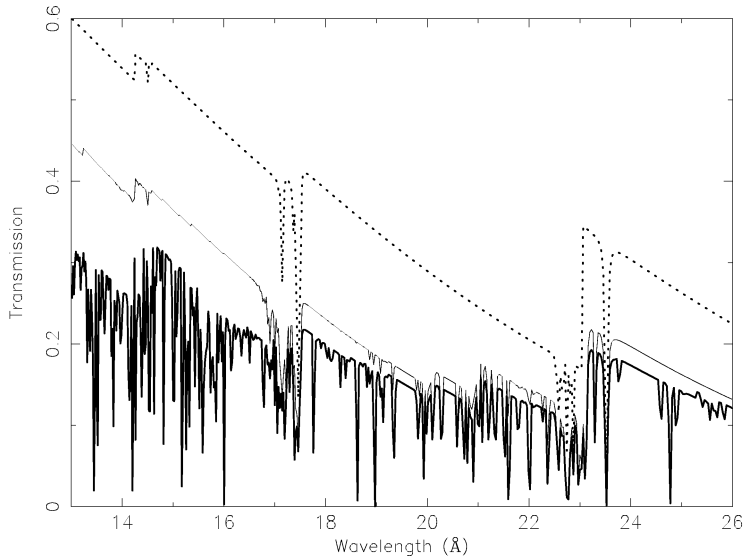

Figure 7.12: The transmission of the neutral absorber (dotted line), the neutral and lowly ionized absorber (thin line) and the transmission also including the medium and highly ionized absorbers (thick line).

159

Table 7.5: The model column densities of the most prominent ions in the spectrum of IC 4329A. For each ion we indicated the absorption component that is dominant in producing absorption from this ion.

Ion	log N_H (m^2)	comp	Ion	log N_H (m^2)	comp
N VII	22.1	5	Ne X	21.6	5
O I	22.2	2	Fe IV	20.0	3
O II	20.6	3	Fe VI	20.1	3
O III	21.8	3	Fe XVIII	20.0	5
O IV	21.6	3	Fe XIX	20.0	6
O V	20.9	3,4	Fe XX	20.2	6
O VI	21.0	4	Fe XXI	20.2	6
O VII	21.7	5	Fe XXII	20.4	6
O VIII	22.4	5	Fe XXIII	20.3	6
Ne IX	21.4	5			

line; and 1.4×10^{49} photons s^{-1} or an EW < 0.03 Å for the Ne IX forbidden line. There are 1 σ significant emission features at 8.54 Å and 11.65 Å, however, as there is no straightforward identification for these features these are probably due to hot pixels or noise.

7.5.3 Absorption at z = 0: component 7

The last absorbing system detected is due to hot gas at $z = 0$, previously detected in the spectra of other AGN (Rasmussen et al. 2003; Nicastro et al. 2002; Steenbrugge et al. 2003; Behar et al. 2003). In the IC 4329A spectrum there are two absorption lines due to this local gas, i.e. with zero redshift. We identified both as due to O VII, the strongest line being the resonance line at 21.6 Å (see Fig. 7.10). For this line we measure an equivalent width of 0.03 ± 0.02 Å. The absorption line at 18.62 Å (see Fig. 7.9) is expected to be weaker and has an EW of 0.01 ± 0.01 Å. Interestingly, no O VIII Lyα line is detected. The O VI line is too blended with a redshifted O I absorption line to be detectable. The O V line at 22.374 Å is also not detected at $z = 0$. Assuming that the absorbing gas is in collisional equilibrium, we determine provisionally a temperature range between 0.03 and 0.2 keV. However, from detecting only two O VII lines we cannot conclude that the gas is in collisional equilibrium. Assuming that the gas is photoionized, which is less likely as the source of radiation is not known, we

Table 7.6: Absorption components in the IC 4329A spectrum as determined from the RGS spectra. The second order was also included in the fit, so as to have a more accurate measurement of the velocity width as well as the outflow velocity. The outflow velocity was frozen to 0 km s^{-1} for the component 2 and 3 as some of the stronger lines in the spectrum have uncertain wavelength, or are detected only in the form of blends.

comp.	1	2	3	4	5	6	7
origin	Gal.	IC 4329A	IC 4329A	IC 4329A	IC 4329A	IC 4329A	Gal/ISM
model	hot	hot	xabs	xabs	xabs	xabs	see text
N_H^a	0.455^e	1.732 ± 0.009	1.32 ± 0.03	0.32 ± 0.03	6.6 ± 0.4	2.0 ± 0.5	–
$\log \xi^b$	–	–	-1.37 ± 0.06	0.56 ± 0.10	1.92 ± 0.03	2.70 ± 0.06	–
T^c	0.5^e	0.5^e	–	–	–	–	–
v^d	0^e	0^e	0^e	-200 ± 100	-100 ± 100	20 ± 160	–
σ_v^d	50^e	< 50	45 ± 20	90 ± 60	70 ± 10	140 ± 75	–

^{a} in 10^{25} m^{-2}.
^{b} in 10^{-9} W m.
^{c} in eV.
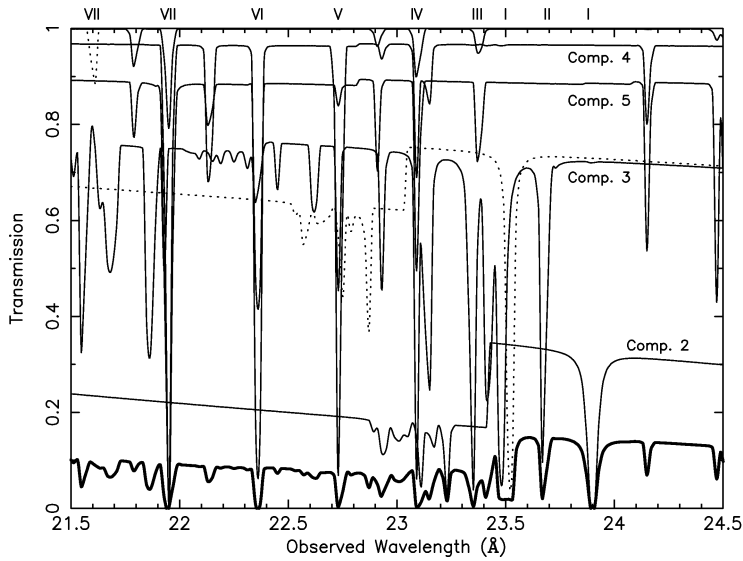^{d} in km s^{-1}.
^{e} fixed parameter.

Figure 7.13: Part of the spectrum detailing the transmission for the seven different absorption components. The thick line indicates the best fit spectral model, i. e. with all seven absorption models applied. The dotted line at the top with only an O VII absorption line is component 7, the other dotted line is component 1, or Galactic absorption. The solid line on the top represent component 6, the other components are labeled in the plot. In roman numerals the ionization state of oxygen is indicated, from neutral oxygen (I) to O VII (VII).

find an ionization parameter of $\log \xi \sim 0.8$. The presence of these absorption lines in the spectrum indicates that using AGN spectra it is possible to obtain a measure for the amount of highly ionized local gas, as well as an indication of its temperature or ionization balance.

7.5.4 Broad emission lines

Compared to the best fit with our absorption model, there appears to be an excess at the wavelengths around N VII Lyα and O VIII Lyα in both the RGS and pn spectra. These excesses can be fit by either broad Gaussians or by diskline profiles. For the diskline profile we used one set of parameters for the inner and outer edge of the accretion disk, the emissivity slope q (as defined in Sect. 7.4.2) and the inclination angle i. The

Table 7.7: Best fit results for the emission lines observed in the soft X-ray part of the spectrum. The lines were fitted using Gaussians (columns 2 and 3) and disklines (column 4 and 5), in both cases the energy of the line was frozen to its rest-energy at the redshift of IC 4329A. The disklines parameters were fit for both disklines simultaneously.

	Gaussian	Gaussian	diskline	diskline
$norm^a$	25 ± 1	1.4 ± 0.2	20.4 ± 0.5	4.2 ± 0.3
λ^b	24.78	18.97	24.78	18.97
$FWHM^c$	4.5 ± 0.1	4.1 ± 0.3		
EW (Å)	5.8 ± 0.2	0.57 ± 0.08	3.8 ± 0.1	0.26 ± 0.02
R_{in}^c			1.3	
R_{out}^c			400	
q			1.9 ± 0.4	
i (deg)			80.9 ± 0.4	

^{a} in 10^{51} photons s^{-1}.

^{b} in Å and in the restframe.

^{c} in Å.

^{d} in GM/c^2.

result of the model with and without these diskline profiles can be seen in Fig. 7.14. Leaving the wavelength of the lines frozen to the rest wavelength in IC4329A, the diskline model gives a substantial better fit, lowering χ^2 by 368 for 2367 dof. However even in the fit with the disklines, there is still an excess, most pronounced at shorter wavelengths. For the N VII Lyα emission line this excess produces a narrow emission line like feature at 25.05 Å.

Table 7.7 compares the model with Gaussian and disklines profiles. Adding the disklines reduces the modified black body temperature, as the excess is partly fitted by this continuum component. However, the newly derived temperature for the modified black body is still quite high, compared to other Seyfert 1 galaxies. We did not include a C VI Lyα emission line as the absorption at the longer wavelength is too strong. Note that the inclination determined for the disklines is rather high, similar to the inclination of the host galaxy. This is in contrast to the inclination determined from the hard X-ray Fe Kα and Fe XXVI Lyα emission lines, which however are also very well fit with narrow Gaussians.
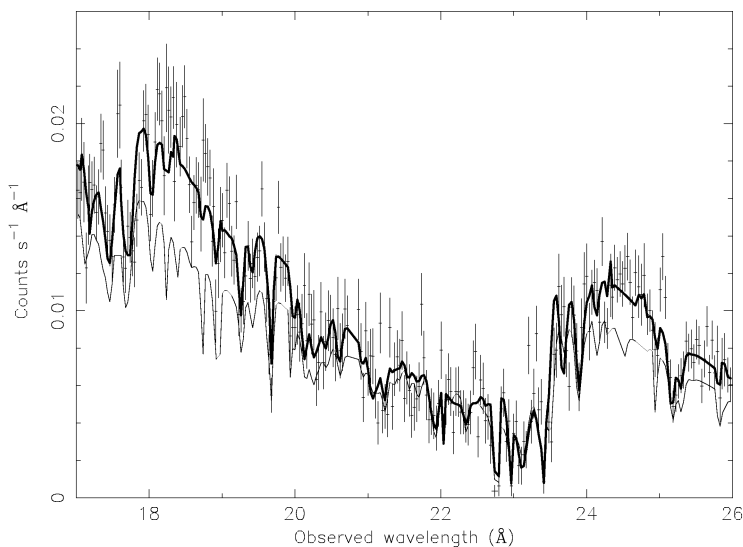
Figure 7.14: The best fit model with the disklines fit (thick line) versus the model without these excesses fit (thin line).

7.6 Discussion

We detect no variability in the softness ratio, although the luminosity varied by about 17 %. Perola et al. (1999) observed in their broad band BeppoSAX spectrum significant variations in the lightcurve between $0.1 - 100$ keV. However, only marginal evidence for variations in the hardness ratios were detected. Singh, Rao & Vahia (1991) found from EXOSAT data that IC 4329A was continuously variable, with one 12% change in luminosity over a 20 ks period, corresponding to a characteristic timescale $\tau = 170$ ks. This characteristic timescale is very similar to those measured from our lightcurve. They did not record variability on timescales shorter than ~ 10 ks.

In the IC 4329A spectrum there are seven different absorbing systems, and disentangling them is rather complicated. First there is absorption due to cold gas in our own Galaxy (component 1) and warm gas in its surrounding (component 7). On the other hand there is strong absorption due to neutral gas in the host galaxy, as determined from the reddening measured in the optical, UV bands and our X-ray spectrum (component 2). This is consistent with the dusty luke-warm absorbers measured in NGC 3227 and Ark 564 (Crenshaw & Kraemer 2001). Further, there is the warm absorber, probably

originating close to the central source. This absorber is photoionized and represented by components $3 - 6$.

This warm absorber has a range in ionization parameters and total hydrogen column density similar to NGC 5548 (Kaastra et al. 2002a; Steenbrugge et al. 2003), NGC 3783 (Blustin et al. 2002; Kaspi et al. 2002), and NGC 7469 (Blustin et al. 2003). As such, the warm absorber seems very similar to other sources observed, with an increase in column density with ionization parameter. The outflow velocity measured is similar to the lowest outflow velocity (component 5) of NGC 5548 (Crenshaw et al. 2003), and is smaller than the outflow velocity observed in NGC 3783 (Blustin et al. 2002). From Table 7.6 there is a slight trend for increasing velocity dispersion with increasing ionization parameter from < 50 km s^{-1} for lowly ionized component 3 to 140 ± 75 km s^{-1} for the highest ionized component 6. No trend of velocity dispersion versus ionization parameter was observed for the high signal to noise ratio LETGS observations of NGC 5548 (Steenbrugge et al. 2003) or other observed Seyfert 1 galaxies. The opposite trend was observed in the Seyfert 2 galaxy NGC 1068 by Brinkman et al. (2002) where the lowest ionization parameters had the largest velocity dispersion.

There is a broad excess measured at some wavelength ranges, most notably near the O VIII Lyα (18.969 Å) and N VII Lyα (24.781 Å) emission lines. These are best fit with disklines (solid line in Fig. 7.7, and the thick line in Fig. 7.14), although even then there remains excess emission for both wavelength bands. The determination of the inclination angle of the accretion disk is an important discriminator between the different models explaining the narrow absorption lines. Assuming the excesses have a diskline profile, we can determine the inclination angle (Laor 1991), namely 80.9° ± 0.4, consistent with the 80.79° inclination angle measured for the host galaxy (Keel 1980). The emissivity slope is 1.9, similar to previously measured emissivity slopes. A Gaussian fit to these excesses is notably poorer, but from the UV band we know that broadened emission lines can be quite complex requiring several Gaussians to fit one line (Crenshaw et al. 2003). Further is the FW0I measured for the soft X-ray lines similar to the 13,000 km s^{-1} as measured in the optical. It is thus unlikely that these excesses have diskline profiles.

In the EPIC spectra we detect narrow Fe Kα and Fe XXVI Lyα emission lines. The intensities of these lines are consistent with the intensities measured with the earlier *Chandra* observation. The intensity of the Fe Kα emission line is consistent between all observations since August 1997. This constant intensity and the narrowness of the line leads us to conclude that the line is probably formed at a large distance from the black hole. Assuming that the Fe Kα and Fe XXVI emission lines have diskline profiles we find a very low inclination angle of 20° and a low emissivity slope of about 1, consistent with McKernan & Yaqoob (2004). The resulting profile is very similar to a Gaussian (dotted line in Fig. 7.7). As a result we cannot distinguish from our

spectra whether these lines have a diskline profile or not. As both determinations of the inclination angle discussed are inconsistent, we conclude that it is unlikely that disklines are detected in IC 4329A with current instrumentation.

7.7 Summary

IC 4329A has a heavily absorbed X-ray spectrum. In the complex high spectral resolution data studied, we detect seven distinct absorbers. From IC 4329A we detect absorption from the host galaxy, which is neutral; and absorption from the warm absorber closer to the nucleus. The warm absorber is similar to the warm absorber detected in NGC 5548, and has four different ionization components. The ionization parameters of the warm absorber components span at least two orders of magnitude. Similar to other Seyfert 1 galaxies, most of the gas in the warm absorber is highly ionized. We conclude that IC 4329A does not have a luke-warm absorber as suggested from a comparative study in the UV band. The lowest ionized component modeled here as absorption from the warm absorber could alternatively be also absorption from the host galaxy. If this is the case, then the gas in the host galaxy is lowly ionized instead of neutral. Two of the seven detected absorption components are not related to IC 4329A: the Galactic absorption and a moderately ionized absorber at redshift zero.

In our best fit to the data we need two broadened lines to fit the emission of the O VIII and N VII Lyα lines. The fit with disklines is statistically better than a fit with two Gaussian lines. However, from broad emission line studies in the optical and UV band, we know that the line profile of these broad lines is complex, and poorly reproduced by a Gaussian line. Therefore, we conclude that the broadened lines are similar to the broad emission lines detected in the optical and UV band, and are not related to the disklines detected in some AGN.

We detect a narrow Fe Kα line, and conclude from the lack of variability since the 1997 ASCA observation, that this line is probably formed at a distance of several pc from the nucleus. If we fit the Fe Kα line with a diskline, we find parameters similar to those obtained from the HEG data (McKernan & Yaqoob 2004). However, this profile can not be distinguished from a Gaussian line with current instrumentation, and we thus prefer the fit with a Gaussian line.

From the lightcurve we find that the flux varied by 17%, and that the characteristic timescale for variability was between 120 ks and 190 ks. This is similar to previous measured characteristic timescales in this source. Consistent with earlier results, we did not detect variability in the softness ratio for this source, indicating that the soft and hard X-ray emission varied simultaneously.

References

Behar, E., Sako, M. & Kahn, S. M., 2001. ApJ, 563, 497

Behar, E., Rasmussen, A. P., Blustin, A., et al., 2003, ApJ, 598, 232

Blustin, A. J., Branduardi-Raymont, G., Behar, E., et al., 2002, A&A, 392, 453

Blustin, A. J., Branduardi-Raymont, G., Behar, E., et al., 2003, A&A, 403, 481

Brinkman, A. C., Kaastra, J. S., van der Meer, R. L. J., et al., 2002, A&A, 396, 761

Crenshaw, D. M. & Kraemer, S. B., 2001, ApJ, 562, L29

Crenshaw, D. M., Kraemer, S. B., Gabel, J. R., et al., 2003, ApJ, 594, 116

Disney, M. J., 1973, ApJ, 181, L55

Done, C., Madejski, G. M. & Zycki, P. T., 2000, ApJ, 536, 213

Elvis, M., Lockman, F. J. & Wilkes, B. J., 1989, AJ, 97, 3

Elvis, M., 2000, ApJ, 545, 63

Gondoin, P., Barr, P., Lumb, D., et al., 2001, A&A, 378, 806

Juett, A. M., Schulz, N. S. & Chakrabarty, D., ApJ, submitted

Kaastra, J. S. & Barr, P., 1989, A&A, 226, 59

Kaastra, J. S., Steenbrugge, K. C., Raassen, A. J. J., et al., 2002a, A&A, 386, 427

Kaastra, J. S., Mewe, R. & Raassen, A. J. J., 2002b, Proceedings Symposium 'New Visions of the X-ray Universe in the XMM-*Newton* and *Chandra* Era'

Kaspi, S., Brandt, W. N., George, I. M., et al., 2002, ApJ, 574, 643

Keel, W. C., 1980, AJ, 85, 3

Laor, A., 1991, ApJ, 376, 90

Markowitz, A., et al., in preparation

McKernan, B. & Yaqoob, T., 2004, submitted to ApJ

Miyoshi, S., Yamashita, K., Okumura, Y., et al., 1988, PASJ, 40, 127

Morrison, R. & McCammon, D., 1983, ApJ, 270, 119

Nicastro, F., Zezas, A., Drake, J., et al., ApJ, 573, 157

Palmeri, P., Mendoza, C., Kallman, T. R., Bautista, M. A. & Meléndez, M, 2003, A&A, 410, 359

Perola, G. C., Matt, G., Cappi, M., et al., 1999, A&A, 351, 937

Rasmussen, A., Kahn, S. M. & Paerels, F. B. S., ASSL Conference Proceedings Vol. 281 'The IGM/Galaxy Connection: The Distribution of Baryons at z=0'

Singh, K. P., Rao, A. R. & Vahia, M. N., 1991, ApJ, 377, 417

Steenbrugge, K. C., Kaastra, J. S., de Vries, C. P. & Edelson, R., 2003, 402, 477

Urry, C. M. & Padovani, P., 1995, PASP, 107, 803

Willmer, C. N. A., Focardi, P., Chan, R., Pellegrini, P. S. & Nicolaci Da Costa, L., 1991, AJ, 101, 57

Wilson, A. S. & Penston, M. V., 1979, ApJ, 232, 389

Chapter 8

Intergalactic X-ray absorption toward TON 1388

K.C. Steenbrugge & J.S. Kaastra

Abstract

We present a high resolution X-ray spectrum of QSO Ton 1388 (PG 1116+215) as observed with the LETGS of *Chandra*. We find no evidence for intrinsic absorption features in the QSO spectrum and put upper limits to the column density of photoionized gas in front of the X-ray continuum source. However, we find evidence for discrete X-ray absorption lines of Ne, O, N and C from intervening material in the line of sight toward Ton 1388. These absorption lines are associated with 3 of the 16 previously detected Lyα absorbers, at redshifts of 0.0413, 0.0812 and 0.1670, indicating a multi-temperature environment. Finally, we find evidence for a weak kpc-scale X-ray jet in this QSO.

8.1   Introduction

Baryons constitute only 4 % of the total mass density of the universe (see for example Burles & Tytler 1998). While at large redshifts most of these baryons are detected, in the local universe still a large fraction is missing. It is presumed to be in the form of a

169

Warm-Hot Intergalactic Medium (WHIM; Cen & Ostriker 1999) with temperatures in the range of 10^5–10^7 K, and containing half of the present-day baryon mass. However, until recently it has been extremely difficult to observe this baryonic mass component. Its thermal emission is mainly emitted in the strongly absorbed EUV band, and its hardest components in the soft X-ray band are strongly contaminated by all kinds of Galactic and extragalactic foreground and background emission.

Only recently the presence of the WHIM has been shown by the observation of O VI absorption lines in HST and FUSE ultraviolet spectra toward a few bright quasars (for example Tripp, Savage & Jenkins 2000; Oegerle et al. 2000). These absorption line systems have redshifts in the range of 0.1–0.3 and are often associated with large scale galaxy structure close to the line of sight. In X-rays, the first detection of O VII absorption from the local group has been published by Nicastro et al. (2002). The first indications for absorption at higher redshifts have been reported by Mathur et al. (2003) in the line of sight of the quasar H 1821+643. Evidence for O VII emission from the WHIM around a few nearby clusters has been reported by Kaastra et al. (2003).

Absorption studies of the WHIM have the advantage that the gas can be detected with small aperture detectors out to large redshifts without significant attenuation. For similar small apertures, currently necessary to obtain high resolution X-ray spectra, emission studies are limited by the $1/r^2$ dependence of X-ray flux on distance. Absorption line studies are by their nature restricted to bright X-ray sources, preferentially with little intrinsic spectral structure and at large redshifts. The number of such sources is rather limited. Here we report on a deep Chandra LETGS spectrum of the quasar Ton 1388.

Ton 1388 (also known as PG 1116+215) is a relatively nearby, $z = 0.177$ (Barkhouse & Hall 2001) radio quiet quasar. It is X-ray bright, with a luminosity of $(6.2 \pm 0.8) \times 10^{37}$ W in the 2-10 keV band (Nandra et al. 1996). The galactic column density toward Ton 1388 is low, namely $N_H = 1.40 \times 10^{20}$ cm^{-2} (Lockman & Savage 1995).

Ton 1388 was observed four times with ROSAT (Ulrich & Molendi 1995). It has a constant hard power-law slope of 2.7, while the count rate varied by a factor of 1.5. Using ASCA, Nandra et al. (1996) detected an Fe Kα line on top of a featureless continuum. A high accretion rate and/or a complete ionization of the accretion disk are possible explanations given by the authors for the featureless continuum.

In the UV band, Tripp, Lu & Savage (1998) detected a total of 16 Lyα absorbers in front of Ton 1388, related to 13 galaxies. The observed lines all have a redshift between 0.01639 and 0.17366, and the equivalent width (EW) for the H I Lyα lines ranges from 54 to 447 mÅ, some lines from lowly ionized Si ions were also detected.

Here we discuss the possible detection of absorption lines from the IGM toward TON 1388. The data reduction is discussed in Sect. 8.2, Sect 8.3 details the spectral analysis. The summary and discussion are given in Sect 8.4.

Table 8.1: Upper limits to the total column density for different ionization parameters in Ton 1388. Note that the increasing column density limits for higher ionization states is a direct result of the fact that most elements are fully ionized.

$\log \xi^a$	$\log N_H{}^b$	$\log \xi^a$	$\log N_H{}^b$
0.5	< 23.81	2.5	< 24.07
1.0	< 23.13	3.0	< 24.28
1.5	< 23.33	3.5	< 25.31
2.0	< 23.67		

^{a} in 10^{-9} W m.
^{b} in m^{-2}.

8.2 Observation and data reduction

The *Chandra* data were obtained as part of the Guaranteed Time Observation program on June 29, 2002, with a total exposure time of 90.5 ks. The data were taken with the Low Energy Transmission Grating (LETG) in combination with the High Resolution Camera (HRC-S). The data was reduced using in-house software, the used procedure being described in detail by Kaastra et al. (2002a). The spectral resolution of the LETGS is 0.05 Å. The wavelength scale, as calibrated using the Capella spectrum, is accurate to about 3 mÅ in the spectral bands with O VII and O VIII lines, and is 10 mÅ for the longer wavelength band (Kaastra et al. 2002a; van der Meer et al. 2002). In the spectral region up to 40 Å the relative effective area is accurate to a few percent, and the absolute effective area is accurate to about 10%. In the response matrix up to the ± tenth order are included. For more details see Kaastra et al. (2002a). All spectral analysis in this paper was done with the SPEX software (Kaastra et al. 2002b).

The zeroth order image shows some evidence for a second component at a distance of $0.90'' \pm 0.15''$ at position angle $329° \pm 6°(N \rightarrow E)$ with a flux of 4.3 ± 1.5 % of the flux of the core. This could perhaps be a weak jet. The position angle of this X-ray jet coincides with the position angle of the large scale radio jet (330° at a distance of $78''$, Kellerman et al. 1994). The total flux shows a steady 9 % decrease during the observation.

8.3 Spectral analysis

The spectrum of Ton 1388 is fitted by a power-law with Galactic absorption. The average flux (in the 2-10 keV band) during our observation is $(5.1 \pm 0.1) \times 10^{-15}$ W m^{-2}, similar to the ASCA value of $(4.2 \pm 0.5) \times 10^{-15}$ W m^{-2}. The photon index derived from our spectrum is 2.2 ± 0.2, consistent with the photon index of 2.0 found for the ASCA observation (Nandra et al. 1996). The overall fit to TON 1388 is shown in Fig. 8.1.
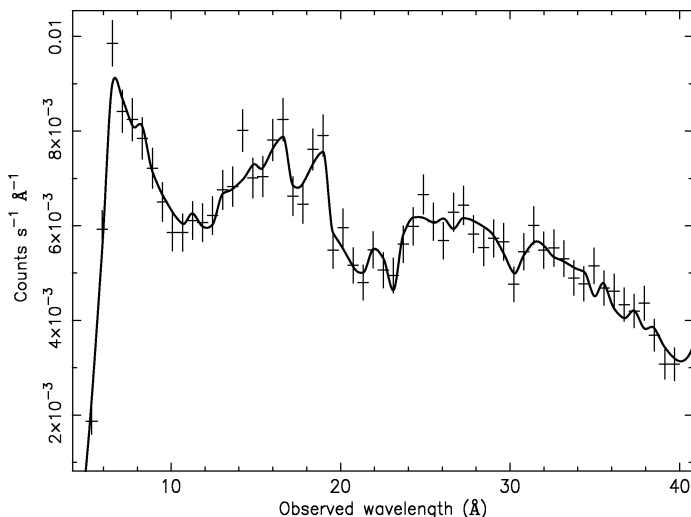
Figure 8.1: Ton 1388 spectrum rebinned to a bin size of 0.6 Å to detail the continuum fit. The narrow absorption lines listed in Table 8.2 are included in the model.

Although the spectrum is rather noisy, there is evidence for some deep absorption lines indicated in Figs. 8.2 to 8.5. We first tried to fit these features with a warm absorber associated with the quasar. We fitted the spectrum with a *xabs* model for a photoionized warm absorber (Kaastra et al. 2002a). Assuming an ionization parameter, ξ, between 3 and 3000 (in 10^{-9} W m) we determined upper limits of the total hydrogen column density, $N_{\rm H}$, of the absorber (see Table 8.1). We did not detect a warm absorber in Ton 1388, consistent with the ASCA results obtained by Nandra et al. (1996). The warm absorber, if present, is thus either fully ionized or has a small column density. Therefore the absorption lines that we observe must have a different origin. We focus now upon individual absorption features.

Table 8.2: List of all the absorption features detected with at least 3 σ significance at a wavelength smaller than the instrumental C-edge.

λ_{obs}^a	Iden.	EW	σ	λ_o^b	z_{abs}
11.70	Fe XXII[c]	42±10	3.9	11.71	0
12.61	Ne X	40±11	3.8	12.13	0.0413
15.45	Fe XIX[c]	31±10	3.1	13.57	0.1386
19.79	O VIII	38±13	3.0	18.97	0.0413
20.71	uniden.	42±13	3.2		
21.59	O VII[c]	39±13	3.0	21.60	0
	O VIII[c]	39±13	3.0	18.97	0.1386
23.35	O VII[c]	46±17	3.1	21.60	0.0812
26.76	N VII	43±11	3.8	24.78	0.0812
35.13	C VI	41±14	3.0	33.73	0.0413
35.90	uniden.	53±13	4.1		
36.66	Ar XII[c]	50±12	4.0	31.37	0.1670
39.37	C VI	52±17	3.2	33.73	0.1670

[a] observed wavelength in Å.
[b] rest wavelength in Å.
[c] see text for discussion about the identification.

We calculated the equivalent width (EW) and significance of all absorption features seen in the twice rebinned spectrum for wavelengths between 5 and 40 Å. These EWs were determined from the residuals of our best continuum fit. A Gaussian line profile was assumed in the determination of the significance. This was done to avoid uncertainties due to the continuum fit. In the Figures only narrow absorption features with at least 3 σ significance are fitted. For the absorption line identification we compared the strongest known X-ray lines at the redshift of the 16 Lyα absorbers listed by Tripp et al. (1998). The identifications are listed in Table 8.2, together with the statistical significance and the measured EW's. Some of the lines are spurious: no Fe XXII absorption is expected from the Galaxy. Similarly, the X-ray detection of the absorber at z=0.1386 is spurious, as the O VIII Lyα line coincides with the Galactic O VII resonance line; and Fe XIX is not expected to be visible without corresponding lines from neighboring ions. The presence of Ar XII is unexpected, although it has been detected before in active galactic nuclei (see Brinkman et al. 2002). Further are there two absorption lines of Ar XI with over 2 σ significance at the same redshift. The O VII line at 23.35 Å coincides with the instrumental O-edge, and thus its significance is somewhat

173

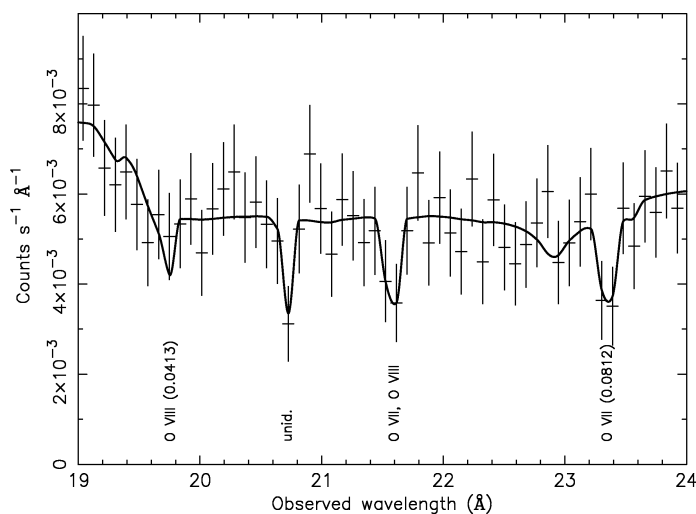uncertain. There remain two lines that we could not identify with prominent absorption lines in the X-rays.

Figure 8.2: Detail of the Ton 1388 spectrum, not identified features in the model are instrumental. Only those features that have at least 3 σ significance in the twice rebinned spectrum, and are listed in Table 8.2 are modeled.

We focus upon the following three possible absorbers: $z = 0.0413, 0.0812, 0.1670$, which have at least two lines that are detected with a 3 σ significance. Fig. 8.2 details the spectral region with absorption lines from O VII and O VIII. Fig. 8.3 shows the narrow absorption features seen at longer wavelengths, while Fig. 8.4 details the spectral region between 10 and 16 Å. Fig. 8.5 shows the N VII absorption line for the Lyα absorber at z = 0.0812. The absorption features that are identified, but not modeled, have less than 3 σ significance, but can be identified with one of the three absorbers identified above.

As an alternative method to detect absorbing systems we determined the EW and the statistical significance of O VIII Lyα, N VII Lyα, C VI Lyα and the O VII resonance line for all 16 Lyα absorbers as well as their combined significance (Table 8.3). The EW was derived in the same way as described above, using the fit residuals from the global continuum fit. The probability distribution was determined from Monte Carlo simulations of random noise producing absorption lines in a random redshifts between 0 and the redshift of Ton 1388. The three absorbing systems that we found above
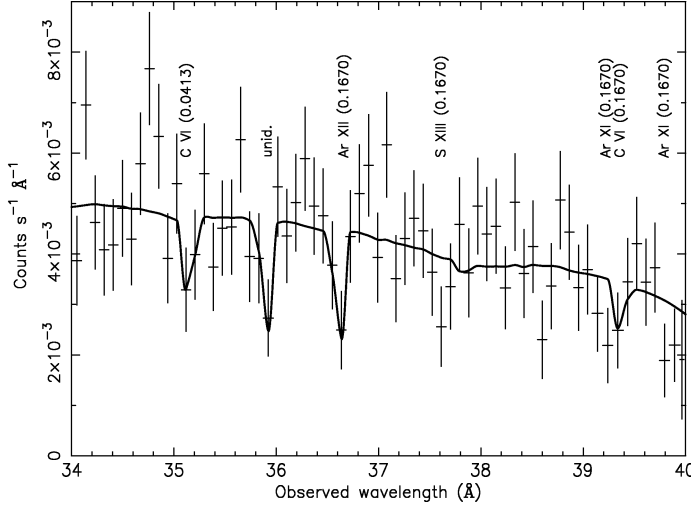
174

Figure 8.3: Same as Fig. 8.2, but for the $34-40$ Å wavelength range.

from the individual line identifications have a total probability of being due to random fluctuations of only 0.07, 0.04 and 0.05, respectively.

To further ascertain that we have "detected" these Lyα absorbers, we checked for physical consistency by comparing the observed EW's with those expected from photoionization or collisional ionized plasma models. Using the observed EW ratios we determined the ionization parameter or temperature, respectively. Then by using these parameters we determined which other ions should give detectable absorption lines, and assuming solar abundances (Anders and Grevesse 1989), determined their formal EW's from our standard spectrum with a total column density $N_{\mathrm{H}} = 10^{24}$ m^{-2} and a velocity broadening of 100 km s^{-1}. All lines are expected to be unsaturated since the observed EW's are relatively small, and for all the lines with expected EW > 0.001 Å, we compared the expected versus the measured EW. The total column density $N_{\mathrm{H},24}$ (in units of 10^{24} m^{-2}) was then determined from the following equation:

$$N_{\mathrm{H},24} = \frac{\sum (EW_{\mathrm{obs}} \times EW_{\mathrm{mod}}/\sigma^2)}{\sum (EW_{\mathrm{mod}}^2/\sigma^2)}, \tag{8.1}$$

where σ is the nominal error on the EW. The results are summarized in Table 8.4. As a consistency check, we also calculated the formal EW's for a model with $N_{\mathrm{H}} = 10^{23}$ m^{-2} and a velocity broadening of 30 km s^{-1} and found similar results.
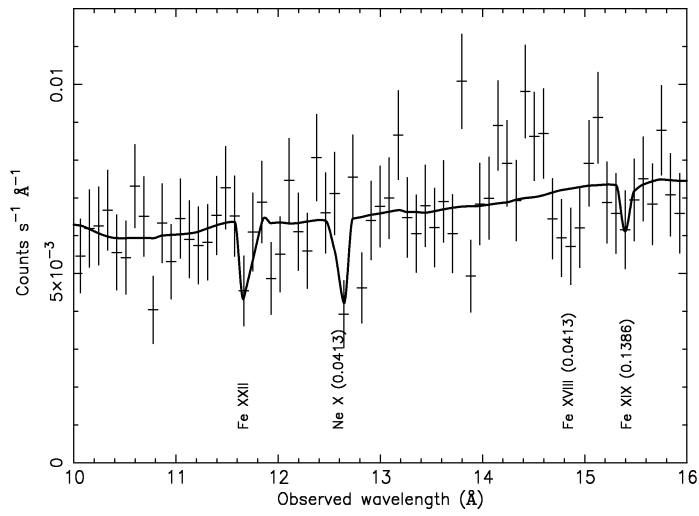
175

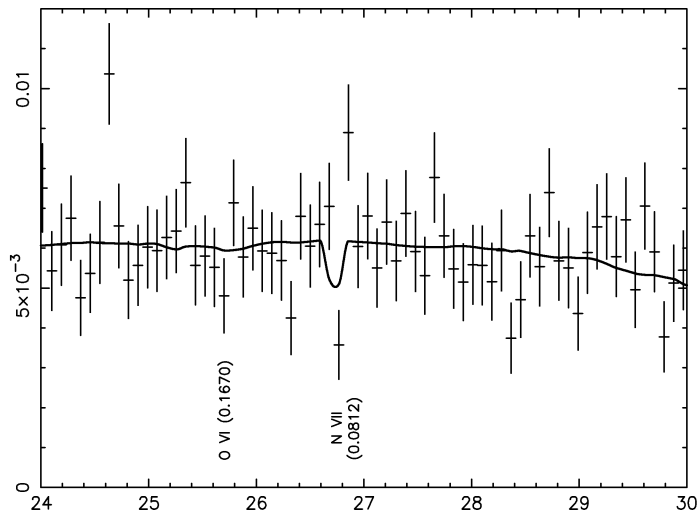Figure 8.4: Same as Fig. 8.2, but for the $10-16$ Å wavelength range.

Figure 8.5: Same as Fig. 8.2, but for the $24-30$ Å wavelength range.

176

Table 8.3: The EW's in mÅ of C VI Lyα, N VII Lyα, O VII resonance line and O VIII Lyα. Negative numbers denote absorption lines, positive emission lines. We also list the random probabilities for an EW of this value for the four lines and a combined probability. For the 3 "detected" Lyα absorbers we find P_{tot} = 0.07, 0.04 and 0.05.

z_{abs}	CVI EW	NVII EW	OVII EW	OVIII EW	P_{CVI}	P_{NVII}	P_{OVII}	P_{OVIII}	P_{tot}
0.0164	-21±16	5±16	2±17	-13±13	0.23	0.66	0.52	0.14	0.27
0.0195	-30±15	3±16	-9±15	2±14	0.12	0.62	0.21	0.59	0.21
0.0284	0±17	-16±14	24±19	-12±14	0.66	0.12	0.92	0.18	0.44
0.0322	35±19	-10±14	-9±16	-12±15	0.99	0.25	0.23	0.21	0.56
0.0413	-41±14	4±16	-11±16	-38±13	0.03	0.64	0.19	0.29	0.07
0.0591	-13±17	0±16	36±22	8±18	0.36	0.54	0.97	0.73	0.85
0.0608	-8±18	-18±14	3±19	8±17	0.46	0.09	0.54	0.74	0.37
0.0812	-7±18	-43±11	-46±17	-12±15	0.49	0.06	0.04	0.19	0.04
0.0928	8±20	22±17	1±17	-35±13	0.77	0.93	0.50	0.03	0.42
0.1191	-17±19	20±17	6±16	9±17	0.32	0.92	0.66	0.77	0.83
0.1316	12±21	-15±14	-22±14	2±17	0.85	0.14	0.04	0.59	0.26
0.1386	-24±18	-14±14	32±18	-39±13	0.22	0.16	0.97	0.02	0.12
0.1655	-22±22	-8±16	12±17	5±17	0.28	0.31	0.80	0.66	0.47
0.1662	-44±19	-9±15	2±15	-3±17	0.09	0.28	0.55	0.46	0.16
0.1670	-52±17	-8±16	4±16	-12±16	0.02	0.31	0.61	0.21	0.05
0.1738	7±23	9±17	29±18	3±17	0.73	0.78	0.97	0.62	0.98

Table 8.4: Properties of the detected absorption systems. The redshift is taken from the UV absorption (Tripp et al. 1998). For the photoionized case (PIE) the ionization parameter, ξ, and the total hydrogen column density, N_H are listed. For the collisional ionization case (CIE) we list the temperature, T, and the total hydrogen column density, N_H.

absorber	PIE		CIE	
z_{abs}	$\log\xi$ (10^{-9} W m)	N_H (10^{24} m^{-2})	T (10^6 K)	N_H (10^{24} m^{-2})
0.0413	2.0	1.52±0.41	1.0	0.66±0.25
0.0812	1.8	0.59±0.35	1.7	0.71±0.25
0.1670	1.3	0.62±0.22	1.2	0.55±0.27

For the X-ray absorber at $z = 0.0413$ we detect O VIII, Ne X, C VI and have a $> 2\,\sigma$ detection of Fe XVIII. Photoionization models imply that O VII, N VII and Ne IX should also be present, and the upper limits measured for these lines are consistent with the predicted values. In a collisional ionized plasma, C VI and Ne X/Fe XVIII are produced at different temperatures. Therefore we need two temperature components, namely one at 1.0×10^6 K and the other at 4.6×10^6 K. For the 1.0×10^6 K temperature component O VII and Ne IX are present; for the 4.6×10^6 K component oxygen, nitrogen and carbon are completely ionized. The other two X-ray absorbers only need one temperature component to describe the X-ray absorber. All three X-ray absorbers are also well modeled by a single ionization parameter.

8.4 Summary and discussion

We have found evidence for X-ray absorption from three earlier detected Lyα absorbing systems at $z = 0.0413$, 0.0812 and 0.1670. The confidence level for these detections are 93%, 96% and 95%, respectively, based upon only the C VI, N VII, O VII and O VIII lines. Assuming photoionization and taking all the relevant absorption lines into account, our derived column densities (Table 8.4) imply a cofidence level of 99.989%, 95% and 99.76%, respectively. The results for collisionally ionized models are less significant, but from our data we cannot exclude them.

For the highest redshift Lyα absorber, $z = 0.1670$ recent FUSE data showed absorption from O VI (Sembach, Tripp & Savage 2002). In the X-rays we found a $\geq 2\,\sigma$ significant detection for this ion. For this Lyα absorber there is an indication that it is

associated to a cluster of galaxies or even a supercluster. In a four square-degree field on the sky, centered on Ton 1388, we found seven clusters of galaxies. Only one has a measured redshift, namely Abell 1234, with $z = 0.1663$. This cluster of galaxies is separated by 14 Mpc in projected distance from the Lyα absorber.

Nicastro et al. (2002) detected local ($z \sim 0$) absorption of O VII, O VIII and Ne IX in the line of sight toward PKS 2155-304. They found a similar ionization state and total column density ($N_\mathrm{H} = 2.1 \times 10^{23}$ m^{-2}) as we derived for the three Lyα absorbers seen toward Ton 1388. The authors conclude that the local gas is photoionized and that Ne is overabundant compared to O. Mathur, Weinberg & Chen (2003) detected at least one $> 2\,\sigma$ significant absorption line for three of the six redshifted Lyα absorbers toward H1821+643. The authors also found evidence for two absorbers, which were not detected in previous UV studies. From the line ratios the authors deduced that the gas is photoionized, and they infer EW's for O VII between 7.3 ± 6.3 and 15.1 ± 5.8 mÅ. For the O VIII line the EW's range between 5.2 ± 4.9 and 11.1 ± 5 mÅ. These values are between a half and a third of the EW's we determined, but are consistent at the $2\,\sigma$ level.

However, from UV data (e.g. Savage et al. 2002 toward PG 0953+415; Jenkins et al. 2003 toward PHL 1811) lower total column densities and ionization states for Lyα absorbers are found. Savage et al. (2002) report for the $z = 0.06807$ Lyα absorber toward PG 0953+415 $N(\mathrm{O\ VI}) = 1.66 \times 10^{18}$, $N(\mathrm{N\ V}) = 3.2 \times 10^{17}$, $N(\mathrm{C\ III}) = 4.47 \times 10^{17}$ and $N(\mathrm{C\ IV}) = 1.17 \times 10^{18}$ all in m^{-2}.

This difference in measured column density could still be consistent with one absorber, if the Lyα absorbers detected in the X-rays are in a high ionization state. Actually the detection of O VII, O VIII and Ne X does support this view. A difference in ionization between different Lyα absorbers could then explain why neither Mathur et al. (2003) nor we detect in the X-rays the Lyα absorber with the largest EW in the UV band. Alternatively, the Lyα absorbers could have a ionization gradient instead of the assumed single ionization state. In that case the column density for highly ionized gas is small for the Lyα absorbers not detected in the X-rays.

References

Anders, E. & Grevesse, N., 1989, Geochim. Cosmochim. Acta 53, 197

Barkhouse, W. A. & Hall P. B., 2001, AJ, 121, 2843

Brinkman, A. C., Kaastra, J. S., van der Meer, R. L. J. et al., 2002, A&A, 396, 761

179

Burles, S., & Tytler, D., 1998, ApJ, 499, 699

Cen, R., & Ostriker, J.P., 1999, ApJ, 514, 1

Jenkins, E. B., Boweb, D. V., Tripp, T. M., et al., 2003, AJ, in press

Kaastra, J. S., Steenbrugge, K. C., Raassen, A. J. J., et al., 2002a, A&A, 386, 427

Kaastra, J. S., Mewe, R., Raassen, A. J. J., 2002b, Proceedings Symposium 'New Visions of the X-ray Universe in the XMM-Newton and Chandra Era'

Kaastra, J. S., Lieu, R., Tamura, T., Paerels, F. B. S. & den Herder, J. W., 2003, A&A, 397, 445

Kellerman, K. I., Sramek, R. A, Schmidt, M., Green, R. F.& Shaffer, D. B., 1994, AJ, 108, 1163

Lockman, F., J., & Savage, B., D., 1995, ApJ, 97, 1

Mathur, S., Weinberg, D.H., & Chen, X., 2003, ApJ, 582, 82

van der Meer, R. L. J., Kaastra, J. S. & Mendez, M., 2002, http://cxc.harvard.edu.ccw_02/proceeding/presentations/van_der_meer.html

Nandra, K., George, I. M., Turner, T. J., et al., 1996, ApJ, 464, 165

Nicastro, F., Zezas, A., Drake, J., et al., 2002, ApJ, 573, 157

Oegerle, W.R., Tripp, T.M., Sembach, K.R., et al., 2000, ApJ, 538, L23

Savage, B. D., Sembach, K. R., Tripp, T. M., Richter, P., 2002, ApJ, 564, 631

Sembach, K. R., Tripp, T. M. & Savage, B. D., 2002, AAS, 201, 7910

Tripp, T. M., Lu, L. & Savage, B. D., 1998, ApJ, 508, 200

Tripp, T.M., Savage, B.D., & Jenkins, E.B., 2000, ApJ, 534, L1

Ulrich, M.-H. & Molendi, S., 1995, A&A, 293, 641

Chapter 9

Summary and outlook

Three out of the six articles presented in this thesis are based upon our study of the well known Seyfert 1 galaxy NGC 5548. The main conclusions derived in this thesis are therefore based upon the study of high signal-to-noise ratio spectra of NGC 5548. These conclusions are detailed separately from the conclusions drawn from our analysis of NGC 4593, IC 4329A and Ton 1388. In this Chapter we also discuss future studies which can be done with current instrumentation or require new missions, such as Astro-E2. Finally we give a short discussion on the need for improvements in atomic data to be able to fully exploit the current and future spectra.

9.1 Results from NGC 5548

9.1.1 Relation between UV and X-ray absorber

An important question before the advent of high resolution X-ray spectroscopy was whether the absorption detected in the UV band and the X-ray band were from the same medium, or were unrelated. From low resolution spectroscopy it was known that there is a one to one correlation between UV and X-ray absorbers. However, it did seem that the ionization parameter and the column densities detected in the X-ray were sufficiently different to suggest that these were different absorbers (Crenshaw et al. 2003, however see Mathur, Elvis & Wilkes 1995 for a different view). In Chapter 4 we report the detection of an O VI absorption line in the XMM-*Newton* spectrum of NGC 5548. An O VI absorption line, from a different transition, was already detected in the UV band, clearly establishing a relation between absorption observed in both

wavelength bands. However, the column density measured in the X-ray band is still an order of magnitude larger than the column density measured in the UV band. An elegant solution to this conundrum was proposed by Arav et al. (2002; 2003). In the proposed method one can only determine lower limits to the column densities from UV observations. This restriction is due to non-black saturation, i.e. although the line is saturated, the flux measured at the particular wavelength is not zero. This non-black saturation results from a geometry where the absorber does not cover the narrow emission line region. A second reason for this restriction is the velocity dependent covering factor, i.e. the line profile is due to the covering factor, and not intrinsic to the line.

In Chapter 5 we took advantage of the higher spectral resolution of the *Chandra* spectrometers to determine the velocity structure of the absorption lines detected in the X-ray spectra of NGC 5548. The measured velocity structure is consistent with the velocity structure determined from simultaneous UV spectra (Crenshaw et al. 2003). Especially, in the X-ray spectra we resolve the highest outflow velocity component, namely the -1041 km s^{-1} component over a wide range in ionization parameter containing ions such as lowly ionized O V and highly ionized Si XIV. This indicates that within the error bars the X-ray and UV absorbers have the same kinematics. In addition, the X-ray absorber spans a range in ionization parameter that overlaps with the ionization parameter derived from the UV absorber. These conclusions firmly establish the fact that the UV and X-ray absorber are different manifestations of the same phenomenon.

9.1.2 Geometry of the absorber

The accretion disk emits radiation in the extreme UV and soft X-ray band, i.e. the soft excess component. The radiation emitted by the disk is Compton scattered by soft electrons to produce the hard X-ray continuum observed. Thus by studying AGN in the X-ray band, we study the geometry of the direct surroundings of the central SMBH. The main difference between the two models presented in Chapter 1 is the inclination angle under which one expects to observe a Seyfert 1 or a Seyfert 2 galaxy, i.e. detect an absorption or emission spectrum in the X-ray band. However, determining the inclination angle of the accretion disk is rather difficult. An exciting possibility is the detection of relativistically broadened emission lines, because the line profile is a function of the inclination angle, as well as the inner radius and the emissivity distribution. However, relativistically broadened emission lines are less frequently detected than was expected based upon ASCA low resolution spectra.

A second difference is the opening angle of the outflow or ionization cone. In the standard picture there is an ionization cone, with a rather large opening angle of

about 45° along which clouds are outflowing (Urry & Padovani 1995). The observed absorption is presumably formed in this cone. In the picture by Elvis (Elvis 2000) the outflow occurs in rather narrow streams. In Chapters 4 and 5 we calculate the opening angle of the outflow from the ionization distribution and outflow velocity measured for the warm absorber, adopting Schwarzschild geometry. For the assumptions of steady state accretion and a mass accretion rate lower than the Eddington accretion rate, we determine using the formulae for mass accretion rate, mass loss rate and ionization parameter an upper limit to the opening angle between 0.07 and 10^{-7} sr. Assuming a Kerr geometry, the opening angle is nearly an order of magnitude smaller. This indicates that the absorption occurs in narrow streams. The lowest ionized absorber has the smallest opening angle while the highest ionized absorber has the largest opening angle.

From the derived opening angle it seems that the lowest ionized absorber is in the center of the outflow, which has a density gradient perpendicular to the flow direction. Such a picture is very similar to the outflow geometries obtained by Proga et al. (2000) in their simulations of radiation driven winds. In a wind with a density gradient, there is a continuous ionization distribution perpendicular to the flow, instead of different clouds having different ionization states. In Chapters 4 and 5 we show that most of the gas is highly ionized. This seems to be general property of the warm absorbers observed with high spectral resolution instruments, and seems consistent with the results obtained from wind simulations by Proga et al. (2000). From the small opening angle of the outflow it seems that the model by Elvis (2000) better describes the warm absorber.

9.1.3   Ionization structure

We conclude in Chapter 4 that the ionization structure of the warm absorber is consistent with a continuous distribution in ionization parameter. In Chapter 5 we obtained a very good fit to the LETGS and HETGS spectra of NGC 5548 with a model assuming a continuous ionization distribution. In the same Chapter we indicate that, if the ionization distribution has discrete components, then at least five components are needed to explain the spectrum. Of these five ionization components at least the lowest ionized and possibly the highest ionized component cannot be in pressure equilibrium with the other ionization components. More generally, the observed UV absorber can not be in pressure equilibrium with the higher ionized X-ray absorber. However, the above conclusions can not prove that the ionization structure is continuous, as there are other confinement methods possible such as confinement through magnetic fields.

From our analysis we argue that in the case of NGC 5548 the ionization distribution is continuous and has a power law distribution. Neither the standard model (Urry &

Padovani 1995) nor the model by Elvis (2000) predicts a continuous ionization distribution, as both models rely on clouds in pressure equilibrium confined by a hot gas. Interestingly, the highest velocity outflow component seems to have a different ionization distribution. Namely, the ratio for highly ionized gas over lowly ionized gas is substantially higher than for the other velocity components.

9.1.4 Can the outflow escape?

An important question regarding the matter distribution surrounding the SMBH is the distance of the warm absorber from the central SMBH. This distance is important in determining whether the outflow can escape the SMBH and the accretion disk, or must fall back upon it. From the time lag between the measured variability in the luminosity and the ionization parameters it is in principle possible to determine the distance of the warm absorber. However, there is a caveat, in Chapter 5 we discuss that for an outflow with a density structure perpendicular to the outflow, spectral variability in the warm absorber should only be detected in the neutral or very lowly ionized absorber and possibly the highly ionized absorber, assuming a cut-off in column density for high ionization parameters. In a wind with a continuous ionization distribution it is thus not possible to estimate the distance from the ionizing source. In NGC 5548 we did not detect any spectral variability, with the exception of O V over a timespan of 2 years. Thus for this object we can not determine a distance of the warm absorber, however, we can determine the minimum distance needed for the outflow to be able to escape the SMBH and the accretion disk. In the Chapter 5 we calculate that the highest velocity outflow will escape if the distance of the outflow from the SMBH is larger than 0.58 pc. In the model by Elvis (2000) the measured outflow velocity is not the final radial velocity for the outflow, and thus the distance between the SMBH and the outflow can be even smaller.

9.1.5 Broadened emission lines

In the LETGS spectrum of NGC 5548 we detect weak broadened emission lines, similar to the broad emission lines detected in optical and UV spectra. We detect the blend of the O VII triplet emission lines with 3 σ significance, and several weaker lines. In Chapter 6 we determine the physical parameters of the medium producing the highly ionized and the simultaneously observed lower ionized UV broadened emission lines. We made a model for two different distances. We choose a distance of 2 light days, the shortest distance of the BLR derived from reverberation mapping; and a distance of 20 light days, the distance of the BLR obtained by reverberation mapping of Hβ. For both distances a single ionization parameter is sufficient to describe both the X-ray

and UV lines. Although the covering factor and column density are different for the different distance models, the ionization parameter in the different distance models is the same. We thus conclude that there is a range in densities over the thickness of the broad line region. From the different covering factor and column density we conclude that we are looking through the edge of a rotationally flattened structure. These broadened X-ray emission lines should be quite common as stronger lines are detected in the *Chandra* LETGS spectrum of Mrk 279 and NGC 4151, and the XMM-*Newton* spectrum of IC 4329A.

9.2 Results on NGC 4593, IC 4329A and Ton 1388

9.2.1 NGC 4593

In Chapter 3 we analyze the LETGS and XMM-*Newton* spectra of NGC 4593. In the LETGS spectrum we detect a highly ionized absorber which causes a depression between $10 - 18$ Å. We detect also a much weaker lowly ionized absorber which is not in pressure equilibrium with the highly ionized absorber if we assume a similar spectral energy distribution (SED) to the SED of NGC 5548 and other AGN. In this spectrum an intermediate ionized absorber is very weak or missing. The missing medium ionization component is difficult to explain in both a model with clouds and a continuous density outflow. In a density stratified wind a highly ionized outflow could shield other outflows, such that we detect only highly and lowly ionized absorption. The RGS spectra are noisy, but consistent with the LETGS spectrum.

A timing analysis of the LETGS data showed that the hard X-ray power law component is more variable than the soft X-ray excess. At the end of the observation a flare occurred, for which the decay was not correlated to the change in the soft X-ray excess. The derived variability contradicts the theory that the detected hard X-ray continuum is produced by inverse Compton scattering of soft electrons from the accretion disk. The variability is consistent with the picture of magnetic flares. Several earlier observers (Dewangan et al. 2002; Turner et al. 2001) have detected similar variability properties.

9.2.2 IC 4329A

In Chapter 7 we analyze the XMM-*Newton* spectra of IC 4329A which is a Seyfert 1 galaxy seen nearly edge-on. From the reddening observed in the optical and the UV band, and the similarity of host galaxy properties with Ark 564 and NGC 3227, Crenshaw et al. (2001) conclude that this Seyfert has a dusty luke-warm absorber, i.e. an absorber including dust grains which has a rather low ionization parameter.

185

This dusty luke-warm absorber is located in the plane of the host galaxy at a distance greater than 100 pc from the nucleus, and is not related to the warm absorber observed in other Seyfert 1 galaxies. Indeed, in the X-ray band we detect absorption from the host galaxy. However, with the large effective area of the RGS we were able to detect a highly ionized absorber, similar to the warm absorber observed in other Seyfert 1 galaxies. The ionization structure of IC 4329A is similar to that of NGC 5548, with the caveat that for the lowly ionized absorber detected it is difficult to determine whether it is from the host galaxy or the warm absorber. We confirm earlier observations (Perola et al. 1999) that the hardness ratio for this source is independent of luminosity. This result differs from the hardness ratio results in other Seyfert 1 galaxies where in general the spectrum becomes softer with increasing luminosity.

9.2.3   TON 1388

In Chapter 8 we report the possible detection of intervening, intergalactic ionized gas, related to the Lyα absorbers detected in UV spectra. The LETGS spectrum is noisy and thus a spectrum with a higher signal-to-noise ratio is necessary to confirm the presence of these intervening absorbers. If confirmed, the absorption detected would then be a signature of highly ionized gas which is probably located in filaments between clusters of galaxies. Models show that part of the gas in these filaments must have a high temperature. This quasar does not have a strong warm absorber, and is thus an ideal source to study possible intervening absorbers. We measure an upper limits to the hydrogen column density of $10^{23.7}$ m^{-2} for an ionization parameter of $\xi = 100$ in units of 10^{-9} W m, about 1.5 orders of magnitude less than in NGC 5548.

9.3   Outlook

9.3.1   Current instrumentation

Further study is required to confirm that the ionization distribution in the case of NGC 5548 is continuous. A continuous ionization distribution model should be tested with spectra of other Seyfert 1 galaxies. Such a study should look for spectral variability and can be done with the spectral resolution of the current generation of X-ray spectrometers, but requires high signal-to-noise spectra. The spectral variability expected is different for a model with clouds than for a model with a density gradient. In the former all ionization parameters detected should vary simultaneously with a change in luminosity. In the latter only the column density, and possibly the ionization parameter of the lowly ionized and possible highly ionized absorber should vary with changes

in luminosity. Another result that needs further study is whether it is a general property of warm absorbers that most of the gas is highly ionized.

From low resolution spectra it was concluded that there is a one to one ratio between UV absorbers and X-ray absorbers; however, this conclusion should be tested with high resolution spectra. The model by Elvis (2000) predicts that in 10 to 15 % of Seyfert 1 galaxies we do not see the warm absorber, due to inclination angle of the absorber.

In this thesis we determined that if the distance of the absorber from the SMBH is at least 0.6 pc then the outflow with the highest velocity can escape the SMBH. The impact of these enriched outflows on the host galaxy or the intergalactic medium should be studied. An important question is whether the gas is able to leave the host galaxy, and/or whether it is stopped by the host galaxy, possibly triggering star formation.

9.3.2   Future instrumentation

As should always be the case, the conclusions obtained in this thesis should be tested with higher spectral resolution data when they become available. In particular the continuous ionization distribution model should be tested, since with higher resolution the distinction between three ionization components, five ionization components and a continuous ionization distribution will be more significant. Better spectral resolution will allow deblending of the different outflow velocity components, which now form a blend in the X-ray band. This will give the final proof whether all the velocity components detected in absorption in the UV band have a counterpart in the X-ray band, and are thus observed over a wide range in ionization parameters. These five different outflow velocities are difficult to explain in any model with only one outflow structure, such as both models discussed in Chapter 1. This will also allow us to study the ionization distribution of each velocity component, which is now only rarely possible.

An important question related to the ionization distribution of the absorber is whether the distribution has a cut-off at the high ionization part, or whether most of the gas is completely ionized. The conclusion about the highest ionized absorber is important in estimating the mass that is outflowing in these absorbers. This result will also allow us to determine whether the highest ionized and most massive absorber is in pressure equilibrium with the lower ionized absorbers. If not, then pressure equilibrium models are ruled out, as this highest ionized component should pressure confine the other absorbers. These questions are well suited to be studied with the Astro-E2 satellite, as it will obtain high spectral resolution spectra for the high energies, using micro-calorimeters.

Higher signal-to-noise ratio data are needed to confirm and study in detail the broadened emission lines observed in some X-ray spectra. The fraction of Seyfert 1 galaxies that do show these broadened X-ray emission lines should be determined.

This should allow to determine if these broadened emission lines are consistent with the ionization measured from the optical and the UV spectra as was concluded in Chapter 6. High signal-to-noise ratio and high spectral resolution will allow us to distinguish between broadened and relativistically broadened emission lines in the soft X-ray spectrum.

An obvious open question is the dependence of the spectrum on the inclination angle of the accretion disk, which can distinguish between both models described in Chapter 1. However, the measurement of the inclination angle of the accretion disk is complicated in the absence of relativistically broadened emission lines. ASTRO-E2 will carry onboard a hard X-ray telescope that is sensitive between 10 and 700 keV, and which can be used simultaneously with the soft X-ray telescope. This will allow for the study of the reflection component in AGN, and as a result will put much tighter constraints on the relativistically broadened Fe Kα emission line. If relativistically broadened Fe Kα lines are detected they will yield a direct measurement of the inclination angle of the inner accretion disk and thus allow to distinguish between the standard model for AGN (Urry & Padovani 1995) and the model be Elvis (2000).

More sensitive instruments are needed to confirm the reported detections of the warm hot intergalactic medium. These future observations should constrain the ionization mechanism (collisionally ionized or photoionized), elemental abundances and the total amount of baryons in such a warm state. This in turn will determine if the warm hot intergalactic medium can account for the locally missing baryons.

9.3.3 Atomic data

As already mentioned in Chapter 1 there are uncertainties in the atomic data and codes used for fitting and modeling the X-ray spectra. Measuring the dielectronic recombination rates for iron are especially important, as now only estimated oscillator strengths for Fe VI to Fe XV are known. Accurate iron dielectronic recombination rates will allow iron to be fitted with the rest of the ions, without the noticed overabundance for lowly ionized iron. Fitting iron alone will allow us to derive strong constraints on the ionization distribution of the absorber due to the large ionization range sampled, and the result is independent of elemental abundances. The calculated wavelengths for lines at wavelengths above 60 Å, and inner shell lines should be improved. This will allow us to use all the ions in the analysis, and to study possible abundance effects more easily.

References

Arav, N., Korista, K. T. & de Kool, M., 2002, ApJ, 566, 699

Arav, N., Kaastra, J. S., Steenbrugge, K. C., et al., 2003, ApJ, 590, 174

Behar, E., Rasmussen, A. P., Blustin, A. J., et al., 2003, ApJ, 599, 933

Crenshaw, D. M. & Kraemer, S. B., 2001, ApJ, 562, 29

Crenshaw, D. M., Kraemer, S. B., Gabel, J. R., et al., 2003, ApJ, 594, 116

Dewangan, G. C., Boller, Th., Sing, K. P. & Leighly, K. M., 2002, A&A, 390, 65

Elvis, M., 2000, ApJ, 545, 63

Mathur, S., Elvis, M. & Wilkes, B., 1995, ApJ, 425, 230

Perola, G. C., Matt, G., Cappi, M., et al., 1999, A&A, 351, 937

Proga, D., Stone, J. M. & Kallman, T. R., 2000, ApJ, 543, 686

Reeves, J. N., Nandra, K., George, I. M., et al., 2004, ApJ, 602, 648

Turner, T. J., Romano, P., George, I. M., et al., 2001, ApJ, 561, 131

Urry, C. M. & Padovani, P., 1995, PASP, 107, 803

Hoofdstuk 10

Nederlandse samenvatting

10.1 Actieve melkwegstelsels

Melkwegstelsels bestaan uit vele miljarden sterren die door zwaartekracht bijeen gehouden worden. Het licht van de meeste melkwegstelsels is afkomstig van de individuele sterren in het melkwegstelsel. Er bestaan ook melkwegstelsels die meer licht uitstralen dan uitsluitend het licht van de sterren. Uit foto's met een hoge ruimtelijke resolutie blijkt dat het extra licht afkomstig is uit een heel klein gebied in de kern. Deze stelsels worden actieve melkwegstelsels genoemd, en mijn proefschrift gaat over deze stelsels. De extra lichtkracht wordt verklaard door accretie van gas op een zwart gat. Over het algemeen wordt aangenomen dat alle grote melkwegstelsels zo'n actieve fase gehad hebben. Dit wordt afgeleid uit onder andere het feit dat de meeste actieve melkwegstelsels ver van ons verwijderd zijn, wat door de eindige snelheid van het licht betekent dat we ze op jongere leeftijd zien dan de meer nabij gelegen melkwegstelsels. Een ander argument is dat gewone melkwegstelsels, zoals het onze, ook zware zwarte gaten in hun centrum hebben. Ze zijn alleen niet actief doordat er weinig of geen accretie plaats vindt. Aangenomen wordt dat deze zwarte gaten hun huidige massa gekregen hebben door accretie in een vroeger tijdperk.

    Algemeen wordt aangenomen dat de lichtkracht van actieve stelsels geproduceerd wordt door de accretie op een zeer zwaar ($10^6 - 10^9$ zonsmassa) zwart gat. Een zwart gat is een object dat zo compact is dat niets, ook geen licht, eruit kan ontsnappen. Gas, of sterren die te dicht langs het zwarte gat passeren, zullen er onherroepelijk in vallen. Indien een ster in vrije val in het zwarte gat valt, zal er maar een zeer beperkte hoeveelheid energie ontsnappen. Indien echter het gas een accretieschijf vormt, doordat het

gas een groot impulsmoment heeft, zullen er enorme hoeveelheden energie vrijkomen. Namelijk, door de constante wrijving in de schijf verliest het gas energie. Dit energie-verlies wordt voor een groot deel uitgezonden als hoog-energetische fotonen, maar het kan ook gebruikt worden om jets te vormen.

Quasars en Seyfert melkwegstelsels vormen elk een subgroep binnen de groep van actieve melkwegstelsels. In een quasar zendt de kern zo veel licht uit, dat het licht van het melkwegstelsel waartoe het behoort, overstraald wordt. Op vroegere opnames lijken deze stelsels dan ook op sterren, vandaar de naam quasi stellar radio sources, of kortweg quasars. In dit proefschrift wordt de quasar Ton 1388 bestudeerd.

10.1.1 Seyfert stelsels

Seyfert stelsels zijn een groep van actieve melkwegstelsels, die door Seyfert in 1943 geclassificeerd zijn. Seyfert stelsels hebben een relatief lage lichtkracht in vergelijking met andere actieve melkwegstelsels. Uniek aan Seyfert stelsels zijn de waargenomen verbrede emissielijnen in optische spectra. Deze groep wordt nog onderverdeeld in Seyfert 1 en Seyfert 2 stelsels, al naargelang de breedte van de waargenomen emissie-lijnen. Seyfert 1 en Seyfert 2 stelsels vertonen "nauwe" lijnen in hun optische spec-tra, gevormd door gas met snelheden van ongeveer 1000 km s^{-1}. Seyfert 1 stelsels hebben daarnaast ook nog sterk verbrede lijnen, waaruit wordt afgeleid dat het gas snelheden heeft van ongeveer 10 000 km s^{-1}. Seyfert 2 stelsels hebben deze brede lijnen niet, maar in sommige Seyfert 2 stelsels zijn deze sterk verbrede emissielijnen toch waargenomen in spectra genomen met een optisch polarisatiefilter. Hieruit leidt men af dat de emissie afkomstig van het gas dat de brede lijnen uitstraalt, verstrooid wordt door botsingen met deeltjes die zich tussen de bron en de waarnemer bevinden. De helft van de Seyfert 1 stelsels vertonen in de Röntgenband een absorptiespectrum, met daarnaast enkele smalle en brede emissielijnen. Seyfert 2 stelsels hebben een spec-trum met uitsluitend nauwe emissielijnen in het Röntgengebied, en maar een heel zwak continuüm. In dit proefschrift worden de Seyfert 1 stelsel NGC 5548, NGC 4593 en IC 4329A bestudeerd.

Algemeen wordt aangenomen dat het verschil tussen Seyfert 1 en Seyfert 2 stelsels, wordt veroorzaakt door een verschil in de hoek waaronder het melkwegstelsel wordt waargenomen. In Seyfert 2 stelsels kijken we door een dikke laag stof en koud gas, die de Röntgenstraling volledig absorbeert. In Seyfert 1 stelsels kijken we direct naar de kern waardoor we de straling die uitgezonden wordt door de accretieschijf en het gas vlakbij het zwarte gat waarnemen. Er is soms een dunne laag van gas tussen de waarnemer en de accretieschijf dat die straling op bepaalde golflengtes absorbeert.

Er zijn twee modellen die verschillende aspecten over de kern van een melkweg-stelsel beschrijven. Beide modellen verklaren de verbreding van de emissielijnen door

192

Doppler verbreding: het gas dat naar de waarnemer toedraait is blauw verschoven, het gas dat van ons wegdraait is rood verschoven. Hoe sneller het gas draait, hoe groter de verschuiving en dus hoe breder de lijn. Keplers derde wet geeft een relatie tussen de afstand van het gas en de snelheid waarmee het ronddraait. Hoe kleiner de afstand tot het zwarte gat, hoe sneller het gas ronddraait. In het ene model ziet de waarnemer het oppervlak van de accretieschijf als een Seyfert 1 stelsel wordt waargenomen. In een Seyfert 2 stelsel zouden we de zijkant van de accretieschijf zien, indien deze niet geabsorbeerd was. Het absorberende, koude gas ligt in een band rond de accretieschijf voor beide soorten melkwegstelsels. De absorptie waargenomen in dit model wordt de Röntgenspectra van Seyfert 1 stelsels niet direct verklaard. We kunnen aannemen dat het absorberende gas zich in wolken vrij ver van het zwarte gat bevindt, op de afstand waar ook de nauwere emissielijnen worden uitgezonden.

In het andere model zien we een Seyfert 1 stelsel zonder absorptie als we het oppervlak van de de accretieschijf waarnemen, en een Seyfert 1 stelsel met absorptie als we de accretieschijf onder een grotere hoek waarnemen. De absorptie waargenomen in Seyfert 2 stelsels wordt veroorzaakt door enkele wolken koud gas, welke niet noodzakelijk als een band rond de accretieschijf liggen. De absorptielijnen waargenomen in Röntgenspectra worden gecreëerd door wolken in een uitstromende wind. De wind wordt door stralingsdruk omgebogen. In deze wind bevinden zich ook de wolken die de brede emissielijnen uitstralen. Uit de verschillen tussen beide modellen is het duidelijk dat het gas dat zich in de onmiddellijke omgeving van het zwarte gat bevindt nog niet goed begrepen is.

10.2 Röntgenspectra van actieve melkwegstelsels

In dit proefschrift gebruiken we de eerste generatie Röntgen instrumenten met hoge spectrale resolutie aan boord van de *Chandra* en XMM-*Newton* satellieten om actieve melkwegstelsels en in het bijzonder Seyfert 1 stelsels te bestuderen. De accretieschijf straalt een continuüm van laag-energetisch Röntgenfotonen en extreme UV-fotonen uit. De extreme UV-fotonen worden door ons Melkwegstelsel geabsorbeerd. Röntgenspectroscopie is dus de ideale manier om de onmiddellijke omgeving van het zwarte gat te bestuderen.

10.2.1 Conclusies voor het Seyfert 1 stelsel NGC 5548

Drie hoofdstukken in dit proefschrift behandelen het Seyfert 1 stelsel NGC 5548. Dit is één van de Seyfert 1 stelsels die goed bestudeerd zijn en waarvan hoge kwaliteit optische en UV-spectra bestaan. Voor dit stelsel hebben we verscheidene Röntgenspectra

van zeer hoge kwaliteit. Door combinatie van de nieuwe gegevens verkregen uit Röntgen-spectra en de kennis over dit stelsel uit al dan niet gelijktijdige UV-spectra, zijn de meeste conclusies in dit proefschrift gebaseerd op de studie van dit melkweg-stelsel.

Overeenkomst tussen absorptie waargenomen in UV- en Röntgenspectra

Een belangrijke vraag is of de absorptie waargenomen in Röntgen- en UV-spectra, afkomstig is van hetzelfde medium, of van verschillende gaslagen. Het verschil geme-ten in de kolomdichtheden uit beide spectra is een belangrijke reden om aan te ne-men dat beide absorptiecomponenten van een verschillend gas afkomstig zijn. De kolomdichtheid is een maat voor de hoeveelheid ionen in een kolom tussen de waarne-mer en de emissiebron. De kolomdichtheden gemeten in UV-spectra zijn ongeveer een factor tien kleiner dan deze gemeten in Röntgenspectra.

De ionisatiegraad van de absorptie waargenomen in UV-spectra werd geacht lager te zijn dan de ionisatiegraad gemeten in lage spectrale resolutie Röntgenspectra. We hebben, gebruikmakend van hoge resolutie spectra van NGC 5548 ook laag-geïoniseerde ionen gedetecteerd, zoals O VI, C IV en N V. Lijnen van deze ionen worden ook in UV-spectra waargenomen. We hebben verder aangetoond dat de snel-heidsstructuur van de absorptie waargenomen in UV- en Röntgenspectra dezelfde is, ondanks de soms grote verschillen in ionisatiegraad. We concluderen dat de absorptie waargenomen in UV- en Röntgenspectra dus van hetzelfde gas afkomstig is.

Ionisatieverdeling van het waargenomen gas

We hebben aangetoond dat het overgrote deel van het gas hoog-geïoniseerd is. We hebben geprobeerd de verdeling van de ionisatiegraad van het absorberende gas te bepalen. Zijn er enkele verschillende absorptiecomponenten met ieder een eigen io-nisatiegraad, of is er een continue verdeling van ionisatietoestanden? Aangezien we van laag-geïoniseerd tot bijna volledig geïoniseerd ijzer waarnemen, kunnen we uit-sluiten dat er maar één ionisatiegraad is. Beide modellen besproken in 10.1.1 voor-spellen dat de ionisatieverdeling discontinu is, één ionisatiegraad per wolk. Compo-nenten met een verschillende ionisatiegraad zijn in deze modellen in drukevenwicht met elkaar. Het hoogst geïoniseerde gas vormt de wind, terwijl de lager geïoniseerde componenten als wolken in deze wind bestaan. Door het drukevenwicht zijn de wolken stabiel en hebben een lange levensduur. In hoofdstuk 5 concluderen we dat de absorptie evengoed gemodelleerd kan worden met een continue ionisatieverdeling. In hetzelfde hoofdstuk verklaren we de continue ionisatieverdeling met een wind die een dichtheid-stratificatie heeft loodrecht op de uitstroomrichting.

194

Op grond van onze hoge-kwaliteit spectra besluiten we dat de laagst geïoniseerde component niet in drukevenwicht kan zijn met de andere ionisatiecomponenten. We tonen in hetzelfde hoofdstuk ook aan dat de snelheidsstructuur voor alle ionisatiepa- rameters hetzelfde is. Dit toont duidelijk een verwantschap aan tussen het laag- en hoog-geïoniseerde gas, en is een reden om het continue ionisatieverdeling model te prefereren.

Geometrie van de wind

Een verschil tussen beide modellen, is de openingshoek van de wind. Een model voor- spelt een grote openingshoek van ongeveer 60°, waarin er enkele kleinere wolken zijn. De grote openingshoek is nodig om het aantal Seyfert 1 stelsels waar we absorptie waarnemen te verklaren. Het andere model voorspelt een nauwe wind, met een ope- ningshoek van slechts 6°. Het aantal Seyfert 1 stelsels met absorptie wordt verklaard door een wind die afbuigt. In hoofdstuk 4 tonen we aan, dat onder de aanname dat de accretie in een evenwichtstoestand gebeurt, de wind een kleine openingshoek heeft. Dit resultaat prefereert duidelijk het tweede model.

Kan het gas ontsnappen?

Uit de gemeten blauwverschuiving van de absorptielijnen weten we dat het gas wegstroomt van het zwarte gat. In Hoofdstuk 5 berekenen we de afstand die het gas moet hebben om te kunnen ontsnappen aan de zwaartekracht van het zwarte gat. Deze afstand is voor het gas met de grootste uitstroomsnelheid ongeveer 0.58 pc of 1.9 licht- jaar, een erg kleine afstand tot het zwarte gat. Indien het gas kan ontsnappen uit het gravitatieveld van het zwarte gat, zijn er twee mogelijkheden. Het verlaat het melk- wegstelsel en verrijkt het intergalactisch medium. De wind is verrijkt met metalen, ele- menten die in het oorspronkelijke gas van het intergalactisch medium niet voorkomen. De wind komt door wrijving tot stilstand in het melkwegstelsel en zal zijn energie overdragen op het interstellair gas. De overdracht van energie leidt mogelijk tot ster- vorming.

Verbrede emissielijnen

In hoofdstuk 5 en 6 tonen we aan dat ook in Röntgenspectra verbrede emissielij- nen worden waargenomen. Deze verbrede lijnen lijken op de verbrede emissielijnen waargenomen in optische en UV-spectra. In Röntgenspectra zijn deze lijnen echter erg zwak en moeilijk te detecteren. Uit modellering van deze lijnen concluderen we, dat ze dezelfde ionisatieparameter en verbreding hebben als de gelijktijdig waargenomen

195

verbrede UV lijnen. Dit betekent dat de verbrede lijnen waargenomen in Röntgen- en UV-spectra uitgestraald worden door hetzelfde gas, en dus eenzelfde afstand hebben tot het zwarte gat. Uit lichtkrachtvariaties waargenomen in optische en UV-spectra leidt men een afstand tussen de 2 en 20 lichtdagen af. Indien deze emissie over al deze afstanden uitgestraald wordt, dan heeft het gas dezelfde ionisatiegraad op alle afstanden. Dit betekent dat de dichtheid van het gas verandert met de afstand tot het zwarte gat. Uit de modellen vinden we verder dat de fractie van het gas dat de accretieschijf bedekt en de kolomdichtheid groter moeten zijn voor een kleinere afstand. Uit deze twee feiten concluderen we dat we door de rand van een door rotatie afgeplatte wolk kijken.

10.2.2 Conclusies voor de overige bestudeerde melkwegstelsels

NGC 4593

In Röntgenspectra van het Seyfert 1 stelsel NGC 4593 detecteren we enkel zeer hoog- en zeer laag-geïoniseerd gas (Hoofdstuk 3). NGC 4593 is een uitzondering op andere Seyfert 1 stelsels, waar middelmatig- tot hoog-geïoniseerd gas een belangrijke absorptiecomponent is. Uit de lichtkromme blijkt dat het hoog-energetische Röntgencontinuüm veranderlijker is dan het laag-energetische Röntgencontinuüm. Dit is in tegenstelling tot de theorie waarin de hoog-energetische Röntgenfotonen het resultaat van invers-Compton verstrooiing zijn. Door de verstrooiing verkrijgen de laag-energetische fotonen, uitgestraald door de accretieschijf, een hogere energie. Uit de vervaltijd van een waargenomen lichtkrachtflits leiden we af dat magnetische reconnectie verantwoordelijk kan zijn voor het veranderlijke hoog-energetische Röntgencontinuüm.

IC 4329A

In de Röntgenspectra van het Seyfert 1 stelsel IC 4329A (Hoofdstuk 7) detecteren we absorptie van zowel gas dat zich nabij het zwarte gat bevindt, als neutraal gas dat zich in de schijf van het stelsel bevindt. Het neutrale gas bevindt zich op enkele duizenden lichtjaar van het zwarte gat. In het spectrum detecteren we ook niet verschoven absorptielijnen van geïoniseerd gas. Dit betekent dat het gas zich in ons Melkwegstelsel of in de onmiddellijke omgeving ervan bevindt, en dus niet afkomstig is van IC 4329A. We tonen aan dat met hoge spectrale resolutiespectroscopie het mogelijk is om de absorptie gegenereerd door deze verschillende media te onderscheiden.

Het gas dat zich in de nabijheid van het zwarte gat bevindt, heeft dezelfde eigenschappen als het gas gedetecteerd in andere Seyfert 1 stelsels, zoals NGC 5548. Dit weerlegt de conclusie uit een vergelijkend breedband UV studie, dat dit stelsel enkel ab-

sorptie vertoont van een stoflaan in de schijf van het melkwegstelsel. In Röntgenspectra detecteren we ook enkele verbrede lijnen. Echter, door de verschillende absorptiecomponenten, is het spectrum te complex om te kunnen concluderen of deze lijnen van hetzelfde gebied komen als de verbrede lijnen gedetecteerd in UV-spectra, of relativistisch verbreed zijn.

Ton 1388

In het Röntgenspectrum van de quasar Ton 1388, bestudeerd in Hoofdstuk 8, detecteren we geen absorptie van gas dat zich nabij het zwarte gat of in het melkwegstelsel bevindt. Er zijn echter enkele absorptielijnen in het spectrum, geproduceerd door hoog-geïoniseerd gas dat tussen ons en de quasar ligt. Kosmologische modellen voorspellen dat een groot deel van de baryonische massa (de deeltjes waaruit de Aarde en mensen bestaan) opgeslagen is in filamenten tussen melkwegstelsels en clusters van melkwegstelsels. Dit gas is bij hoge roodverschuiving (dus in het jonge heelal) te zien als neutraal waterstof gas. Echter, lokaal (dus in het huidige heelal) wordt er veel minder neutraal waterstof gedetecteerd. Het gas wordt in de filamenten nog steeds verhit, en is nu deels hoog-geïoniseerd. Dit hoog-geïoniseerde gas is alleen te detecteren met Röntgenspectrometers, en kan dan ook nu pas voor het eerst bestudeerd worden.

Curriculum Vitae

Op 9 oktober 1976 ben ik geboren te Gent (België). In mei 1994 voltooide ik mijn middelbare studie aan het Koninklijk Atheneum III te Gent, in de richting wiskunde-wetenschappen. Daarna volgde ik vier jaar de opleidingen sterrenkunde en fysica aan Boston University. In mei 1998 behaalde ik aldaar summa cum laude een Bachelors of Arts diploma in sterrenkunde en fysica, met de vermelding "with distinction". Mijn Bachelors of Arts thesis onderzoek was naar de bewegingen van deeltjes in de magnetosfeer van de aarde, gebruikmakend van archief data van de CCRES satelliet. Dit onderzoek was onder begeleiding van prof. dr. Hughes. In september 1998 vervolgde ik in Leiden mijn studie sterrenkunde. Tijdens de doctoraalfase heb ik onder leiding van dr. Jos de Bruijne, dr. Ronnie Hoogerwerf en prof. dr. de Zeeuw onderzoek gedaan naar de radiële snelheden van mogelijke leden van de OB associatie Perseus 2.

Op 1 oktober 2000 begon ik met mijn promotie onderzoek aan het SRON National Institute for Space Research onder leiding van dr. Kaastra en prof. dr. Schilizzi. Voor mijn proefschrift heb ik Röntgen-spectra met hoog scheidend vermogen van actieve melkwegstelsels bestudeerd. Dit is een nieuw onderzoeksterrein, enkel mogelijk door de lancering van de *Chandra* en XMM-*Newton* satellieten. De resultaten van dit onderzoek zijn beschreven in deze thesis. Voor mijn onderzoek ben ik op werk bezoek geweest te Columbia University (USA), Leicester University (UK), University of California Berkeley (USA), University of Colorado Boulder (USA) en Center for Astrophysics (USA). De resultaten van mijn onderzoek heb ik gepresenteerd op conferenties in Nederland, US, UK, Duitsland en Frankrijk. Op Corsica (Frankrijk) heb ik een zomer school over zwarte gaten in het heelal gevolgd, waar ik ook onze resultaten presenteerde.